

The formation of the faintest galaxies in cosmological simulations: from the impact of primordial magnetic fields to the metal enrichment of present day dwarfs by first stars

Présentée le 10 février 2023

Faculté des sciences de base
Laboratoire d'astrophysique
Programme doctoral en physique

pour l'obtention du grade de Docteur ès Sciences

par

Mahsa SANATI

Acceptée sur proposition du jury

Prof. F. Carbone, président du jury
Dr Y. Revaz, directeur de thèse
Prof. M. Jeon, rapporteuse
Prof. D. Schleicher, rapporteur
Dr J. Loizu, rapporteur

My goal is simple. It is a complete understanding of the universe, why it is as it is and why it exists at all.

- Stephen Hawking

Acknowledgment

I would like to thank:

Yves for being the best supervisor anyone could wish for.

Pascale and Jennifer, for their support when things get difficult and for their scientific insights.

The members of my jury Prof. Jeon, Prof. Schleicher, and Dr. Loizu for their comments and the interesting discussion.

Prof. Jean-Paul Kneib and Prof. Michaela Hirschmann for funding my PhD.

Cheng, Florian, Mladen and Nicolas for answering my innumerable questions about how computers work and how galaxies are observed, with great patience and expertise.

My fellow PhD students and Post-Docs at EPFL and the Observatory of Geneva for all the good memories. It was a true privilege to work with such an exceptional group of people.

Prof. Daniel Pfenniger, for his support to start my scientific career.

Dr. Patrick Charbon, for his invaluable guidance in difficult moments.

Gunnel, Hugues and all of my friends who made Switzerland a second home to me.

My family for their love and kindness which knows no boundaries.

Jonas for his superpower in transforming tragic moments to comedy.

I would like to dedicate this dissertation to Woman, Life, Freedom.

Résumé

Le modèle cosmologique standard prédit un assemblage hiérarchique des structures cosmiques. Dans cette théorie, l'un des principaux défis consiste à comprendre quel est le rôle des plus petites galaxies observées, presque indiscernables dans la formation de galaxies plus massives telles que la nôtre, la Voie lactée. Est-ce que ces galaxies dites galaxies "naines" ressemblent-elles aux premières galaxies formées dans l'Univers ? Leurs petites tailles, la prépondérance de matière noire ainsi que leur profile de masse sont des arguments en faveur de cette hypothèse. Leurs caractéristiques en font d'excellentes candidates pour tester indirectement les modèles cosmologiques aux petite échelle mais également la nature de la matière noire.

Comparativement aux autres galaxies plus massives, les galaxies naines ont été formé de manière simple. Elle sont majoritairement composées de vieilles étoiles. Quelques milliards d'années après le Big-Bang, durant la période connue sous le nom d'Époque de Réionisation, elles ont formé les premières étoiles et ont alors joué un rôle majeur dans l'illumination de l'Univers primordial. Contrairement à la majorité des systèmes plus grands, les galaxies naines actuelles n'ont subi que peu ou pas d'évolution après l'Époque de réionisation. Leur propriétés témoignent ainsi des conditions existantes durant l'univers primitif.

Dans la première partie de cette thèse, à l'aide de simulations cosmologiques, nous montrerons l'impact des conditions initiales générées dans l'Univers primordial, en particulier les champs magnétiques primordiaux, sur la formation et l'évolution des galaxies naines. Nous effectuerons deux types de simulations : (i) des simulations ne prenant en compte que la matière noire, utilisées pour calculer l'abondance, la masse et la distribution des halos noirs hébergeant des galaxies naines, et (ii) des simulations hydrodynamiques utiles pour vérifier les propriétés des populations stellaires dans chaque galaxie. Nous montrerons que l'impact des champs magnétiques primordiaux sur la formation des galaxies est double : 1. Le nombre de halos de matière noire autour de la Voie lactée capables d'héberger des galaxies naines est augmenté. 2. La formation plus précoce d'étoiles ainsi qu'un taux plus élevé de formation stellaire génère une grande quantité de photons ionisants à haut "red-shift". Grâce à cette étude, nous montrerons que les champs magnétiques primordiaux ont un rôle de premier plan dans l'initiation de la formation des structures dans l'Univers. Ceci

nous permettra d’obtenir de fortes contraintes sur les propriétés des champs magnétiques primordiaux.

L’effet direct des champs magnétiques primordiaux sur la formation des galaxies d’une part, et l’impact direct du support de pression magnétique sur le milieu interstellaire des galaxies d’autre part, restent encore évasifs. Dans cette seconde partie, nous efforcerons de tenir compte de ces deux aspects simultanément. Nous effectuerons un ensemble de simulations magnéto-hydrodynamiques de galaxies naines peu lumineuses. Dans ces simulations, le champ magnétique initial sera choisi de manière uniforme et nous inclurons l’effet des champs primordiaux tout en modifiant la cosmologie classique. Dans cette partie, nous concluons qu’en raison du puit de potentiel peu profond caractéristique des naines de faible masse, contrairement à celui des galaxies plus massives, la pression magnétique peut non seulement diminuer considérablement la masse stellaire, mais également retarder le début de la formation d’étoiles d’environ 1 milliard d’années. Cet effet peut entièrement empêcher l’effondrement des nuages de gaz dans les halos de masse les plus faibles et entraîner une augmentation du nombre de halos sombres à redshift de 0. Cependant l’impact du champ magnétique originel primordial domine comparativement et impacte à long terme.

Dans la troisième partie de cette thèse, tirant parti des expériences de simulations de galaxies naines et des résultats des deux premières parties, nous nous attarderons sur certaines des caractéristiques subtiles des plus faibles galaxies naines, quasi imperceptibles: les naines ultra faibles (UFDs). Nous explorerons comment les premières générations d’étoiles sans métaux (Pop III) pourraient augmenter la métallicité moyenne de ces petites galaxies peu lumineuses. En réalisant des simulations zoom combinant l’évolution chimique et la dynamique, nous identifierons les conditions nécessaires à la formation des premières étoiles dans leurs mini-halos. Nous dériverons ainsi des contraintes sur les schémas d’éjection de métal. Dans ce travail, nous montrons que les étoiles massives (Pop III) qui explosent en tant que supernovae par production de paires, augmentent la teneur en métaux des UFDs. Cependant, étant très rares et parfois absents dans les UFDs les plus faibles, ces supernovae ont un impact limité sur la partie à basse luminosité de la relation métallicité-luminosité. En conclusion, malgré un nombre limité de membres d’UFDs confirmés par spectroscopie, l’analyse de ce travail révèle que le plateau observé relativement riche en métaux est absente des modèles.

Prises ensembles, ces trois parties ont augmenté notre connaissance des premières étapes de la formation des galaxies. Comment la cosmologie de l’Univers primordial, en particulier les champs magnétiques primordiaux, souvent négligés dans les modèles, impactent la formation et l’évolution des premières galaxies? Quel est l’impact des champs magnétiques sur le milieu interstellaire et l’histoire de la formation stellaire des galaxies naines? Quel est l’impact des premières étoiles sur l’enrichissement en métaux qui se produit au cours du processus de formation des galaxies? Ces questions ont été explorées dans cette thèse

de doctorat.

Mots-clés

Formation des galaxies, galaxies naines, galaxies naines ultra-faibles, réionisation, premières étoiles, champs magnétiques, champs magnétiques primordiaux, simulations magnétohydrodynamique, étoiles de population III, supernova à instabilité de paire

Abstract

In the theory of the bottom-up assembly of cosmic structures, one of the main challenges is to connect the smallest, most inconspicuous galaxies we observe today to the building blocks of more massive galaxies such as our own, the Milky Way. Do these so-called dwarf galaxies resemble the first galaxies formed in the Universe? Their small size and the preponderance of dark matter in dwarf galaxies, as well as their inner mass distribution, reinforce this idea. These characteristics, on the other hand, make them excellent probes for cosmological models on small scales and the nature of dark matter. Having the simplest assembly histories of all galaxies, dwarfs are also dominated by old stellar populations. They hosted the first stars and played a major role in lighting up the dark Universe, a few billion years after the Big Bang during the period known as the Epoch of Reionization. Unlike essentially all larger systems, the present-day dwarfs underwent little to no further evolution after the reionization and constitute pristine relics of the early-Universe.

In the first part of this thesis, using cosmological simulations, we show the impact of initial conditions generated in the early Universe, particularly primordial magnetic fields, on the formation and evolution of dwarf galaxies. We perform two types of simulations: (i) dark matter only simulations, used to compute the abundance, mass and distribution of dark halos hosting dwarf galaxies, and (ii) hydrodynamical simulations to check the properties of stellar populations in each galaxy. We show that the impact of primordial fields on galaxy formation are twofold: 1. The number of dark halos around the Milky Way able to host dwarf galaxies is boosted. 2. An earlier onset of star formation plus a higher rate of forming stars induces a large amount of ionizing photons at high redshifts. Through this work we show that primordial magnetic fields have a significant role in initiating the structure formation in the Universe, and obtain strong constraints on the properties of primordial magnetic fields.

The net effect of primordial magnetic fields on galaxy formation on the one hand, and the direct impact of magnetic pressure support on the interstellar medium of galaxies, on the other hand, still remains elusive. Following the result obtained in the first part of this thesis, we then address the challenge of accounting for both aspects, simultaneously. In this study, we generate a set of magneto-hydrodynamical simulations of faint dwarf galaxies. The magnetic field in these simulations is initialized to uniform values and we include the

effect of primordial fields through modifying the classical cosmology. We conclude that because of the shallow potential well in low mass dwarfs, contrary to that of more massive galaxies, magnetic pressure not only can immensely decrease the stellar mass, but also can delay the onset of star formation by ~ 1 Gyr. This effect can entirely prevent the collapse of gas clouds in the lowest mass halos and result in an increased number of dark halos at redshift $z = 0$. Yet the impact of primordially sourced magnetic field dominates over its later-time impacts.

In the third part of this thesis, leveraging experiences in dwarf galaxy simulations, and the results obtained in the first two parts, we target the elusive characteristics of the faintest galaxies, ultra faint dwarfs (UFDs). We explore how the first generations of metal-free stars (Pop III) could increase the mean metallicity of those small and faint galaxies. Running zoom-in chemo-dynamical simulations, we identify the necessary conditions for the formation of first stars in their host mini-halos and derive constraints on the metal ejection schemes. In this work, we show that massive Pop III stars which explode as energetic pair-instability supernovae increase the metal content of UFDs. However, being very rare and sometimes absent in the faintest UFDs, they have a limited impact on the global faint end of the metallicity-luminosity relation. In conclusion, despite a limited number of spectroscopically confirmed members of UFDs, the analysis in this work reveals that the metal-rich tail is missing in the models.

Taken together these three parts have increased our knowledge of the early stages of galaxy formation. How the cosmology in the early-Universe, in particular primordial magnetic fields, which are frequently neglected in models, impact the formation and evolution of the first galaxies. What is the impact of magnetic fields on the interstellar medium and the star formation history of dwarf galaxies? What is the impact of first stars on the metal-enrichment occurring during the process of galaxy formation? These question have been explored in this PhD thesis.

Keywords

Galaxy formation, dwarf galaxies, ultra-faint dwarf galaxies, magnetic fields, primordial magnetic fields, magnetohydrodynamical simulations, reionization, population III stars, pair-instability supernovae, chemo-dynamical simulations

Contents

	i
Acknowledgment	iii
Résumé	v
Abstract	ix
1 Introduction	1
1.1 Cosmology and the Early Universe	2
1.2 Matter power spectrum	3
1.3 Hierarchical structure formation	9
1.4 The Success of Λ CDM	10
2 Dwarf galaxies	13
2.1 Classification	15
2.2 Dwarf galaxies as probes for dark matter	15
2.2.1 Λ CDM challenges in small scales	16
2.2.2 Λ CDM alternatives	21
2.3 Dwarf galaxies as hosts of first stars	27
2.3.1 First star formation	27
2.3.2 Environment of first stars	28
2.3.3 Initial mass function	31
2.3.4 First supernovae	34
2.3.5 Chemical evolution of primordial gas	38
3 Primordial magnetic fields	41
3.1 Generation of Primordial magnetic fields	43
3.2 Primordial magnetic field power spectrum	44
3.3 Magnetic matter power spectrum	45
3.4 Observational Signatures	48
4 Numerical Techniques	55

4.1	Gravity	55
4.1.1	Gravity calculation	56
4.1.2	Tree particle-mesh algorithm	57
4.2	Gas dynamics	59
4.2.1	Smoothed particle hydrodynamics	60
4.2.2	Finite volume discretization	66
4.3	Time integration	67
5	Constraining the primordial magnetic field	69
6	Dwarf galaxies in a primordially magnetized Universe	91
7	First stars in the faintest dwarf galaxies	107
8	Conclusions & Prospects	125
8.1	Summary	125
8.2	Outlook	128
8.2.1	The impact of primordial magnetic fields on reionization	128
8.2.2	New probe for modifications to the Λ CDM cosmology	130
8.2.3	Pre-enrichment of dwarfs before the formation of the Milky Way	131
9	Bibliography	133
10	Annex	145

Chapter 1

Introduction

Understanding the formation of first galaxies and the emergence of the first generation of stars, is one of the most interesting frontiers in modern cosmology. With the new window that James Webb Space Telescope (JWST) and The Square Kilometre Array (SKA) open on the young Universe, a few billion years after the Big Bang, theoretical models are needed to understand the physics at work in this poorly-explored epoch.

For studying these early stages in the formation of the Universe, the faintest objects in the galactic zoo - the dwarf galaxies - attract a great deal of attention. The combination of their proximity, their small size and the preponderance of dark matter in dwarfs, make them extremely valuable laboratories for testing the key predictions of the standard model of cosmology, the Λ +CDM (Λ CDM) model. The abundance and physical properties of dwarf galaxies are among the most fundamental predictions of the Λ CDM. In addition, the dark halo of dwarf galaxies provide one of the smallest scale probes for the nature of dark matter, reachable in sub-galactic systems.

This work aims at studying the formation and evolution of dwarf galaxies in the context of cosmological simulations. It is focused on the role played by initial conditions, set in the early Universe, in shaping the physical properties of galaxies we observe today. Along these lines, we study how the primordial magnetic fields modify the first phases in the formation of a galaxy through their impact on the initial matter power spectrum. Then we address this impact in opposition to the pressure support produced by magnetic fields in the interstellar medium of galaxies, to find the dominant agent. Lastly, we study the formation and evolution of the faintest galactic systems, the ultra faint dwarf galaxies, and the character of first stars in their chemical enrichment.

The eight chapters written in this doctoral thesis are organized as follows. First the key concepts are introduced followed by describing the cosmology and the physics at early Universe in this chapter. A general definition and classification of dwarf galaxies in Chapter 2, is complemented by the importance of dwarf galaxies in cosmology in Section 2.2, and the

importance of dwarf galaxies in the early Universe in Section 2.3. Chapter 3 describes the magnetic fields of a primordial origin, their contribution to the matter power spectrum, and their potential impact on dwarf galaxies. Chapter 5 illustrates our approach to constraining the properties of primordial magnetic fields. In Chapter 6 we discuss the importance of primordial fields in the magneto-hydrodynamical simulations of galaxy formation. The metal-enrichment of dwarf galaxies is outlined in Chapter 7, within the context of the initial mass function of first stars. Finally, in Chapter 8, we summarize the key prospects of the work presented in this thesis.

1.1 Cosmology and the Early Universe

The combination of a collisionless and non-relativistic matter, the so-called Cold Dark Matter (CDM)(Peebles 1982), with the expanding term in the Friedman-Lemaitre-Robertson-Walker (FLRW) model Λ , defines the standard framework of cosmology. Λ CDM, originally proposed by Ostriker & Steinhardt (1995), suggests that the structure formation in the Universe is ruled by the physics at work in the dark sector: since the gravitational potential of the baryonic matter is insufficient to explain the structure formation in the Universe, cosmological models predict the existence of an exotic non-baryonic ingredient, dark matter.

The second key component in the modern cosmology Λ , is based on the discovery that more distant a galaxy is, the faster it moves away from us. Coupled with the Copernican principle that we are not in a unique position, it introduced the concept of an expanding Universe. The expansion of the space is characterized by the scale factor $a(t)$. As the Universe expands, the momentum of particles decay as $L(t) \propto 1/a(t)$, meaning the wavelength of photons increases as $\lambda \propto a(t)$. Therefore the expansion of the Universe can be also explained by redshift z .

Another important input into the standard model of cosmology, stems from the accidental detection of the cosmic microwave background radiation (CMB) (Penzias & Wilson 1965). This shows the first observable radiation from the dense, hot beginning of the Universe, when photon decoupled from matter and started to travel freely through space. The subsequent detection of a Planck spectrum with a present day temperature $T = 2.725$ for CMB (Mather et al. 1994), firmly indicates the thermal equilibrium between matter and radiation at an early stage in history. As the wavelength of photons redshift with the expansion of the Universe, the initial spectrum of CMB should also have been Planckian with a higher temperature $T \propto 1/a(t)$. By this latter, CMB provides the firmest evidence for a hot *Big Bang* ¹.

¹The heat of Big Bang is associated with the amount of dark energy that triggered the inflation

Last but not least, the standard model requires an accelerating expansion epoch, known as *inflation*, to explain a number of puzzling features in the early Universe, for example the CMB anisotropies (see e.g., [Linde 1990](#)). Inflation also provides suitable conditions for the generation of primordial magnetic fields ([Ratra 1992](#); [Turner & Widrow 1988](#)). Several reasons make inflation an ideal candidate mechanism for generating magnetism very early on. For instance, quantum fluctuations induced by inflation may excite the quantum fields including the electromagnetic field. In addition, at the time that inflation takes place, the Universe is not yet pervaded by a highly conducting charged plasma. Thus it is possible for the magnetic flux to grow. Then a similar process to superadiabatic amplification² can generate primordial seed fields on the scale of megaparsec (hereafter Mpc). Magnetic fields of this type, are the main focus of this thesis (see Section 3 for a detailed discussion).

For studying the evolution of the Universe from this early stage to the present day observations, we can use numerical simulations. The initial conditions and the primordial ingredients are known, and the dynamics of the Universe are assumed to be governed by general relativity. In the simplified version of this theory, the Universe is described by a set of space-like hyper surfaces Σ . The time is then defined as the label of each Σ . General relativity also presumes a set of fundamental observers whose world lines described by non self-intersecting geodesics which are orthogonal to the Σ space-like hyper surfaces. The Universe for these fundamental observers is assumed to be homogeneous and isotropic ([Narlikar 2002](#)).

One of the key predictions of Λ CDM, by virtue of the advanced supercomputers, is the abundance, morphology and distribution of dwarf galaxies around a more massive spiral host, like the Milky Way(MW). The plethora of nearby observations makes these predictions testable.

1.2 Matter power spectrum

In the Λ CDM model (described in Section 1.1), all cosmic structures are possibly seeded by the primordial quantum field fluctuations. In the early Universe, the causal connection between these small over-densities of order 1 part in 10^5 , shapes a nearly scale invariant power spectrum $P(k) \propto k^n$, as a function of wave number k , with $n \simeq 1$ ([Harrison 1970](#); [Peebles & Yu 1970](#); [Planck Collaboration et al. 2016](#); [Zeldovich 1972](#)). In an expanding background, these fluctuations then grow due to the gravitational instability. As time evolves, matter accumulates in these initially over-dense regions. Eventually, enough matter will be attracted to each dense region to provide the initial conditions for the large

²Superadiabatic amplification means that magnetic fields larger than the size of the horizon, evolving in a poorly conducting inflationary Universe, decayed slower than the standard a^{-2} law (see Section 3).

scale structures we observe today. The growth of these density perturbations, can be schematically formulated as

$$\ddot{\delta} + [\textit{Pressure} - \textit{Gravity}] \delta = 0, \quad (1.1)$$

where *Gravity* acts to increase an over-density of size δ with grabbing more matter, while *Pressure* is generated by the random thermal motion of particles, acts to prevent that (see e.g. [Dodelson 2003](#)). When the Universe is radiation dominated, because of a strong pressure, the growth of these density perturbations follows an extremely slow logarithmic pace, until the epoch of matter domination. This transition takes place at the recombination epoch, when protons and electrons combined to create the neutral hydrogen. After recombination, the evolution of matter perturbations can be pursued by using the following equations:

- The Euler equation,

$$\rho_b \left[\frac{\partial v}{\partial t} + H(t)v + \frac{v \cdot \nabla v}{a} \right] = -\frac{1}{a} \nabla p_b - \frac{1}{a} \rho_b \nabla \phi - \frac{4\rho_\gamma}{3} n_e \sigma_T v, \quad (1.2)$$

where, a stands for the scale factor, $H(t) = \dot{a}(t)/a(t)$ the Hubble constant, $(1/a)\nabla\phi$ gravitational force due to density perturbations, ρ_γ the photon mass density, n_e the electron number density, and σ_T the Thompson cross-section for electron-photon scattering. Assuming the density and velocity perturbations are small enough, in the linear regime, we can neglect the nonlinear terms, namely, $v \cdot \nabla v$, and keep only the baryonic density up to the first order $\rho_b = \bar{\rho}_b(1 + \delta_b)$ with $\bar{\rho}_b$ being the unperturbed background density of baryons, and δ_b its fractional density perturbation. Leading to the remaining equation,

$$\bar{\rho}_b \left[\frac{\partial v}{\partial t} + H(t)v \right] = -\frac{1}{a} \nabla p_b - \frac{1}{a} \bar{\rho}_b \nabla \phi - \frac{4\rho_\gamma}{3} n_e \sigma_T v. \quad (1.3)$$

The Euler equation for dark matter density perturbations is the same as equation 1.3. The difference is the last term corresponding to baryon-photon interactions which is at the origin of the Silk damping ³. This last term thus vanishes for the cold dark matter which is assumed not to have interactions with photons.

$$\bar{\rho}_{\text{DM}} \left[\frac{\partial v}{\partial t} + H(t)v \right] = -\frac{1}{a} \nabla p_b - \frac{1}{a} \bar{\rho}_{\text{DM}} \nabla \phi, \quad (1.4)$$

Similar to baryonic density perturbations, for dark matter we also keep only the first order $\rho_{\text{DM}} = \bar{\rho}_{\text{DM}}(1 + \delta_{\text{DM}})$, with $\bar{\rho}_{\text{DM}}$ being unperturbed term for the dark matter background density, and δ_b its fractional density perturbation.

³During the epoch of recombination, photons travelling from hot to cold regions, equalising their temperatures, and shape the over-densities map. The silk scale corresponds to the the size of galaxies at the present day.

- The continuity equation,

$$\frac{\partial \rho_b}{\partial t} + 3H(t)\rho_b + \frac{\nabla \cdot (\rho_b v)}{a} = 0, \quad (1.5)$$

Linearizing equation 1.5 for v and $\rho_b = \bar{\rho}_b(1 + \delta_b)$, we obtain,

$$\frac{\partial \delta_b}{\partial t} + \frac{1}{a} \nabla \cdot v = 0 \quad (1.6)$$

- The Poisson equation,

$$\frac{\nabla^2 \phi}{a^2} = 4\pi G \delta \rho_m = 4\pi G [\bar{\rho}_b \delta_b + \bar{\rho}_{\text{DM}} \delta_{\text{DM}}]. \quad (1.7)$$

$\rho_m = (\rho_{\text{DM}} + \rho_b)$ stands for the summation over both baryonic and dark matter perturbed components. G is the gravitational constant.

- The Equation of state,

$$p_b = \rho_b c_b^2 \quad (1.8)$$

where $c_b^2 = (kT/\mu)$ is the sound speed, k the Boltzmann constant, and μ the mean molecular weight.

After taking the divergence of equation 1.3, we use the continuity equation 1.6 to substitute for $\nabla \cdot v$, the Poisson equation 1.7 for the gravitational potential, and the equation of state 1.8 for $\nabla^2 p_b$. The result is the following equation describing the growth of density perturbations due to the baryonic matter,

$$\frac{\partial^2 \delta_b}{\partial t^2} + \left[2H(t) + \frac{4\rho_\gamma}{3\rho_b} n_e \sigma_T a \right] \frac{\partial \delta_b}{\partial t} = c_b^2 \nabla^2 \delta_b + 4\pi G [\bar{\rho}_b \delta_b + \bar{\rho}_{\text{DM}} \delta_{\text{DM}}] \quad (1.9)$$

and collisionless cold dark matter

$$\frac{\partial^2 \delta_{\text{DM}}}{\partial t^2} + 2H(t) \frac{\partial \delta_{\text{DM}}}{\partial t} = c_b^2 \nabla^2 \delta_b + 4\pi G [\bar{\rho}_b \delta_{\text{DM}} + \bar{\rho}_{\text{DM}} \delta_{\text{DM}}] \quad (1.10)$$

Coupled equations 1.9 and 1.10 then can be solved for the total matter perturbations $\delta_m = (\bar{\rho}_{\text{DM}} \delta_{\text{DM}} + \bar{\rho}_b \delta_b) / (\bar{\rho}_{\text{DM}} + \bar{\rho}_b)$ to derive the power spectrum via

$$\langle \delta_m(k) \delta_m^*(k') \rangle = (2\pi)^3 P(k) \delta^3(k - k'), \quad \delta(k) = \int d^3x \delta(x) e^{-ik \cdot x} \quad (1.11)$$

where the δ function projects the random phase approximation. The power spectrum of a smooth distribution is small, whereas with lots of highly under/over-dense regions the value of $P(k)$ will be large.

Afterwards, the modifications to this linear primordial power spectrum can be break into a wave number-dependent and a scale factor-dependent term: the transfer function $T(k)$ and the growth function $D(z)$ (Dodelson 2003; Kolb & Turner 1990; Padmanabhan 2002). The

transfer function encapsulates the different ambient cosmological conditions, for instance, if the Universe is radiation or matter dominated. It is defined as the ratio of amplitude of a density perturbation in the post-recombination era to its primordial value,

$$T(k) \equiv \frac{\delta(k, z=0)}{\delta(k, z=\infty)} \frac{\delta(0, z=\infty)}{\delta(0, z=0)}, \quad (1.12)$$

where $\delta(k, z)$ is the density perturbation for wavenumber k and redshift z . Dark and baryonic matter have a distinct transfer function, however, after recombination, the baryonic pressure dramatically drops and the baryon perturbations rapidly catch up with dark matter perturbations, equalize their transfer functions (Eisenstein & Hu 1998).

The growth function, on the other hand, is responsible for the wavelength-independent growth as a function of time (Eisenstein 1997). In a flat Universe, the growth function at redshifts $z < 1100$ can be written as (Peebles 1993)

$$D(z) \equiv D(a) = \frac{5\Omega_m}{2} [\Omega_m(1+z)^3 + \Omega_\Lambda]^{1/2} \int_z^\infty \frac{1+z}{(\Omega_m(1+z)^3 + \Omega_\Lambda)^{3/2}} dz \quad (1.13)$$

where Ω_m and Ω_Λ are the dimensionless cosmological matter, and vacuum energy (or dark energy) density parameters, respectively. In a matter domination regime, the growth function is simply proportional to the scale factor.

The processed power spectrum is thus formulated as

$$\Delta^2(k, a) = \frac{dk}{2\pi^2} k^2 P(k) T^2(k) D^2(a). \quad (1.14)$$

Since the power spectrum has dimensions of $(\text{length})^3$, one associates the dimensionless power spectrum $d^3k P(k)/(2\pi)^3$ with the excess power in a bin of width dk . Here large Δ determines essential properties of nonlinear cosmological structure, while small Δ corresponds to small inhomogeneities in the linear regime.

Figure 1.1 shows the processed power spectrum for Λ CDM. It is obtained by assuming a linear function. On scales smaller than $k \simeq 0.2 h \text{ Mpc}^{-1}$, where h is the dimensionless Hubble constant ($H_0 = 100 h \text{ km s}^{-1} \text{ Mpc}^{-1}$), the matter distribution falls in the non-linear regime. As shown in the right side of Fig. 1.1, which represents the map of over-densities in the early Universe, this power spectrum, in the linear regime, is then used to generate the initial conditions for launching the cosmological simulations, and examine the evolution of over-densities in the non-linear regime.

In the linear regime, for perturbations of small size, which re-enter the horizon well before matter-radiation equality, Δ is approximately independent of k . Moreover, during the radiation dominated epoch, due to the decay of gravitational potential, the transfer

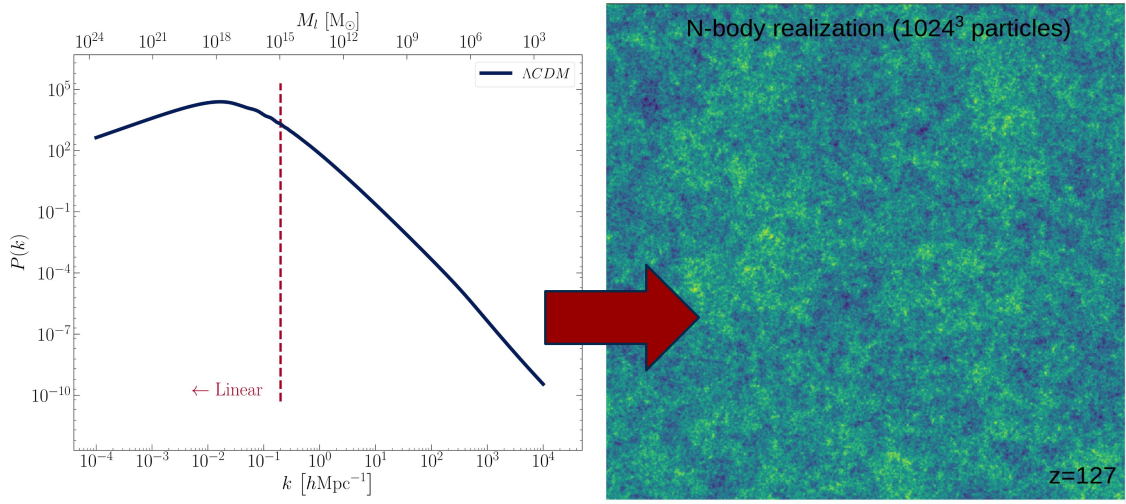


Figure 1.1: Left: The Λ CDM dimensionless power spectrum $P(k)$ as a function of linear wave number k and corresponding linear mass M_l . The vertical dashed line separates large scales which are still evolving linearly and small scales which follow a non-linear growth. Right: Illustration of the map of dark matter over-densities generated using $N = 1024^3$ particles in a cosmological box of size $L = 40 h^{-1} \text{ Mpc}$. The matter power spectrum at redshift $z = 127$ in left is used to generate this density field in the early Universe. Adapted from [Zavala & Frenk \(2019\)](#).

function is much smaller than unity. The smaller the perturbations are, they enter the horizon earlier and undergo more suppression. This makes $P(k)$ to be a decreasing function of wave number on small scales.

In a different manner, on large scales, the inflationary-induced perturbations imposed the slope index of $n = 1$. Thus the power spectrum is a simple power law as a function of wave number, $P(k) \propto k$. The reason is that perturbations of these sizes enter the horizon in the matter domination epoch, and the transfer function for them is unity. This corresponds to scales larger than the comoving horizon at matter-radiation equality ($k \leq 1.2 \times 10^{-2} h \text{ Mpc}^{-1}$).

It is useful to associate the scale of density perturbations in a Fourier space to the distribution of matter in galaxies. Thus in Fig. 1.1, we make a map between the wave number and the matter content within a sphere of comoving Lagrangian radius r_l ,

$$M_l = \frac{4\pi}{3} r_l^3 \rho_m = \frac{\Omega_m H_0^2}{2G} r_l^3 = 1.71 \times 10^{11} \text{ M}_\odot \left(\frac{\Omega_m}{0.3} \right) \left(\frac{h}{0.67} \right)^2 \left(\frac{r_l}{1 \text{ Mpc}} \right)^3 \quad (1.15)$$

where the mass scale M_l , defined at redshift $z = 0$, is the equivalent of the Jeans mass (Jeans 1902), above which the gravitational instability overcomes the pressure support and leads to the growth of density perturbations.

Along this line, to evaluate the formation of objects of a given mass, it is practical to use the statistical distribution of the smoothed density field. In a real space representation, a window (filter) function, for example a Gaussian window function $W(kR) = \exp(-k^2 R^2/2)$, is normally used to smooth out the density perturbation field, $\int d^3r \delta(x) W(kr)$. As such, in a sphere of radius R , window function is unity and outside, its value is zero. The space thus can be divided into a number of spheres, and the variance of matter perturbations inside individual spheres of radius R in Fourier space is

$$\sigma^2(M, a) \equiv \sigma^2(R, a) = \int_0^\infty \frac{dk}{k} \Delta^2(k, a) \left[\frac{3j_1(kR)}{kR} \right]^2, \quad (1.16)$$

where the enclosed mass M in radius R is $M = 4/3 \pi \rho_m R^3$, and j_1 is the spherical Bessel function of first order $j_1(x) = (x \cos x - \sin x)/x^2$. At redshift $z = 0$ and for a radius of $8 h^{-1} \text{ Mpc}$, the normalization of the present day power spectrum is itemized as σ_8 . The practicality of $\sigma(M, a)$ function lies in the fact that its value determines the abundance of formed objects by estimating when a structure of a given mass can collapse. Its value is given in Fig. 1.2 as a function of mass and redshift. According to Peebles (1980), the formation of first halos hosting galaxies occurs if perturbations in a spherically symmetric over-dense region compared to the background density, exceed $\sigma(M, a) = 1.68$.

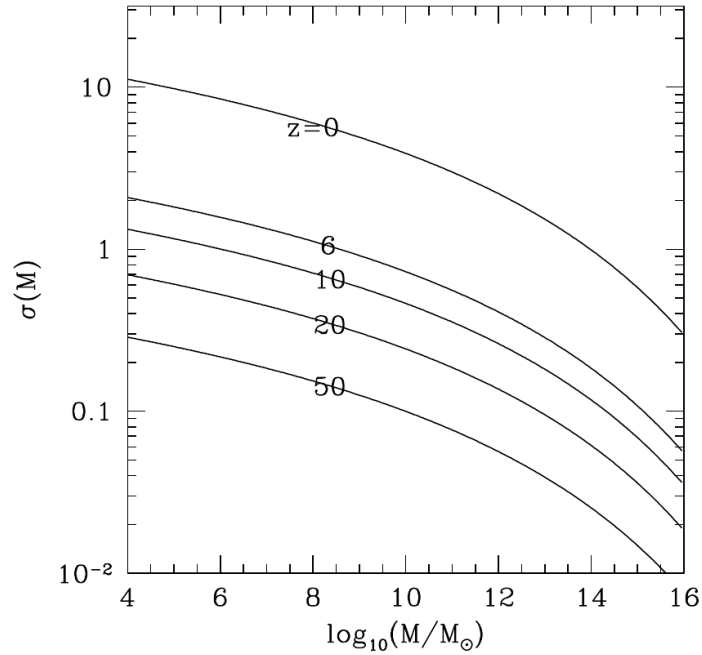


Figure 1.2: **The variance of density perturbations** linearly extrapolated as a function of mass M and redshift z . the formation of first halos hosting galaxies occurs if perturbations in a spherically symmetric over-dense region compared to the background density, exceed $\sigma(M, a) = 1.68$. Taken from [Loeb \(2010\)](#)

1.3 Hierarchical structure formation

Λ CDM cosmology connects the over-dense regions in the early Universe to the final configuration of dark matter halos. As soon as the evolution of density perturbations become nonlinear, their mass content stops growing. This point marks the collapse of perturbations in the dark matter density field. Eventually these over-dense regions decouple from the background matter density, and form a gravitationally self-bound structure, a virialized dark matter halo. This architecture is shown in Fig 1.3. The outer edge of this bounded dark matter regions R_{vir} , is defined by assuming an idealized spherical collapse of total mass M_{vir} .

The internal structure of a dark halo forming from collisionless CDM particles initially predicted to follow a power law density profile $\rho \propto r^{-\alpha}$ known as cusp ([Bertschinger 1985](#); [Fillmore & Goldreich 1984](#)). Later, the N-body simulations of ([Dubinski & Carlberg 1991](#)) showed that the inner profile of the first dark halos remarkably deviates from a simple power law. Their density profiles appeared to be well characterized by a steep outer profile which bends to an inner cusp, following $\rho \propto r^{-1}$,

$$\rho(r) = \frac{\rho(r_s)}{(r/r_s)(1 + r/r_s)^2}. \quad (1.17)$$

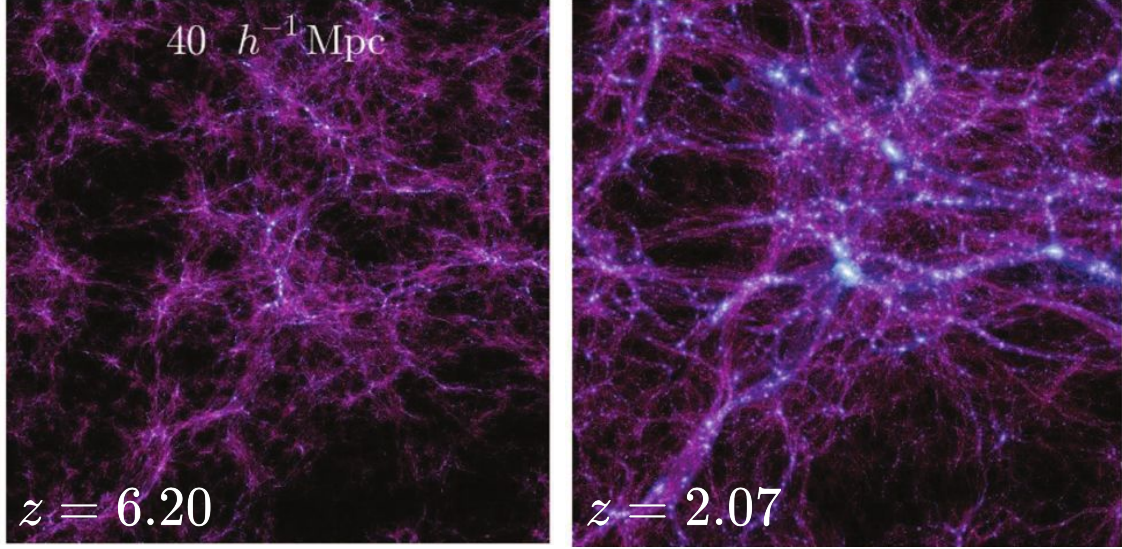


Figure 1.3: **The growth of density perturbations** and the emergence of the first dark halos hosting galaxies. The side of the cube is $40 h^{-1} \text{Mpc}$. Adapted from the result of Millennium II simulations at redshifts $z = 6.20$ and $z = 2.07$ [Boylan-Kolchin et al. \(2009\)](#). over-dense regions decouple from the background matter density, and form a gravitationally self-bound structure, a virialized dark matter halo.

This functional form of equation 1.17, known as Navarro–Frenk–White (NFW) ([Navarro et al. 1997](#)), provides a good description of dark halo profiles, while it is independent of the cosmological parameters, the slope of the matter power spectrum and the halo mass. Here r is the distance from the center of the halo, r_s is the characteristic radius in which the log-slope of the density profile is -2 , thus $\rho(r_s)$ represents the central density. [Bullock et al. \(2001\)](#) noticed a correlation between r_s and the formation time: Halos which form earlier have a higher concentration of matter in the central region for a given virial mass. This pattern, showed in Fig. 1.4, is explained by the earlier clustering of lower mass halos when the averaged background density of matter in the Universe is higher (e.g. [Navarro et al. 1997](#); [Wechsler et al. 2002](#)). It suggests that the structure formation follows a hierarchical assembly of dark halos, with smaller a halo hosting a galaxy is, earlier its formation initiates.

1.4 The Success of Λ CDM

After a brief discussion on the principles of Λ CDM, I would like to finish this chapter with describing the successful predictions of this cosmological theory. Indeed, Λ CDM provides an undeniably powerful framework for describing the structure formation of the Universe

in the linear regime, and its evolution with time. The following list summarizes many successes of the standard model.

- **The polarization of the Cosmic Microwave Background (CMB).** The most precise analysis of CMB constraints has been performed using the Planck data. The standard model predicts the CMB temperature, redshifted to the present day, to be $T_0 = 2.725$ K. It is consistent with the spectra measured by [Planck Collaboration et al. \(2016\)](#).
- **The location of the Baryon Acoustic Oscillations (BAO).** The two point correlation function measured from the SDSS catalogue ([Eisenstein et al. 2005](#)) peaks at $100 h^{-1}$ Mpc. The location and the amplitude of the peak are in agreement with the Λ CDM predictions.
- **The Big Bang nucleosynthesis.** At the post-Big Bang epoch when the temperature of the Universe was a few mega electron volt (MeV), nucleosynthesis of elements began. The standard model predicts that some primordial light elements (D, He^3, He^4, Li) formed during the initial hot and dense phase of the Universe, which is confirmed by the observational data from [Cooke et al. \(2014\)](#) and ([Planck Collaboration et al. 2016](#)).

Despite many success of Λ CDM mentioned above, it still fails at predicting and explaining the formation of small galactic structures, on length scales below 1 Mpc and mass scales below $10^{11} M_\odot$. The main challenges the standard model is still facing and the potential solutions are given in Section [2.2.1](#).

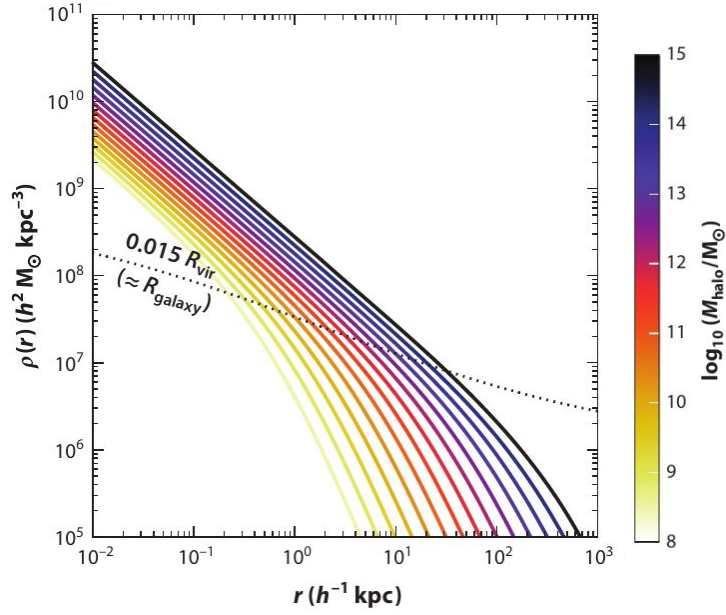


Figure 1.4: **The $z = 0$ density profile of NFW dark matter halos**, expanding from the smallest halos hosting dwarf galaxies ($M_{\text{vir}} \sim 10^8 M_\odot$) to those of galaxy clusters ($M_{\text{vir}} \sim 10^{15} M_\odot$). The lines are color-coded according to the virial mass of dark halos. For a given physical radius, the concentration of mass is lower in lower mass halos than in the more massive ones. This is displayed via the dotted line which compares the density of halos at their half-light radius, $r_{1/2} = \epsilon \text{ conc} R_{\text{vir}}$, with $\epsilon = 0.015$ obtained from abundance matching (e.g. [Behroozi et al. 2013a](#); [Moster et al. 2010](#))

Chapter 2

Dwarf galaxies

In the theory of the bottom-up assembly of cosmic structures, described in Section 1.3, the smallest dark halos inhabiting the faintest galaxies, are the building blocks for larger halos which host more massive galaxies like the MW. Granted that the smallest, most inconspicuous galaxies we observe today, the so-called dwarf galaxies, resemble the first galaxies formed in the Universe, their role in studying the early Universe and the first stages of structure formation is extremely important.

Dwarf galaxies are the most abundant type of galaxies observed. The best studied populations of dwarf galaxies have been discovered in our proximity (McConnachie 2012, updated online catalog), but also in the nearby Virgo cluster (Binggeli et al. 1985). The primary focus of this thesis are the faint dwarf galaxies observed in our neighborhood, the Local Group. It corresponds to an area of ~ 3 Mpc around the MW, including nearby galaxies such as Andromeda (= M31). In this volume, the collection of satellite galaxies gravitationally bound to the MW, are separated by ~ 800 kpc from M31 and its satellites. These two systems are shown in Fig. 2.1. The Local Group is a part of the Local Volume which consists of galaxy groups such as, the M81 group, the CVn-I group, the Centaurus group, and the Sculptor group, within the radius of ~ 11 Mpc (Karachentsev et al. 2004). All member galaxies in this volume have relative radial velocities smaller than 550 km/s with respect to the Local Group.

Dwarf galaxies in the Local Group are divided into satellites orbiting a spiral host, and field galaxies, which are distributed outside of the virial radius of the MW and M31. Surprisingly, the exact definition of a dwarf galaxy is beyond being obvious. In the following I discuss the possible classifications based on their main characteristics.

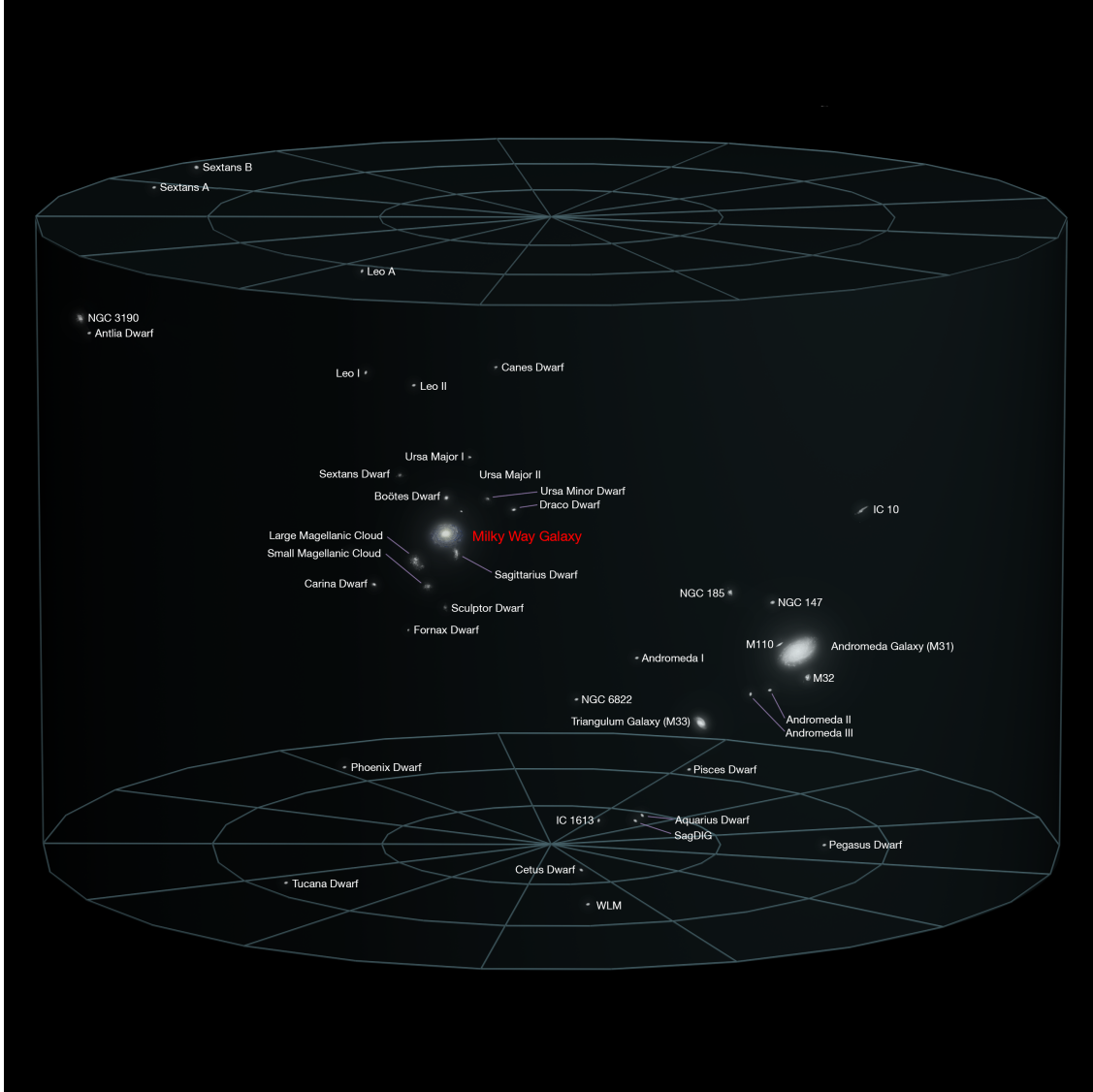


Figure 2.1: **The Local Group** is an area of ~ 3 Mpc around the MW, including nearby galaxy Andromeda and its dwarf satellites. Some of the bright MW satellite galaxies are the Sagittarius, Large Magellanic Cloud, Small Magellanic Cloud, Ursa Minor, Draco, Carina, Sextans, Sculptor, Fornax, Leo I, Leo II, Ursa Major I and Ursa Major II. Credit: ESO/Andrew Z. Colvin/N. Bartmann

2.1 Classification

Before the Sloan Digital Sky (SDSS) and other modern surveys, the known satellite population was limited to dwarf galaxies with V-band luminosity larger than $2.5 \times 10^5 L_{\odot}$. The SDSS, the Pan-Andromeda Archaeological Survey (PAndAS) (Richardson et al. 2011), and the Dark Energy Survey (DES) (Drlica-Wagner et al. 2015; Koposov et al. 2015) have pushed this limit to ~ 1000 times less luminous objects for both the MW and M31 satellites.

Different schemes are proposed for the classification of dwarf galaxies. Morphological structure has been mainly used to evaluate the observed data (see e.g, Sandage & Binggeli 1984). However, the gas content and the color of galaxies, can be used in addition to morphology (Karachentsev et al. 2004, 2013). Here we use a combined naming convention adopted from Bullock & Boylan-Kolchin (2017) and Sandage & Binggeli (1984), for the purpose of this thesis. The term *dwarf* refers to galaxies with $M_{\star} \lesssim 10^9 M_{\odot}$, which can be further subdivided into several classes according to the following criteria:

- **Classical dwarf spheroidals (dSphs):** dSphs covers a wide range of bright galaxies with $M_{\star} \gtrsim 10^5 M_{\odot}$. Their smooth intensity function and nearly flat radial profile is stemming from their featureless morphology. dSph galaxies are typically depleted of gas and have no ongoing star formation. They are mainly characterized as the satellite population of a larger system.
- **Dwarf irregulars (dIrrs):** The vast majority of field dwarf galaxies in the Local Group fall into the dIrrs class. They are identified by their ongoing star formation. These late type galaxies, which usually still contain gas, show disordered morphological features. Their stellar mass range is similar to that of dSphs.
- **Ultra-faint dwarfs (UFDs):** Extending the stellar mass of classical dSphs towards fainter objects, the mass range $M_{\star} \approx 10^2 - 10^5 M_{\odot}$ is reserved for UFDs. Contrary to more luminous dwarfs, their star formation is quenched by reionization at $z \gtrsim 6$ than extending to lower redshifts.

The main objects of interest in this thesis are the classical dSphs and UFDs.

2.2 Dwarf galaxies as probes for dark matter

Since the existence of the elusive dark matter was suggested (Zwicky 1933), its particle nature is used to determine the essential properties of nonlinear structure formation in cosmology. As the driving force for structure formation in the Universe, dark matter enabled the formation of galaxies, and structured the environment they reside in. In the

study of dark matter, the faintest objects in the galactic zoo – dwarf galaxies, come under the spotlight, for several reasons:

- Although the stellar mass of dwarfs span approximately seven decades $M_\star \approx 10^2 - 10^9 M_\odot$, they occupy a narrow band in the halo mass space $\approx 10^9 - 10^{11} M_\odot$ (e.g., [Strigari et al. 2008](#)). The lowest mass dark halos, in galactic scales, are therefore inhabited by dwarfs. Unlike larger systems, the baryonic matter content of dwarf galaxies is dynamically negligible, making them the most dark matter dominated galactic systems. Furthermore, the short and inefficient star formation in dwarf galaxies diminishes the role of stellar feedback in shaping their internal structure ([Oñorbe et al. 2015](#)). Thus the inner density profile of dwarfs, due to the small size of their halos, present a promising target for measuring the behaviour of dark matter in scales as small as a few tens of parsec (hereafter pc), specifically in the most compact UFDs (e.g., [Calabrese & Spergel 2016](#); [Errani et al. 2018](#)).
- The proximity of dwarf galaxies to us, provides a plethora of accurate observations in the Local Group. For instance, observing their stellar dynamics (e.g., [Battaglia et al. 2008](#); [Walker et al. 2009](#)) constrain the shape of dark matter density profile and the dark matter mass enclosed in their host halos. Besides, these observations makes it possible to indirectly experiment their dark matter halos. One of the indirect traces of dark matter is through annihilation. Λ CDM predicts that if dark matter consists of weakly interacting massive particles the annihilation of two dark matter particles can be detected with electromagnetic signatures. The rate of annihilation scales with ρ_{DM}^2 , thus the center of dark halos are the best place to look for annihilation fluxes. Although dwarf galaxies are less bright and more distant than the galactic center, being free of foreground contamination makes them great candidates.
- As one of the fundamental predictions of Λ CDM is the abundance of substructures, the number density of dwarf satellites around the MW, in comparison with the observations of satellites in the Local Group, can directly place tight constraints on the mass range eligible for dark matter particles (e.g., [Jethwa et al. 2018](#)).

Because of the arguments listed above, dwarf galaxies provide the smallest scale probes for the Λ CDM. Their abundance and internal structure can potentially challenge the validity of the standard model, and its successful predictions listed in Section 1.4.

2.2.1 Λ CDM challenges in small scales

High resolution Dark Matter Only (DMO) simulations, in a cosmological framework, detect serious tensions between the predictions of Λ CDM on small scales (kpc to Mpc), and the observations in the Local Group. The following list summarizes these tensions (see e.g., [Sales et al. 2022](#), for a recent review).

- **The missing satellites problem.** The Λ CDM predictions for the abundance of dwarf galaxies can be projected in N-body simulations of MW-sized halos (e.g., [Kuhlen et al. 2009](#); [Springel et al. 2008](#); [Stadel et al. 2009](#)). While we expect ~ 500 of subhalos with masses $M_{\text{halo}} \gtrsim 10^7 M_{\odot}$ from simulations, less than 100 satellite galaxies are observed inside the virial volume of the MW ([Drlica-Wagner et al. 2015](#)). This discrepancy, first detected by [Moore et al. \(1999\)](#), reveals the over-prediction of nearby satellites in a Λ CDM paradigm. A natural solution to this problem is to consider that dark matter halos of low mass are inefficient in accreting gas and forming galaxies. Hydrodynamical simulations showed that this problem only exist in dark matter only simulations ([Bovill & Ricotti 2009](#); [Bullock et al. 2000](#); [Sawala et al. 2016](#)) and can be solved by considering the effect of UV background and stellar feedback.
- **The too big to fail problem.** Exploring the solution mentioned above for the missing satellites problem, unveils a mismatch between the predicted central masses in dark halos of the observed dwarf galaxies [Boylan-Kolchin et al. \(2011\)](#). In DMO simulations ([Diemand et al. 2008](#); [Springel et al. 2008](#)), the cumulative count of massive halos (potential hosts of bright dwarf galaxies) is consistent with the count of MW bright satellites. However, the most massive halos are highly dense, and fail to form galaxies. The brightest dwarf galaxies consequently inhabit the medium sized halos, and the most massive dark halos predicted in a Λ CDM paradigm, are missing in observations. The SPLASH (Spectroscopic and Photometric Landscape of Andromeda’s Stellar Halo) survey ([Tollerud et al. 2012](#)) shows this mystery of massive halos are too big too fail hosting galaxies, persists for M31 satellites as well, with a more distinct sign in dSphs than in elliptical dwarfs.

One solution suggested for resolving this tension is to assume a lower mass for a MW-like host halo in simulations, since the mass of subhalos is directly dependent on the latter ([Vera-Ciro et al. 2013](#); [Wang et al. 2012](#)). This solution however, may not allow the formation of massive satellites, namely, the Large Magellanic Cloud (LMC) or explain the large velocity of Leo-I ([Boylan-Kolchin et al. 2013](#)). The other solution is considering the baryonic effects, which lower the halo mass in the inner regions instead of expecting dwarf galaxies to occupy lower mass halos (see below: the solution to the cusp-core problem). The proposed solutions may alleviate the tension for the MW and M31 satellite galaxies, though the situation is less clear for the field galaxies where the problem is also observed ([Garrison-Kimmel et al. 2014](#)).

- **The cusp-core problem.** As discussed in Section 1.3, the inner density of dark halos in N-body simulations follows a cuspy NFW profile. Meanwhile the measurements of galaxy rotation curves suggests a constant-density core of kiloparsec (kpc) size (e.g. [de Blok et al. 2008](#); [McGaugh et al. 2001](#)). Therefore Λ CDM halos forming in DMO simulations are denser and cuspier in their centers compared to observed galaxies.

As measuring the mass profile in the most inner regions of the rotation curve is not straightforward, this discrepancy is also occasionally referred to as the inner mass deficit problem (Oman et al. 2019; Weinberg et al. 2015). In this phrasing, Λ CDM predicts more dark matter in the inner regions of dwarf galaxies compared to quantity inferred from rotation curves observed (see e.g. Sales et al. 2022).

One of the solutions suggested to this tension is the effect of baryonic physics. For instance, supernovae feedback may temporarily push the gas outside of a galaxy, by expanding it, and perturb the gravitational potential. Due to such oscillations in the central gravitational potential, energy is transferred into dark matter particle orbits. The density of dark matter in the inner regions is thus reduced, quantitatively flattening the cusp to core (Pontzen & Governato 2012).

- **The diversity of rotation curves problem.** A closer look into the cusp-core problem, unveils a related and more challenging tension. This problem was first detected in the hydrodynamical simulations of Oman et al. (2015) in a cosmological context. On one hand, the inner shape of dwarfs in these simulations vary systematically with their mass. Observed inner rotation curves, on the other hand, demonstrate a large diversity for dwarf galaxies of similar masses. The three dwarf galaxies shown in Fig. 2.2, have similar maximum velocity $V_{\text{max}} \sim 80 \text{ km s}^{-1}$ in the outer rotation curve. As V_{max} stands for the total halos mass, a comparable profile is expected for these three observed dwarfs. Nevertheless, one represents a core, one is in agreement with NFW profiles, and the other is more concentrated. As discussed for the cusp-core problem, considering baryonic physics, dwarf galaxies with a core profile may form, however, reproducing the diversity remains problematic to all current simulations. Currently it remains as a strong inconsistency between Λ CDM predictions and observations.
- **The diversity of sizes problem.** The stellar morphology of dwarfs, manifest another diversity tension, the scatter in the dwarf sizes, which is defined by their half light radius. The observed galaxies encompass a broad range of sizes at a fixed luminosity/stellar mass. However, Λ CDM, including the baryonic physics, does not predict the formation of small and compact galactic systems, while simultaneously retaining the level of star formation burstiness to reproduce the physical properties of more extended and diffuse dwarf galaxies. This tension is shown in Fig. 2.3, as a comparison across different models in colors and observations in the Local Group in gray squares with error bars. The luminosity-size relation is generally reproduced by the simulations of MW-like halos and their subhalos (Agertz et al. 2020; Applebaum et al. 2021; Wheeler et al. 2019), as well as simulations of individual dwarfs (Jeon et al. 2017; Revaz & Jablonka 2018). However, each individual simulation set, demonstrates a noticeably narrower dispersion than observations.

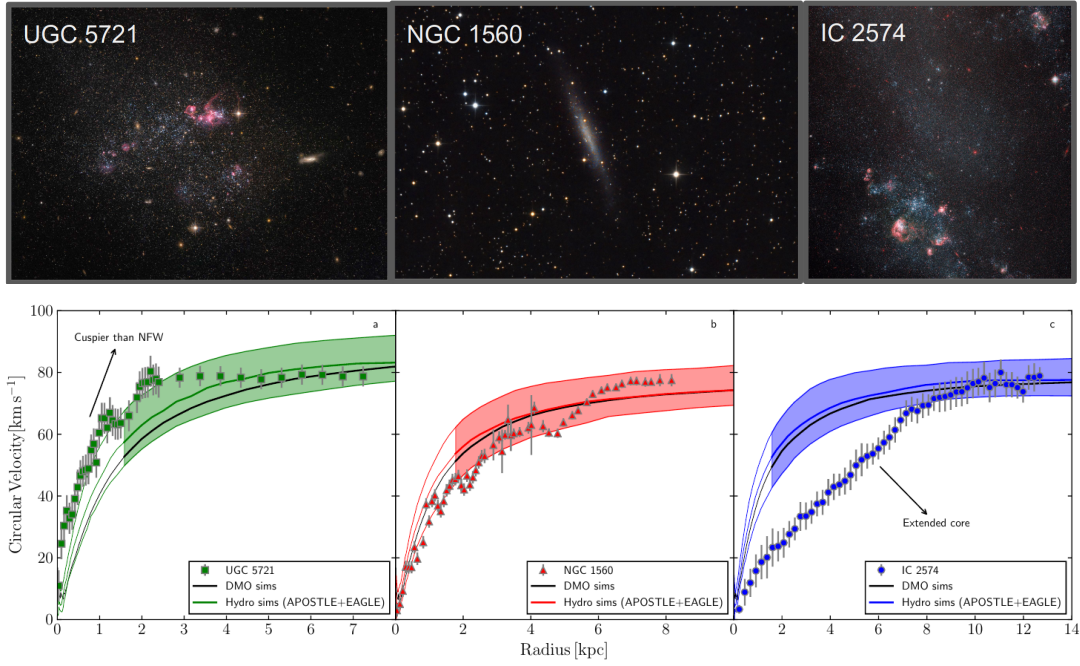


Figure 2.2: **The diversity of the rotation curves problem.** The circular velocity as a function of radius in DMO and hydrodynamical simulations is compared to the observed rotation curves of three dwarf galaxies with similar maximum velocity $V_{\text{max}} \sim 80 \text{ km s}^{-1}$ in the outer rotation curve (representing the total halo mass). The observed rotation curves represents a broad diversity in the inner regions. From left to right, UGC 5721 (Swaters et al. 2003) follows a steeply increasing profile which is more concentrated than NFW, while the profile of NGC 1560 (de Blok & Bosma 2002) is well described by NFW, and IC 2574 (Oh et al. 2011) profile depicts an extended core. Colored lines display the halos with $V_{\text{max}} \sim 80 - 100 \text{ km s}^{-1}$ in the APOSTLE and EAGLE simulations, and black lines show their DMO counterparts. Adapted from Sales et al. (2022).

The challenge of forming compact systems may be mitigated by increasing the resolution of numerical simulations. This way, the artificial numerical effects, namely the impact of a large gravitational softening length ϵ , can be avoided. Assuming all stars in a subhalo are on circular orbits, the maximum circular velocity is then numerically modeled as Springel et al. (2008)

$$V'_{\text{max}} = V_{\text{max}} [1 + (\epsilon/r_{\text{max}})^2]^{1/2}. \quad (2.1)$$

where r_{max} is the radius at which the maximum circular velocity V_{max} is realized. According to equation 2.1, the orbit of stars in high resolution simulations can be studied more precisely, as the softening length will be smaller than the size of a typical dwarf galaxy, and V'_{max} is closer to V_{max} . However, the size of model galaxies for example in Applebaum et al. (2021); Grand et al. (2021) have not necessarily shrunk after surpassing the resolution obstacle.

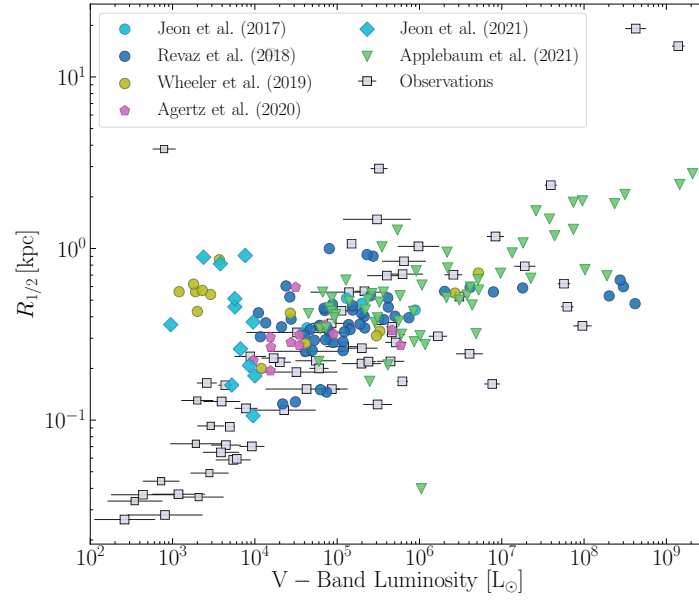


Figure 2.3: **The diversity of sizes problem.** The size of dwarf galaxies as a function of their V-band luminosity. The observed dwarfs in the Local Group, shown in gray squares with error bars, display wide range of sizes at a fixed luminosity. This scatter is inconsistent with Λ CDM predictions and not reproduced by current high resolution simulations, shown in colors.

- **The plane of satellite problem.** This problem stems from the 3-D spatial and velocity distribution of satellite galaxies. Λ CDM predicts an isotropic/prolate substructure distribution for dwarf satellites, which should orbit in random trajectories. Meanwhile, the orbit of dwarf galaxies is aligned in a thin planar configuration, perpendicular to the spiral disc of the MW (Pawlowski et al. 2012), with most of them co-orbiting in the same sense, similar to the rotation of planets around the sun. This inconsistencies, first realised by Kroupa et al. (2005) as a new crisis for the Λ CDM, were later observed by Koch & Grebel (2006) for the M31 as well. Recent observations of neighboring galaxies such as Centaurus A (Müller et al. 2018, 2021) and M101 (Müller et al. 2017) shows the same pattern.

Theoretical models argue that the presence of a massive galaxy like LMC or M32, may significantly induce the planarity alignment of the satellite population (Samuel et al. 2021). Motions of LMC, for instance if it passes MW from a close distance, can lead to the clustering of the MW satellites (Garavito-Camargo et al. 2021). Besides, there is evidence that LMC subhalos have been accreted into the MW halo in groups. This places the satellite population in a similar orbit (Li & Helmi 2008; Santos-Santos et al. 2021). Large volume simulations containing the cosmological structure around the Local Group are required to unveil the alignment of the planer structure of dwarf galaxies around MW, M31 and Local Group.

Tension	level
Missing satellites	no tension
Too big to fail	weak tension
Cusp-core	uncertain
Diversity of rotation curves	strong tension
Diversity of sizes	weak tension
Plane of satellites	strong tension

Table 2.1: **Classification of some small scale challenges to Λ CDM**, stemming from the inconsistency of numerical simulations with observations of both satellite and field dwarf galaxies.

In summary, a better understanding of the baryonic physics in cosmological simulations, namely the supernovae feedback, and environmental effects can mitigate some of the tensions mentioned above. Yet resolving stronger disagreements between theoretical predictions of Λ CDM and observations remains elusive. Table 2.1 classifies the strength level of current challenges.

2.2.2 Λ CDM alternatives

As discussed above, reproducing the physical and morphological properties of dwarf galaxies have been widely addressed in hydrodynamical simulations. In the recent years, small scale challenges to the Λ CDM (discussed in Section 2.2.1) have been a strong motivation for multiple alternative cosmologies, such as warm dark matter (WDM, Lovell et al. 2012) and self-interacting dark matter (SIDM, Robles et al. 2017). As mentioned earlier in this chapter, the abundance and inner mass profile of dwarf satellite galaxies is potentially sensitive to the nature of dark matter. In the following we discuss their impact on the formation and evolution of dwarf galaxies.

Warm Dark Matter Figure 2.4 shows the dimensionless matter power spectrum Δ^2 in a WDM paradigm compared to the classical model (see Section 1.2). The difference, appears as a cutoff induced by warm but non-relativistic dark matter particles, in small mass scales, i.e, $k \gtrsim 1.5 h \text{ Mpc}^{-1}$. This cutoff is induced by a larger free-streaming length of warm compared to cold dark matter particles. The more massive dark matter particles are, the earlier they become non-relativistic, when the horizon size is smaller. Therefore, the free-streaming length λ_{fs} scales reversely with increasing the particle mass m_{WDM} (Mayer 2022) as

$$\lambda_{\text{fs}} \simeq 44 \left(\frac{m_{\text{WDM}}}{1 \text{ keV}} \right)^{-1.11} h^{-1} \text{ kpc}. \quad (2.2)$$

Here, λ_{fs} is larger for WDM particles with $m_{\text{WDM}} \sim 1 \text{ keV}$ compared to $m_{\text{CDM}} \sim 100 \text{ GeV}$

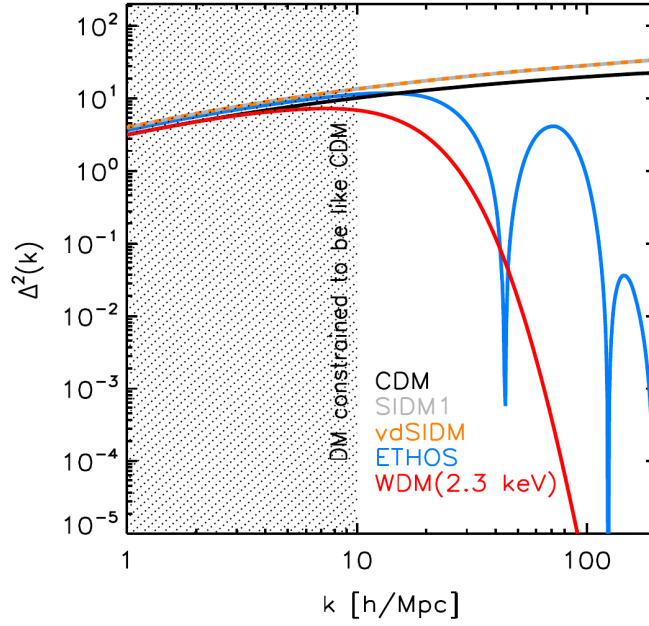


Figure 2.4: **The linear dimensionless matter power spectrum** at redshift $z = 0$, as a function of wave number, for different dark matter model: CDM, WDM, SIDM, velocity dependent SIDM, and the combination of SIDM and WDM known as ETOS. Taken from [Zavala & Frenk \(2019\)](#).

([Green et al. 2005](#)). By streaming in large distances, WDM particles may equalize inhomogeneities in the primeval density map. In other words, after recombination, they may even out the over-dense regions of small size to the background density. The growth of low-mass dark substructures in the early Universe therefore will be abolished. Estimating the mass scale of over-dense regions which can grow in the early Universe $M_{\text{fs}} = 4\pi/3 (\lambda_{\text{fs}}/2)^3 \rho_0 = 7.1 \times 10^6 (m_{\text{WDM}}/1 \text{ keV})^{-3.33} M_{\odot}$, where ρ_0 is the mean cosmological background density shows that WDM models significantly modify the evolution of substructures below M_{fs} .

As discussed in equation 1.14, the dependency of the nonlinear cosmological structure formation is encapsulated in the transfer function $T(k)$. In the WDM paradigm, $T(k)$ in small scales is dramatically reduced. [Bode et al. \(2001\)](#) argued that the transfer function, which is relating the WDM dimensionless power spectrum $\Delta_{\text{WDM}}^2(k)$ to the CDM power spectrum $\Delta_{\text{CDM}}^2(k)$, as $\Delta_{\text{WDM}}^2(k) = T^2(k) \Delta_{\text{CDM}}^2(k)$, is given by

$$T(k) = [1 + (\alpha k)^{2\nu}]^{-5/\nu}, \quad (2.3)$$

where $\nu = 1.12$ and α is a function of WDM particle mass ([Viel et al. 2005](#)),

$$\alpha = 0.049 \left(\frac{m_{\text{WDM}}}{\text{keV}} \right)^{-1.11} \left(\frac{\Omega_{\text{WDM}}}{0.25} \right)^{0.11} \left(\frac{h}{0.67} \right)^{1.22} h^{-1} \text{ Mpc}. \quad (2.4)$$

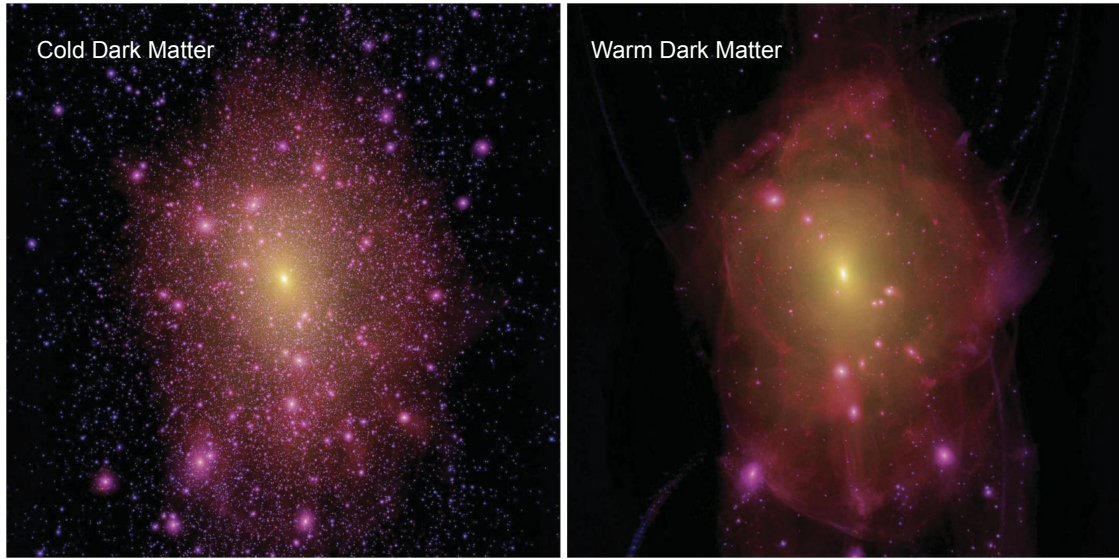


Figure 2.5: **MW in warm and cold dark matter Universe.** Projected dark matter distribution of a MW-like halo in two different models: CDM in left, and warm dark matter with a free-streaming cutoff in galactic scales $m_{\text{WDM}} \sim 2.3 \text{ keV}$ in right. On small scales, since the structure formation from a suppressed power spectrum predicts less abundant and more massive satellites inside a MW-sized halo, WDM models may solve the missing satellites problem. Taken from [Lovell et al. \(2012\)](#)

where Ω_{WDM} is the dimensionless cosmological density parameters for WDM. On large scales, predictions of the WDM cosmology, similar to the standard model particles, is in a great agreement with observations. On small scales, since the structure formation from a suppressed power spectrum predicts less abundant and more massive satellites inside a MW-sized halo, WDM models may solve the missing satellites problem ([Lovell et al. 2012](#)) (As mentioned earlier the missing satellite problem can also be solved with including the effects of baryonic physics in dark matter only simulations). This effect is shown in Fig. 2.5, for a MW-mass halo and its satellites. Furthermore, WDM is also a promising alternative to mitigate the too big to fail problem. Due to the erasure of small over-dense regions, the timescale for more massive systems to accumulate matter and collapse is increased. As the assembly of halos is delayed, their central structure is formed when, due to the expansion, the density of Universe is decreased. This latter leads to a significant reduction in the central density of massive halos and is the key to solve the too big to fail problem ([Anderhalden et al. 2013](#)).

Sterile neutrinos are the most accepted candidate for WDM ([Abazajian 2006](#); [Boyarsky et al. 2019](#); [Dodelson & Widrow 1994](#); [Shi & Fuller 1999](#)). The name sterile is given as they are massive neutrinos with minimal coupling through the electroweak interactions, with lifetimes longer than the age of the Universe.

Self Interacting Dark Matter If no interactions beyond gravity is known between baryons and dark matter, nothing prevents dark matter particles to interact among themselves. Originally envisioned by (Carlson et al. 1992; Spergel & Steinhardt 2000), the main characteristic of the SIDM model is to lean on the non-gravitational self-interactions of dark matter particles. Thus the main difference between this model and the classical CDM can be described by the cross-section of the collisional interactions σ_{SIDM} . The interactions between individual SIDM particles initially assumed to be elastic scatters, independent of their relative velocity (Carlson et al. 1992; Spergel & Steinhardt 2000). The mean free path of SIDM particles λ_{fs} then scales reversely with σ_{SIDM} .

Figure 2.6 shows the distribution of dark matter in a galactic halo. Logically, in low density regions, the rate of scattering is lower. Thus the difference between the collisional and collisionless dark matter is negligible in the outskirts. However, on sub-galactic scales, the inner density profile varies between the two. When particles are collisional, the mean free path might be smaller than the size of the galactic halo. SIDM particles in this case experience many scatters over a local dynamical time. These interactions distribute the energy and momentum. As a result, while collisionless CDM particles shape a dense cuspy profile, energy-exchanging interactions of SIDM particles lowers the density contrast between inner and outer regions. This effect is showcased in Fig. 2.6 for a MW-like dark halo, where the density profile for a SIDM model remains the same as in the standard CDM outside ~ 1 kpc, whereas inside this radius the profile differs.

The reduction in the central density of SIDM halos, known as the cusp to core transition, leads to the conversion of a high density and cuspy profile into a cored profile (see e.g., Burkert 2000; D’Onghia & Burkert 2003; Rocha et al. 2013). The size of the core depends on the ratio of the cross section parameter to the mass of dark matter particle m_{SIDM} . SIDM models with $\sigma_{\text{SIDM}}/m_{\text{SIDM}} \approx 0.5 - 10 \text{ cm}^2/\text{g}$ in cosmological simulations generate dwarf galaxies with a cored profile of size $\sim 0.3 - 1.5 \text{ kpc}$ which do not suffer from the cusp-core and the too big to fail problem (e.g., Elbert et al. 2015; Rocha et al. 2013; Vogelsberger et al. 2012).

On large scales, structure formation in a SIDM is identical to the successful CDM model. However, for being a promising alternative to the standard model, SIDM should be able to produce the density profile of cosmic structures from the smallest ultra faint dwarfs to the clusters of galaxies. The upper constraint on the self-scattering cross section derives from the galaxy cluster observations (Miralda-Escudé 2002). This latter requires $\sigma_{\text{SIDM}}/m_{\text{SIDM}} \simeq 0.1 \text{ cm}^2 \text{ gr}^{-1}$. Whereas, Kaplinghat et al. (2016) showed that at least $\sigma_{\text{SIDM}}/m_{\text{SIDM}} \gtrsim 1 \text{ cm}^2/\text{g}$ is needed to explain the kinematics of the dSphs around the MW.

This suggests that the cross section should be large enough to alleviate the small scale challenges of CDM, and also small enough to be consistent with the observational con-

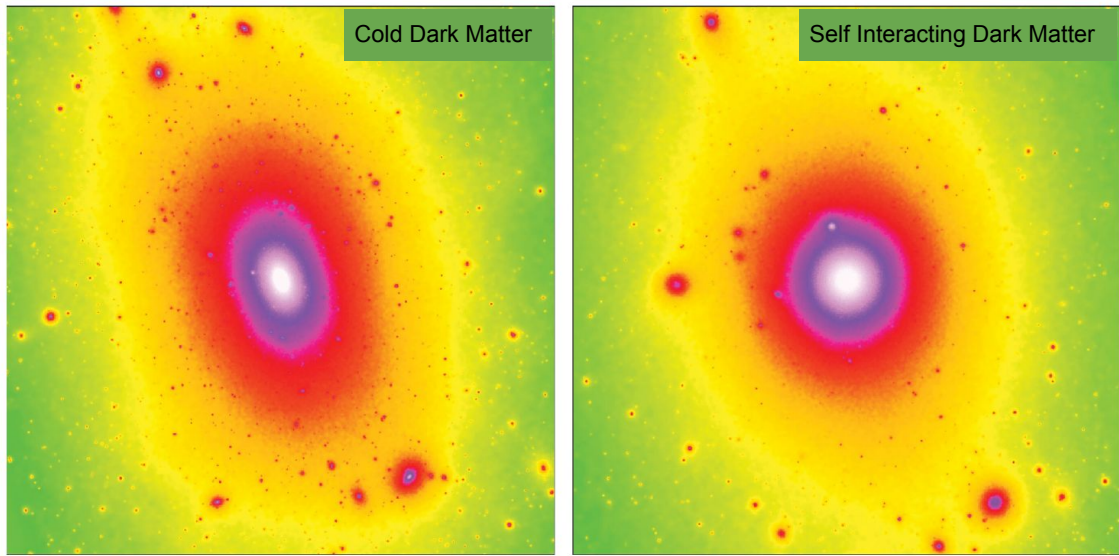


Figure 2.6: **MW in self-interacting and cold dark matter Universe.** Projected dark matter distribution of a MW-like halo in two different models: CDM in left, and collisional self interacting dark matter with $\sigma/m \gtrsim 1 \text{ cm}^2/\text{g}$ in right. The side length of the projection box is 270 kpc. SIDM models generate dwarf galaxies in cosmological simulations with a cored profile of size $\sim 0.3 - 1.5 \text{ kpc}$ which do not suffer from the cusp-core and too big to fail problem. Taken from [Vogelsberger et al. \(2012\)](#).

straints. Therefore, a constant value for σ_{SIDM} is unlikely to reproduce the halo shape of dwarf galaxies and galaxy clusters at the same time, and motivates a velocity dependent cross section $\sigma_{\text{SIDM}}(v)$ (Feng et al. 2010; Loeb & Weiner 2011; Vogelsberger et al. 2012). In these models, cross section scales reversely with the rms speed of dark matter particles. The velocity varies from $\sim 10 \text{ km s}^{-1}$ for dwarf galaxies to $\sim 1000 \text{ km s}^{-1}$ for galaxy clusters.

It is also possible to combine the WDM and SIDM to create a hybrid model of self-interacting dark matter particles with a truncated power spectrum in small scales. This theory first introduced by Cyr-Racine et al. (2016), as an effective theory of structure formation (ETHOS). The dimensionless matter power spectrum in this model is shown in Fig. 2.4. This model later fine-tuned by Vogelsberger et al. (2016), in order to solve the too big to fail and the missing satellite problems. It contains self interactions with a velocity dependent cross section parameter which is $\sigma_{\text{SIDM}}/m_{\text{SIDM}} \sim 0.3 \text{ cm}^2/\text{g}$ for the typical velocities of MW satellites. Simultaneously, it contains the cutoff in the matter power spectrum for WDM particles with $m_{\text{WDM}} \sim 3.4 \text{ keV}$.

2.3 Dwarf galaxies as hosts of first stars

In addition to their small size and the preponderance of dark matter in dwarf galaxies, which make them excellent probes for cosmological models on small scales, another fascinating feature is their old stellar population. The faintest among them, UFDs, reside in the lowest mass dark matter halos. Therefore, their gravitational field is less likely to retain the gas when it is pushed out by stellar feedback and UV-radiation during the EoR. Thus their properties must be dominated by the physics at work in the young Universe and it is thus natural that their stellar population contains an important signature from the first stars.

2.3.1 First star formation

The first generation of stars, the so-called Population III (Pop III) were formed from primordial gas, pristine of metals¹. After recombination, they shone the first light on the cosmic dark ages and played a key role in the reionization history of the Universe. The metal enrichment by Pop III stars set the floor for the transition to the next generations or Population II (Pop II) and the build up of the first galaxies.

Similarly to the present-day star formation, the Jeans instability (Jeans 1902) in primordial gas is responsible for the formation of first stars. In an infinite, uniform, and stationary distribution of self-gravitating primordial gas, the scale k of a perturbation δ determines that it is oscillating or exponentially growing. In a similar manner to Section 1.2, writing equation 1.9 for perturbations in a proto-star gas cloud, we can define the Jeans scale k_J ,

$$\frac{\partial^2 \delta}{\partial t^2} + 2 \left(\frac{\dot{a}}{a} \right) \frac{\partial \delta}{\partial t} = \delta (-c_s^2 k^2 + 4\pi G \bar{\rho}), \quad k_J \equiv \frac{1}{c_s} (4\pi G \bar{\rho})^{1/2}. \quad (2.5)$$

Here $\bar{\rho}$ is the average mass density of gas and c_s is the speed of sound. The co-moving spatial Laplacian ∇ equation 1.9 is replaced by the Fourier mode k . The critical mass characterizing the Jeans instability is the mass enclosed in a sphere of radius $\lambda_J/2$, where $\lambda_J = 2\pi/k_J$, and then can be defined as

$$M_J \equiv \frac{4\pi}{3} \bar{\rho} \left(\frac{2\pi}{k_J} \right)^3 = 50 M_\odot \mu^{-2} \left(\frac{n}{1 \text{ cm}^{-3}} \right)^{-1/2} \left(\frac{T}{1 \text{ K}} \right)^{3/2} \quad (2.6)$$

If the mass of an isothermal gas sphere exceeds this critical mass M_J , gravity overcomes the pressure gradients and the gas cloud collapses. Here the number density n appears in the definition of the gas density $\bar{\rho} = \mu m_p n$, where m_p is the proton mass, and μ is the

¹The gas at this stage only contains the primordial elements (D, He^3, He^4, Li) nucleosynthesised by the Big Bang and it is devoid of heavy elements.

mean molecular weight of the gas particles, whose value depends on the ionized fraction of gas. For atomic and molecular neutral primordial gas $\mu \approx 1.22$ and $\mu \approx 2.33$, respectively, whereas for a fully ionized gas $\mu \approx 0.59$, and for a gas with ionized hydrogen but singly ionized helium $\mu \approx 0.61$. Each value is appearing in different equations follows, depending on the state of gas. The temperature T enters the equation through the sound speed $c_s = (kT/\mu m_p)^{1/2}$.

Equation 2.6 reveals that the lower the density, as is the case in the early Universe, the larger is the critical mass for collapse. Here the approximation used to compute the Jeans mass is to consider the value of c_s at high redshifts. Right after recombination, the residual ionization, via the Compton scattering, keeps the gas temperature coupled to the CMB temperature. This is true down to a redshift of (Peebles 1993)

$$1 + z_t \approx 137 \left(\frac{\Omega_b}{0.0486} \right)^{2/5} \quad (2.7)$$

Afterwards for redshifts $z \lesssim z_t$, the gas temperature evolves adiabatically as $[(1+z)/(1+z_t)]^2$. The evolution of Jeans mass can be calculated up to the present time, as a function of redshift z , and the dimensionless cosmological parameters, namely, the density of matter Ω_m and baryons Ω_b (normalized to the 2016 Planck data)

$$M_J \simeq 5 \times 10^3 M_\odot \left(\frac{\Omega_m}{0.315} \right)^{-1/2} \left(\frac{\Omega_b}{0.0486} \right)^{-3/5} \left(\frac{z+1}{10} \right)^{3/2} \quad (2.8)$$

2.3.2 Environment of first stars

From equation 2.6 it is apparent that a gas cloud with a higher temperature is more stable. Thus besides the mass of a minihalo, another key factor required for gravitational collapse and the formation of first stars is the ability of gas to cool. The gas enclosed in a minihalo may dissipate its gravitational binding energy away through radiation. The time scale of this process, known as the cooling time, is defined as

$$t_{\text{cool}} = \frac{1}{\gamma - 1} \frac{nkT}{\Lambda}, \quad (2.9)$$

where n is the number density of gas particles, γ is the adiabatic index, T is the gas temperature and Λ is the radiative cooling rate of gas per unit volume. The longer the cooling time is for a minihalo, less unlikely it forms stars as an isolated object. Instead, one major merger on average is expected per Hubble time, $t_{\text{Hubble}} = 10^9 [(1+z)/7]^{-3/2}$ year (Lacey & Cole 1993). Therefore, it is more probable that the minihalo undergoes many mergers with comparable or more massive minihalos before it sufficiently cool to form stars.

Therefore, to determine the minimum mass of a star forming minihalo, it is of great importance to understand how cooling works within the primeval gas. Despite the chemical simplicity of the zero-metallicity gas, there are several cooling and heating channels, each becomes important in a specific density and temperature regime (see [Glover 2013](#), for a review).

Atomic H and He For temperatures above $T \sim 10^4$ K, atomic line cooling is very efficient. The process occur via the collisional excitation of atomic hydrogen and helium, as well as singly ionized helium. Using the Virial theorem $2K + U = 0$, to relate the potential energy U of a collapsing gas cloud to its kinetic energy K , we can define the Virial temperature,

$$T_{\text{vir}} = 1.98 \times 10^4 \left(\frac{\mu}{0.6} \right) \left(\frac{M}{1.5 \times 10^7 M_{\odot}} \right)^{2/3} \left[\frac{\Omega_m}{\Omega_m(z)} \frac{\Delta_c}{18 \pi^2} \right]^{1/3} \left(\frac{1+z}{10} \right) \text{ K}, \quad (2.10)$$

where $\Delta_c = 18 \pi^2 + 82 d - 39 d^2$, with $d \equiv \Omega_m(z) - 1$, is the ratio of the over-density to the critical density defined as $\rho_c \equiv 3H^2(t)/8\pi G$, at the time of collapse ([Bryan & Norman 1998](#)). At redshifts higher than $z = 6$, the cosmological matter density parameter can be approximated as $\Omega_m \simeq 1$. For a gas cloud of temperature $T = 10^4$ K and above, we can calculate the mass required to onset the gravitational collapse inverting equation 2.10,

$$M_{\text{atom}} \simeq 7.5 \times 10^7 \left(\frac{\mu}{0.6} \right)^{-3/2} \Omega_m^{-1/2} \left(\frac{1+z}{10} \right)^{-3/2} M_{\odot}. \quad (2.11)$$

Evidently M_{atom} is ~ 1000 times higher than the Jeans mass obtained from equation 2.6. This shows that lower mass systems must have a Virial temperature less than 10^4 K, and cool through another channel, than atomic H and He, to form stars.

Molecular hydrogen Before metals comes into play, the most abundant and hence the most important molecule in the primordial cosmic gas is molecular hydrogen, H_2 . The most dominant formation process for H_2 is through the reaction chain ([McDowell 1961](#); [Peebles & Dicke 1968](#)),



The rate at which the molecular hydrogen forms, is strongly dependant on the fractional ionization of the gas. When the ionization is low, H_2 formation is limited by the rate of H^{-1} formation via reaction 2.12. Afterwards, the generated H^{-1} ions rapidly form

H_2 in reaction 2.13 through the associative detachment with atomic hydrogen. However, when the fractional ionization is large, the H^{-1} ions are mainly destroyed in a mutual neutralization reaction $\text{H}^+ + \text{H}^- \rightarrow \text{H} + \text{H}$. At high redshifts, close to recombination, there is a high residual of the ionization fraction in the IGM. Thus the mutual neutralization is insignificant in the first star forming gas clouds.

A small fraction of molecular hydrogen may also form through the interaction with ionized hydrogen as intermediary molecule (Saslaw & Zipoy 1967),



It is worth mentioning that despite the high abundance of molecular hydrogen, it is not a particularly efficient coolant in primordial gas. Specifically at high densities, the H_2 cooling rate scales linearly with density (e.g, 201 2013), contrary to low density regions where $\Lambda \propto n^2$. Thus following equation 2.9, in highly dense clouds, the H_2 cooling time becomes independent of density. Whereas the time associated to the free-fall collapse scales inversely with increasing density $t_{\text{ff}} = [3\pi/(32G\rho)]^{1/2}$. Thus in dense regions, cooling by molecular hydrogen becomes inefficient. This can be formulated in the mass of gas clouds which can cool sufficiently within a Hubble time (201 2013),

$$M_{\text{crit}} \simeq 9 \times 10^5 \left(\frac{\mu}{1.2} \right)^{-3/2} \Omega_m^{-1/2} \left(\frac{1+z}{10} \right)^{-3/2} M_{\odot}. \quad (2.16)$$

Here we converted the critical Virial temperature in equation 2.10 to a critical mass. It implies that at redshifts below $z \simeq 40$, a large number of gaseous halos which are less massive than M_{crit} , are unable to form stars, due to insufficient cooling within a Hubble time. Haiman et al. (2001) suggested that depending on the onset of reionization, these non star forming minihalos potentially played a significant role as sinks of ionizing photons.

Deuterium hydride Originally proposed by Lepp & Shull (1984), deuterated hydrogen HD, is another important coolant in the pristine gas. Even though the initial ratio of deuterium to hydrogen is small, is substantially increases in low temperature gas, by the following reaction, known as chemical fractionation,



However, in the formation of first stars, HD plays a minor role as a coolant compared to the molecular hydrogen (Bromm et al. 2002). The reason is due to the low temperature, $T \sim$

150 K (Glover & Abel 2008), required for HD cooling to be efficient. This low temperature is typically not accessible during the collapse of the first metal-free gas minihalos.

To summarize, the environment that Pop III stars formed in was completely different from the star formation at the present time which is happening in cold molecular clouds which are filled with dust and pervaded by magnetic fields. The host minihalos of first stars formed after recombination out of hot atomic hydrogen which was pulled by the gravitational fields of dark matter over-dense regions. The cooling in these minihalos was inefficient due to the lack of dust and metals, and the deficiency of strong magnetic fields from an astrophysical source, such as supernovae explosions. These conditions lead to a high temperature for the primordial gas. The hydrostatic equilibrium thus predicts that the initial mass of Pop III stars to be much higher than of those formed today, to counterbalance their internal thermal pressure (Carlberg 1981; Larson 1998; Silk 1983). However, the mass range of first stars still remains elusive. The following section describes the existing models for their initial mass.

2.3.3 Initial mass function

Since Salpeter (1955) first derived an analytical form for the initial mass function (IMF) from the observational data of field stars with masses between 0.4 to $10 M_{\odot}$, it has become a fundamental clue to understand the formation of stars and evolution of galaxies. IMF is defined as the relative number of stars, as a function of their individual initial mass, that forms during a single star forming episode (Carigi 2011).

A power law initially used to express the IMF, $\Phi(m) = m^{-\Gamma}/\beta$, where m is the star mass, Γ the slope of the power law and β the normalization constant to ensure that the integral of $\Phi(m)$ over the entire mass range is unity.

$$\int_{M_{\min}}^{M_{\max}} \Phi(m) dm = 1, \quad (2.18)$$

where $[M_{\min}, M_{\max}]$ defines the allowed mass interval for a star. Generally, IMF is determined over a large mass interval, from the lowest mass stars to the most massive, all forming in a single star formation burst.

In the late 1970s it was recognized that the IMF does not follow a single power law for all stellar progenitor masses. To resolve this inconsistency between the IMF models and observations, Kroupa et al. (1993) suggested a multi-segment power law with a shallower slope at lower masses. A log-normal function then was proposed to describe the IMF in mass ranges below $1 M_{\odot}$ (Adams & Fatuzzo 1996). As stellar mass is characterized by the product of a handful of variables, the distribution of $\log m$ follows a Gaussian form, given by

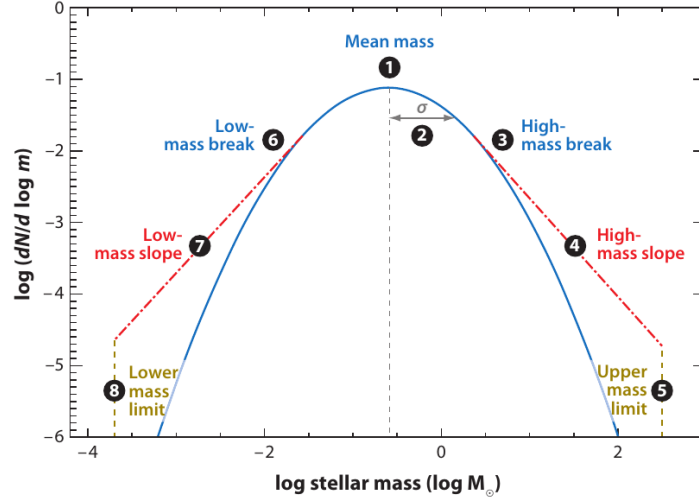


Figure 2.7: **Schematic shape of the IMF.** The solid line shows IMF approximated as a log-normal distribution with (1) the characteristic mass m_c , (2) dispersion σ , (3,6) the high/low-mass break between the log-normal function and the power-law which is shown in the red dotted line, (4,7) high/low-mass slope, (5,8) upper/lower mass limits. Taken from [Bastian et al. \(2010\)](#).

$$\Phi(m) \sim \exp \left(-\frac{(\log m - \log m_c)^2}{2\sigma^2} \right), \quad (2.19)$$

which is shown in Fig. 2.7, The behaviour of a power-law IMF ($dN/d \log m$) is represented by a straight line in this log-log plot. Through the definition given in 2.19, IMF can be described by a few key parameters: the characteristic mass m_c , dispersion σ , the power-law slope α , and break points between the power-low and log-normal distributions, and finally the lower and upper mass limits.

Constraints on the shape of the IMF are generally empirical, and the most stringent limits are those come from the study of nearby stars in the Local Group. Different analytical IMF models for Pop II stars are shown in Fig. 2.8, in comparison with the observational data of stellar clusters ([Kroupa 2002](#)), associations ([Massey 2003](#)), nearby star-forming regions ([Rebull et al. 2010](#)), and the field ([Luhman et al. 2009](#)). For instance the multi-segment IMF in ([Kroupa 2002](#)) for Pop II stars is given by

$$\Phi(m) = \frac{m^{-\Gamma}}{\beta}, \quad \text{with} \quad \Gamma = \begin{cases} -0.7, & 0.01 \leq m/M_\odot < 0.08 \\ +0.3, & 0.08 \leq m/M_\odot < 0.50 \\ +1.3, & 0.50 \leq m/M_\odot < 1.00 \\ +1.3, & 1.00 \leq m/M_\odot \end{cases} \quad (2.20)$$

Defining an accurate IMF, however, requires corrections to the observed star counts. One

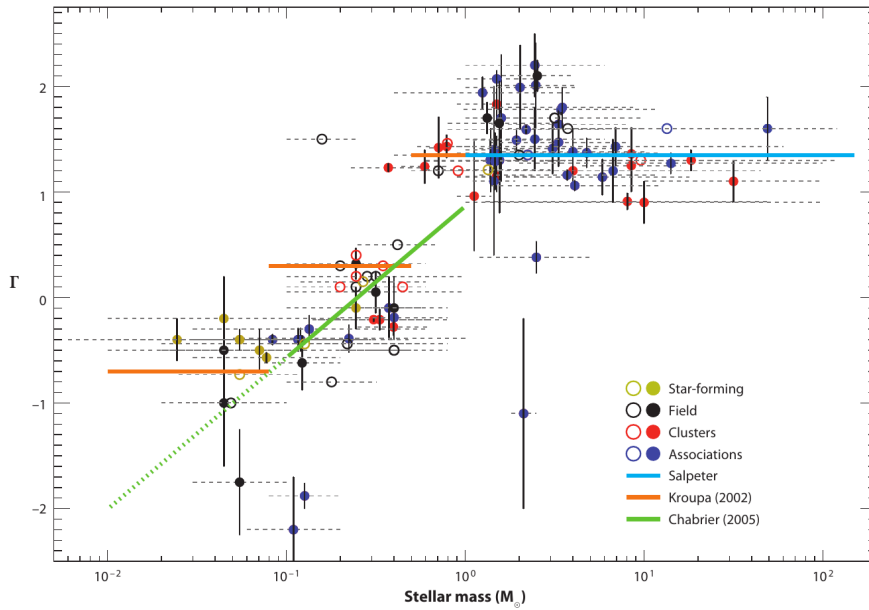


Figure 2.8: **A comparison between different IMFs.** The analytical models proposed by [Salpeter \(1955\)](#), [Kroupa \(2002\)](#), and [Chabrier \(2003\)](#), are compared to the observational data of stellar clusters ([Kroupa 2002](#)), associations ([Massey 2003](#)), nearby star-forming regions ([Rebull et al. 2010](#)), and the field ([Luhman et al. 2009](#)). Γ represents the slope in each model.

needs to consider the variations in the star formation rate over time, the number of binary or multiple stellar systems and also environmental factors. Thus in the search for corrections to the IMF, it is crucial to sample the most extreme conditions. For instance, the environment of the first stars is completely different from the star formation nurseries at the present time. It motivates the idea of a different IMF for the first massive stars compared to the second generation of low-mass long-lived stars.

Along this line, the first attempts to determine the IMF of first stars initiated by [Abel et al. \(2002\)](#); [Bromm et al. \(1999\)](#). Their detailed numerical simulations of the first star formation suggested a monolithic collapse of an immense gas cloud, eventually developing into a very massive star of about $30 - 100 M_{\odot}$. More recent simulations which can zoom into the center of the star forming regions and achieve a high numerical resolution in these regions, argue that most of the Pop III stars are formed as binaries ([Glover et al. 2010](#); [Turk et al. 2009](#)). This reveals the possibility that Pop III could have an IMF very much alike massive Pop II stars. Following 2.20, it leads to a simple power law with a unique slope $\alpha = -1.3$.

Besides the slope, the mass interval of first stars $[M_{\min}, M_{\max}]$, is another key factor to characterize their IMF. However, the existing simulations are still premature to draw firm conclusions about the minimum and maximum mass eligible for Pop III. In general, most

of these studies agree that the first generation of stars, have formed in multiple stellar systems and had a wide range of masses (e.g. [Klessen 2019](#)). The low-mass limit of first stars depends on various physical mechanisms at work in the early Universe. For example, the level of turbulence in gas may lead to the disk fragmentation ([Greif et al. 2011](#); [Stacy & Bromm 2013](#); [Turk et al. 2009](#)). In addition, radiative feedback ([Krumholz et al. 2009](#); [Rosen et al. 2016](#)) and magnetic fields ([Bovino et al. 2013](#); [Latif et al. 2013](#); [Machida & Doi 2013](#); [Machida et al. 2008](#)) as main contributors to the ISM energy budget, naturally play a role. Potential impact of dark matter annihilation is also a considerable factor ([Freese et al. 2008](#); [Hirano et al. 2011](#); [Iocco 2008](#); [Yoon et al. 2008](#)). The abundance patterns observed in metal-poor stars also provides constraints on the mass range of Pop III stars may explode as different type of supernovae. This latter is discussed in details in Section 2.3.5.

On the other hand, the direct observation of first stars is out of reach for ground-based observatories such as the European Extremely Large Telescope ([Tamai & Spyromilio 2014](#)) or the Thirty Meter Telescope ([Skidmore et al. 2015](#)), but even for the more advanced generation, such as JWST ([Gardner et al. 2006](#)), Euclid ([Laureijs et al. 2011](#)), and the Wide-Field Infrared Survey Telescope ([Spergel et al. 2015](#)). The high redshift constraints on the initial mass of the first stars therefore must be indirect, stemming from potential observations of supernovae explosions, which mark the end of their short lives ([Klessen 2019](#)).

2.3.4 First supernovae

As metals are absent in the primeval gas, the first generation of stars are expected to have a low atmospheric opacity. It causes the mass loss through the stellar winds to be negligible for Pop III (e.g. [Kudritzki & Puls 2000](#)). Therefore, elements are ejected by supernovae of different progenitor masses, play the main role in the metal enrichment of ISM at the beginning.

Metals associated with the explosion of first massive stars are possibly originated from core-collapse supernovae (CCSNe) or highly energetic pair-instability supernovae (PISNe). Figure 2.9 shows the final fate of Pop III forming from zero metallicity gas. In the following a description of these two types of supernovae in addition to the Type Ia supernovae (SNIa) which is not expected to occur in Pop III scenarios, as well as Failed supernovae (FSNe) which end the life of a star without ejecting metals.

Type Ia The typical range of initial masses is about $3 - 8 M_{\odot}$ for those stars that can be progenitors of SNIa (e.g., [Kobayashi et al. 2000](#)). Typically there is a close-binary stellar system, with the more massive star accretes material from its neighboring company and evolves to form a white dwarf. The accretion continues till the white dwarf reaches the

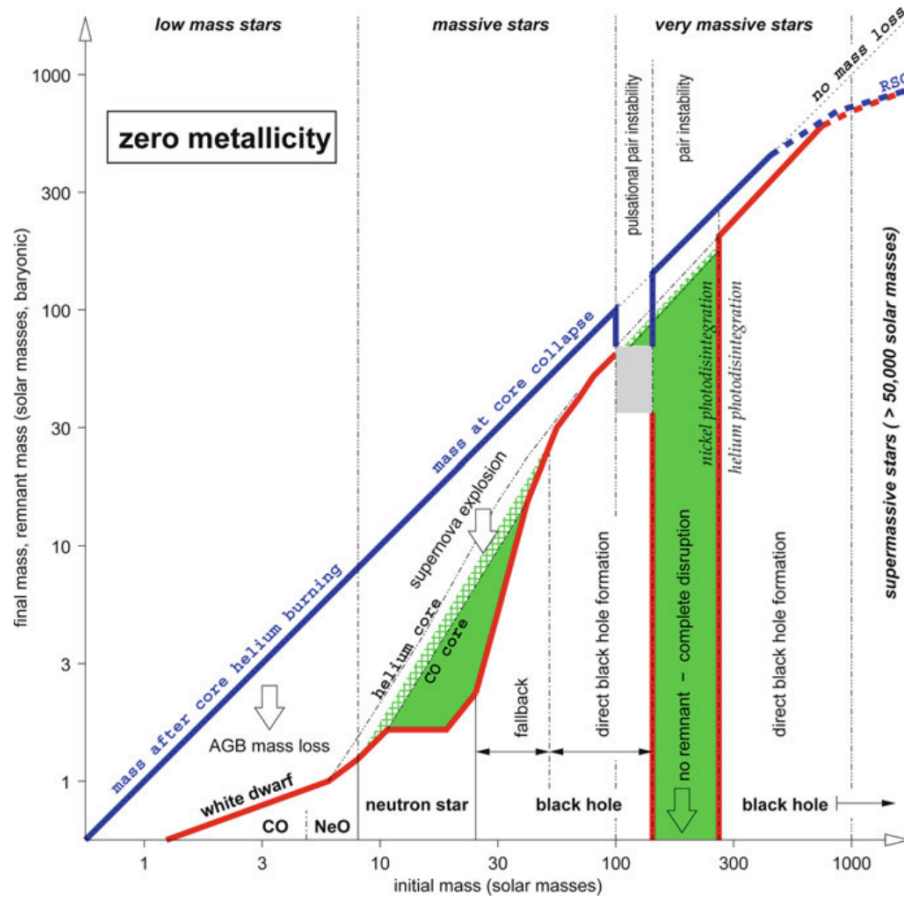


Figure 2.9: **Initial mass function of Pop III stars forming from gas with zero metallicity.** The x-axis shows the progenitor masses. The y-axis shows both the mass loss in winds and supernovae explosions when each event begins, as well as the mass of the remnants. Taken from [Woosley et al. \(2002\)](#)

Burning stage		20 M _⊙ , Pop I		200 M _⊙ , Pop III	
Fuel	Main product	T (10 ⁹ K)	Time (year)	T (10 ⁹ K)	Time (year)
H	He	0.02	10 ⁷	0.15	210 ⁶
He	O, C	0.2	10 ⁶	0.3	210 ⁵
C	Ne, Mg	0.8	10 ³	1.2	10
Ne	O, Mg	1.5	3	2.5	310 ⁻⁶
O	Si, S	2.0	0.8	3.0	210 ⁻⁶
Si	Fe	3.5	0.02	4.5	310 ⁻⁷

Figure 2.10: **Nuclear burning phases in massive stars.** Columns respectively show the hydrostatic nuclear burning stages, the main products, the temperature and burning time scales for a star with a solar composition and a Pop III star with a primordial composition. Taken from [Heger \(2012\)](#).

Chandrasekhar mass limit ², and then the evolution of the star as a supernova initiates. At this phase two scenarios are possible:

- In a **single degenerate** model, the lower mass star belongs to the main sequence. In this scenario, hydrogen-rich gas is transferring from the binary companion to the C + O white dwarf at a sufficiently high rate, $10^{-7} - 10^{-6} \text{ M}_{\odot} \text{ yr}^{-1}$, to increase its mass to till surpassing the Chandrasekhar limit ([Nomoto 1982](#); [Whelan & Iben 1973](#)).
- In a **double degenerate** model, the binary companion, like the more massive companion, is a C + O white dwarf. Thus in this scenario, these two carbon-oxygen stars are merging and their combined mass surpasses the Chandrasekhar mass limit ([Iben & Tutukov 1984](#); [Webbink 1984](#)).

Both scenarios have their pros and cons. Although observational evidence disfavours the single degenerate model (e.g., [Shen et al. 2012](#)), theoretical models have indicated that the production mechanism of a typical SNeIa can not be explained by the merging of a double white dwarf system ([Saio & Nomoto 1985, 1998](#); [Segretain et al. 1997](#)), and the predicted lifetimes are incompatible with the chemical evolution in the solar neighborhood.

Core collapse supernova Stars with progenitor masses in range $\sim 8 - 30 \text{ M}_{\odot}$ pass all of the nuclear burning phases listed in Table 2.10, namely, hydrogen, helium, carbon, neon, oxygen, and silicon burning. At the end of the nuclear burning stages, they form an iron core that eventually collapses. What happens after the core collapses is considerably determined by the initial mass of the star.

- For **lower mass stars** of $M \lesssim 20 \text{ M}_{\odot}$, a neutron star is formed. In less than a second,

²the Chandrasekhar mass limit is the maximum mass of a stable white dwarf.

a shock generated by the neutrino energy deposition is driven outward. This causes the hot neutron star undergoing a supernova explosion with a peculiar energy of about 10^{51} erg.

- For **more massive stars** of $20 \lesssim M \lesssim 30 M_{\odot}$, the hydrogen envelope is lost through the stellar winds. The rate of mass loss is a function of various parameters, such as initial mass, metallicity, and evolutionary stages. These restrict the accuracy in computing the upper mass limit of stars explode as CCSNe.

Failed supernova Stars with initial masses $30 \lesssim M \lesssim 140 M_{\odot}$ are expected to fall into a black hole rather than forming a neutron star (Smartt 2009). However, the exact transition mass regime is still unclear. One of the reasons is due to the uncertainty associated with the maximum mass of neutron stars (Demorest et al. 2010). Another complication stems from the possibility that massive neutron stars, forming in the first CCSNe scenario, may leave behind a black hole after the supernovae explosion (Zhang et al. 2008).

Pair instability supernova Originally introduced by Barkat et al. (1967), PISNe are associated with very massive stars with initial masses of about $140 - 300 M_{\odot}$, with a negligible mass loss during their lifetimes. This corresponds to a range of helium cores of about $\sim 67 - 129 M_{\odot}$ (Nomoto et al. 2013). The physical mechanism leading to a PISNe explosion is as follows:

- Hydrostatic equilibrium in a sphere of ideal gas requires a higher central temperature for a higher stellar mass (see equation 2.6). Meaning that in such massive stars, the radiation pressure is dominant and, with a good approximation, the total pressure scales as $P \propto \rho^{4/3+\beta/6}$, with $\beta \ll 1$ (Woods et al. 2019). This *softness* of the equation of state places these stars close to marginal stability, and very sensitive to small perturbations (Fowler 1964; Goldreich & Weber 1980; Kippenhahn et al. 2013).
- The high energy/temperature after the central carbon burning phase triggers the creation of electron positron pairs. After the pair creation, the pressure is reducing, which pushes the star towards instability.
- At this stage, due to a sudden drop in the radiation pressure, further compression is not counterbalanced by a sufficient pressure support. This leads to a run away collapse in the star.
- The temperature increases during the collapse and sets the condition for nuclear burning, which in turn further increases the entropy. During this phase, first ${}^8\text{O}$ and ${}^{10}\text{Ne}$, and then ${}^{14}\text{Si}$ burns in a few seconds, while the star is collapsing.
- In the course of rapid compression and burning, the temperature raises to the point that the electron-positron pairs have enough energy to dominate the pressure term

in the equation of state. At this final phase, nuclear burning entirely disrupts the star, releases a large amount of heavy elements, and leaves no remnants behind.

The kinetic energy released in the ISM by PISNe can be 50 times of a CCSNe. If a Pop III star is more massive than $M > 300 M_{\odot}$, the thermonuclear energy release is insufficient to halt the collapse and the star undergoes a direct implosion into a black hole. This provides an upper mass limit for the PISNe scenario. The transition from PISNe with no remnants, to black hole with no ejection, is rather sharp. There is no evidence of partial explosions in between (Heger 2012).

2.3.5 Chemical evolution of primordial gas

So far, different types of supernovae are described. In the following, the chemical evolution of the primordial gas, after the first supernovae explosions is explained. At the end of the lifetime $\tau(m)$ of each individual star, a fraction of its mass is potentially ejected into the ISM via an explosion, and the rest fraction remains in the stellar core in the form of remnants w (Tinsley 1980),

$$m_{\text{ejacta}}(m) = (1 - w(m)) m. \quad (2.21)$$

Here the ejected gas mass m_{ejacta} , depends on the initial stellar mass m . For computing the total gas mass ejected by supernovae into the ISM per unit time, the total number of stars dN of mass M between m and $m + dm$ which are formed at $t - \tau(m)$, should be counted. dN is normally defined by two functions:

$$dN(m, t) = \frac{1}{m} \Phi(m) \Psi(t) dm. \quad (2.22)$$

(i) The first one is $\Phi(m)$, representing the IMF, which as described above is the fraction of stars having a star of mass $M \in [m, m + dm]$, (ii) The second one is $\Psi(t)$, representing the star formation rate, which is expected to scale proportionally with the ISM gas budget at each time scale t ,

$$\Psi(t) = \frac{1}{\tau_s} f_g(t), \quad (2.23)$$

where f_g is defined as the ratio of the gas mass to the total baryonic mass in a galaxy, and τ_s is the total star formation time scale in a galaxy. The total ejected gas mass per unit time is then the integration over the whole mass interval

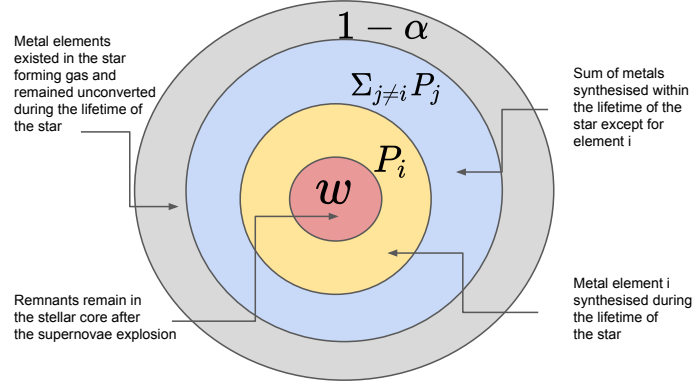


Figure 2.11: **Scheme of the construction of a star of metal element i .** A fraction p_i of metal element i can be synthesised during the lifetime of a star and ejected by a supernova explosion, or existed in the star forming gas and remained unconverted during the star's lifetime. Inspired by Poirier (2004).

$$M_{\text{ejacta}}(t) = \int_0^N m_{\text{ejacta}}(m) dN(m, t - \tau(m)) = \int_{M_{\min}}^{M_{\max}} (1 - w(m)) \Psi(t - \tau(m)) \Phi(m) dm, \quad (2.24)$$

where we substitute for m_{ejacta} from equation 2.21, and dN from equation 2.22. The gas enrichment can then be followed along the same line. It means that the quantity of metals ejected by stars per unit time must be computed. All of the metals ejected in the course of a supernovae explosion falls into one the following categories:

- A fraction p_i of metal element i can be synthesised during the lifetime of a star and ejected by a supernova explosion.
- A fraction of metal element i may be existed in the star forming gas and remained unconverted during the star's lifetime. Its fraction is given by $Z_i(t)(1 - w - \sum_i p_i)$, where w is the remnant of the explosion, $\sum_i p_i$ is the sum of all synthesised elements, and Z_i represents the fraction of element i in the total unsynthesised gas at time t .

The value of $\alpha = (w + \sum_i p_i)$ is usually referred to as the *helium core*, shown in Fig. 2.11. Similar to equation 2.24, the total ejected mass E_{ejacta} of each element per unit time is given by

$$E_{\text{ejacta},i}(t) = \int_{M_{\min}}^{M_{\max}} [p_i(m) + (1 - \alpha(m)) Z_i(t - \tau(m))] \Psi(t - \tau(m)) \Phi(m) dm, \quad (2.25)$$

The two terms in the brackets, stands for the first and second categories mentioned above for the ejected metals. Figure 2.12 shows the value for the helium core, remnants and

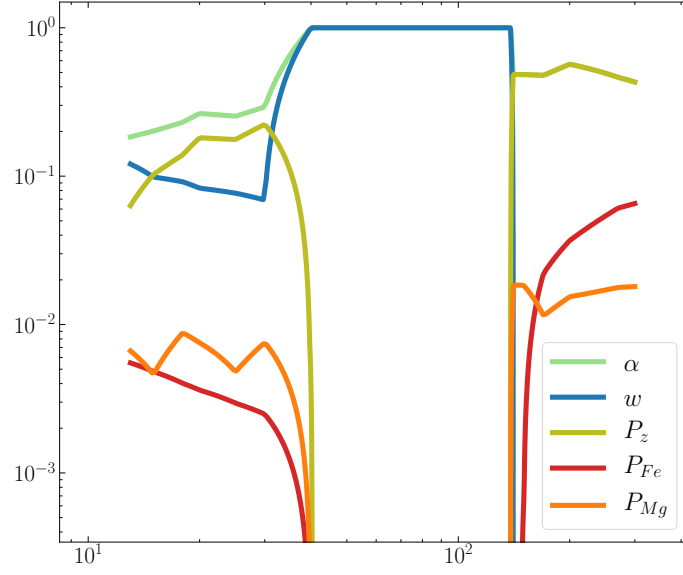


Figure 2.12: **Origin of the yields.** The fraction of helium core α , remnants w , ejected metals P_z , and ejected Fe and Mg, P_{Fe} and P_{Mg} , respectively, as a function of progenitor mass for a Pop III star.

total ejected metals, in addition to the two elements studied in details in this thesis, iron and magnesium, as a function of the progenitor stellar mass.

It appears from equation 2.25 that the main parameters play a part in shaping the chemical enrichment of a galaxy are the IMF, the star formation history, and the stellar yields, outlining which elements and in what amounts are produced by stars of differing masses. In Chapter 7, the impact of these parameters on the metal enrichment of dwarf galaxies is described in details. Indeed, the lasting effect of Pop III stars, is their production and distribution of metals in the early Universe.

Chapter 3

Primordial magnetic fields

Another aspect of galaxy formation, explored in this thesis, are magnetic fields. In particular I studied the role of magnetic fields with a primordial origin in the process of galaxy formation and evolution. This has become of interest as recent observational evidence has supported weak magnetism of $\sim 10^{-16}$ gauss, even in the intergalactic medium (IGM) voids (Neronov & Vovk 2010). This observation is based on the absence of a signal, when looking at blazars located behind the IGM voids. As shown in Fig. 3.1, through the collision of a highly-energetic gamma ray with a photon, an electron-positron pair is created. These then collide with other passing photons and generate the second but lower energy gamma rays. If the blazar light passes through a magnetized void, the electron-positron pair will be deflected and the lower energy gamma rays will be pointed away from the observer. Indeed, Neronov & Vovk (2010) showed that the low energy gamma ray is missing in the observations of a suitably located blazar. The presence of fields in these relatively quiet environments is difficult to explain purely by astrophysical processes in the late Universe (Bertone et al. 2006; Furlanetto & Loeb 2001), and would perhaps favor a primordial origin.

As mentioned in Section 1.1, cosmic magnetic fields are possibly a relic from the inflationary epoch in the early Universe. Inflation provides an ideal mechanism for producing large-scale primordial magnetic fields:

- First, the inflationary expansion provides the kinematic means of producing long wavelength effects, at very early times, on scales smaller than the Hubble radius or the size of the horizon ($\equiv H_0^{-1}$). It may produce electromagnetic wave modes which correlate on large scales, by simply stretching them. A downside is, however, that the fields become very weak when being diluted in inflation.
- Second, inflation provides the dynamical means of exciting the electromagnetic field fluctuations while they are sub-horizon. These modes can be transformed to classical fluctuations when they re-enter the horizon later.

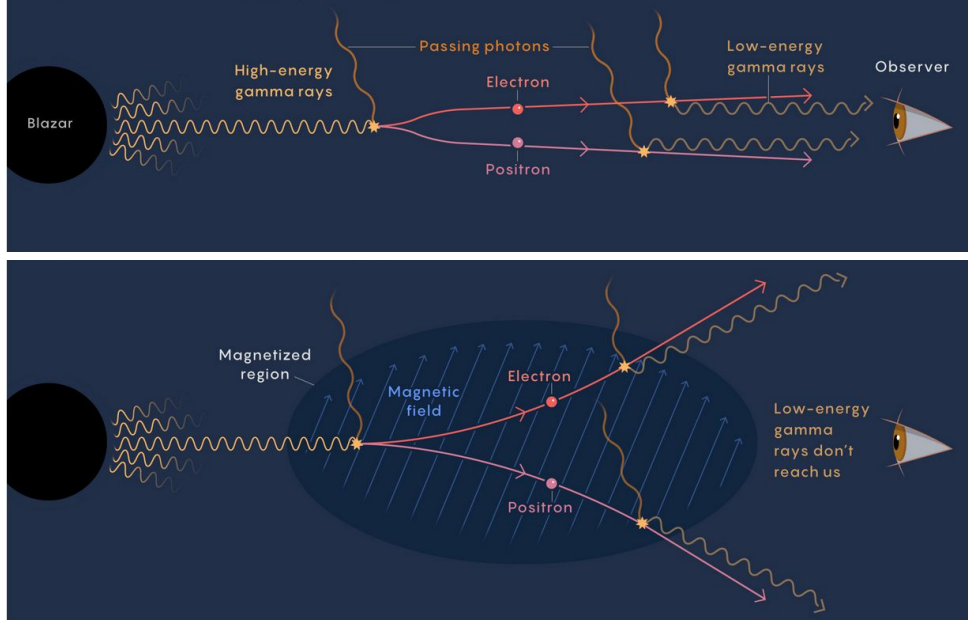


Figure 3.1: **Evidence for extra-galactic magnetic fields from observations of TeV blazars.**
Credit: Samuel Velasco/Quanta Magazine

- Finally, during inflation, the Universe is devoid of charged particles, as the plasma density is diluting by expansion. This makes the fluid at this epoch not to be a good conductor. Thus magnetism generating from a zero field is not yet prevented by the flux conservation ¹.

There is however an important obstacle for generating primordial fields during inflation: the electromagnetic field is conformally coupled and during inflationary expansion phase that the energy density is dominated by the vacuum energy, electromagnetic field does not *feel* the expansion.

Electrodynamics in an isotropic and homogeneous space-time is formulated by the FRW metric. The action for electromagnetic fields and their interactions with charged particles is given by

$$S = - \int \sqrt{-g} d^4x \frac{1}{16\pi} g^{\mu\alpha} g^{\nu\beta} F_{\mu\nu} F_{\alpha\beta}, \quad (3.1)$$

where the electromagnetic field tensor $F_{\mu\nu} = A_{\nu,\mu} - A_{\mu,\nu}$ is characterized by the standard electromagnetic 4-potential A_μ . The geometry of space-time is defined by the metric tensor $g_{\mu\nu}$ through the interval between two infinitesimally separated events $ds^2 = g_{\mu\nu} dx^\mu dx^\nu$. The action is invariant under conformal transformations of metric and potential. It follows

¹Although one may argue that the perfect conductivity does not prevent the dynamo effect either. For example, Biermann Battery ([Biermann 1950](#)) could play a role when the density and the temperature gradients, ∇n and ∇T , are not parallel to each other, $\nabla n \times \nabla T \neq 0$ (see e.g. equation 150 in [Subramanian 2016](#)).

that electromagnetic fluctuations can not be amplified via inflation and B always decreases as a^{-2} , or the density of magnetic energy $\rho_B \propto a^{-4}$. To change the evolution of magnetic fields with expansion and producing appreciable primordial magnetic flux, the conformal invariance of S should therefore be broken.

3.1 Generation of Primordial magnetic fields

During inflation, there are different ways for breaking the conformal invariance of the electromagnetic field, namely, (i) coupling of electromagnetic field action to scalar fields ϕ like inflaton, responsible for inflation, (ii) gravitational couplings of the photon, namely with $R_{\mu\nu}A_\mu A_\nu$ where $R_{\mu\nu}$ is the Ricci tensor measuring the curvature of space-time, (iii) having a charged massless, scalar field ψ to couple with the photon, and (iv) the coupling of the photon to axions θ

$$S = \int \sqrt{-g} d^4x \left[-\frac{f^2(\phi, R)}{16\pi} F_{\mu\nu} F^{\mu\nu} + g_2 \theta F_{\mu\nu} F^{\mu\nu} - D_\mu \psi (D^\mu \psi)^* \right], \quad (3.2)$$

where g_2 is the coupling constant of order 2. The spatial projection of the covariant derivative is defined as $D_\mu B^\alpha = h^\mu_\beta h^\alpha_\nu B^\nu$, with h^μ_ν being the spatial metric. Once the conformal invariance is broken, a process known as super-adiabatic amplification enhance modes with wavelengths longer than H_0^{-1} . In this way, the energy density of a given mode, is decreased only as a^{-2} instead of treated adiabatically as a^{-4} . This mechanism leads to the generation of primordial seed fields coherent on the scale of Mpc [Turner & Widrow \(1988\)](#).

In addition to the generation of coherent large scale magnetic fields during inflation, [Hogan \(1983\)](#) suggested that a small fraction of the energy released during the primitive electroweak or quark-hadron transitions may also be converted into cosmic magnetic fields in large scales. Presumably, bubbles of the new phase form and decouple from the background old phase. They then expand and collide, till the volume occupied by the new phase dominates over the old phase. The turbulence generated through these collisions may amplify the magnetic fields in a dynamo mechanism ([Kazantsev 1968](#)).

Besides dynamo effect, another magneto-amplification scenario is worth mentioning is chiral anomaly of weak interactions. It stem from the imbalance in the number density of left- (μ_L) and right-handed (μ_R) electrically charged fermions: $\mu_5 \equiv \mu_L - \mu_R$, the so-called chiral chemical potential ([Boyarsky et al. 2012](#)). A non-zero μ_5 may produce electric current along the magnetic field, and leads to large scale dynamo actions. [Schober et al. \(2022\)](#) simulations support the dynamo effect even for fluctuating μ_5 with zero mean. Turbulence produced via this process is magnetically dominated. This results in the generation of magnetic fields through the α -effect, or a source term of current scaling

with the magnetic field, with its proportionality depending on μ_5 . [Schober et al. \(2022\)](#) showed that in this case, the fluctuations of μ_5 should be correlated on length scales much larger than those characterize the maximum of the dynamo growth rate. Then a small-scale chiral dynamo mechanism could lead to the magnetic field amplification.

The evolution of the primordial fields generated either in the inflationary phase or during electroweak or quark-hadron phase transitions, depends on various factors, such as its initial strength and spectrum. The strength of the large scale fields, as the Universe expands, generally decreases as $B \propto 1/a^2$, except when it is subsequently amplified by a dynamo in collapsing objects. The dynamo mechanism is only a channel of amplification and requires seed magnetic fields. There are also magneto-genesis scenarios for the generation of galactic fields via the magnetic flux, that is entangled in the collapsing gas, during the formation of a galaxy. However, in this case, a very strong primeval field is required, which has at least the same field strength that is observed today, $\sim 3 \times 10^{-6}$ gauss ([Ôki et al. 1964](#); [Piddington 1964](#); [Turner & Widrow 1988](#)).

3.2 Primordial magnetic field power spectrum

Primordial magneto-genesis scenarios mentioned above conventionally result in a homogeneous, isotropic and Gaussian random initial field, which is characterized by a power law spectrum,

$$P_B(k) = A k^{n_B}, \quad (3.3)$$

where n_B represents the slope, and A the amplitude of the spectrum. The nonlinear evolution of this initial field can then be expressed in the Fourier space ([Landau & Lifshitz 1987](#)), as the root mean square of magnetic field fluctuations

$$\langle B_i(k) B_j^*(k') \rangle = (2\pi)^3 \delta(k - k') \frac{P_{ij}(k)}{2} P_B(k), \quad (3.4)$$

where $P_{ij}(k) = \delta_{ij} - k_i k_j / k^2$ is the transverse projection tensor, which projects all quantities into the Fourier 3-space orthogonal to k_i . The importance of the projection tensor lies in the fact that estimating the perpendicularly projection to the line of sight is easier than measuring the tensor field from the observations in large-scale structure ([Kurita & Takada 2022](#)).

Commonly the amplitude A is defined in terms of the variance of the magnetic field strength at the present time B_λ , smoothed at the scale of $\lambda = 2\pi/k_\lambda = 1 h^{-1} \text{ Mpc}$,

$$B_\lambda^2 = \langle B_i(x, t_0) B_j^*(x, t_0) \rangle = \frac{1}{\pi^2} \int_0^{k_c} dk k^2 (2\pi)^3 \delta(k - k') \frac{P_{ij}(k)}{2} P_B(k), \quad (3.5)$$

where $k_c = 1 \, h \, \text{Mpc}^{-1}$. Then from equation 3.5 the amplitude A is expressed as (Shaw & Lewis 2012):

$$A = \frac{(2\pi)^{n_B+5} B_\lambda^2}{2\Gamma(\frac{n_B+3}{2}) k_\lambda^{n_B+3}}. \quad (3.6)$$

3.3 Magnetic matter power spectrum

In Section 1.2, we discussed the growth of dark matter and baryonic matter perturbations. Before recombination, due to the high rate of photon-baryon scatterings, radiations and baryonic matter behave as a sole tightly coupled conducting fluid. After the photons start to free stream, they decouple from baryons and become a single conducting fluid. Since the beginning of the radiation free streaming, magnetic fields play a significant role in the Universe now contains a highly ionized plasma. Thus equation 1.9 is no longer a good approximation to describe the evolution of baryonic perturbations. Instead the magneto-hydrodynamics equations are needed to describe the growth of matter perturbations:

- The Euler equation 1.3 must be completed with the magnetic term (Wasserman 1978)

$$\bar{\rho}_b \left[\frac{\partial v}{\partial t} + H(t)v \right] = -\frac{1}{a} \nabla p_b + \frac{1}{\rho_b} J \times B - \frac{1}{a} \bar{\rho}_b \nabla \phi - \frac{4\rho_\gamma}{3} n_e \sigma_T v. \quad (3.7)$$

Here, the current density J depends on E and B through the Ohm's law,

$$J = \rho_b v + \sigma(E + v \times B) \quad (3.8)$$

with ρ_b is the fluid charge density, v is the baryon velocity and conductivity σ is measured in its rest frame. The electric field E is given by the time-space components of the electromagnetic tensor $F_{\mu\nu}$, contrary to the magnetic field B which is given by the space-space components. $F_{\mu\nu}$ is anti-symmetric, with zero diagonal components and six independent components of the electric and magnetic fields, three of each one.

$$F^{0i} = E^i \quad F^{12} = B^3 \quad F^{23} = B^1 \quad F^{31} = B^2. \quad (3.9)$$

- The induction equation,

$$\frac{\partial(a^2 B)}{\partial t} = \frac{1}{a} \nabla \times \left[v \times (a^2 B) - \eta \frac{1}{a} \nabla \times (a^2 B) \right]. \quad (3.10)$$

Here $\eta = (4\pi\sigma)^{-1}$ is the magnetic diffusivity. Peebles (1980); Wasserman (1978) showed that the perturbed velocity term does not have a significant impact on the

distortion of the primordial fields. In addition, in the ideal magneto-hydrodynamics, assuming a highly conductive medium, diffusivity is negligible and $\eta \rightarrow 0$. The induction equation 3.10 thus is solved as $B(x, t) = B_{\text{rec}}(x)a^2(t_{\text{rec}})/a^2(t)$. $B_{\text{rec}}(x)$ refers to the value of the magnetic field at recombination ($t = t_{\text{rec}}$), as the growth of compression modes is suppressed before this epoch (Subramanian & Barrow 1998). The value of $B_{\text{rec}}(x)$ is smoothed at a scale of 1 Mpc.

- The Maxwell equations,

$$\nabla \cdot B = 0, \quad \nabla \times E = -\frac{\partial B}{\partial t}, \quad \nabla \cdot E = 4\pi\rho_b, \quad \nabla \times B = 4\pi J + \frac{\partial E}{\partial t} \quad (3.11)$$

- The continuity equation, the Poisson equation, and the equation of state are the same as equation 1.6, equation 1.7, and equation 1.8, respectively.

Similar to Section 1.2, after taking the divergence of equation 3.7, we do some manipulations including the continuity equation 1.6 for $\nabla \cdot v$, the Poisson equation 1.7 for the gravitational potential, and the equation of state 1.8 for the pressure. The result is formulated below, describing the growth of density perturbations due to the baryonic matter, in the presence of the primordial magnetic fields.

$$\begin{aligned} \frac{\partial^2 \delta_b}{\partial t^2} + \left[2H + \frac{4\rho_\gamma}{3\bar{\rho}_b} n_e \sigma_T a \right] \frac{\partial \delta_b}{\partial t} = c_b^2 \nabla^2 \delta_b + 4\pi G [\bar{\rho}_b \delta_b + \bar{\rho}_{\text{DM}} \delta_{\text{DM}}] \\ + \frac{\nabla \cdot [(\nabla \times B_{\text{rec}}) \times B_{\text{rec}}] a^4(t_{\text{rec}})}{4\pi \bar{\rho}_b a^6(t)}. \end{aligned} \quad (3.12)$$

This is the the same as equation 1.9 with an additional term for the Lorentz force associated with the tangled field $F_L = (\nabla \times B) \times B$. The equation for the dark matter perturbations is the same as in equation 1.10. To solve these two coupled equations for the total matter perturbations δ_m , taking the curl of equation 3.7, and using $a(t)/a(t_{\text{rec}}) = (t/t_{\text{rec}})^{2/3}$ in the early Universe ($1100 \gtrsim z \gtrsim 10$), we obtain

$$\delta_m(x, t) = \frac{t_{\text{rec}}^2 \nabla \cdot [(\nabla \times B_{\text{rec}}) \times B_{\text{rec}}]}{4\pi \bar{\rho}_m(t_{\text{rec}}) a^2(t_{\text{rec}})} \left[\frac{9}{10} \left(\frac{t}{t_{\text{rec}}} \right)^{2/3} + \frac{3}{5} \frac{t_{\text{rec}}}{t} - \frac{3}{2} \right] \quad (3.13)$$

And lastly, the matter power spectrum is derived using equation 1.11.

Thus far, the impact of a stochastic primordial magnetic field on the growth of over-dense regions in the early Universe is discussed. However, there are two physically motivated effects to additionally consider: the effect of magnetic Jeans length and damping because of the radiation viscosity.

The magnetic Jeans scale is the counterpart of the Jeans scale discussed in Section 2.3.1 (see equation 2.5). As density perturbations grow due to the gravitational collapse, the pressure in the baryonic matter is raised and eventually interrupt the growth and make the perturbations stable. As one of the prime contributors to the pressure support, magnetic fields naturally play a part in shaping the evolution of over-dense regions. Large scale fields can be compressed, in the course of the collapse of over-densities. For scales below the magnetic Jeans length, this process further increases the magnetic pressure and counteracts the gravitational collapse. The magnetic counterpart of the Jeans instability is very close to using the Alfvén velocity instead of c_s in the expression of the ordinary Jeans length which gives (Peebles 1980),

$$4\pi G\rho_m = \frac{k_{J,B}^2 B_\lambda^2}{8\pi\rho_b} \quad k_{J,B} = \frac{4\pi\sqrt{2\rho_m\rho_b}G}{B_\lambda} \quad (3.14)$$

The left side term represents the gravitational instability, while the right side incorporates the magnetic pressure. However (Kim et al. 1996) could drive a more accurate expression for the magnetic Jeans scale which occurs at the transition between growing modes and oscillatory modes,

$$k_{J,B} = \frac{5\pi\rho_b\sqrt{G}}{B_\lambda} \quad (3.15)$$

Along this line, the simplest way to encapsulate the magnetic Jeans effect is to modify the baryon sound speed c_s in equation 2.5 as $c_s^2 \rightarrow c_{s,b}^2 + \alpha v_A^2$, where $c_{s,b}$ is the unmagnetized baryon sound speed, α is an angular factor determined by the velocity and the field orientation, and v_A is the Alfvén velocity,

$$v_A^2 = \frac{1}{4\pi\rho_b} B_\lambda^2 \quad (3.16)$$

where ρ_b is the density of the conducting fluid, using the fact that during the epoch of matter domination $\rho_m = \rho_b$. Perturbation growth is suppressed below the magnetic Jeans scale.

The second nonlinear contribution need to be addressed is damping. After recombination, baryons are no longer coupled to the photons. However, the remaining scattering applies a non-negligible drag force to the conducting fluid. The presence of this homogenous radiation drag force leads to the damping of propagating magnetic waves. Subramanian & Barrow (1998) showed that damping of magnetic fields on small scales can be approximated as

$$B(k) = B_0(k) \exp\left(-k^2 \int^\tau v_A^2 \tau_c d\tau\right) \quad (3.17)$$

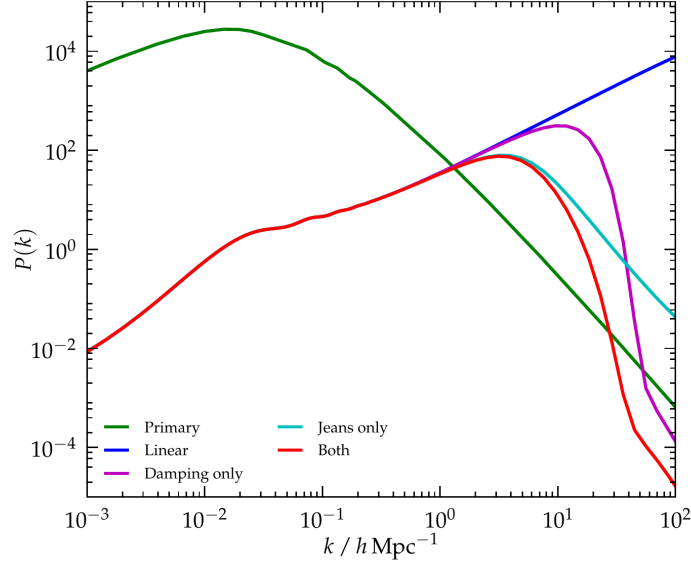


Figure 3.2: **The magnetic matter power spectrum** including the additional nonlinear effects. The linear power spectrum is compared to the impact of magnetic pressure support and damping, and the combined of both effects. All power spectra, calculated with magnetic field strength of $B_\lambda = 5$ nG and spectral index $n_B = -2.9$, are compared to the classical Λ CDM. Taken from [Shaw & Lewis \(2012\)](#).

where $\tau_c = 1/(an_e\sigma_T)$ is the time of the last scattering, with n_e is the electron number density, and σ_T the Thompson cross-section for electron-proton scattering. Thus depending on the strength of the magnetic field, the scale of the perturbations which survives damping varies. In general it is of order of the Alfvén velocity multiplied by the baryon-photon Silk damping scale.

These two nonlinear effects mentioned above are compared to the linear magnetic power spectrum which grows as $p(k) \propto k$ in Fig. 3.2. Including the magnetic Jeans effect increases the pressure support and thus the Jeans length. This leads to small perturbations to oscillate instead of grow. On larger scales, damping causes a slower growth of perturbations. This appears in the form of a cutoff in the matter power spectrum. In Fig. 3.2, both of these effects are calculated for a magnetic field of strength $B_\lambda = 5$ nano Gauss (nG) and spectral index $n_B = -2.9$. The comparison to the primary adiabatic mode is for illustrating the impact of primordial magnetic fields on the Λ CDM matter power spectrum.

3.4 Observational Signatures

A stochastic primordial magnetic field not only modifies the matter power spectrum and initiation of structure formation in the early Universe, but causes additional perturbations

in the CMB temperature and polarization map. Both these effects modify the matter distribution in the local Universe with observable signatures. Here we look at the limits current cosmological data sets place on the properties of magnetic fields in the early Universe.

CMB anisotropies and polarization Primordial magnetic fields include density perturbations to those induced by inflation. These perturbations are mapped on the last scattering surface of the CMB photons, where primordial fields are predicted to leave a variety of signals (Durrer 2007; Planck Collaboration et al. 2016; Subramanian et al. 2006; Widrow et al. 2012). Therefore, CMB anisotropies provide one of the key probes for both detecting and constraining the primordial magnetic fields.

The trace of a stochastic initial field on the CMB map could be observed in the excess temperature and polarization anisotropies. The unique signature of primordial fields, however, stem from the CMB non-Gaussianity. The magnetically produced anisotropies are predicted to display a strongly non-Gaussian pattern. Furthermore, the existence of a tangled field in the IGM may lead to the Faraday rotation effect in the polarized component of the CMB, and produce a B-mode signal in addition to the inflationary induced E-mode signal (see e.g., Ade et al. 2015; Planck Collaboration et al. 2016).

The overall analysis of CMB, constrains the primordial magnetic field to have a amplitude of a few nano Gauss smoothed over the spatial scale of 1 Mpc, and the spectral index $n_B > -3$. For a nearly scale invariant spectrum with $n_B = -2.9$, considering the impact of magnetic fields on heating and ionization (Chluba et al. 2015; Kunze & Komatsu 2015; Sethi & Subramanian 2005), this limit is tighten to $B_\lambda < 0.70$ nG.

Weak gravitational lensing The potential intervening of primordial fields in early structure formation can also be probed with gravitational lensing (Bartelmann & Schneider 2001; Munshi et al. 2008). In weak lensing, the shape of a large sample of background (intrinsically) elliptical galaxies are evaluated, to measure the shearing distortion of their shapes. The two-point shear correlation function is related to the matter power spectrum, in angular scale ℓ , according to the following relation,

$$\xi(\theta) = \frac{1}{2\pi} \int_0^\infty d\ell \ell P_k(\ell) J_{0,4}(\ell\theta), \quad (3.18)$$

where θ is the angular separation between the galaxy pairs, and $J_{0,4}$ Bessel functions. The cosmological shear field in the standard Λ CDM scenario is a curl-free quantity and stands for an E-type field. Along these lines, decomposing the observed shear signal into E (non-rotational) and B (rotational) components, we can recognize the contribution of magnetic fields. Detecting non-zero B-modes then implies a non-gravitational contribution to the shear field.

[Pandey & Sethi \(2012\)](#) compared the two-point shear correlation function with the CFHTLS data (Canada – France – Hawaii Telescope Legacy Survey, [Fu et al. 2008](#)). They detected an excess power in the shear correlation function for a nearly scale-free magnetic field. This way, they constrained the upper limit of the primordial fields to $B_\lambda < 1 - 3 \text{ nG}$ depending on the value of the spectral slope.

Lyman- α clouds Lyman- α absorption lines in the spectrum of the high redshift quasars propose a direct observational constraint for the smallest scale structures ([Croft et al. 2002](#); [Seljak et al. 2005](#)). Therefore, they can be a powerful probe for the excess in the matter power spectrum induced by primordial fields at small scales. Semi-analytical models of [Pandey & Sethi \(2013\)](#) compared the impact of a nearly scale invariant magnetic power spectrum on the Lyman- α opacity to the observational data from [Faucher-Giguère et al. \(2008\)](#), and obtained the upper limit of $0.3 - 0.6 \text{ nG}$.

Reionization signals With the formation of the first galaxies and the emergence of the first stars, Universe evolved from an almost neutral state to its current completely ionized state, during a period known as the epoch of reionization. The spectra of the high redshift quasars, constrains the fraction of neutral hydrogen (HI) at redshifts $z \gtrsim 6$ ([Fan et al. 2006](#)). Consistently, Planck data constrains the beginning of reionization to redshift $z \simeq 10$.

The presence of primordial magnetic fields supposedly accelerates the formation of the subgalactic structures. As more sources of ionizing photons might be born due to this effect with a larger radius of ionized hydrogen around each source, this potentially must cause the reionization to start earlier than in the standard Λ CDM Universe.

The observational constraints on the EoR, therefore can be used to limit the strength and power spectrum of the primordial magnetic fields. However, due to the uncertainties associated with the impact of magnetic fields on the ISM of galaxies and the rate of star formation, obtaining precise constraints for the primordial magnetic fields is not an easy task. In a nutshell, the efficiency of star formation in galaxies that form in a primordially magnetized Universe, needs to be much lower than in a standard Λ CDM, to be in agreement with the limits of the reionization redshift. The constraints derived this way by [Pandey et al. \(2015\)](#) for a nearly scale invariant field, with $n_B = -2.85$ to -2.95 , are $B_\lambda = 0.059 - 0.358 \text{ nG}$.

Redshifted 21 cm signal Here I first explain the origin of the 21 cm signal and then its usage for detecting magnetic fields. As the only radio source at high redshifts, observation of the 21 cm emission is one of the most promising probes of the thermal and ionization history of the Universe (see e.g., [Pritchard & Loeb 2012](#)). This signal arises from the interaction of the magnetic dipole moment of the proton and that of the electron, which leads to the hyper-fine splitting of the ground state of the atomic hydrogen into two

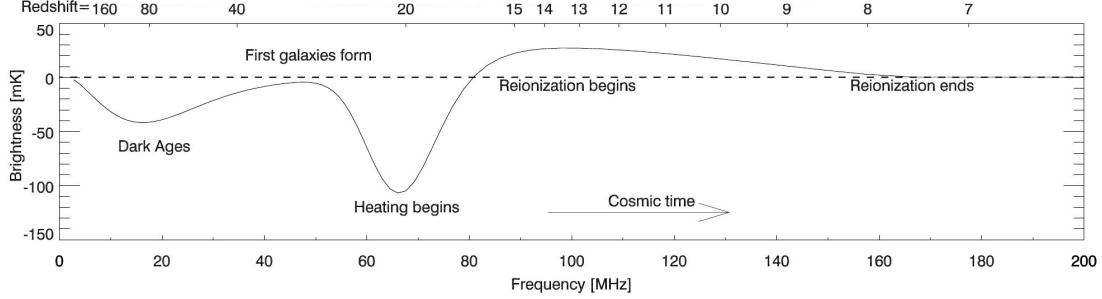


Figure 3.3: **The expected evolution of the sky-averaged 21 cm brightness** from dark ages to the epoch of reionization. Solid curve represents the 21 cm cosmic hydrogen signal and dashed line shows $\Delta T_b = 0$ in equation 3.19. Taken from [Pritchard & Loeb \(2012\)](#).

distinct levels separated by a small energy $\Delta E = hc/\lambda_{21} = 5.9 \times 10^{-6}$ eV, with h being the Planck's constant, and c the speed of light, gives $\lambda_{21} = 21$ cm. We may express the brightness temperature of the signal against the CMB as,

$$\Delta T_b = 27 Q_{\text{HI}} \left(\frac{1 - Y_p}{0.76} \right) \left(\frac{\Omega_b h^2}{0.023} \right) \left(\frac{0.15}{\Omega_m h^2} \frac{1+z}{10} \right)^{1/2} \left(1 - \frac{T_\gamma}{T_s} \right) \text{mK}, \quad (3.19)$$

where Q_{HI} is the neutral fraction of hydrogen, Y_p is the helium fraction in the total hydrogen content, T_γ is the CMB radiation temperature and T_s is the spin temperature of the HI line ([Furlanetto et al. 2006](#)). The time evolution of the signal is shown in Fig 3.3.

- **$200 \gtrsim z \gtrsim 1100$:** The earliest the signal arises is after thermal decoupling of the baryonic matter from the CMB at redshift $z \simeq 200$. Before that, following the recombination epoch, the residual ionization keeps the temperature of the cosmic gas locked to the CMB temperature via Compton scattering. The kinetic and spin temperature of baryons, T_K and T_s respectively, are hence coupled to the radiation temperature T_γ . Therefore, $\Delta T_b = 0$ in equation 3.19, and there is no observable signal at $200 \gtrsim z \gtrsim 1100$.
- **$40 \lesssim z \lesssim 200$:** As the Universe expands, the gas is able to cool adiabatically as $T_K \propto (1+z)^2$, while $T_\gamma \propto (1+z)$. Therefore, the gas temperature falls off faster with expansion than the CMB temperature, and at this stage $T_K < T_\gamma$. Due to the

collisional coupling, also $T_s < T_\gamma$. Hence $\Delta T_b < 0$ in equation 3.19, and the early signal is seen in absorption against the CMB.

- $z_\star \lesssim z \lesssim 40$: As the expansion of the Universe continues, the density of gas further drops, till the collisional coupling becomes ineffective. At this stage the signal would be diminished, since the radiative coupling to the CMB sets $T_s = T_\gamma$.
- $z_\alpha \lesssim z \lesssim z_\star$: Once the first stars and possibly the first black holes are formed at redshift z_\star , they emit both Lyman- α photons and X-rays. The thermal energy required for Lyman- α coupling of gas is considerably less than that for heating it to $T_K > T_\gamma$. Thus T_s once again is coupled to the gas temperature which remains below the CMB temperature. With $T_s \sim T_K < T_\gamma$, the second absorption signal is expected.
- $z_r \lesssim z \lesssim z_\alpha$: Eventually heating becomes significant. When the temperature of gas approaches T_γ , emission lines from hotter regions are expected, till the gas reaches the same temperature everywhere. After this heating transition, the temperature of gas raises above T_γ , which leads to emission lines until the end of the EoR. The 21 cm signal remaining from this epoch, are originated from the collapsing clouds of neutral hydrogen, known as damped Lyman- α systems.

Primordial magnetic fields can alter the expectations of this standard model in different ways. In the post-recombination era, the Universe is mostly neutral with a low radiative viscosity. Thus tangled magnetic fields can deposit their energy into the IGM via ambipolar diffusion² and/or decaying magneto-hydrodynamics turbulence. Both processes can significantly increase the ionization fraction and heat the IGM in the early Universe (e.g. Jedamzik et al. 1998; Subramanian & Barrow 1998). In the presence of a sufficiently strong field, T_s does not fall below T_γ , and the 21 cm signal is only observable in emission (Sethi & Subramanian 2009). This prediction is testable with the recent observations from the EDGES (Experiment to Detect the Global EoR Signature, Bowman et al. 2018) which show strong absorption at redshifts $14 \lesssim z \lesssim 22$. Such results suggest that primordial magnetic fields either have a weak amplitude or a nearly scale invariant spectral index.

While the effect of magnetic diffusion and decaying of magnetic turbulence are well studied in the literature, the impact of primordial magnetic fields on the structure formation has been less explored. Since primordial magnetic fields cause modifications to the formation of first galaxies, they would leave indicative imprints on the 21 cm line at high redshift as well.

²Ambipolar diffusion is the source of diffusion for positive and negative electrical charges when they interact with an electric field. In a plasma various positive and negative species diffuse at the same rate.

In summary, the observational signatures mentioned above, are further pushing the limits on both detecting and constraining the primordial magnetic fields. Specially with the next generation radio telescope SKA, exploring magnetic fields even in the intergalactic medium voids will be possible with the Faraday technique. At this stage, numerical simulations provide a powerful tool for studying this poorly-explored phenomenon, and comparing theories with the observed data. But how primordial magnetic fields can be probed in simulations?

As discussed, the magnetically induced perturbations, for a scale-invariant field, may dominate the standard Λ CDM matter power spectrum, in large wave numbers, and therefore affect the formation of the small scale structures. Since direct observational constraints of the matter power spectrum do not reach scales smaller than those probed by the Lyman- α forest, we need to rely on dwarf galaxies to explore structure formation on yet smaller scales. The influence of primordial magnetic fields, which predominantly modify the number and properties of dwarfs, could thus lead to a substantial revision of our understanding of the standard cosmological model. This latter is discussed in details Chapter 5, in the context of cosmological simulations.

Chapter 4

Numerical Techniques

Cosmological structure formation and the dynamics of astrophysical systems involve non-linear processes, which can not be modelled analytically. As a consequence numerical techniques are required to understand the complexity of the gas dynamics in the nonlinear regime. In this thesis, two different codes are used for modeling the nonlinear processes involved in the formation of a galaxy, **GEAR** ([Revaz & Jablonka 2012](#)) and **RAMSES** ([Teyssier 2002](#)). The former uses the Smoothed Particle Hydrodynamics (SPH), which is a particle-based method, while the latter works with Adaptive Mesh Refinement (AMR), which is a grid-based method.

In general, the main difference between particle-based and grid-based codes is in using Lagrangian or Eulerian discretization techniques, while there are exceptions. The first one, breaks down the total mass into particles, and the second one divides space into finite volumes. This is described in more details later in this chapter. It is also explained why different solvers for hydrodynamics may lead to considerable differences in the outcome, unlike dark matter only simulations where the choice of method does not affect the results. Furthermore, the particle-based and grid-based methods for solving gravitational interactions and gas dynamics are introduced.

4.1 Gravity

A dark matter object - like the halo of a galaxy - can be defined as a discrete N-body system. Its state is described by the phase-space distribution function $f(r, v; t)$ of non-relativistic, collisionless matter. The evolution of f in principle is followed by the collisionless Boltzmann equations, supplemented by the Poisson equation for the gravitational field ϕ ,

$$\frac{df}{dt} = \frac{\partial f}{\partial t} + \sum_i^N v_i \frac{\partial f}{\partial r_i} - \sum_i^N \frac{\partial \phi}{\partial r_i} \frac{\partial f}{\partial v_i} = 0, \quad (4.1)$$

$$\rho(r; t) = \int f(r, v; t) d^3v, \quad (4.2)$$

$$\nabla^2 \phi(r) = 4\pi G \rho(r). \quad (4.3)$$

These coupled equations are solved by discretizing the distribution function f as an ensemble of N phase-space components $\{r_i, v_i\}$ with $i = 1, \dots, N$. Here each of these discrete elements is translated into a particle in a N -body simulation. Computing the evolution of f , for the phase-space distribution of the whole system, is then downsized to self-consistent dynamical evolution of a system of N particles. In this formulation, each fiducial micro-particle in a simulation represent a region in phase-space, which contains a large number of real particles in a physical system. Thus the information in a N -body model is always incomplete and limited to the resolution of the simulation.

4.1.1 Gravity calculation

The gravitational potential of the distribution formulated in equation 4.3, which is produced by N particles with masses m_i , at coordinates r_i in a domain of dimension L^3 , and assuming periodic boundary conditions, is given by

$$\phi(r) = -G \sum_{j=1}^N \sum_{n=-\infty}^{\infty} \left\{ \frac{m_j}{[(r_j - r + q_n)^2 + \varepsilon(r_j - r + q_n)^2]^{1/2}} - m_j \varphi_n(r) \right\}^1 \quad (4.4)$$

where $\varepsilon(r)$ represents the gravitational softening law. The purpose of this function, is force softening, meaning to avoid large angle scatterings. It prevents the numerical expenses to model the orbits at the potential singularity. Softening length must have a finite range, meaning that it is zero for distances larger than half the box length $\varepsilon(r > L/2) = 0$. In most cosmological models of structure formation, a fixed gravitational softening $\varepsilon_0 \ll L/2$ is used, which defines the smallest length-scale resolved. In this case, $-Gm/\varepsilon_0$ defines the depth of the gravitational potential. In equation 4.4, q_n represents the periodic boundary conditions. It denotes the periodic displacement vectors given by $q_n = nL$, where $n = (n_x, n_y, n_z)$ is a vector of integer triplets, and sum over n is over these triplets. Finally, $\varphi_n(r)$ in the subtracted term, is the potential of a homogeneous cuboid of size L^3 and unit mass at displacement position q_n .

In cosmological simulations, it is convenient to introduce comoving coordinates, comoving momenta and comoving densities, as internal computational variables, instead of their physical counterparts. The connection to the physical variables is via the scale factor. For

¹This is the complete form given in (Springel et al. 2021).

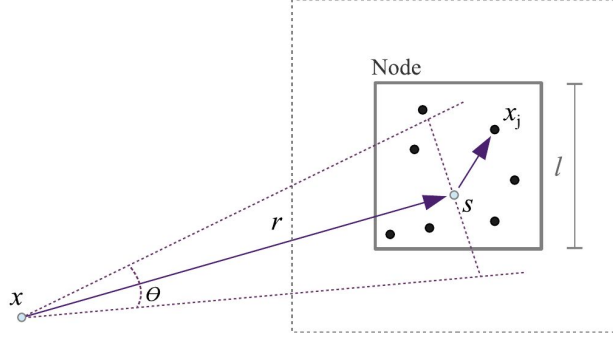


Figure 4.1: **Tree node.** s which is the position of the center of mass for particles in a group with size l , has the distance r to the particle at position x which is under the force evaluation. This group to this particle is seen at angle $\theta = l/r$. Taken from (Springel et al. 2021).

instance, the physical coordinate r_{physic} is described in terms of the comoving coordinate r_{com} as

$$r_{\text{physic}} = a(t) r_{\text{com}} \quad (4.5)$$

It implies that in an infinite expanding space, modelled in a box of size L^3 , with a periodic boundary condition, the Newtonian equation of motion in comoving coordinates is given by

$$\frac{d}{dt}(a^2 \dot{r}_{\text{com}}) = -\frac{1}{a} \nabla \phi(\dot{r}_{\text{com}}). \quad (4.6)$$

Now that the collisionless fluid is discretized to a N -body system and the gravitational potential for each particle is defined, the next step would be summing over all particles. For that there are different methods to reduce the $\mathcal{O}(N^2)$ computational cost induced by the summations. In the following, the particle-mesh algorithm, which is the method used in GEAR, is described.

4.1.2 Tree particle-mesh algorithm

One of the popular approaches for calculating the potential in a N -body system, is the hierarchical tree algorithm (Appel et al. 1985; Barnes & Hut 1986; Dehnen 2000), which arranges particles in a hierarchy of groups. The strength of a tree algorithm lies in reducing the computational cost from $\mathcal{O}(N^2)$ to $\mathcal{O}(N \log N)$, by grouping distant particles and approximating their multipole forces to the lowest value, when computing the forces exerted on a target particle (Appel et al. 1985). This is shown in Fig. 4.1, where s which

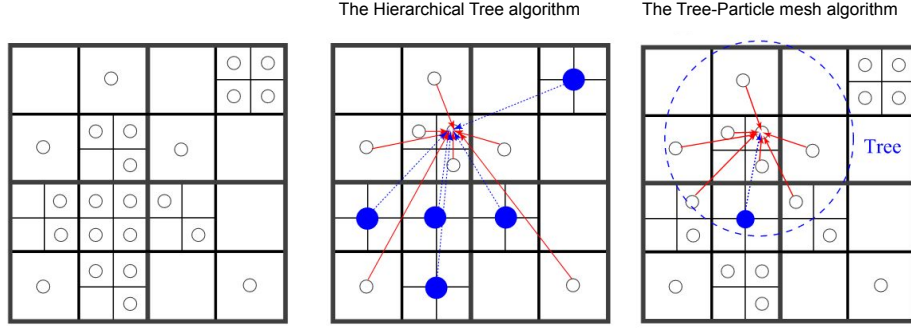


Figure 4.2: **The schematic view of the hierarchical tree and the tree-particle mesh algorithms.** White circles stand for particles. Blue circles represent the multipole expansions of tree nodes. Red arrows show the particle-particle interactions, while the blue arrows show the particle-multipole interactions. The dashed blue circle shows the cutoff radius of the tree-particle mesh algorithm. Within this radius, forces are calculated by the hierarchical tree algorithm. Adapted from [Ishiyama et al. \(2012\)](#).

is the position of the center of mass for particles in a group with size l , has the distance r to the particle at position x which is under the force evaluation. Thus this group to this particle is seen at angle $\theta = l/r$. *Tree walk* for calculating the forces, starts from the node that a target particle is in. If θ for another node is smaller than a critical angle θ_c , its force is added to the accumulation, and the tree walk along this branch stops. Otherwise, all the sub-nodes of this tree node must be considered.

In a tree, the space is recursively divided into cubic smaller finite volumes. The idea, for instance in the popular Barnes-Hut oct-tree ([Barnes & Hut 1986](#)), with its sketch in Fig. 4.2, is to start from a cube that consists of all particles. This parent cube is then divided into 8 identical sub-cubes of half the size in each dimension. This pattern is recursively repeated till each children contains only one particle.

Another technique for reducing the computational cost of N -body simulations is the particle-mesh method ([Hockney & Eastwood 1988](#); [Klypin & Shandarin 1983](#); [White et al. 1983](#)). The idea is to overlay space with a discrete mesh and then assigning masses to each grid in the mesh. Then the Poisson equation can be solved for potential per grid by using Fast Fourier Transform (FFT) technique. Lastly, the gravitational forces at the position of individual particles on the mesh is computed by differentiating and interpolating the potential.

The strength of the hierarchical tree method, compared to particle-mesh techniques (e.g.

(Klypin & Shandarin 1983) is not to be limited by resolution. However, when the density contrast in a mass distribution is not sufficiently high, this method can be very slow. Xu (1995) combined the hierarchical tree algorithm with the particle-mesh technique in the Fourier space, to use the best of both worlds. This method which is described here as the particle-mesh tree, is the one used in simulations run with the **GEAR** code. In this scheme, the tree algorithm is restricted to the short-range scales, while the particle mesh is used for computing the long-range gravitational forces. A brief description of this technique follows.

The first step is to consider the potential in the Fourier space and then separate the long-range and short-range parts of each mode as

$$\phi_k = \phi_k^{\text{long}} + \phi_k^{\text{short}}, \quad (4.7)$$

where

$$\phi_k^{\text{long}} = \phi_k e^{-k^2 r_s^2}, \quad \phi_k^{\text{short}} = \phi_k \left[1 - e^{-k^2 r_s^2} \right]. \quad (4.8)$$

This way, the convolution in real space is transformed to a simpler point-by-point multiplication in Fourier space. The difference between the two terms in equation 4.8 is only in a short-range cut-off factor. Here r_s can be interpreted as a force-split scale, controlling the force computation accuracy. The long-range potential is solved efficiently with the mesh-based method in the Fourier space. Whereas, the short-range potential is computed by tree algorithm in the real space, with a very small r_s against the simulation box size $r_s \ll L$. In computing the short-range potential with a hierarchical tree algorithm, any tree node which is further than a finite cut-off range will be neglected in the tree walk. Since the tree walk is restricted to the surrounding of a target particle, rather than the whole volume, this hybrid method is faster than the hierarchical tree.

So far the details of computing gravity in cosmological simulations have been described. However, even though gravity is the driving force for structure formation in the universe, as it enables the formation of galaxies and the environment they reside in, at small scales, gas hydrodynamics become very important. In the following section, equations which govern the dynamics of the baryonic component are briefly described.

4.2 Gas dynamics

In hydrodynamical simulations, the principal equations solved, are the Euler equations, which are the conservation laws for mass, momentum and energy. Here I compare the Eulerian form of these equations which is principally used in grid-based codes, to their

Lagrangian form, with the convective derivatives $d/dt = \partial/\partial t + v \cdot \nabla$, used in particle-based codes,

- Conservation of mass

$$\text{Eulerian : } \frac{\partial \rho}{\partial t} + \nabla(\rho v) = 0, \quad \text{Lagrangian : } \frac{d\rho}{dt} + \rho \nabla \cdot v = 0, \quad (4.9)$$

- Conservation of momentum

$$\text{Eulerian : } \frac{\partial}{\partial t}(\rho v) + \nabla(\rho v v^T + P) = 0, \quad \text{Lagrangian : } \frac{dv}{dt} + \frac{\nabla P}{\rho} = 0, \quad (4.10)$$

- Conservation of energy

$$\frac{\partial}{\partial t}(\rho e) + \nabla[(\rho e + P)v] = 0, \quad \text{Lagrangian : } \frac{d\epsilon}{dt} + \frac{P}{\rho} \nabla \cdot v = 0, \quad (4.11)$$

which assume an inviscid fluid, meaning that the internal friction of the gas flow can be neglected. In equation 4.11, $e = \epsilon + v^2/2$ is the specific total energy (energy per unit mass), and ϵ is the specific thermal energy. Equations 4.9, 4.10 and 4.11, must be supplemented with the equation of state for an ideal gas,

$$P = (\gamma - 1) \rho \epsilon, \quad (4.12)$$

with the adiabatic index γ . These together represent the gas hydrodynamics, which are gravitationally coupled to dark matter via the Poisson equation 4.3. For solving the equations above, in the following two techniques for approximating the continuum dynamics of fluids through the use of particles and grids respectively, are introduced.

4.2.1 Smoothed particle hydrodynamics

Kernel interpolation

In SPH, the described particles in Section 4.1.1 (discrete points which are interpolated) move with the local fluid velocity, and derivatives are calculated with an approximation instead of finite differences. In this way, thermodynamical quantities, such as density and pressure, are obtained by smoothing over neighboring particles. For that the principle idea is using a kernel for defining the smoothed interpolated version of any field $F(r)$, such as the density field,

$$F(r) = \int F(r') W(r - r', h) dr', \quad (4.13)$$

where the smoothing length h defines the finite width of the kernel W , meaning for $r = 2h$ kernel drops to zero. At the limit of an infinitely small smoothing region, the original $F(r)$ function should be recovered. Thus apart from being normalized, i.e. $\int W(r - r', h) d^3 r' =$

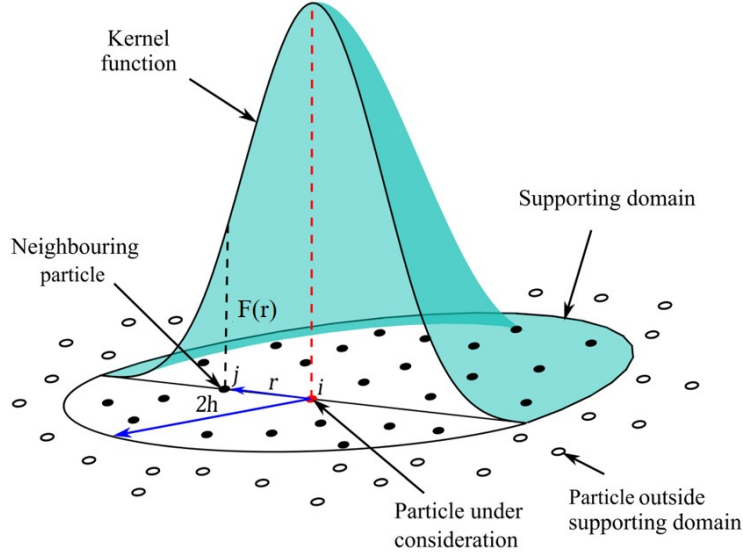


Figure 4.3: **Kernel interpolation.** The value of field $F(r)$ in equation 4.13, is shown by using the kernel function W in equation 4.20. The kernel drops to zero at $r = 2h$. Adapted from Nguyen et al. (2020)

1, at the limit of $h \rightarrow 0$, the kernel should have a δ -distribution. The most widely used kernel in SPH codes, used also in GEAR, is the M_4 cubic spline kernel,

$$W_{M_4}(q) = \frac{8}{\pi} \begin{cases} 1 - 6q^2 + 6q^3, & 0 \leq q \leq \frac{1}{2}, \\ 2(1 - q)^3, & \frac{1}{2} < q \leq 1, \\ 0, & q > 1, \end{cases} \quad (4.14)$$

in three-dimensional normalization, with $q = r/2h$. Figure. 4.3 shows the kernel interpolation for a distribution of particles. Each point in this figure has an associated position r_i , mass m_i and density ρ_i . These are not real particles in a physical system, but rather they are macro particles which sample the phase-space in a Monte-Carlo fashion.

Equations of motion

For deriving an estimation for density, using $F(r) \equiv \rho(r)$ in equation 4.13 gives

$$\rho_i = \sum_j m_j W(r_i, r_j, h_i). \quad (4.15)$$

This density estimation, which stems from summing over the kernel-weighted masses in the neighborhood of the point r_i , plays a key role in deriving the SPH equations from Lagrangian. In the standard SPH, known also as *vanilla* SPH, the Euler equations for an inviscid ideal gas can be generated from the Lagrangian

$$L = \int \rho \left(\frac{v^2}{2} - \epsilon \right) dV. \quad (4.16)$$

Discretizing Lagrangian one can then derive the equations of motion for N particles,

$$L = \sum_i^N \left(\frac{1}{2} m_i v_i^2 - m_i \epsilon_i \right). \quad (4.17)$$

Alternatively, hydrodynamics of an ideal gas can be formulated in terms of entropy rather than internal energy, as in **GEAR**, and generated by Lagrangian of the form

$$L = \sum_i^N \left(\frac{1}{2} m_i v_i^2 - m_i A_i(s) \frac{\rho_i^{\gamma-1}}{\gamma-1} \right), \quad (4.18)$$

where $A_i(s) = 1/(\gamma-1) \ln(P_i/\rho_i^\gamma)$ is the specific entropic variable ([Lucy 1977](#)) of particle i , with density ρ_i and mass m_i . The pressure is given by the ideal gas law as $P_i = A_i(s) \rho_i^\gamma$ with the adiabatic index γ . The question rises here is how to determine the smoothing length requires for estimating the density. For calculating the allowed size of the kernel, one way is to insure that the number of particles within the kernel volume are approximately constant, $\rho_i h_i^3 / m_i = \text{const.}$

We then can recover the Euler equations by using this additional condition in

$$\frac{d}{dt} \frac{\partial L}{\partial \dot{r}_i} - \frac{\partial L}{\partial r_i} = 0, \quad (4.19)$$

where partial derivatives are with respect to the coordinate r_i . For instance the Euler equation [4.10](#), or the conservation of momentum, with this additional condition represents pair-wise pressure forces,

$$\frac{dv_i}{dt} = - \sum_{j=1}^N m_j \left[f_i \frac{P_i}{\rho_i^2} \nabla_i W_{i,j}(h_i) + f_j \frac{P_j}{\rho_j^2} \nabla_i W_{i,j}(h_j) \right], \quad (4.20)$$

where $W_{i,j}(h) = W(|r_i - r_j|, h)$ is used, and the correction factor f_i is defined as

$$f_i = \left[1 + \frac{h_i}{3\rho_i} \frac{\partial \rho_i}{\partial h_i} \right]^{-1}. \quad (4.21)$$

Correction factors can be calculated in parallel to the density estimation, with the supplementary summation over $\partial \rho_i / \partial r_i$. Equations [4.9](#) and [4.11](#) for the conservation of mass and energy, respectively, are also recovered, as the particle masses and their specific entropies stay constant.

In summary, using kernel interpolants in a SPH discretization, a complex system of partial differential equations is transformed into a set of simple differential equations, where only the momentum conservation needs to be solved explicitly. In the next section, the concept of viscosity in SPH is introduced, which is required to allow a treatment of shocks.

Artificial viscosity

The SPH particle formulation does not naturally capture shocks. The reason is that the discontinuities are smoothed out by construction, and also when using the entropy formulation, the entropy is perfectly conserved. An artificial viscosity thus needs to be added for dissipating kinetic energy into heat and preventing the unphysical oscillations. The introduced viscosity must perform like a friction force, damping the relative motion of particles.

The difficulty is to tune the viscosity such that it generates the correct amount of entropy at the shock front, but at the same time diminishes outside of the shock (Cullen & Dehnen 2010; Hosono et al. 2016; Read & Hayfield 2012). Monaghan & Gingold (1983) proposed a form for viscosity which results in modeling shocks with negligible oscillations and sharp discontinuities. A modified version of this function introduced by Rosswog et al. (2000) and used in GEAR, is

$$\Pi_{i,j} = \begin{cases} -\alpha [c_{ij}\mu_{ij} + 2\mu_{ij}^2] / \rho_{ij} & \text{if } v_{ij} \cdot r_{ij} < 0 \\ 0 & \text{otherwise,} \end{cases} \quad (4.22)$$

where

$$\mu_{i,j} = \frac{h_{ij} v_{ij} \cdot r_{ij}}{|r_{ij}|^2 + \epsilon h_{ij}^2}. \quad (4.23)$$

Here $\Pi_{i,j}$ is the viscosity factor, $r_{ij} \equiv r_i - r_j$ is the distance of the pair, and c_{ij} is the mean sound speed. The parameter α with the typical value between 1/2 and 1, describes how strong the viscous force is. ϵ is added to prevent singularities if the trajectories of two particles get very close for which the value $\epsilon = 0.01$ is used in GEAR, and μ_{ij} is introduced to protect against the penetration of particles when the high speed shocks, with a high Mach number ($M = v/c$), take place in the flow.

The role of $\Pi_{i,j}$ function 4.22 is to increase the entropy where shocks suppose to occur, to mimic the shock waves in SPH. Therefore, the total energy, is no longer conserved, as the work done against the viscous force generates heat. Thus for writing the conservation law for energy this latter needs to be considered in terms of the rate with which the entropy raises

$$\frac{dA_i}{dt} = \frac{1}{2} \frac{\gamma - 1}{\rho_i^{\gamma-1}} \sum_{j=1}^N m_j \Pi_{i,j} v_{i,j} \cdot \nabla_i \bar{W}_{i,j}, \quad (4.24)$$

where $v_{i,j} \equiv v_i - v_j$ is the relative velocity of the pair. In addition, adding the viscous force to the equation of motion gives

$$\frac{dv_i}{dt} = - \sum_{j=1}^N m_j \Pi_{i,j} \nabla_i \bar{W}_{i,j}, \quad \text{with} \quad \bar{W}_{i,j} = \frac{1}{2} [W_{i,j}(h_i) + W_{i,j}(h_j)], \quad (4.25)$$

where $\bar{W}_{i,j}$ is the kernel for the two involved particles. As the viscous force is anti-symmetric and along the interaction line of a pair of particles, the linear and angular momentum are still conserved.

Describing the basic concepts in SPH, in the next section I introduce the key aspects of the grid-based methods used in **RAMSES**. First I describe the fundamental data structure, and then solving the hydrodynamics in a finite volume scheme.

Fully Threaded Tree

Figure 4.4, shows The Fully Threaded Tree (FTT) as a refinement method used particularly in the AMR code **RAMSES**. In this method, cells in the tree can be categorized as either split, meaning they have children cells, or leaves, which do not have children cells. For leaf cells, the pointer to the children is set to *null*. In this figure, root cell 1, has two children (cells 2 and 3). In three dimensions, the number of its children will be eight as each dimension is split in two.

The cell size Δx is related to the level l of the cell i by $\Delta x_i = 1/2^l L$, with L being the size of the computational domain at level zero (cell 1 in Fig. 4.4). The neighbor-neighbor relation (indicated by double arrows in Fig. 4.4) is not allowed for leaves of different sizes that face each other. Here cell 5 has cell 3 as its neighbor, but cell 3 has cell 2 as its neighbor, and not cell 5. Thus a j th neighbor of a cell i either has the same size as the cell itself, $\Delta x_j = \Delta x_i$, or it is two times larger, $\Delta x_j = 2\Delta x_i$. In the former case, the neighbor may be a leaf or a split cell, while in the latter case it must be a leaf.

In the FTT method, building blocks are groups of 3 dimensional sibling cells called *octs*, rather than single cells. Each oct belongs to a level l of refinement. Thus $l = 0$ is the coarsest level in a Cartesian grid, and defines the base of the tree structure. Octs are sorted in a doubled-linked list. This way, each oct at level l points to the previous and the next oct in the list. Each oct of a given level l , also points to the parent cell at level $l - 1$, and to the child octs at level $l + 1$. Therefore in order to store FTT structure in memory, 17 integers are required per oct. These 17 integers are listed below as the information that must be accessible for each cell i :

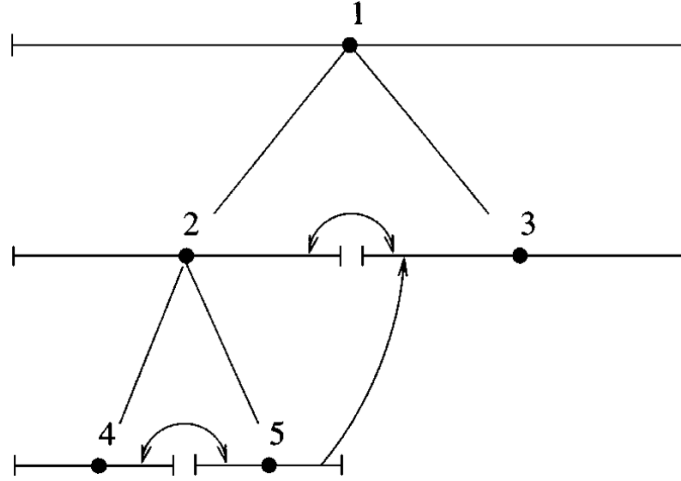


Figure 4.4: **Logical relation between cells in a fully threaded tree.** Each cell is illustrated by a horizontal barred line, with the length is the length showing its geometrical size. Straight lines without arrows show the pointers to parents and children. 1 and 2 are split cells, while 3 and 4 are leaves. Arrows show the pointers to neighbors. Taken from [Khokhlov \(1998\)](#).

l_i - level of the cell in the tree

k_i - if the cell is split or not (True/False binary)

Pr_i - pointer to a parent cell

$Ch_{i,j}$ - pointer to children cells, with $j = 1, \dots, 8$ (2^{dim})

$Nb_{i,j}$ - pointer to neighbors, with $j = 1, \dots, 6$ ($2 \times dim$)

At the coarsest level $l = 0$, the Poisson equation 4.3 can be solved by using the standard FFT technique ([Cooley & Tukey 1965](#); [Hockney & Eastwood 1988](#)). For fine levels with $l > 0$, there are iterative solvers for potential in real space. One of the simple versions of such iteration schemes is the so-called Gauss-Seidel algorithm, which is based on using the updated value of the hydro quantities as soon as they become available, to compute further updated values. Mapping $\phi_n \rightarrow \phi_{n+1}$, the Gauss-Seidel algorithm in two dimensions for unit mesh spacing is given by

$$\phi_{n+1}^{i,j} = \frac{1}{4} (\phi_n^{i+1,j} + \phi_n^{i-1,j} + \phi_n^{i,j+1} + \phi_n^{i,j-1}) - \frac{1}{4} \rho^{i,j}. \quad (4.26)$$

As shown in the chess-board like pattern in Fig. 4.5, this iteration is applied first to update the potential for all the black-marked cells, with i odd and j odd or i even and j even. This is followed by an update of all the red-marked cells, with i odd and j even or i even and j odd. The strength of this method stems from using the updated values from the first half-step in the second half-step.

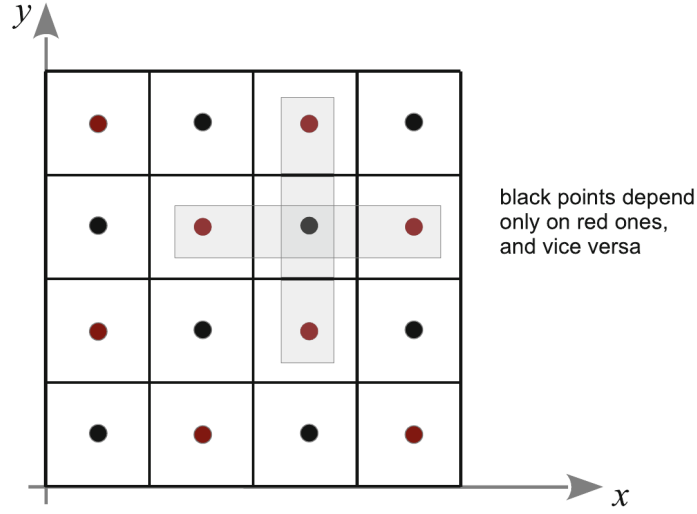


Figure 4.5: **Red-Black Ordering.** A chessboard-like pattern which decompose cells into two sets whose update is only dependent on cells from the opposite set. Taken from [Revaz et al. \(2016\)](#).

In the next section, I describe how to solve the hydrodynamics in a finite volume discretization.

4.2.2 Finite volume discretization

In the finite volume discretization scheme, the physical quantities such as density, temperature, and fluid velocity, are computed inside the cells. After storing the cell-averaged value of each quantity, for updating them, the Euler equations 4.9, 4.10 and 4.11, are solved by computing the fluxes across cell boundaries. Thus the Euler equation can be given in a vector differential conservation form,

$$\frac{\partial U}{\partial t} + \nabla \cdot F = 0, \quad (4.27)$$

where $U = (\rho, \rho v, \rho e)$ is a state vector and F is the flux vector, which can be written in the familiar form of Euler equations 4.9, 4.10, and 4.11 as

$$F = (\rho v, \rho v v^T + P, (\rho e + P)v). \quad (4.28)$$

Equation 4.27, in the finite volume scheme is given by

$$\frac{U_{n+1}^i - U_n^i}{\Delta t} + \frac{F_{n+1/2}^{i+1/2} - F_{n+1/2}^{i-1/2}}{\Delta x} = 0, \quad (4.29)$$

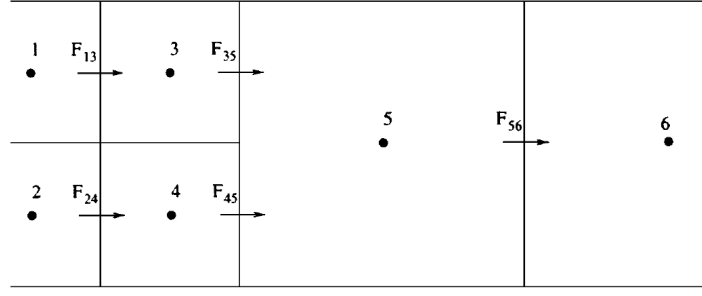


Figure 4.6: **Flux computation at two different levels of a tree.** Due to the Courant conditions, fluxes at interfaces between refined level (1 – 3 and 2 – 4), and fluxes between course and fine levels (3 – 5 and 4 – 5) are evaluated twice as often as fluxes in coarse level (5 – 6). Taken from [Khokhlov \(1998\)](#).

where U_{n+1}^i encompasses the averaged values of the conserved physical quantities at time t_n and for cell i with size Δx

$$U_n^i \equiv \frac{1}{\Delta x} \int_{x^{i-1/2}}^{x^{i+1/2}} U(x, t_n) dx. \quad (4.30)$$

At each time step, the time-centered flux terms F must be computed across cell interfaces. Fig. 4.6 illustrates the flux evaluation. In this particular example, the tree consists of only two levels with $l_{\max} = l_{\min} + 1$, occupied by leaves. Cells 1, 2, 3, and 4 belong to level l_{\max} , while 5 and 6 belong to level l_{\min} . At level l_{\max} , fluxes $F_{1,3}$, $F_{2,4}$, $F_{3,5}$, and $F_{4,5}$ are computed. Then the old state U_n in cells 1, 2, 3, and 4 will be updated with the new state U_{n+1} . At level l_{\min} fluxes across cell interfaces (3, 5) and (4, 5) are evaluated, however, due to the Courant condition (see Section 4.3), after two time steps at level l , one time step at level $l - 1$ is integrated. Thus the state of cell 5 is not updated yet. After these two time steps $F_{5,6}$ are computed, U_n for cell 5 is updated and finally its state is changed.

Solving gravity and gas hydrodynamics, the remaining task is integrating the equations of motion in time, which is explained in the next section.

4.3 Time integration

The time integration can be performed by a single time step scheme or the adaptive time step algorithm. In the former one, the equations of motion are integrated from t to $t + \Delta t$, with the same time step Δt for all refinement levels. Whereas in the adaptive time step scheme, the time evolution in each level is independent and defined by the Courant Friedrich Lewy ([Courant et al. 1928](#)) stability condition (hereafter Courant condition). Since the Courant condition implies that $v\Delta t/\Delta x \leq \text{const.}$, when level $l = 0$ is advanced in time using one course time step Δt , level $l = 1$ is advanced in time using two time

steps, and level $l = 2$ using four time steps.

Knowing the acceleration $a_n = -\nabla\phi_n$ at time t_n from equation 4.26, particle positions and velocities are then updated by a similar scheme to the so-called Leapfrog (Hockney & Eastwood 1988) as,

$$v_{n+1/2} = v_n - \nabla\phi_n \frac{\Delta t_n}{2}, \quad (4.31)$$

$$x_{n+1} = x_n - v_{n+1/2} \frac{\Delta t_n}{2}, \quad (4.32)$$

$$v_{n+1} = v_{n+1/2} - \nabla\phi_{n+1} \frac{\Delta t_n}{2}. \quad (4.33)$$

Since for equation 4.33, the value of acceleration at t_{n+1} is needed, to avoid an extra call to the Poisson solver 4.26, this calculation is postponed to the next time step.

In summary, both particle-based and grid-based methods for discretizing the fluid equations have strengths and weaknesses. The main advantage of the former is its pseudo-Lagrangian aspect, which makes it adaptive in cosmological simulations in a large spatial and dynamical range. Whereas, the latter as a finite volume scheme, provides a more realistic solution for the shocks and discontinuities.

Chapter 5

Constraining the primordial magnetic field

The next chapter corresponds to a first author paper published during my PhD thesis in Astronomy & Astrophysics Journal [AA/2020/38382](#)

Constraining the primordial magnetic field with dwarf galaxy simulations

Mahsa Sanati¹, Yves Revaz¹, Jennifer Schober¹, Kerstin E. Kunze², and Pascale Jablonka^{1,3}

¹ Institute of Physics, Laboratory of Astrophysics, École Polytechnique Fédérale de Lausanne (EPFL), 1290 Sauvigny, Switzerland
 e-mail: mahsa.sanati@epfl.ch

² Departamento de Física Fundamental, Universidad de Salamanca, Plaza de la Merced s/n, 37008 Salamanca, Spain

³ GEPI, CNRS UMR 8111, Observatoire de Paris, PSL University, 92125 Meudon, Cedex, France

Received 8 May 2020 / Accepted 23 July 2020

ABSTRACT

Using a set of cosmological hydro-dynamical simulations, we constrained the properties of primordial magnetic fields by studying their impact on the formation and evolution of dwarf galaxies. We performed a large set of simulations (8 dark matter only and 72 chemo-hydrodynamical) including primordial magnetic fields through the extra density fluctuations they induce at small length scales ($k \geq 10 h \text{ Mpc}^{-1}$) in the matter power spectrum. Our sample of dwarfs includes nine systems selected out of the initial $(3.4 \text{ Mpc } h^{-1})^3$ parent box, resimulated from $z = 200$ to $z = 0$ using a zoom-in technique and including the physics of baryons. We explored a wide variety of primordial magnetic fields with strength B_λ ranging from 0.05 to 0.50 nG and magnetic energy spectrum slopes n_B from -2.9 to -2.1 . Strong magnetic fields characterized by a high amplitude ($B_\lambda = 0.50, 0.20 \text{ nG}$ with $n_B = -2.9$) or by a steep initial power spectrum slope ($n_B = -2.1, -2.4$, with $B_\lambda = 0.05 \text{ nG}$) induce perturbations on mass scales from 10^7 to $10^9 M_\odot$. In this context emerging galaxies see their star formation rates strongly boosted. They become more luminous and metal rich than their counterparts without primordial magnetic fields. Such strong fields are ruled out by their inability to reproduce the observed scaling relations of dwarf galaxies. They predict that dwarf galaxies are at the origin of an unrealistically early reionization of the Universe and that they also overproduce luminous satellites in the Local Group. Weaker magnetic fields impacting the primordial density field at corresponding masses $\lesssim 10^6 M_\odot$, produce a large number of mini dark matter halos orbiting the dwarfs, however out of reach for current lensing observations. This study allows us, for the first time, to constrain the properties of primordial magnetic fields based on realistic cosmological simulations of dwarf galaxies.

Key words. methods: numerical – dark ages, reionization, first stars – galaxies: dwarf – Galaxy: evolution – magnetic fields

1. Introduction

Magnetic fields have been observed on all cosmic scales probed so far, from planets and stars (Stevenson 2010; Reiners 2012) to galaxies (Beck 2001; Beck & Wielebinski 2013) and galaxy clusters (Clarke et al. 2001; Govoni & Feretti 2004; Vogt & Enßlin 2005). There ample observational evidence of magnetic fields with strengths ranging from a few to tens of microgauss, coherent on scales up to ten kpc, detected through radio spectropolarimetry in spiral galaxies like M 51 (Fletcher et al. 2011; Beck 2015), and ultraluminous infrared galaxies (ULIRGs; Robishaw et al. 2008; McBride & Heiles 2013), but also in high redshift galaxies (Bernet et al. 2008; Mao et al. 2017) and in the interstellar and intergalactic medium (Han 2017). However, understanding the origin and strength of the fields is still a challenge for modern astrophysics.

There are various theories proposed to explain the generation of magnetic fields on large scales and their amplification by a dynamo in collapsed objects (Ichiki & Takahashi 2006; Ryu et al. 2008; Naoz & Narayan 2013; Schober et al. 2013), or the generation of magnetic fields on small scales (Widrow 2002; Hanayama et al. 2005; Safarzadeh 2018). However, recent observational evidence based on blazar emissions suggests that intergalactic medium voids could host a weak magnetic field $\sim 10^{-16}$ gauss, coherent on Mpc scales (Neronov & Vovk 2010; Kandus et al. 2011). Such a field is difficult to be explained by turbulence

alone in the late universe (Furlanetto & Loeb 2001; Bertone et al. 2006) and would perhaps favor a primordial origin in the early universe (Subramanian 2016; Kahnishvili et al. 2020; Jedamzik & Pogosian 2020).

New observational signatures of primordial magnetic fields have recently been obtained from the Lyman- α forest clouds (Pandey & Sethi 2013), the two-point shear correlation function from gravitational lensing (Pandey & Sethi 2012), the Sunyaev-Zel'dovich statistics (Tashiro et al. 2009), the cosmic microwave background (CMB) anisotropies (Shaw & Lewis 2010; Planck Collaboration Int. XXVI 2015; Zucca et al. 2017; Paoletti et al. 2019), CMB spectral distortions (Jedamzik et al. 2000; Kunze & Komatsu 2014; Wagstaff & Banerjee 2015) large-scale structure (Kahnishvili et al. 2010), and the reionization history of the Universe (Pandey et al. 2015). The above observations provide new upper limits on the strength of the fields which appeared to be limited to 47 pG for scale-invariant fields (Jedamzik & Saveliev 2019) and a few nG in more general states coherent on 1 Mpc. It is thus of great interest to ask whether such primordial fields can be confirmed and how their characteristics can be constrained further.

To answer this issue we need to journey back to the early universe. The present-day large-scale structures are thought to be seeded by quantum field fluctuations when the relevant scales were causally connected, leading to a nearly scale-invariant fluctuation spectrum (Dodelson 2003; Kolb & Turner 1990;

Padmanabhan 2002). These scales then crossed the universe horizon during the inflationary expansion phase, and re-entered only later to serve as the initial conditions, leading to the growth of large-scale structures. It is likely that the origin of the magnetic fields also arose during various phase transitions in the early universe (Turner & Widrow 1988a; Adshead et al. 2016; Domcke et al. 2019; Fujita & Durrer 2019) by a small fraction of the energy released during the electroweak or quark-hadron transitions and converted to large-scale magnetic fields (Hogan 1983; Ratra 1992a).

A primordial magnetic field (PMF) in the post-recombination epoch generates density fluctuations in addition to the standard inflationary fluctuations. The magnetically induced perturbations for a scale-invariant magnetic spectrum may dominate the standard Lambda cold dark matter (ΛCDM) matter power spectrum on small length scales and therefore can affect the formation of the first galaxies (Kim et al. 1996; Wasserman 1978b). The ΛCDM paradigm implies a hierarchical formation of galaxies in which dwarf galaxies, including the ultrafaint dwarfs (UFDs; Simon 2019), as observed today are the best analogs to the smallest initial building blocks. A modification of the nearly power-law spectrum of the ΛCDM model on small scales ($k \geq 10 h \text{Mpc}^{-1}$) will thus directly affect the number and properties of dwarf galaxies with interesting outcomes for understanding the cosmological model and origin of the magnetic field.

Changing the abundance of dwarf galaxies and their structure can potentially shed new light on the long-standing tensions existing between dark matter only (DMO) ΛCDM cosmological simulations and Local Group observations (see Bullock & Boylan-Kolchin (2017) for a recent review). Among the existing tensions, the overprediction of low mass systems around the Milky Way, the so-called missing satellite problem (Klypin et al. 1999; Moore et al. 1999), and the too-big-to-fail problem (Boylan-Kolchin et al. 2011, 2012) are certainly the most emblematic. Along with the number of observed satellites, their mass profile is also known to suffer from tensions. DMO simulations predict that the dark matter halos follow a universal cuspy profile (Navarro et al. 1996, 1997), while observations favor cored ones (Moore 1994; Flores & Primack 1994, see Read et al. 2018 for a short review). While improvements in the baryonic treatment of cosmological simulations allowed for a reduction of those tensions (Chan et al. 2015; Sawala et al. 2016), (Wetzel et al. 2016; Verbeke et al. 2017; Revaz & Jablonka 2018; Pontzen & Governato 2014; Oñorbe et al. 2015; Chan et al. 2015; Fitts et al. 2017; Hausammann et al. 2019), modification or alternative to the ΛCDM have also been proposed, such as, like warm dark matter (Lovell et al. 2012; Governato et al. 2015; Fitts et al. 2019), self-interacting dark matter (Vogelsberger et al. 2014; Harvey et al. 2018; Fitts et al. 2019) or wave dark matter (Chan et al. 2018).

On the other hand, many observations available for dwarf galaxies in the Local Group may be used to constrain the amplitude of PMFs. Any model including the effect of PMFs must (i) reproduce the abundances of detected satellites around the Milky Way (Newton et al. 2018; Nadler et al. 2018; Drlica-Wagner et al. 2020); (ii) reproduce the well-known observed scaling relations (Mateo 1998; Tolstoy et al. 2009; McConnachie 2012; Simon 2019), as well as more detailed properties like line-of-sight (LOS) velocity dispersion, stellar abundance patterns, and star formation histories (Tolstoy et al. 2009); and (iii) must be in agreement with the Milky Way local reionization history. By hosting the first generation of stars and lightning up the dark ages (Choudhury et al. 2008; Salvadori et al. 2014; Wise

et al. 2014; Robertson et al. 2015; Bouwens et al. 2015; Atek et al. 2015), dwarf galaxies played a key role during the epoch of reionization.

The above arguments make dwarf and UFD galaxies excellent laboratories to study the subtle impact of initial conditions imposed after the inflation and how they rule the formation of first structures. As such, they may be used to get new constraints on the properties of PMFs (Safarzadeh & Loeb 2019).

Revaz & Jablonka (2018) have recently demonstrated that cosmological simulations performed with the code GEAR reproduce a wide range of observed properties of the Local Group dwarf galaxies. Relying on this previous work, we take the opportunity to study for the first time the formation and evolution of a suite of dwarf galaxies that emerge from a ΛCDM cosmology where the primordial density fluctuations include the effect of PMFs. Our goal is to determine the impact of these primordial fields on the properties of dwarf galaxies.

This paper is organized as follows. Section 2 recalls the theory around PMFs and their effect on the density fluctuation power spectrum. Section 3 describes in detail our numerical framework as well as the simulations performed. The results are presented in Sect. 4. We first discuss results relying on dark matter only simulations and show how the PMFs affect the matter halo mass function on small scales. We then focus on zoom-in hydro-dynamical simulations. We study the impact of PMFs on the properties of dwarf galaxies and in particular on scaling relations. We then estimate how the modified properties of dwarfs directly impact the reionization history of the Universe as well as the cumulative number of bright satellites around the Milky Way. Limits on the properties of PMFs are obtained by comparing with existing observational constraints. A brief conclusion is given in Sect. 5.

2. Impact of primordial magnetic fields on the density fluctuations

We consider the effect of PMFs generated before recombination by processes occurring during the inflationary epoch (e.g., Turner & Widrow 1988b; Ratra 1992b). It has been shown in the seminal works of Wasserman (1978a) and Kim et al. (1996) that after the recombination epoch, PMFs may induce motions in the ionized baryons through the Lorentz force which drives compressional and rotational perturbations causing density fluctuations in the gas. These perturbations propagate down to the neutral gas and also to the dark matter through the gravitational coupling, and a direct impact on the total matter power spectrum is expected.

Characterizing this impact, however, is non-trivial and a large literature has been dedicated to describe it. Hereafter, without entering into too much detail, we briefly review the principal steps that allow us to determine the origin of the effect of primordial magnetic fields on the total matter power spectrum.

2.1. Primordial magnetic field

Following Wasserman (1978a), Kim et al. (1996), and Gopal & Sethi (2003), we first assume that the tangled magnetic field results from a statistically homogeneous and isotropic vector random process. The two-point correlation function of a non-helical field in Fourier space can then be expressed as

$$\langle \hat{B}_i(\mathbf{k}) \hat{B}_j^*(\mathbf{k}') \rangle = (2\pi)^3 \delta(\mathbf{k} - \mathbf{k}') \frac{P_{ij}(\mathbf{k}, \mathbf{k}')}{2} P_B(k), \quad (1)$$

M. Sanati et al.: Dwarf galaxies as a probe of Primordial Magnetic Fields

where $P_{ij}(\mathbf{k}) = \delta_{ij} - \frac{k_i k_j}{k^2}$, $k = |\mathbf{k}|$ is the comoving wave number and $P_B(k)$ is the magnetic field power spectrum. Without further information on the exact origin of the PMFs, it is usually assumed that its power spectrum follows a simple power law

$$P_B(k) = A k^{n_B} \quad (2)$$

where n_B is the slope index and A is the amplitude of the magnetic spectrum, which is defined through the variance of the magnetic field strength B_λ^2 on a scale $\lambda = 1 \text{ Mpc} \equiv k_\lambda^{-1}$, namely (Shaw & Lewis 2012):

$$A = \frac{(2\pi)^{n_B+5} B_\lambda^2}{2\Gamma(\frac{n_B+3}{2}) k_\lambda^{n_B+3}}. \quad (3)$$

With these definitions, n_B and B_λ fully characterize the PMFs. They constitute our main free parameters.

2.2. Growth of perturbations

In the linearized Newtonian theory, the evolution of density fluctuations in the presence of PMFs is described by the two following coupled equations for the baryonic fluid perturbation field $\delta_b(\mathbf{x}, t) = \delta\rho_b(\mathbf{x}, t)/\bar{\rho}_b$ and for the collisionless dark matter $\delta_{DM}(\mathbf{x}, t) = \delta\rho_{DM}(\mathbf{x}, t)/\bar{\rho}_{DM}$ (see, e.g., Subramanian & Barrow 1998; Sethi & Subramanian 2005):

$$\begin{aligned} \frac{\partial^2}{\partial t^2} \delta_b + \left[2H + \frac{4\rho_\gamma}{3\rho_b} n_e \sigma_T a \right] \frac{\partial}{\partial t} \delta_b &= c_b^2 \nabla^2 \delta_b + 4\pi G a^2 \\ &\times [\rho_b \delta_b + \rho_{DM} \delta_{DM}] + \frac{S(\mathbf{x}, t)}{a^3} \end{aligned} \quad (4)$$

and

$$\frac{\partial^2}{\partial t^2} \delta_{DM} + 2H \frac{\partial}{\partial t} \delta_{DM} = 4\pi G a^2 [\rho_b \delta_b + \rho_{DM} \delta_{DM}]. \quad (5)$$

Here a is the scale factor, $H = \dot{a}/a$ the Hubble constant, ρ_b and ρ_γ the baryon and photon mass density, n_e the electron number density, σ_T the Thomson cross section for electron-photon scattering, and c_b the baryon sound speed. The magnetic field source term, S , represents normalized to the baryon density at the present time, $\bar{\rho}_b(t_0)$:

$$S(\mathbf{x}, t) = \frac{\nabla \cdot [\mathbf{B} \times (\nabla \times \mathbf{B})]}{4\pi \bar{\rho}_b(t_0)}. \quad (6)$$

The baryon pressure term $c_b^2 \nabla^2 \delta_b$ in Eq. (4) is sub-dominant with respect to the magnetic pressure as long as the background magnetic field is larger than $5 \times 10^{-11} \text{ G}$ (Subramanian & Barrow 1998) and may thus be ignored. The damping term involving the Thomson cross section corresponds to the radiation viscosity. Prior to recombination, this term leads to the damping of small-scale magnetic waves (Jedamzik et al. 1998; Subramanian & Barrow 1998), a physical process similar to Silk damping (Silk 1968). This induces a sharp cutoff of the magnetic field when entering the recombination epoch, and subsequently of its contribution in the total matter power spectrum.

We introduce the total matter density perturbation:

$$\delta_m(\mathbf{x}, t) = (\bar{\rho}_{DM} \delta_{DM} + \bar{\rho}_b \delta_b) / (\bar{\rho}_{DM} + \bar{\rho}_b). \quad (7)$$

We can then solve Eqs. (4) and (5) and get the time evolution of δ_m . The additional term in the evolution of δ_m , due only

to the presence of the magnetic fields, is found to be (Sethi & Subramanian 2005):

$$\delta_m \sim \frac{3}{5} \frac{\Omega_b}{\Omega_m^2} \left[\frac{3}{2} \left(\frac{t}{t_{\text{rec}}} \right)^{2/3} + \left(\frac{t_{\text{rec}}}{t} \right) - \frac{5}{2} \right] S(\mathbf{x}, t_{\text{rec}}) t_{\text{rec}}^2, \quad (8)$$

where t_{rec} is the time at recombination and Ω_m and Ω_b are the matter and baryon density parameters.

The important point to get from the previous equations is that the spatial dependence of $\delta_m(\mathbf{x}, t)$ can be followed through the magnetic field source term $S(\mathbf{x}, t_{\text{rec}})$. We thus expect the total matter power spectrum to directly depend on the power spectrum of the magnetic field.

It is worth noting that the most significant evolution of the magnetic field takes place before recombination (Kahniashvili & Tevzadze 2013a; Brandenburg et al. 2017a,b). During recombination the ionization degree drops to a tiny value. Afterward, the magnetic field is more or less frozen into the gas, i.e., it just passively follows the cosmic expansion, ensuring that the magnetic flux is conserved.

2.3. Impact on the total matter power spectrum

The modification of the total matter power spectrum due to the influence of magnetic fields was first addressed by Kim et al. (1996) and was extended by Gopal & Sethi (2003). The total matter power spectrum is the ensemble average of the density fluctuations in Fourier space, $P(k, t) = \langle \delta_m(k, t) \delta_m^*(k, t) \rangle$, that we can obtain from the evolution equation (Eq. (7)) and introducing the ensemble average of the PMFs, Eqs. (6) and (2).

After the decoupling of photons, the ionized matter density fluctuations are affected by the magnetic Alfvén waves if the crossing time, $\tau_A \sim 1/k v_A$, is smaller than the inverse Hubble rate (Banerjee & Jedamzik 2004), where v_A is the Alfvén velocity $v_A = B_\lambda / \sqrt{\mu_0 \rho_0}$, with μ_0 the permeability or magnetic constant. As the magnetic energy B_λ^2 scales with $P_B(k) k^3$, $\tau_A \sim \sqrt{\mu_0 \rho_0} k^{-(3+n_B)/2}$. For $n_B > -5$, the crossing time is then shorter for larger k , amplifying the perturbations faster on smaller scales.

In the limit where $k \ll k_B$, with $k_B \equiv (v_A \sqrt{\pi/\rho_0 G})^{-1}$, the magnetic wave number above the Alfvén waves damp instabilities (the equivalent of the Jeans wave number), at the lowest order in k/k_{max} (i.e., $k_{\text{max}} \equiv k_B$), the solution for the total matter power spectrum is (Gopal & Sethi 2003)

$$P(k) \sim A k^{2n_B+7} + B k_{\text{max}}^{2n_B+3} k^4 + C k_{\text{max}}^{2n_B+1} k^6 + \dots, \quad (9)$$

which strongly depends on the magnetic slope index n_B . For the scale-invariant case, $n_B \equiv -3$, $P(k) \sim k$, and $\tau_A \sim k^{-1}$, thus small-scale perturbations are strongly amplified, as long as $\tau_A < 1/H(t)$, up to about k_B where they are sharply quenched (see Sect. 2.2).

2.4. Adopted total matter power spectrum

We generated the matter power spectrum using a modified version of the CAMB code which includes the effects of PMFs (for details see Shaw & Lewis 2012). In this version the non-linear effects of the magnetic Jeans length (magnetic pressure) and the damping due to the radiation viscosity (when the photon free streaming length is small) are both explicitly computed. As such, contrary to other studies, there is no need to artificially include a cutoff wave number.

Figures 1 and 2 display the matter power spectrum due to the magnetic field (dashed lines) together with its contribution to

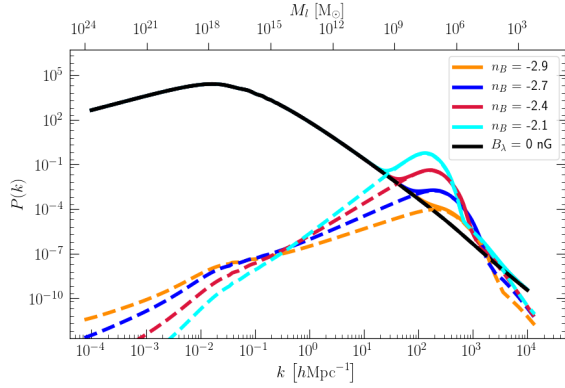


Fig. 1. Contribution of the magnetically induced power spectrum for a variety of magnetic field indexes (dashed colored lines) to the total matter power spectrum solid colored lines). The unperturbed Λ CDM spectrum is shown as the black continuous line. The magnetic field strength is kept constant at $B_\lambda = 0.05$ nG.

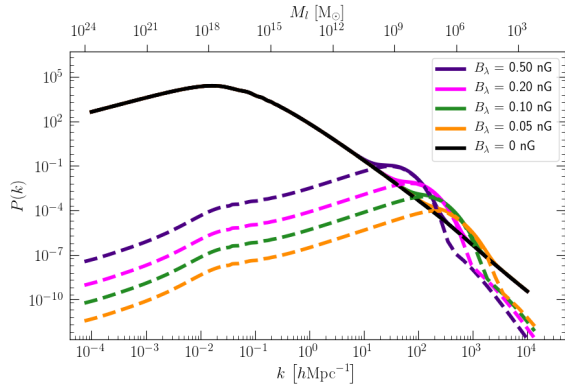


Fig. 2. Contribution of the magnetically induced power spectrum to the total matter power spectrum. Same as Fig. 1, but with constant spectral slope, $n_B = -2.9$, and varying magnetic field amplitudes.

the total matter power spectrum (plain lines). The black continuous line corresponds to the unperturbed Λ CDM power spectrum. The dependence with respect to the magnetic field amplitude ($B_\lambda = 0.05, 0.10, 0.20, 0.50$ nG) is shown in Fig. 1 keeping the spectral index constant ($n_B = -2.9$). The dependence with respect to the spectral index with $B_\lambda = 0.05$ nG is shown in Fig. 2. The range of parameters explored is chosen in such a way that they impact the power spectrum without violating the existing constraints, as do those presented in Sect. 1.

It is worth mentioning, for the magnetic spectral index, that a range of both positive and negative values are suggested. In this study, we considered PMFs generated during the inflation, which tend to have negative values for n_B , (Turner & Widrow 1988a; Ratra 1992a; Giovannini & Shaposhnikov 2000, Martin & Yokoyama 2008). However, positive values for n_B are also plausible in other magnetogenesis processes, like the electroweak phase transition (Grasso & Rubinstein 2001; Kandus et al. 2011; Durrer & Neronov 2013) and Higgs field gradients (Vachaspati 1991), or in the case of subsequent evolution of the

PMFs, for example via the chiral anomaly (Boyarsky et al. 2012; Rogachevskii et al. 2017; Schober et al. 2018).

As expected from Eq. (9), on large scales (small k), for $n_B = -2.9$ the slope is nearly 1 and increases for increasing n_B . Small-scale structures are thus strongly magnetically amplified and reach an amplitude larger than the one induced by inflation alone. On very small scales, the power spectrum is sharply quenched owing to the magnetic pressure and radiation viscosity damping. The total power spectrum is thus characterized by a bump at the smallest amplified scales, $k \sim 10\text{--}1000 h \text{ Mpc}^{-1}$, depending on the exact values of n_B and B_λ . In Figs. 1 and 2 we link the wave number and the mass contained within a sphere of comoving Lagrangian radius r_l at $z = 0$ by defining the mass scale M_l (the equivalent of the Jeans mass), assuming a background mean density given by the cosmological parameters (see e.g., Bullock & Boylan-Kolchin 2017):

$$M_l = \frac{4\pi}{3} r_l^3 \rho_m = \frac{\Omega_m H_0^2}{2G} r_l^3 = 1.71 \times 10^{11} M_\odot \left(\frac{\Omega_m}{0.3} \right) \left(\frac{h}{0.67} \right)^2 \left(\frac{r_l}{1 \text{ Mpc}} \right)^3 \quad (10)$$

The bumps precisely cover masses expected for the total mass of dwarf galaxies. Therefore, PMFs could significantly influence the formation and properties of those objects.

From Figs. 1 and 2 it appears that a steeper slope or a stronger amplitude would affect the power spectrum for $k < 10 h \text{ Mpc}^{-1}$. Such a modification is ruled out by the observations of the Lyman- α forest (Tegmark & Zaldarriaga 2002; Pandey & Sethi 2013).

3. Simulations

We performed a set of Λ CDM cosmological simulations with initial conditions that match the perturbed range of the total matter power spectrum described above. We used the same $(3.4 \text{ Mpc } h^{-1})^3$ box adopted by Revaz & Jablonka (2018) to study dwarf galaxies. The cosmology is the one described by the Planck Collaboration XIII (2016) with $\Omega_\Lambda = 0.685$, $\Omega_m = 0.315$, $\Omega_b = 0.0486$, $H_0 = 67.3 \text{ km s}^{-1} \text{ Mpc}^{-1}$, $n_s = 0.9603$, and $\sigma_8 = 0.829$. The relatively small box size used, prevents us from fully taking into account environmental effects such as those due to the proximity of a massive galaxy like the Milky Way.

Two types of simulations have been realized: (i) dark matter only (DMO) simulations of the entire box, used to compute the halo mass function and its dependency on the PMFs, and (ii) hydro-dynamical simulations of a selection of dwarf galaxies with the zoom-in technique. They allow us to check the effect of PMFs on the properties of stellar populations.

3.1. Initial conditions

The initial conditions were generated using the code MUSIC (Hahn & Abel 2011). Instead of using, the Eisenstein & Hu (1998), the default MUSIC power spectrum, we designed a special plug-in to use the total matter power spectrum obtained from the modified CAMB code. Compared to the Eisenstein & Hu function, the plug-in includes baryonic pressure which leads to additional power on scales larger than $k \approx 100 h \text{ Mpc}^{-1}$, and results in an almost 10 % difference in the mass content of structures formed in models without a magnetic field.

For the DMO simulations we used the resolution of level 9. This corresponds to $(2^9)^3$ particles, covering the entire box. For the hydro-dynamical simulations we used the zoom-in technique

M. Sanati et al.: Dwarf galaxies as a probe of Primordial Magnetic Fields

Table 1. Combination of explored parameters B_λ and n_B used for the seven simulations performed with a magnetically perturbed power spectrum.

Model	B0.05n2.9	B0.05n2.7	B0.05n2.4	B0.05n2.1	B0.10n2.9	B0.20n2.9	B0.50n2.9
B_λ [nG]	0.05	0.05	0.05	0.05	0.10	0.20	0.50
n_B	-2.9	-2.7	-2.4	-2.1	-2.9	-2.9	-2.9

Notes. The models are referred to in the paper by the model names given below.

Table 2. Values of the fitting parameters used in Eq. (12) for different PMF models.

Model	B0.05n2.9	B0.05n2.7	B0.05n2.4	B0.05n2.1	B0.10n2.9	B0.20n2.9	B0.50n2.9
c	3.00	6.71	7.79	7.35	4.50	4.06	3.86
u	5.30	6.14	7.07	7.85	6.17	7.08	8.45
s	0.80	0.60	0.57	0.52	0.70	0.70	0.67

to gradually degrade the resolution from level 9 to level 6 outside the refined regions. With this setting the mass resolution of dark matter, gas, and stellar particles is $22'462 h^{-1} M_\odot$, $4'096 h^{-1} M_\odot$, and $1'024 h^{-1} M_\odot$, respectively.

3.2. Code evolution

The simulations were run with the chemo-dynamical Tree/SPH code GEAR developed by Revaz & Jablonka (2012, 2018), and Revaz et al. (2016). GEAR is a fully parallel code based on Gadget-2 (Springel 2005). It operates with individual and adaptive time steps (Durier & Dalla Vecchia 2012) and includes recent SPH improvements such as the pressure-entropy formulation (Hopkins 2013). GEAR includes radiative gas cooling and redshift-dependent UV-background heating through the GRACKLE library (Smith et al. 2017). The metal line cooling is computed through the Cloudy code (Ferland et al. 2013) for solar abundances which is scaled according to the gas metallicity. Hydrogen self-shielding against the ionizing radiation is incorporated by suppressing the UV-background heating for gas densities above $n_H = 0.007 \text{ cm}^{-3}$ (Aubert & Teyssier 2010). Star formation relies on the stochastic prescription proposed by Katz (1992), Katz et al. (1996). We used an efficiency of star formation parameter $c_\star = 0.01$. The star formation recipe is supplemented by a modified version of the Jeans pressure floor (Hopkins et al. 2011; Revaz & Jablonka 2018) by adding a non-thermal term in the equation of state of the gas to avoid any spurious gas fragmentation. The chemical evolution includes Type Ia and II supernovae (SNe) with yields taken from Tsujimoto et al. (1995) and Kobayashi et al. (2000), respectively. GEAR includes thermal blastwave-like feedback, for which 10% of the explosion energy of each SN, taken as 10^{51} erg, is released in the interstellar medium (i.e., the SN efficiency is $\epsilon = 0.1$). The initial mass function (IMF) is sampled with the random discrete scheme (RIMFS) of Revaz et al. (2016). The released chemical elements are mixed using the smooth metallicity scheme (Okamoto et al. 2005; Tornatore et al. 2007; Wiersma et al. 2009).

3.3. Set of simulations

Each type of simulation, DMO, and zoom-in, is run eight times. A first run is performed without magnetically induced perturbations and seven others explore the effect of B_λ and n_B parameters with values given in Table 1 and corresponding to the total matter power spectra of Figs. 1 and 2.

Table 3. Dwarf galaxies simulated with the zoom-in technique.

Model ID	L_V [$10^6 L_\odot$]	M_\star [$10^6 M_\odot$]	M_{200} [$10^9 M_\odot$]	SF Class
h050	4.2	9.6	2.6	Extended
h070	2.0	5.8	1.8	Extended
h061	0.2	0.5	1.9	Quenched
h141	0.2	0.6	0.8	Quenched
h111	0.2	0.5	1.1	Quenched
h122	0.1	0.4	1.0	Quenched
h159	0.4	1.1	0.7	Quenched
h168	0.1	0.3	0.6	Quenched
h177	0.2	0.5	0.5	Quenched

Notes. For each of them we provide the total V-band luminosity L_V , total stellar mass M_\star , virial mass M_{200} , and the star formation type for the unperturbed models at $z = 0$.

We selected nine halos from the 27 dwarfs presented in Revaz & Jablonka (2018) and re-simulated them with the same zoom-in technique. The selection covers galaxies with $L_V < 10^7 L_\odot$, where L_V stands for the total V-band luminosity, and different star formation histories. Seven dwarfs are dominated by an old stellar population, being quenched by the UV background after at most four billion years, and two dwarfs are more massive, characterized by extended star formation histories. The list of the re-simulated dwarf galaxies is given in Table 3 with their basic properties as obtained in the unperturbed case at $z = 0$: total V-band luminosity L_V , total stellar mass M_\star , and virial mass M_{200} , where the virial overdensity is 200 times the critical density.

All simulations are started at a redshift of 200, ensuring that the rms variance of the initial density field, σ_8 , lies between 0.1 and 0.2 (Knebe et al. 2009). With the exception of the extreme cases, all halos reached $z = 0$ (the reason for the crash will be discussed in the Appendix, Table A.1).

4. Results

4.1. DMO simulations and halo mass function

Figure 3 displays the dark matter surface density at $z = 0$ of four models: the unperturbed Λ CDM model and three models with the magnetically induced bumps in the power spectrum that

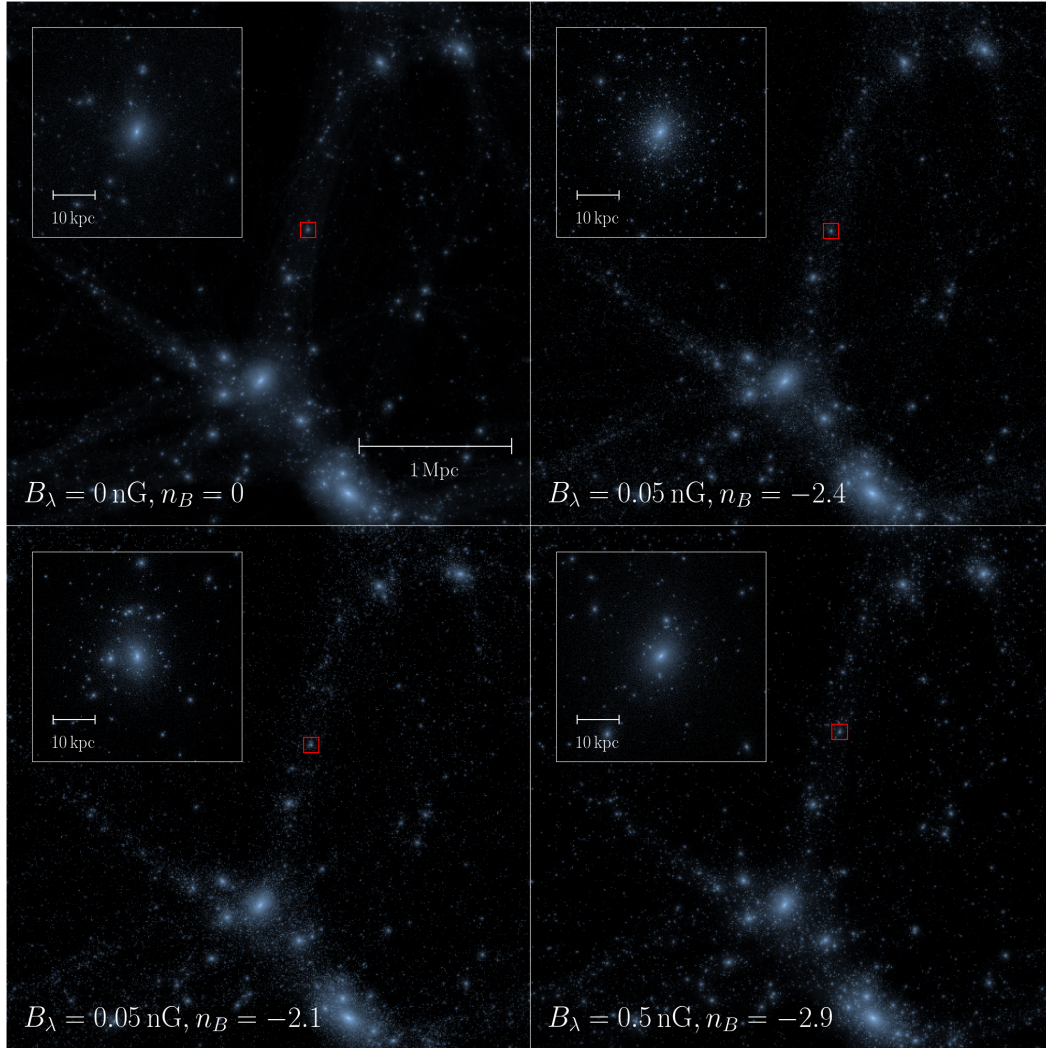


Fig. 3. Surface density projections of three DMO simulations at $z = 0$ with different PMFs, as indicated at the bottom of each panel. Each plot shows the full box; the inset shows a magnification of the dwarf indicated by the red square.

peak at different mass scales: **B0.05n2.4** ($M_{\text{peak}} \cong 5 \times 10^6 M_{\odot}$), **B0.05n2.1** ($M_{\text{peak}} \cong 3 \times 10^7 M_{\odot}$), and **B0.50n2.9** ($M_{\text{peak}} \cong 2 \times 10^8 M_{\odot}$). As expected, the small-scale bump increases the number of dark matter subhalos orbiting around dwarf galaxies. This number decreases with increasing mass of the halos. To quantify the effect of the bump observed in the total matter power spectrum, for all our DMO simulations we investigate the abundance of dark matter halos. We extracted dark matter halos using the Rockstar halo finder (Behroozi et al. 2013) which uses an adaptive hierarchical refinement of the friends-of-friends algorithm. All extracted halos consist of particle groups that are overdense with respect to the local background and contain a minimum of 100 bounded particles.

Figures 4 and 5 show the halo mass function: the number of dark matter halos, dN , per unit mass interval, dM . All mass functions are truncated below $3 \times 10^5 M_{\odot}$, which corresponds to

the limit of our mass resolution. While halos are detected with masses up to about $5 \times 10^{10} M_{\odot}$, the relatively small size of the box does not generate many of them. This makes the curve noisy, and we truncate it above $2 \times 10^9 M_{\odot}$. Between these limits, the unperturbed power spectrum is nicely fitted by a powerlaw,

$$\frac{dN}{dM} = a_0 \left(\frac{M}{m_0} \right)^{\alpha}, \quad (11)$$

with an amplitude of $a_0 = 8.79 \times 10^7 / M_{\text{vir}} = 4.46 \times 10^{-5} M_{\odot}^{-1}$, a pivot point of $m_0 = 10^{-5} M_{\text{vir}} = 1.97 \times 10^7 M_{\odot}$ and a slope of $\alpha = -1.96$. These parameters perfectly match previous studies (see, e.g., Springel et al. 2008). The fit to the halo mass function is shown as a dashed gray line.

The bottom panels of Figs. 4 and 5 show the ratio between the magnetically modified halo mass function and the unperturbed one. Depending on the strength and the spectral index

M. Sanati et al.: Dwarf galaxies as a probe of Primordial Magnetic Fields

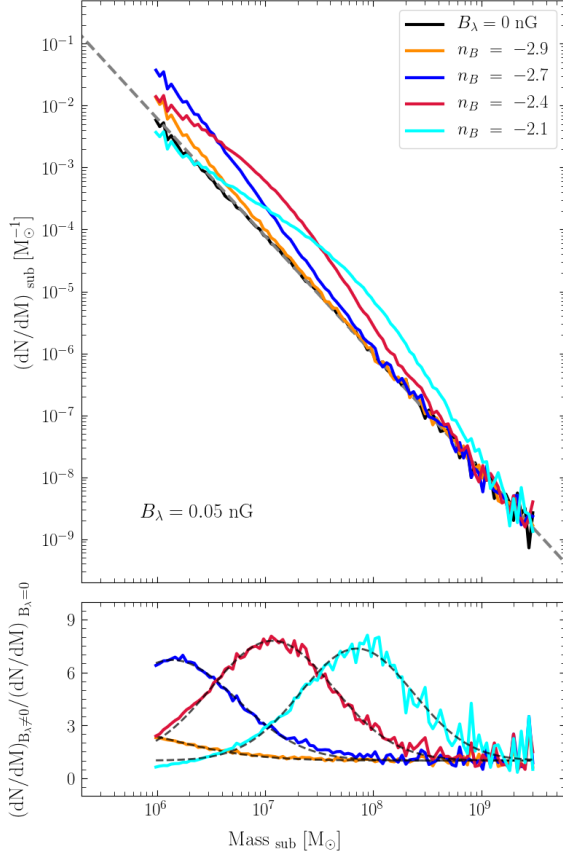


Fig. 4. Halo mass function. The halo mass is calculated within R_{200} . The count of halos is shown per logarithmic mass interval for different slope indexes n_B with a constant magnetic field strength, $B_\lambda = 0.05 \text{ nG}$. The dashed gray line shows a power law $dN/dM \sim M^{-1.96}$ fitted to the unperturbed power spectrum. The bottom panel shows the ratio of the halo mass function of each PMF model to the unperturbed model. The dashed lines correspond to the fit given by Eq. (12).

of the magnetic field, each PMF model affects the halo mass function in a different mass range below $\sim 10^9 M_\odot$, reflecting the corresponding mass of the bump in the power spectrum. For a fixed magnetic amplitude, increasing the slope from $n_B = -2.7$ to -2.1 , shifts the bump from about $10^6 M_\odot$ to $5 \times 10^7 M_\odot$. On average, in a one dex mass range around the maximum of the bump, between 5 and 7 times more halos are present compared to the generic model without magnetic fields. Similarly, when the slope is fixed, increasing the magnetic amplitude, B_λ , shifts the bump upwards, increasing their number by a factor between 3 and 4.

We found the ratio of the perturbed to unperturbed halo mass functions to be well fit by a simple modified Gaussian function:

$$\left(\frac{dN}{dM}\right) / \left(\frac{dN}{dM}\right)_{\text{unperturbed}} = (c - 1) \exp\left[-\frac{(\log_{10}(M) - u)^2}{2s^2}\right] + 1 \quad (12)$$

(see values for c , u , and s given in Table 2). The fit is shown by a dashed line in the bottom panel of Figs. 4 and 5. Equation (12)

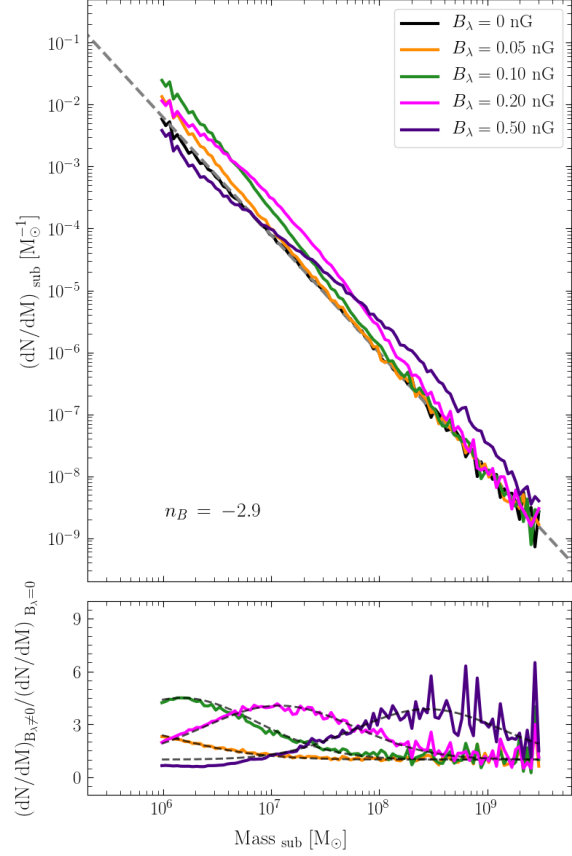


Fig. 5. Halo mass function. Same as Fig. 4, but for varying magnetic field strengths with the spectral slope kept constant to $n_B = -2.9$.

can be used to estimate analytically the magnetically perturbed halo mass function from a known unperturbed one. This is used in Sect. 4.3.2 to compare the predicted number of Milky Way satellites to the observed ones.

4.2. Zoom-in simulations: physical properties

From each zoom-in simulation, we first extracted the halo corresponding to the reference halo in the unperturbed model. Then, based on the positions and particle IDs, we extracted the analog of the same halo from the simulations in the perturbed models. For each extracted galaxy, we computed the following quantities defined inside one virial radius R_{200} ¹: the V-band total stellar luminosity L_V , the stellar mass M_* , the virial mass M_{200} , the stellar LOS velocity dispersion σ_{LOS} , and the mode of the stellar metallicity distribution function $[\text{Fe}/\text{H}]$. The details of the procedures used to obtain these quantities are very similar to the ones used in Revaz & Jablonka (2018). We reported these properties in Table A.1, Figs. A.1 and A.2.

¹ While multiple dark subhalos are usually found within R_{200} at $z = 0$, the stellar component remains very compact ($< 1 \text{ kpc}$). We checked that extracting quantities in a smaller region limited to the size of stellar component does not affect our results.

Figure 6 displays the time evolution of halo **h070** for five different magnetically perturbed models (**B0.50n2.9**, **B0.10n2.9**, **B0.05n2.1**, **B0.05n2.9**), from $z = 11.5$ down to $z = 0$. They are compared to the unperturbed case. Table A.1 and Fig. 6 reveal the effect of PMFs, which can be seen as a sequence along the position and amplitude of the bump in the power spectrum.

In strongly perturbed models with high amplitude B_A or high spectral index n_B (i.e., **B0.50n2.9**, **B0.20n2.9**, **B0.05n2.1**), the bump of the power spectrum peaks at mass ranges comparable to the mass scale of dwarf galaxies (10^7 to $10^9 M_\odot$). Those halos start clumping, accreting gas, and forming stars earlier. A deep potential well is quickly generated that prevents the gas reservoir from being evaporated due to the UV background. Contrary to the unperturbed case where the star formation history is quenched during the epoch of reionization, in the presence of PMFs the star formation is extended over longer periods, up to Gyrs in extreme cases (see Figs. 15 and 16), leading to more massive and brighter galaxies at $z = 0$ with a younger stellar population. Not only the luminosity, but also the dynamics of the systems are affected, e.g., the central LOS velocity dispersion is much larger than its unperturbed analog, see Figs. 7 and 8. In extreme cases like **B0.50n2.9** for more massive halos **h050**, **h070**, **h061**, **h141** the star formation is so intense that it leads to a crash of the code. However, before the crash, as we will see, the models are already too bright and too metal rich to be compatible with observed dwarfs.

In weaker PMF models, namely **B0.05n2.9**, **B0.05n2.7**, as the magnetically induced bump of the power spectrum is in a mass range far below the mass scale of dwarf galaxies ($\lesssim 10^6 M_\odot$) and the amplitude of the bump is not significant, there are no noticeable changes in their built-up history and therefore in their properties. The small differences we see in Table A.1 and Figs. A.1 and A.2 are easily explained by stochasticity. For example, the star formation history is slightly expanded; indeed, the faint systems are very sensitive to perturbations.

With a bump at a mass of about $10^7 M_\odot$, models **B0.05n2.4** and **B0.10n2.9** are intermediate cases. While their luminosity and metallicity are weakly affected, a noticeable difference appears in the number of subhalos orbiting each dwarf at $z = 0$, as seen in Fig. 6. The increased number of dark matter halos could be an excellent marker of the existence of weak PMFs. Unfortunately, nowadays, they are out of reach to observations as their effect on the observed properties of dwarfs is negligible and they are not massive enough to be detected through gravitational lensing with current detection limits of about $10^9 M_\odot$ (Vegetti et al. 2010). New forthcoming facilities like the Square Kilometer Array (SKA) will allow the detection of dark substructures with masses as low as 10^6 – $10^7 M_\odot$ through their perturbation on gravitational arcs (McKean et al. 2015).

4.2.1. Zoom-in simulations: scaling relations

Figures 7 and 8 show the galaxy V -band luminosity L_V as a function of the LOS velocity dispersion σ_{LOS} , while Figs. 9 and 10 show their metallicity (traced by $[\text{Fe}/\text{H}]$) versus L_V . As a comparison to the list of galaxies provided in the compilation of Local Group galaxies by McConnachie (2012), the sample we used is essentially restricted to the satellites brighter than $10^5 L_\odot$. For the $[\text{Fe}/\text{H}]$ versus L_V relation, we used only galaxies that benefit from medium resolution spectroscopy with metallicity derived either from spectral synthesis or calcium triplet (CaT) calibration.

In Revaz & Jablonka (2018) we showed that dwarfs emerging from a classical Λ CDM Universe (i.e., unperturbed model

in this work) nicely follow those relations over four orders of magnitude from 10^5 to $10^9 L_\odot$. The nine halos selected in this study from our sample of dwarf galaxies with the halo mass between 10^8 and 10^9 in the unperturbed model (black circles in Figs. 7–10) reproduce the chemo-dynamical properties of classical dwarf galaxies in this mass range observed around the Milky Way such as Ursa Minor, Draco, Sextans, or Sculptor. While the correlations between their V -band luminosity and line-of-sight velocity dispersion perfectly match those observed in the Local Group, we found our faintest dwarf to have a median metallicity slightly below the observed luminosity-metallicity relation seen in Figs. 9 and 10. This discrepancy, which is not inherent to our models, might be due to the fact that both our IMF and SN yields are kept constant in this work.

The weakly or intermediate perturbed models (**B0.05n2.9**, **B0.05n2.7**, **B0.05n2.4**, and **B0.10n2.9**) still stay on the scaling relations. It is worth noting that model **B0.05n2.7** suffers from a clear decrease in the luminosity (blue squares). In this model, due to the presence of the bump in the power spectrum at a mass of $\sim 10^6 M_\odot$, many small subhalos are formed. Contrary to more perturbed models, they are not massive enough to form stars; however, this decrease in luminosity is not sufficient to rule out this model. The dwarfs emerging from intermediate case **B0.05n2.4** with their velocity dispersion being increased, fall slightly off the relation. This increase is due to the presence of a larger number of small satellite halos that dynamically heat the stellar component.

The picture becomes very different, however, with stronger PMFs. All dwarfs simulated in models **B0.05n2.1** and **B0.50n2.9**, exhibit star formation histories longer than 2 Gyr (Figs. 15 and 16). They subsequently become brighter, but also denser, with strongly increased velocity dispersion. In the extreme case of model **B0.50n2.9**, while galaxies are still following the L_V versus σ_{LOS} relation, they produce such a strong quantity of metals that they lie above the observed metallicity-luminosity relation (Fig. 10).

4.2.2. Luminosity versus halo mass

As strongly magnetically perturbed models lead to an increase in the star formation rate, we expect the number of stars formed for a given halo mass to be modified. While not directly observed, the stellar mass to halo mass relation is important in particular to predict the number of visible satellites around the Milky Way (see Sect. 4.3.2).

To compute this relation, we extracted all halos found in the refined region of zoom-in simulations at $z = 0$. We kept only halos containing at least ten stars and polluted by less than five percent of the boundary particles, i.e., particles coming from a region with a lower resolution. For each PMF model, we then plotted the stellar mass content of each halo as a function of its total mass, taken as M_{200} . The results are shown in Figs. 13 and 14. We computed for every model an area delimited by the mean plus or minus one standard deviation of the distribution of galaxy stellar mass within each mass bins. In both figures, the gray area corresponds to the unperturbed model. For the unperturbed model, to increase the statistics, we used all dwarfs obtained from the sample of Revaz & Jablonka (2018).

Models **B0.05n2.9**, **B0.10n2.9**, **B0.05n2.7**, and **B0.05n2.4** display a stellar mass versus halo mass relation which lie within the bounded area of the unperturbed case. Model **B0.20n2.9** globally lies slightly above. However, the two strongly perturbed models, **B0.50n2.9** and **B0.05n2.1** are

M. Sanati et al.: Dwarf galaxies as a probe of Primordial Magnetic Fields

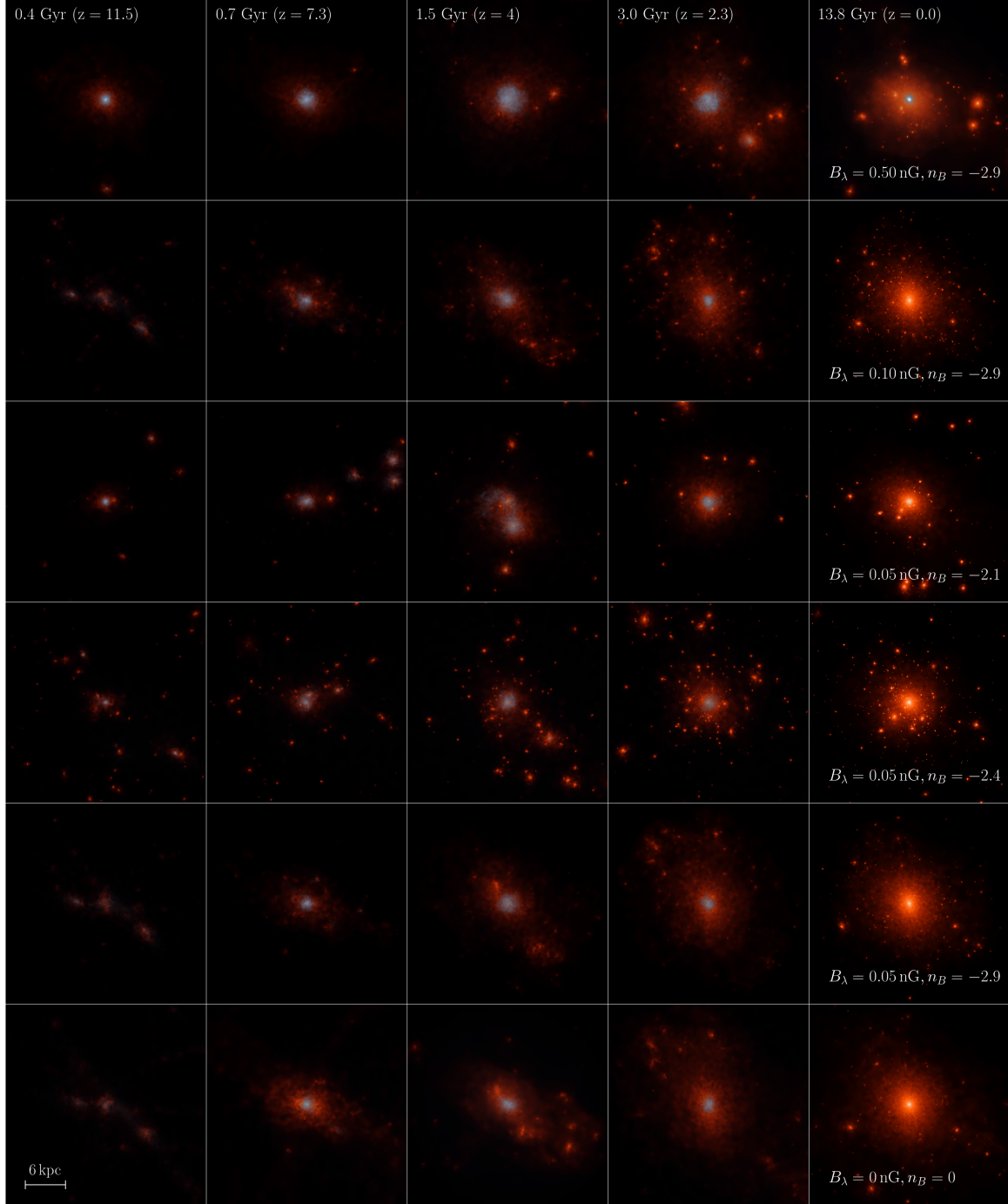


Fig. 6. Time evolution of halo h070 from $z \sim 11$ to $z = 0$ for different magnetically perturbed models. The unperturbed model is shown at the bottom for comparison. In all images are shown the surface density (in comoving units) of the stars (in white), of the gas (in blue), and of the dark matter (in orange). Each box is 20 comoving kpc on a side. In the non-magnetic-field model at high redshifts the gas is dilute and is masked by the orange color of dark matter clumps, which start gathering and then at lower redshifts pull in neutral gas and form stars. However, in the extreme magnetic field model the gas is more concentrated at high redshifts and a dwarf galaxy is formed very early on.

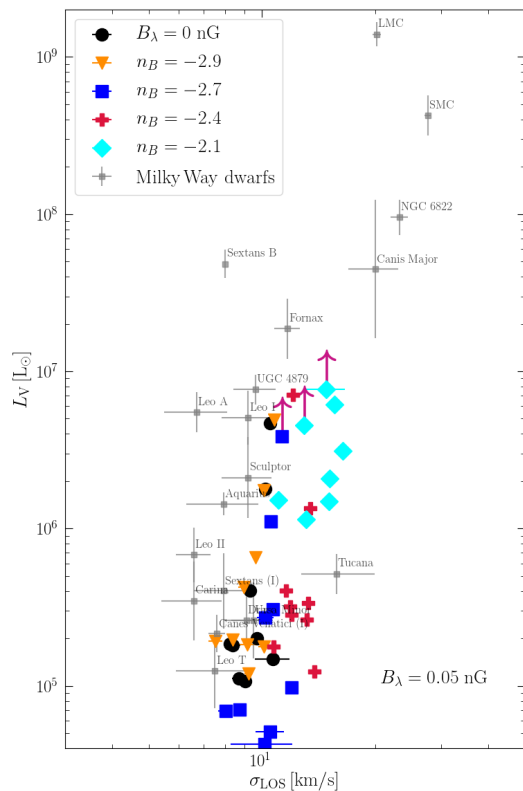


Fig. 7. V-band luminosity as a function of line-of-sight velocity dispersion in each model galaxy compared to the observational data of Milky Way satellites in black squares (see Sect. 4.2.1 for references). The purple arrows indicate models that did not reach $z = 0$ and are expected to have a slightly brighter luminosity.

clearly above. Both produce a much larger quantity of stars, up to one dex, for a given halo mass.

4.3. Cosmic star formation density and the reionization history of the Universe

One striking impact of a strong PMF is to speed up the formation of dark matter halos on the dwarf galaxy scale, where the matter power spectrum is amplified (bumps in Figs. 1 and 2). This induces an earlier onset of star formation. This effect is qualitatively seen in Fig. 6 where at $z = 11.5$ a dwarf is clearly formed in models $\mathbf{B0.50n2.9}$, $\mathbf{B0.05n2.1}$, and $\mathbf{B0.05n2.4}$, while the gas has not yet finished collapsing in the other models.

To estimate this effect quantitatively, Figs. 11 and 12 show the cumulative mass of stars formed during the first Gyr. For each model the upper (resp. lower) edge of the colored area corresponds to the cumulative mass of the dwarf that forms the larger (resp. smaller) quantity of stars. For models B0.50n2.9 and B0.20n2.9 the onset of star formation starts before $z = 50$, while for model B0.05n2.1 it starts before $z = 25$, contrary to the unperturbed model in which all dwarfs form stars after $z = 25$. In addition, the mean star formation rate is much stronger for models B0.50n2.9 and B0.05n2.1 than for the unperturbed model.

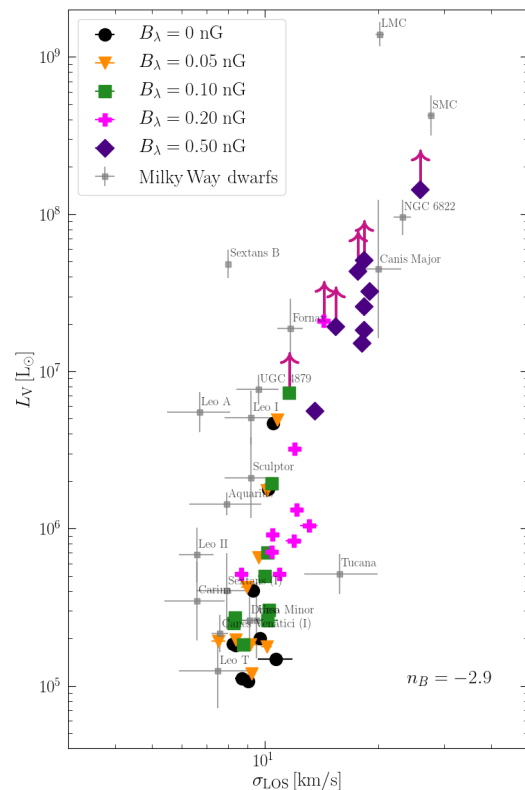


Fig. 8. V-band luminosity as a function of line-of-sight velocity dispersion. Same as Fig. 7, but for models with constant spectral slope and varying magnetic field strengths B_A .

With such an early onset of star formation as well as enhancement of the star formation rate, these models will impact the reionization history of the Universe, i.e., the way the globally neutral inter galactic medium (IGM) becomes slowly ionized after being impacted by energetic UV photons generated by young and massive stars. The transition from a neutral IGM to an ionized one is now well constrained by different observations (see [Fan et al. 2006a](#), for a review): by the Ly- α absorption by the IGM (the Gunn-Peterson effect) of high redshift quasars ([Fan et al. 2006b](#); [Schroeder et al. 2013](#); [Davies et al. 2018a,b](#); [Greig et al. 2019](#); [Bañados et al. 2018](#); [Durovčíková et al. 2020](#)), by the gamma-ray bursts ([Totani et al. 2006](#)), by the prevalence, spectral properties or clustering of Ly- α emitting galaxies ([Ouchi et al. 2010](#); [Ono et al. 2012](#); [Schenker et al. 2014](#); [Tilvi et al. 2014](#)), and by the cosmic microwave background (CMB) polarization through Thomson scattering ([Spergel et al. 2003](#); [Planck Collaboration Int. XLVII. 2016](#)). In the following, we describe the method we used to estimate the evolution of the hydrogen ionized fraction from our simulations.

4.3.1. Evolution of the hydrogen ionized fraction

The time evolution of the ionized fraction of hydrogen Q_{HII} can be estimated using a simple differential equation (Madau et al. 1999; Springel & Hernquist 2003; Kuhlen & Faucher-Giguère 2012; Stoychev et al. 2019):

M. Sanati et al.: Dwarf galaxies as a probe of Primordial Magnetic Fields

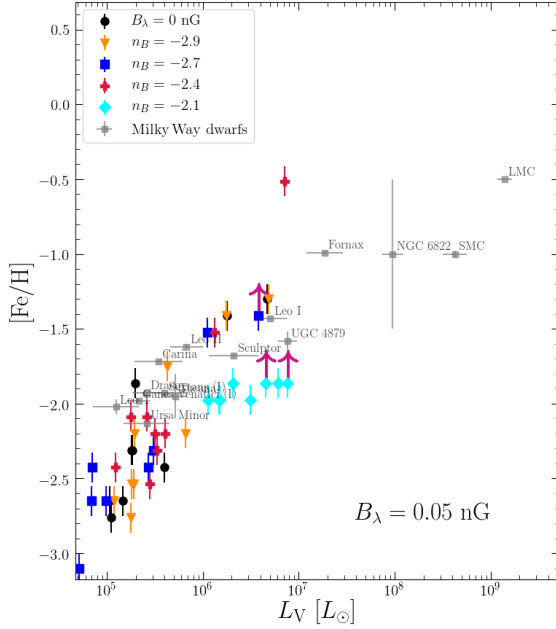


Fig. 9. Mean metallicity vs. stellar V-band luminosity. Each object corresponds to one model galaxy for which $[\text{Fe}/\text{H}]$ is computed as the median of the galaxy stellar metallicity distribution function. Milky Way satellites are identified with black squares (see Sect. 4.2.1 for references). The purple arrows indicate models that did not reach $z = 0$ and are expected to have a slightly higher metallicity.

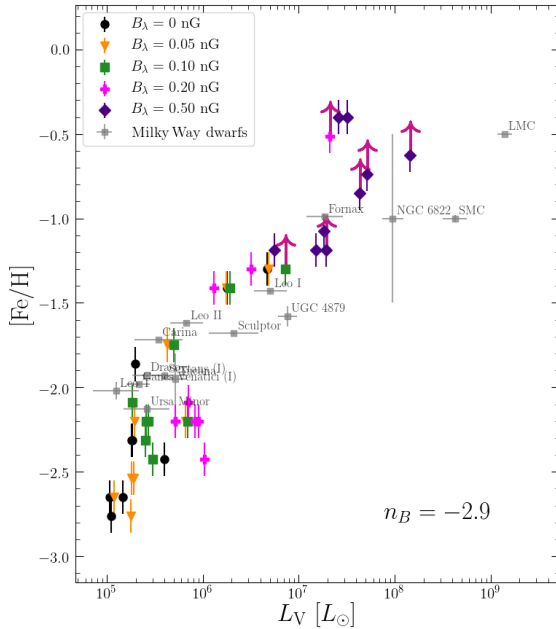


Fig. 10. Mean metallicity vs. stellar V-band luminosity. Same as Fig. 9, but for models with constant n_B and varying magnetic field strengths B_λ .

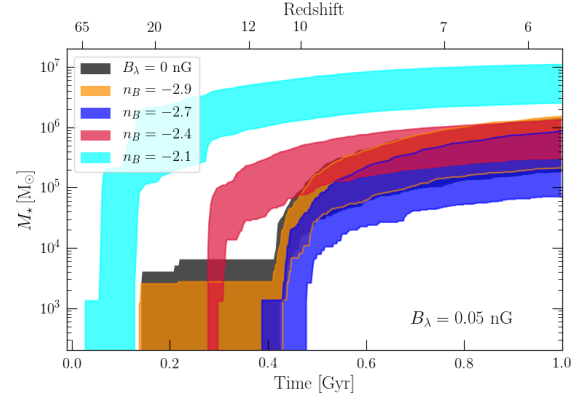


Fig. 11. Cumulative stellar mass in the first Gyr for different models with varying magnetic indices $n_B = -2.9$ to -2.1 . The amplitude of the magnetic field is kept constant at $B_\lambda = 0.05$ nG. The shaded area covers all nine halos simulated in various models.

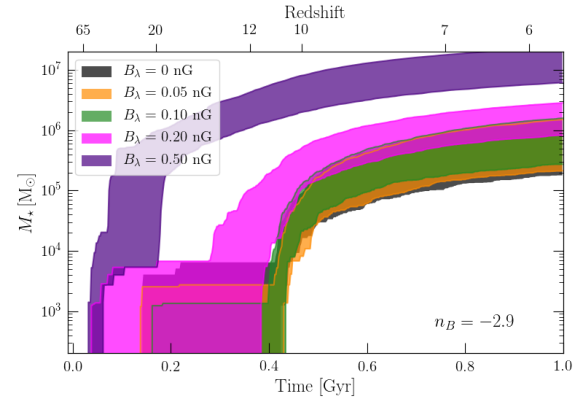


Fig. 12. Cumulative stellar mass in the first Gyr. Same as Fig. 11, but for a constant magnetic index $n_B = -2.9$ and a variety of magnetic amplitudes, from $B_\lambda = 0.05$ to $B_\lambda = 0.5$ nG.

$$\dot{Q}_{\text{HII}} = \frac{\dot{n}_{\text{ion}}}{\bar{n}_{\text{H}}} - \frac{Q_{\text{HII}}}{t_{\text{rec}}}. \quad (13)$$

The first term on the right-hand side describes the ionization source through the number of ionizing photons, while the second term, the sink term, is due to radiative cooling, leading to hydrogen recombination. Furthermore, \dot{n}_{ion} is the global production rate of ionizing photons per unit volume, produced by young and massive stars. It is directly proportional to the cosmic star formation density ρ_{SFR}

$$\dot{n}_{\text{ion}} = \rho_{\text{SFR}} f_{\text{esc}} \chi_{\text{ion}}, \quad (14)$$

where f_{esc} represents the fraction of ionizing photons that escape star forming regions and χ_{ion} the ionizing photon production efficiency for a typical stellar population per unit time and per unit star formation rate. Moreover, \bar{n}_{H} is the mean comoving hydrogen number density defined through the baryonic fraction Ω_b , critical density ρ_c , hydrogen mass fraction X , and hydrogen atom mass m_{H} :

$$\bar{n}_H = \Omega_b X \rho_c / m_H. \quad (15)$$

The sink term is due to the radiative recombination of protons with electrons described by the rate of change of the ionized hydrogen *proper* density n_{HII}

$$\frac{d}{dt} n_{\text{HII}} = -n_e n_p \alpha_{\text{HII}}(T), \quad (16)$$

where $\alpha_{\text{HII}}(T)$ is the temperature dependent recombination rate coefficient (see [Ferland et al. 1992](#), for tabulated values). Defining X and Y to be the mass fraction of hydrogen and helium, respectively, and η the helium ionization degree (0, 1, or 2), we can replace the proper number density of electron n_e by $n_H (Q_{\text{HII}} + \eta \frac{Y}{4X})$ as well as the proper number density of proton n_p by $n_H Q_{\text{HII}}$. The recombination time t_{rec} of Eq. (13) is then

$$t_{\text{rec}} = \frac{1}{C_{\text{HII}} (Q_{\text{HII}} + \eta \frac{Y}{4X}) \bar{n}_H (1+z)^3 \alpha_{\text{HII}}(T)}, \quad (17)$$

where in Eq. (17), we replaced the proper hydrogen density by its comoving expression. An additional clumping factor C_{HII} is added to account for dense regions, self-shielded against ionizing photons that do not contribute to the recombination rate.

For each of our PMF models, we estimated the cosmic star formation density using the following procedure. First, using the Rockstar halo finder, we extracted dark matter halos from our DMO simulations, at a redshift of 6.3². This provided us with a complete dark halo sample covering $(3.4 \text{ Mpc } h^{-1})^3$ at a redshift near the end of the epoch of reionization (EoR). Next, using our zoom-in simulations, we extracted at the same redshift, all progenitors of all halos found at $z = 0$ in the refined region³. This provided us with a sample of halos populated by galaxies for which we accurately know the star formation history. In the last step, we attributed to each dark halo (from the dark matter complete sample), a corresponding galaxy, matching their virial mass. This provided us with an estimate of the star formation in the full box and subsequently with the cosmic star formation density. The main difficulty of the method is correcting for the incompleteness of the galaxy samples extracted from the zoom-in simulations. Indeed, these samples lack the most luminous objects. This does not limit our analysis as more massive and luminous systems are rare and do not dominate the ionizing photons production, and including them would lead to a slightly earlier reionization, worsening the situation.

To circumvent this difficulty, we used a simulation run with the same code and parameters (including the full baryonic physics), which used the same initial perturbation field covering the same cosmological volume, but with a homogeneous resolution corresponding to that of the refined region in the zoom-in simulations. This simulation allowed us to derive a reliable star formation history up to a redshift of 6.3, where it stopped due to computational expenses. We then calibrated the star formation density derived from our unperturbed zoom-in simulation samples to the full box with a homogeneous resolution. We found a correction factor of 3 to be sufficient to recover the complete star formation history up to $z = 6.3$. We then applied this factor to the star formation density of all others models.

² The choice of this redshift is dictated by a calibration simulation that will be introduced later on. It is sufficient to constrain our models.

³ Halos at $z = 0$ are all halos found in the refined region containing at least ten stellar particles, and being polluted by less than five percent of boundary particles, i.e., particles coming from a region with a lower resolution.

The evolution of the neutral hydrogen fraction $1 - Q_{\text{HII}}$ is then obtained from Eq. (13). Setting $X = 0.76$, $Y = 0.24$, $\eta = 1$ ([Faucher-Giguère et al. 2008](#)), $C_{\text{HII}} = 3$ ([Kaurov & Gnedin 2015](#)), and $\chi_{\text{ion}} = 10^{53} \text{ photons } (\text{M}_\odot \text{ yr}^{-1})^{-1} \text{ s}^{-1}$ ([Stoychev et al. 2019](#)), and using a fiducial IGM temperature of $2 \times 10^4 \text{ K}$ ([Hui & Haiman 2003](#)), the data are nicely fitted by our unperturbed full box model, if the escape fraction is set to 12%. Keeping this same parameters for all models, the evolution of the neutral hydrogen fraction $1 - Q_{\text{HII}}$ is displayed in Figs. 17 and 18.

Due to strongly enhanced star formation rates, the subsequently large amount of ionizing photons produced by models B0.05n2.1, B0.05n2.4, B0.20n2.9, and B0.50n2.9 lead to a total reionization of the universe at $z > 9$. This is in total disagreement with observational constraints suggesting a reionization starting around $z = 10$ and ending at about $z = 6$ ([Bolton & Haehnelt 2007](#); [Loeb & Haiman 1997](#); [Fan et al. 2000](#); [Hu et al. 1999](#)). The other models are in much better agreement. It should be noted here that our goal was not to precisely reproduce the observations. This requires a much more precise approach, for example self-consistently computing the radiative transfer of photons through the ISM and IGM. Our goal was rather to demonstrate that models with important magnetic field perturbation are far off the constraints by a comfortable margin, as is the case here.

In our approach, the growth of structures as well as the star formation histories of dwarfs are self-consistently followed. Our results corroborate results from [Pandey et al. \(2015\)](#), who estimated the Universe reionization using a semi-analytical estimation of the dark matter collapsed fraction, directly sensitive to matter power spectrum. They found that models with $B_1 > 0.358, 0.120, 0.059 \text{ nG}$ with respectively $n_B = -2.95, -2.9, -2.85$ are ruled out from existing constraints. Our approach also rules out models with $B_1 \geq 0.05 \text{ nG}$ and $n_B \geq -2.4$.

4.3.2. Number of satellites in the Local Group

In Sect. 4.1 we demonstrated how PMFs may lead to the formation of a larger number of low mass dark matter halos. This increase may potentially impact the number of observed luminous satellites around the Milky Way. In this section, we estimate the number of expected observed dwarf galaxies brighter than a given luminosity inside 300 kpc and compare it with observations. For this purpose, we combined the halo mass functions obtained in Sect. 4.1 with the luminosity-halo mass relations of the zoom-in hydro-dynamical simulations of Sect. 4.2.2.

Assuming the halo mass function in the unperturbed model follows a power law (Eq. (11)), we can obtain an analytical relation of the cumulative abundance of halos $N(> M)$ by multiplying Eq. (11) by the magnetically induced perturbation (Eq. (12)) and integrating over the halo mass:

$$N(> M) = -\frac{a}{b+1} M_h^{b+1} + C \left[1 - \text{erf} \left(\frac{\log_{10}(M) - (b+1)s^2 \ln(10) + u}{\sqrt{2}s} \right) \right], \quad (18)$$

Here, erf is the standard error function and the constant C is given by:

$$C = \frac{1}{\sqrt{2}} \sqrt{\pi} a (c-1) s \ln(10) \cdot \exp \left(\frac{(b+1) \ln(10) ((b+1)s^2 \ln(10) + 2u)}{2} \right). \quad (19)$$

M. Sanati et al.: Dwarf galaxies as a probe of Primordial Magnetic Fields

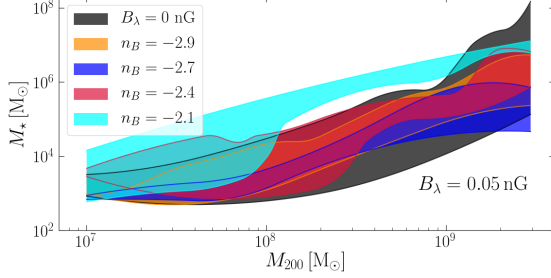


Fig. 13. Stellar mass vs. halo mass relation for different models with a variety of magnetic amplitude B_λ and a constant slope index $n_B = -2.9$.

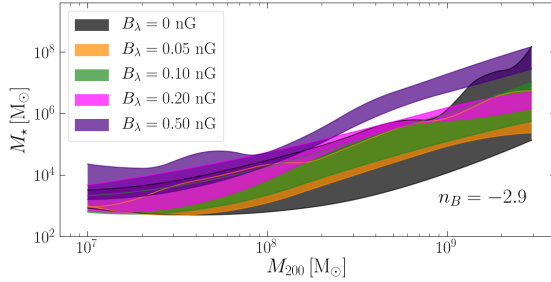


Fig. 14. Stellar mass vs. halo mass relation. Same as Fig. 13, but for models with constant $B_\lambda = 0.05$ nG and different slope indexes n_B .

With this notation, the unperturbed case corresponds to $C = 0$.

To reproduce a realistic halo mass function of the Local Group, which includes the perturbative effects of both Milky Way and Andromeda galaxy, we used the cumulative number of dark matter halos inside 300 kpc predicted by the APOSTLE simulations (Sawala et al. 2017).

The corresponding mass function is obtained by a power law with a slope $b = -1.915$ taken by averaging the slopes of the four different radius bins given in Table 2 of Sawala et al. (2017). The amplitude $a = 1.86 \times 10^9$ guarantees the existence of 800 dark matter halos with masses higher than $10^7 M_\odot$ inside 300 kpc. This unperturbed cumulative halo distribution is then perturbed using Eq. (18). We note that for a perturbed halo distribution, the total number of halos with masses higher than $10^7 M_\odot$ increases (up to about 4300 for model B0.05n2.1), owing to the bump of the power spectrum that moves masses from smaller to larger scales. Inverting numerically Eq. (18), for each of our models, we randomly generated 1000 realizations of dark matter halos using a Monte Carlo approach. Relying on the halo mass versus luminosity relations (Figs. 13 and 14), we then assigned to each halo a stellar luminosity randomly chosen in the corresponding range showed by the shaded area. Having obtained a luminosity for each halo, we computed the cumulative number of satellites brighter than a given luminosity. Results are shown in Figs. 19 and 20.

Except for models B0.05n2.1, B0.50n2.9, and B0.20n2.9, all models predict two times too many satellites for a luminosity higher than $10^4 L_\odot$ where observed satellites show an intriguing dearth. On the contrary, models B0.05n2.1, B0.50n2.9, and B0.20n2.9 are clearly above the observations, predicting the existence of respectively 16, 12, and 4 times more satellites brighter than $10^5 L_\odot$ compared to what is actually observed. This overabundance results from

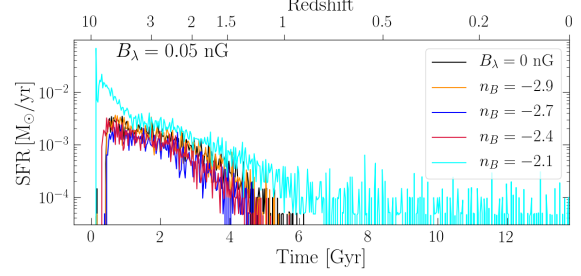


Fig. 15. Star formation rate of halo h070 for different models with varying magnetic indices $n_B = -2.9$ to -2.1 . The amplitude of the magnetic field is kept constant at $B_\lambda = 0.05$ nG.

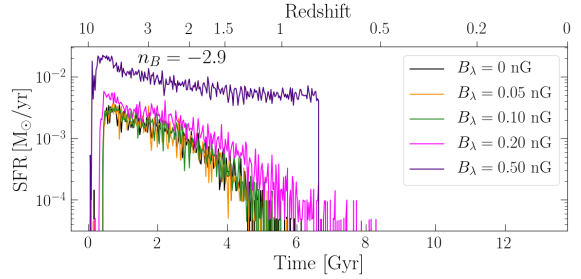


Fig. 16. Star formation rate. Same as Fig. 15, but for a constant magnetic index $n_B = -2.9$ and a variety of magnetic amplitudes, from $B_\lambda = 0.05$ to $B_\lambda = 0.5$ nG.

the combined effect of a larger number of dark matter halos expected in the mass 10^7 – $10^8 M_\odot$ (Figs. 4 and 5) and slightly brighter galaxies populating a given halo mass (Figs. 13 and 14).

We finally note that models with magnetic fields seems to underpredict the number of dwarfs brighter than $10^6 L_\odot$. This is only the result of our incomplete sample which lacks bright dwarfs. The dark area corresponding to the unperturbed case has been obtained using the total sample of Revaz & Jablonka (2018), which includes dwarfs up to $5 \times 10^8 L_\odot$. In this case, an excellent match is obtained with observed dwarfs. The flattening of the curve below $10^3 L_\odot$ is the result of the UV background heating that evaporates gas in the smallest halos and prevents star formation onset and is the result of our resolution limit.

5. Conclusion

We study the impact of primordial magnetic fields (PMFs) on the formation and evolution of dwarf galaxies through the modification of the Λ CDM matter power spectrum at the recombination era. Depending on the strength and the spectral index of the magnetic field, each PMF model affects the matter power spectrum in a different mass range. We examine a variety of PMF models by either changing the amplitude ($B_\lambda = 0.05, 0.10, 0.20, 0.50$ nG) or the slope ($n_B = -2.9, -2.7, -2.4, -2.1$) of the magnetic power spectrum, keeping the other parameters constant.

We first run a set of DMO simulations covering a $(3.4 \text{ Mpc } h^{-1})^3$ box with a resolution of 2×512^3 particles. Next, we re-simulate a set of nine halos extracted from the same volume, from redshift $z = 200$ to $z = 0$, using a zoom-in technique and including a full treatment of baryons with the stellar mass resolution of $1024 M_\odot h^{-1}$. Our sample of halos in the

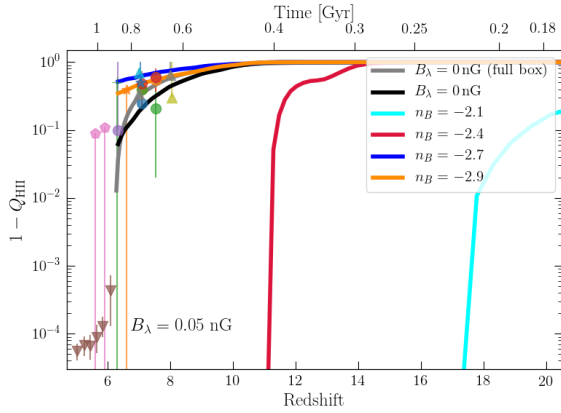


Fig. 17. Time evolution of the neutral hydrogen fraction ($1 - Q_{\text{HII}}$) for models with different slope indexes n_B . The reference simulation (full box) is indicated by the gray curve. The model predictions are compared to observational constraints of the neutral hydrogen fraction from Ly- α absorption of quasars (Fan et al. 2006b) as brown downward triangles; (McGreer et al. 2015) pink pentagons; (Schroeder et al. 2013) purple, (Davies et al. 2018a,b) red, (Greig et al. 2017, 2019) green, (Bañados et al. 2018) orange, and (Durovčíková et al. 2020) blue circles; or gamma-ray bursts (Totani et al. 2006) as a green cross; and by Ly- α emitting galaxies (Ouchi et al. 2010) as an orange star, and (Ono et al. 2012) cyan, (Schenker et al. 2014) gray, and (Tilvi et al. 2014) yellow triangles.

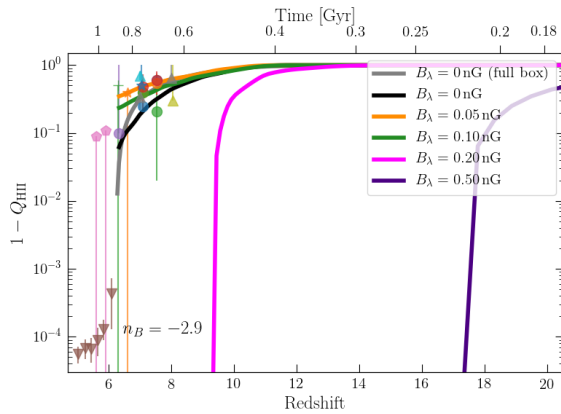


Fig. 18. Time evolution of the neutral hydrogen fraction. Same as Fig. 17, but for models with varying magnetic field strengths, from $B_\lambda = 0.05$ to 0.50 nG.

unperturbed case give birth to dwarf spheroidals, seven of them having a quenched star formation history and two an extended history. Our results are summarized as follows:

1. To quantify the contribution of PMFs in the total matter power spectrum, we compute the halo mass function for all our DMO simulations. The ratio of perturbed to unperturbed mass function is well fitted by a simple Gaussian function. We show that increasing the magnetic amplitude B_λ , or the slope n_B , increases the number of halos around the maximum of the Gaussian function, up to a factor of 7 in the most extreme cases.

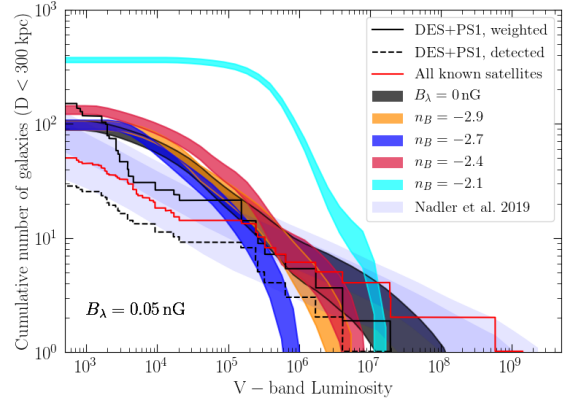


Fig. 19. Predicted cumulative number of satellites brighter than a given luminosity, within 300 kpc around the Milky Way, for models with different slope indexes n_B . For each model the shaded area corresponds to the mean of thousand realizations of dark matter halos plus or minus one standard deviation. Our predictions are compared to the known satellites shown by the red curve. The dashed black line shows detected satellites in the Dark Energy Survey (DES) and Pan-STARRS1 (PS1) as presented in Drlica-Wagner et al. (2020). The solid black line shows the same data but volume corrected, assuming satellites are distributed isotropically. The light blue dashed regions show predictions from cosmological simulations combined with semi-analytical prescriptions (Nadler et al. 2019).

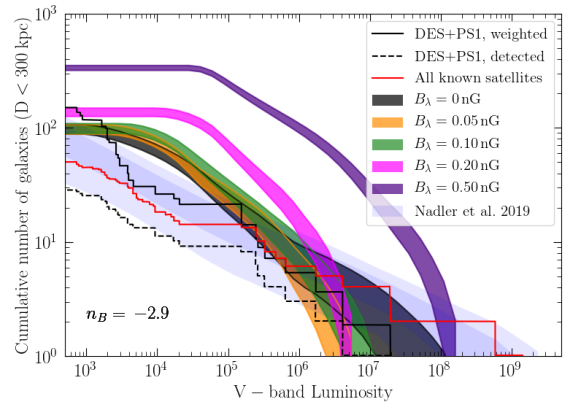


Fig. 20. Predicted cumulative number of satellites brighter than a given luminosity, within 300 kpc around the Milky Way. Same as Fig. 19, but for models with varying magnetic field strengths from $B_\lambda = 0.05$ to 0.50 nG.

2. We extract the observable properties of each galaxy at redshift $z = 0$, including, the LOS velocity dispersion σ_{LOS} , the peak metallicity, and the total V -band luminosity L_V to compare them with well-observed scaling relations, such as the luminosity versus velocity dispersion and metallicity versus luminosity. Strongly perturbed models, with a high amplitude ($B_\lambda = 0.5$ nG, $n_B = -2.9$) or a steep spectral index ($n_B = -2.1$, $B_\lambda = 0.05$ nG) have more power in the mass range of dwarf galaxies, 10^7 to $10^9 M_\odot$. Consequently, in these models, galaxies form more stars and experience an extended star formation history, leading to brighter and more metal rich systems, incompatible with the

M. Sanati et al.: Dwarf galaxies as a probe of Primordial Magnetic Fields

observed Local Group scaling relations. On the contrary, the observed properties of the weakly perturbed models are not sensitively modified.

3. We show that strong magnetic models speed up the structure formation with an impact on the reionization of the Universe. We estimate the fraction of hydrogen ionized in the first Gyr of the Universe history and demonstrate that the earlier onset of star formation and the higher rate of star formation in these models induces a large amount of ionizing photons, enough to reionize the universe at redshifts higher than $z = 9$, incompatible with the observational constraints for the EoR.

4. By combining the abundance of dark matter halos obtained from DMO simulations with the luminosity-halo mass function, we derive the number of luminous satellites expected around the Milky Way and show that with high magnetic amplitude or spectral index not only is the number of small dark matter halos increased in mass ranges 10^7 and $10^8 M_\odot$, but the stellar mass content for a given halo mass also increased, resulting in an overabundance of satellites brighter than $10^5 L_\odot$, is contradiction with observations in the Local Group.

We conclude that galaxies simulated in weakly perturbed models resemble all physical properties of their counterparts in the unperturbed model. However, stronger models (e.g., $B_\lambda = 0.05$ nG with $n_B = -2.4$ or $n_B = -2.1$, and $B_\lambda = 0.20$ nG or $B_\lambda = 0.5$ nG with $n_B = -2.9$) may be ruled out due to the above-mentioned reasoning. Our results are consistent with cosmological observables, (e.g., CMB observations, weak gravitational lensing, Lyman- α data) that constrain the amplitude and the spectral index of the magnetic field power spectrum (Caprini et al. 2004; Lewis 2004; Kahnishvili et al. 2010; Pandey & Sethi 2012; Trivedi et al. 2012; Shaw & Lewis 2012; Pandey & Sethi 2013; Kahnishvili et al. 2013b). We show that even smaller perturbed models can have a detectable impact on the structure formation. Further constraining PMFs could be considered by investigating the ultrafaint dwarf galaxies which are expected to be even more sensitive to perturbations with respect to their classical counterparts.

In this study we considered the contribution of PMFs in the Λ CDM matter power spectrum on mass scales comparable to dwarf galaxies. Regarding the possible direct impact of magnetic fields intrinsic to galaxies, on proto-stellar scales there are different procedures involved in boosting the star formation rate, namely by angular momentum loss due to the magnetic braking (Mouschovias & Paleologou 1980; Ferreira et al. 2000; Martín-Alvarez et al. 2020), or suppressing the star formation due to the magnetic pressure (Burkhart et al. 2009; Molina et al. 2012; Moczek et al. 2017; Sharda et al. 2020). Even so, the net effect is still an open question (see Krumholz & Federrath (2019) for a recent review). It is certainly worth studying whether the modification to the star formation history due to the above procedures dominates over the impact of PMFs during the formation of the first structures. To answer this question it is necessary to include the full magneto-hydrodynamics treatment in our simulations. However, it is too computationally expensive at this moment. We leave this improvement for future studies.

Acknowledgements. We would like to thank Cheng Zhao, Loïc Hausammann, Mladen Ivkovic, and Florian Cabot for very useful discussions. We gratefully acknowledge financial support by Swiss government scholarship FCS. J.S. acknowledges the funding from the European Unions Horizon 2020 research and innovation program under the Marie Skłodowska-Curie Grant No. 665667 and the support by the Swiss National Science Foundation under Grant No. 185863. K.E.K. acknowledges financial support by the Spanish Science Ministry grant PGC2018-094626-B-C22. We acknowledge the support by the International Space Science Institute (ISSI), Bern, Switzerland, for supporting and funding

the international team “First stars in dwarf galaxies”. This work was supported by the Swiss Federal Institute of Technology in Lausanne (EPFL) through the use of the facilities of its Scientific IT and Application Support Center (SCITAS). The simulations presented here were run on the Deneb clusters. The data reduction and galaxy maps have been performed using the parallelized Python `pNbody` package (<http://lastro.epfl.ch/projects/pNbody/>).

References

- Adshead, P., Giblin, J. T., Scully, T. R., & Sfakianakis, E. I. 2016, *J. Cosmol. Astropart. Phys.*, 2016, 039
- Atek, H., Richard, J., Jauzac, M., et al. 2015, *ApJ*, 814, 69
- Aubert, D., & Teyssier, R. 2010, *ApJ*, 724, 244
- Bañados, E., Venemans, B. P., Mazzucchelli, C., et al. 2018, *Nature*, 553, 473
- Banerjee, R., & Jedamzik, K. 2004, *Phys. Rev. D*, 70, 123003
- Beck, R. 2001, *Space Sci. Rev.*, 99, 243
- Beck, R. 2015, *A&ARv*, 24, 4
- Beck, R., & Wielebinski, R. 2013, in *Magnetic Fields in Galaxies*, eds. T. D. Oswalt, & G. Gilmore, 5, 641
- Behroozi, P. S., Wechsler, R. H., & Wu, H.-Y. 2013, *ApJ*, 762, 109
- Bernet, M. L., Miniati, F., Lilly, S. J., Kronberg, P. P., & Dessauges-Zavadsky, M. 2008, *Nature*, 454, 302
- Bertone, S., Vogt, C., & Enßlin, T. 2006, *MNRAS*, 370, 319
- Bolton, J. S., & Haehnelt, M. G. 2007, *MNRAS*, 382, 325
- Bouwens, R. J., Illingworth, G. D., Oesch, P. A., et al. 2015, *ApJ*, 811, 140
- Boyarsky, A., Fröhlich, J., & Ruchayskiy, O. 2012, *Phys. Rev. Lett.*, 108, 031301
- Boylan-Kolchin, M., Bullock, J. S., & Kaplinghat, M. 2011, *MNRAS*, 415, L40
- Boylan-Kolchin, M., Bullock, J. S., & Kaplinghat, M. 2012, *MNRAS*, 422, 1203
- Brandenburg, A., Kahnishvili, T., Mandal, S., et al. 2017a, *Phys. Rev. D*, 96, 123528
- Brandenburg, A., Schober, J., Rogachevskii, I., et al. 2017b, *ApJ*, 845, L21
- Bullock, J. S., & Boylan-Kolchin, M. 2017, *ARA&A*, 55, 343
- Burkhart, B., Falceta-Gonçalves, D., Kowal, G., & Lazarian, A. 2009, *ApJ*, 693, 250
- Caprini, C., Durrer, R., & Kahnishvili, T. 2004, *Phys. Rev. D*, 69, 063006
- Chan, J. H. H., Schive, H.-Y., Woo, T.-P., & Chiueh, T. 2018, *MNRAS*, 478, 2686
- Chan, T. K., Kereš, D., Oñorbe, J., et al. 2015, *MNRAS*, 454, 2981
- Choudhury, T. R., Ferrara, A., & Gallerani, S. 2008, *MNRAS*, 385, L58
- Clarke, T. E., Kronberg, P. P., & Böhringer, H. 2001, *ApJ*, 547, L111
- Davies, F. B., Hennawi, J. F., Bañados, E., et al. 2018a, *ApJ*, 864, 143
- Davies, F. B., Hennawi, J. F., Bañados, E., et al. 2018b, *ApJ*, 864, 142
- Dodelson, S. 2003, *Modern cosmology* (Elsevier)
- Domcke, V., von Harling, B., Morgante, E., & Mukaida, K. 2019, *J. Cosmol. Astropart. Phys.*, 2019, 032
- Drlica-Wagner, A., Bechtol, K., Mau, S., et al. 2020, *ApJ*, 893, 1
- Durrer, R., & Dalla Vecchia, C. 2012, *MNRAS*, 419, 465
- Durovčíková, D., Katz, H., Bosman, S. E. I., et al. 2020, *MNRAS*, 493, 4250
- Durrer, R., & Neronov, A. 2013, *A&ARv*, 21, 62
- Eisenstein, D. J., & Hu, W. 1998, *ApJ*, 496, 605
- Fan, X., White, R. L., Davis, M., et al. 2000, *AJ*, 120, 1167
- Fan, X., Carilli, C. L., & Keating, B. 2006a, *ARA&A*, 44, 415
- Fan, X., Strauss, M. A., Becker, R. H., et al. 2006b, *AJ*, 132, 117
- Faucher-Giguère, C.-A., Lidz, A., Hernquist, L., & Zaldarriaga, M. 2008, *ApJ*, 688, 85
- Ferland, G. J., Peterson, B. M., Horne, K., Welsh, W. F., & Nahar, S. N. 1992, *ApJ*, 387, 95
- Ferland, G. J., Porter, R. L., van Hoof, P. A. M., et al. 2013, *Rev. Mex. Astron. Astrofis.*, 49, 137
- Ferreira, J., Pelletier, G., & Appl, S. 2000, *MNRAS*, 312, 387
- Fitts, A., Boylan-Kolchin, M., Elbert, O. D., et al. 2017, *MNRAS*, 471, 3547
- Fitts, A., Boylan-Kolchin, M., Bozek, B., et al. 2019, *MNRAS*, 490, 962
- Fletcher, A., Beck, R., Shukurov, A., Berkhuijsen, E. M., & Horellou, C. 2011, *MNRAS*, 412, 2396
- Flores, R. A., & Primack, J. R. 1994, *ApJ*, 427, L1
- Fujita, T., & Durrer, R. 2019, *J. Cosmol. Astropart. Phys.*, 2019, 008
- Furlanetto, S. R., & Loeb, A. 2001, *ApJ*, 556, 619
- Giovannini, M., & Shaposhnikov, M. 2000, *Phys. Rev. D*, 62, 103512
- Gopal, R., & Sethi, S. K. 2003, *J. Astrophys. Astron.*, 24, 51
- Governato, F., Weisz, D., Pontzen, A., et al. 2015, *MNRAS*, 448, 792
- Govoni, F., & Feretti, L. 2004, *Int. J. Mod. Phys. D*, 13, 1549
- Grasso, D., & Rubinstein, H. R. 2001, *Phys. Rep.*, 348, 163
- Greig, B., Mesinger, A., Haiman, Z., & Simcoe, R. A. 2017, *MNRAS*, 466, 4239
- Greig, B., Mesinger, A., & Bañados, E. 2019, *MNRAS*, 484, 5094
- Hahn, O., & Abel, T. 2011, *MNRAS*, 415, 2101
- Han, J. L. 2017, *ARA&A*, 55, 111
- Hanayama, H., Takahashi, K., Kotake, K., et al. 2005, *ApJ*, 633, 941

- Harvey, D., Revaz, Y., Robertson, A., & Hausammann, L. 2018, *MNRAS*, **481**, L89
- Hausammann, L., Revaz, Y., & Jablonka, P. 2019, *A&A*, **624**, A11
- Hogan, C. J. 1983, *Phys. Lett. B*, **133**, 172
- Hopkins, P. F. 2013, *Pressure-Entropy SPH: Pressure-Entropy Smooth-particle Hydrodynamics*
- Hopkins, P. F., Quataert, E., & Murray, N. 2011, *MNRAS*, **417**, 950
- Hu, E. M., McMahon, R. G., & Cowie, L. L. 1999, *ApJ*, **522**, L9
- Hui, L., & Haiman, Z. 2003, *ApJ*, **596**, 9
- Ichiki, K., & Takahashi, K. 2006, *Astron. Herald*, **99**, 568
- Jedamzik, K., & Pogosian, L. 2020, ArXiv e-prints [arXiv:2004.09487]
- Jedamzik, K., & Saveliev, A. 2019, *Phys. Rev. Lett.*, **123**, 021301
- Jedamzik, K., Katalinić, V., & Olinto, A. V. 1998, *Phys. Rev. D*, **57**, 3264
- Jedamzik, K., Katalinić, V., & Olinto, A. V. 2000, *Phys. Rev. Lett.*, **85**, 700
- Kahnashvili, T., Tevzadze, A. G., Brandenburg, A., & Neronov, A. 2013a, *Phys. Rev. D*, **87**, 083007
- Kahnashvili, T., Maravin, Y., Natarajan, A., Battaglia, N., & Tevzadze, A. G. 2013b, *ApJ*, **770**, 47
- Kahnashvili, T., Tevzadze, A. G., Sethi, S. K., Pandey, K., & Ratra, B. 2010, *Phys. Rev. D*, **82**, 083005
- Kahnashvili, T., Brandenburg, A., Kosowsky, A., Mandal, S., & Roper Pol, A. 2020, *IAU Gen. Assembly*, 295
- Kandas, A., Kunze, K. E., & Tsagas, C. G. 2011, *Phys. Rep.*, **505**, 1
- Katz, N. 1992, *ApJ*, **391**, 502
- Katz, N., Weinberg, D. H., & Hernquist, L. 1996, *ApJS*, **105**, 19
- Kaurov, A. A., & Gnedin, N. Y. 2015, *ApJ*, **810**, 154
- Kim, E.-J., Olinto, A. V., & Rosner, R. 1996, *ApJ*, **468**, 28
- Klypin, A., Kravtsov, A. V., Valenzuela, O., & Prada, F. 1999, *ApJ*, **522**, 82
- Knebe, A., Wagner, C., Knollmann, S., Dieckershoff, T., & Krause, F. 2009, *ApJ*, **698**, 266
- Kobayashi, C., Tsujimoto, T., & Nomoto, K. 2000, *ApJ*, **539**, 26
- Kolb, E. W., & Turner, M. S. 1990, *S&T*, **80**, 381
- Krumholz, M. R., & Federrath, C. 2019, *Front. Astron. Space Sci.*, **6**, 7
- Kuhlen, M., & Faucher-Giguère, C.-A. 2012, *MNRAS*, **423**, 862
- Kunze, K. E., & Komatsu, E. 2014, *J. Cosmol. Astropart. Phys.*, **01**, 009
- Lewis, A. 2004, *Phys. Rev. D*, **70**, 043011
- Loeb, A., & Haiman, Z. 1997, *ApJ*, **490**, 571
- Lovell, M. R., Eke, V., Frenk, C. S., et al. 2012, *MNRAS*, **420**, 2318
- Madau, P., Haardt, F., & Rees, M. J. 1999, *ApJ*, **514**, 648
- Mao, S. A., Carilli, C., Gaensler, B. M., et al. 2017, *Nat. Astron.*, **1**, 621
- Martin, J., & Yokoyama, J. 2008, *J. Cosmol. Astropart. Phys.*, **2008**, 025
- Martin-Alvarez, S., Slyz, A., Devriendt, J., & Gómez-Guijarro, C. 2020, *MNRAS*, **495**, 4475
- Mateo, M. L. 1998, *ARA&A*, **36**, 435
- McBride, J., & Heiles, C. 2013, *ApJ*, **763**, 8
- McConnachie, A. W. 2012, *AJ*, **144**, 4
- McGreer, I. D., Mesinger, A., & D'Odorico, V. 2015, *MNRAS*, **447**, 499
- McKean, J., Jackson, N., Vegetti, S., et al. 2015, *Advancing Astrophysics with the Square Kilometre Array (ASKA14)*, 84
- Mocz, P., Burkhardt, B., Hernquist, L., McKee, C. F., & Springel, V. 2017, *ApJ*, **838**, 40
- Molina, F. Z., Glover, S. C. O., Federrath, C., & Klessen, R. S. 2012, *MNRAS*, **423**, 2680
- Moore, B. 1994, *Nature*, **370**, 629
- Moore, B., Ghigna, S., Governato, F., et al. 1999, *ApJ*, **524**, L19
- Mouschovias, T. C., & Paleologou, E. V. 1980, *ApJ*, **237**, 877
- Nadler, E. O., Mao, Y.-Y., Green, G. M., & Wechsler, R. H. 2019, *ApJ*, **873**, 34
- Nadler, E. O., Mao, Y.-Y., Wechsler, R. H., Garrison-Kimmel, S., & Wetzel, A. 2018, *ApJ*, **859**, 129
- Naoz, S., & Narayan, R. 2013, *Phys. Rev. Lett.*, **111**, 051303
- Navarro, J. F., Frenk, C. S., & White, S. D. M. 1996, *ApJ*, **462**, 563
- Navarro, J. F., Frenk, C. S., & White, S. D. M. 1997, *ApJ*, **490**, 493
- Neronov, A., & Vovk, I. 2010, *Science*, **328**, 73
- Newton, O., Cautun, M., Jenkins, A., Frenk, C. S., & Helly, J. C. 2018, *MNRAS*, **479**, 2853
- Oñorbe, J., Boylan-Kolchin, M., Bullock, J. S., et al. 2015, *MNRAS*, **454**, 2092
- Okamoto, T., Eke, V. R., Frenk, C. S., & Jenkins, A. 2005, *MNRAS*, **363**, 1299
- Ono, Y., Ouchi, M., Mobasher, B., et al. 2012, *ApJ*, **744**, 83
- Ouchi, M., Shimasaku, K., Furusawa, H., et al. 2010, *ApJ*, **723**, 869
- Padmanabhan, T. 2002, *Theoretical Astrophysics - Volume 3, Galaxies and Cosmology*, 3
- Pandey, K. L., & Sethi, S. K. 2012, *ApJ*, **748**, 27
- Pandey, K. L., & Sethi, S. K. 2013, *ApJ*, **762**, 15
- Pandey, K. L., Choudhury, T. R., Sethi, S. K., & Ferrara, A. 2015, *MNRAS*, **451**, 1692
- Paoletti, D., Chluba, J., Finelli, F., & Rubiño-Martín, J. A. 2019, *MNRAS*, **484**, 185
- Planck Collaboration XIII. 2016, *A&A*, **594**, A13
- Planck Collaboration Int. XXVI. 2015, *A&A*, **582**, A29
- Planck Collaboration Int. XLVII. 2016, *A&A*, **596**, A108
- Pontzen, A., & Governato, F. 2014, *Nature*, **506**, 171
- Ratra, B. 1992a, *ApJ*, **391**, L1
- Ratra, B. 1992b, *ApJ*, **391**, L1
- Read, J. I., Walker, M. G., & Steger, P. 2018, *MNRAS*, **481**, 860
- Reiners, A. 2012, *Liv. Rev. Sol. Phys.*, **9**, 1
- Revaz, Y., & Jablonka, P. 2012, *A&A*, **538**, A82
- Revaz, Y., & Jablonka, P. 2018, *A&A*, **616**, A96
- Revaz, Y., Arnaudon, A., Nichols, M., Bonvin, V., & Jablonka, P. 2016, *A&A*, **588**, A21
- Robertson, B. E., Ellis, R. S., Furlanetto, S. R., & Dunlop, J. S. 2015, *ApJ*, **802**, L19
- Robishaw, T., Quataert, E., & Heiles, C. 2008, *ApJ*, **680**, 981
- Rogachevskii, I., Ruchayskiy, O., Boyarsky, A., et al. 2017, *ApJ*, **846**, 153
- Ryu, D., Kang, H., Cho, J., & Das, S. 2008, *Science*, **320**, 909
- Safarzadeh, M. 2018, *MNRAS*, **479**, 315
- Safarzadeh, M., & Loeb, A. 2019, *ApJ*, **877**, L27
- Salvadori, S., Tolstoy, E., Ferrara, A., & Zaroubi, S. 2014, *MNRAS*, **437**, L26
- Sawala, T., Frenk, C. S., Fattahi, A., et al. 2016, *MNRAS*, **457**, 1931
- Sawala, T., Pihajoki, P., Johansson, P. H., et al. 2017, *MNRAS*, **467**, 4383
- Schenker, M. A., Ellis, R. S., Konidakis, N. P., & Stark, D. P. 2014, *ApJ*, **795**, 20
- Schober, J., Schleicher, D. R. G., & Klessen, R. S. 2013, *A&A*, **560**, A87
- Schober, J., Rogachevskii, I., Brandenburg, A., et al. 2018, *ApJ*, **858**, 124
- Schroeder, J., Mesinger, A., & Haiman, Z. 2013, *MNRAS*, **428**, 3058
- Sethi, S. K., & Subramanian, K. 2005, *MNRAS*, **356**, 778
- Sharda, P., Federrath, C., & Krumholz, M. R. 2020, *MNRAS*, **497**, 336
- Shaw, J. R., & Lewis, A. 2010, *Phys. Rev. D*, **81**, 043517
- Shaw, J. R., & Lewis, A. 2012, *Phys. Rev. D*, **86**, 043510
- Silk, J. 1968, *ApJ*, **151**, 459
- Simon, J. D. 2019, *ARA&A*, **57**, 375
- Smith, B. D., Bryan, G. L., Glover, S. C. O., et al. 2017, *MNRAS*, **466**, 2217
- Spergel, D. N., Verde, L., Peiris, H. V., et al. 2003, *ApJS*, **148**, 175
- Springel, V. 2005, *MNRAS*, **364**, 1105
- Springel, V., & Hernquist, L. 2003, *MNRAS*, **339**, 312
- Springel, V., Wang, J., Vogelsberger, M., et al. 2008, *MNRAS*, **391**, 1685
- Stevenson, D. J. 2010, *Space Sci. Rev.*, **152**, 651
- Stoychev, B. K., Dixon, K. L., Macciò, A. V., Blank, M., & Dutton, A. A. 2019, *MNRAS*, **489**, 487
- Subramanian, K. 2016, *Rep. Prog. Phys.*, **79**, 076901
- Subramanian, K., & Barrow, J. D. 1998, *Phys. Rev. Lett.*, **81**, 3575
- Tashiro, H., Silk, J., Langer, M., & Sugiyama, N. 2009, *MNRAS*, **392**, 1421
- Tegmark, M., & Zaldarriaga, M. 2002, *Phys. Rev. D*, **66**, 103508
- Tilvi, V., Papovich, C., Finkelstein, S. L., et al. 2014, *ApJ*, **794**, 5
- Tolstoy, E., Hill, V., & Tosi, M. 2009, *ARA&A*, **47**, 371
- Tornatore, L., Borgani, S., Dolag, K., & Matteucci, F. 2007, *MNRAS*, **382**, 1050
- Totani, T., Kawai, N., Kosugi, G., et al. 2006, *PASJ*, **58**, 485
- Trivedi, P., Seshadri, T. R., & Subramanian, K. 2012, *Phys. Rev. Lett.*, **108**, 231301
- Tsujimoto, T., Nomoto, K., Yoshii, Y., et al. 1995, *MNRAS*, **277**, 945
- Turner, M. S., & Widrow, L. M. 1988a, *Phys. Rev. D*, **37**, 2743
- Turner, M. S., & Widrow, L. M. 1988b, *Phys. Rev. D*, **37**, 2743
- Vachaspati, T. 1991, *Phys. Lett. B*, **265**, 258
- Vegetti, S., Koopmans, L. V. E., Bolton, A., Treu, T., & Gavazzi, R. 2010, *MNRAS*, **408**, 1969
- Verbeke, R., Papastergis, E., Ponomareva, A. A., Rath, S., & De Rijcke, S. 2017, *A&A*, **607**, A13
- Vogelsberger, M., Zavala, J., Simpson, C., & Jenkins, A. 2014, *MNRAS*, **444**, 3684
- Vogt, C., & Enßlin, T. A. 2005, *A&A*, **434**, 67
- Wagstaff, J. M., & Banerjee, R. 2015, *Phys. Rev. D*, **92**, 123004
- Wasserman, I. 1978a, *ApJ*, **224**, 337
- Wasserman, I. M. 1978b, Ph.D. Thesis, Harvard University
- Wetzel, A. R., Hopkins, P. F., Kim, J.-H., et al. 2016, *ApJ*, **827**, L23
- Widrow, L. M. 2002, *Rev. Mod. Phys.*, **74**, 775
- Wiersma, R. P. C., Schaye, J., Theuns, T., Dalla Vecchia, C., & Tornatore, L. 2009, *MNRAS*, **399**, 574
- Wise, J. H., Demchenko, V. G., Halicek, M. T., et al. 2014, *MNRAS*, **442**, 2560
- Zucca, A., Li, Y., & Pogosian, L. 2017, *Phys. Rev. D*, **95**, 063506

M. Sanati et al.: Dwarf galaxies as a probe of Primordial Magnetic Fields

Appendix A: Physical properties of model galaxies**Table A.1.** Physical properties of all model galaxies.

Model ID	B_l [nG]	n_B –	L_V [$10^6 L_\odot$]	M_\star [$10^6 M_\odot$]	M_{200} [$10^9 M_\odot$]	R_{200} kpc	σ_{LOS} [km s $^{-1}$]	[Fe/H] dex	Redshift ^(a) / Time –/[Gyr]
h050									
B0.00n0.0	0.00	0.0	4.66	10.01	2.66	33.14	10.52	–1.30	0.00/13.8
B0.05n2.9	0.05	–2.9	4.90	10.47	2.67	33.18	10.80	–1.30	0.00/13.8
B0.05n2.7		–2.7	3.84	7.60	2.63	32.98	11.30	–1.41	0.06/13.0
B0.05n2.4		–2.4	7.10	12.29	2.46	32.25	12.09	–0.51	0.00/13.8
B0.05n2.1		–2.1	–2.65	2.19	–	–	–	–	24.6/0.13
B0.10n2.9	0.10	–2.9	7.33	13.76	2.62	32.94	11.61	–1.30	0.04/13.3
B0.20n2.9	0.20		20.99	31.93	2.51	32.49	14.35	–0.51	0.11/12.3
B0.50n2.9	0.50		143.40	147.52	3.51	36.33	25.83	–0.62	0.62/7.8
h070									
B0.00n0.0	0.00	0.0	1.78	5.13	1.80	29.08	10.20	–1.41	0.00/13.8
B0.05n2.9	0.05	–2.9	1.76	5.05	1.78	28.99	10.11	–1.41	0.00/13.8
B0.05n2.7		–2.7	1.11	3.13	1.81	29.13	10.57	–1.52	0.00/13.8
B0.05n2.4		–2.4	1.34	3.84	1.93	29.74	13.46	–1.52	0.00/13.8
B0.05n2.1		–2.1	6.13	17.16	1.61	28.02	15.61	–1.86	0.00/13.8
B0.10n2.9	0.10	–2.9	1.93	5.52	1.79	29.00	10.44	–1.41	0.00/13.8
B0.20n2.9	0.20		3.21	9.34	1.84	29.32	12.00	–1.30	0.00/13.8
B0.50n2.9	0.50		51.22	53.89	2.38	31.90	18.28	–0.74	0.83/6.6
h061									
B0.00n0.0	0.00	0.0	0.20	0.50	1.95	29.85	9.72	–1.86	0.00/13.8
B0.05n2.9	0.05	–2.9	0.18	0.43	1.96	29.91	10.10	–2.76	0.00/13.8
B0.05n2.7		–2.7	0.04	0.09	1.98	30.00	10.16	–3.89	0.00/13.8
B0.05n2.4		–2.4	0.28	0.75	1.79	29.02	12.00	–2.54	0.00/13.8
B0.05n2.1		–2.1	7.68	13.37	1.80	29.05	14.81	–1.86	0.75/7.0
B0.10n2.9	0.10	–2.9	0.30	0.74	1.94	29.82	10.25	–2.42	0.00/13.8
B0.20n2.9	0.20		1.05	2.75	2.02	30.23	13.10	–2.42	0.00/13.8
B0.50n2.9	0.50		43.60	48.94	2.59	32.82	17.66	–0.85	0.69/7.4
h141									
B0.00n0.0	0.00	0.0	0.18	0.49	0.78	21.98	8.22	–2.31	0.00/13.8
B0.05n2.9	0.05	–2.9	0.20	0.52	0.78	21.97	8.36	–2.20	0.00/13.8
B0.05n2.7		–2.7	0.07	0.18	0.78	22.05	8.73	–2.42	0.00/13.8
B0.05n2.4		–2.4	0.26	0.72	0.87	22.78	13.17	–2.09	0.00/13.8
B0.05n2.1		–2.1	4.52	8.39	0.84	22.53	12.94	–1.86	0.67/7.5
B0.10n2.9	0.10	–2.9	0.27	0.71	0.81	22.31	8.33	–2.20	0.00/13.8
B0.20n2.9	0.20		0.71	1.95	0.79	22.10	10.43	–2.09	0.00/13.8
B0.50n2.9	0.50		19.26	20.80	1.08	24.49	15.42	–1.19	1.13/5.4
h111									
B0.00n0.0	0.00	0.0	0.15	0.36	1.06	24.40	10.71	–2.65	0.00/13.8
B0.05n2.9	0.05	–2.9	0.18	0.45	1.05	24.26	9.13	–2.54	0.00/13.8
B0.05n2.7		–2.7	0.10	0.23	1.07	24.43	11.99	–2.65	0.00/13.8
B0.05n2.4		–2.4	0.34	0.91	0.93	23.29	13.26	–2.31	0.00/13.8
B0.05n2.1		–2.1	3.13	8.98	0.88	22.92	16.41	–1.98	0.00/13.8
B0.10n2.9	0.10	–2.9	0.26	0.64	1.06	24.38	10.15	–2.20	0.00/13.8
B0.20n2.9	0.20		0.83	2.21	1.19	25.32	11.94	–2.20	0.00/13.8
B0.50n2.9	0.50		32.33	65.88	1.95	29.86	18.98	–0.40	0.00/13.8

Notes. For each galaxy we computed the V-band total stellar luminosity L_V , the stellar mass M_\star , the virial mass M_{200} , the virial radius R_{200} , the stellar line-of-sight velocity dispersion σ_{LOS} , and the mode of the stellar metallicity distribution function [Fe/H], all defined inside one virial radius. In the first row different PMF models are shown at a variety of magnetic spectral indices between -2.9 to -2.1 for constant $B_l = 0.05$, and in the second row for a constant spectral index at $n_B = -2.9$ and magnetic field strengths in the range $B_l = 0.05 - 0.50$ nG. ^(a)Halos that did not reach $z = 0$ crashed at the redshift specified here. The reason some simulations crashed at $z > 0$ is due to the high gas density coupled to a high stellar mass and strong stellar feedback. The simulation time steps in dense regions is dominated by the Courant condition $\Delta t \sim \Delta x/c_s$ with c_s the sound speed and Δx the spatial resolution. As $\Delta x \sim 1/\rho^{1/3}$, the time steps shrink with increasing density. In the presence of stellar feedback, which heats up the gas in dense regions and subsequently increases the sound speed, the time step shrinkage becomes worse. As the current version of our code uses a limit on the shortest time steps, simulations crash in extreme conditions (hot-dense gas). The problem mainly occurs for the most massive halos where the gas density is higher, triggering a stronger cooling and higher star formation, which leads to a significant gas heating. By removing the time step limit, we can avoid the simulation crash, however at the expense of running simulations for many more CPU-hours.

Table A.1. continued.

Model ID	B_{λ} [nG]	n_B –	L_V [$10^6 L_{\odot}$]	M_{\star} [$10^6 M_{\odot}$]	M_{200} [$10^9 M_{\odot}$]	R_{200} kpc	σ_{LOS} [kms^{-1}]	[Fe/H] dex	Redshift/ Time –/[Gyr]
h122									
B0.00n0.0	0.00	0.0	0.11	0.26	0.93	23.37	9.02	–2.65	0.00/13.8
B0.05n2.9	0.05	–2.9	0.12	0.30	0.96	23.61	9.22	–2.65	0.00/13.8
B0.05n2.7		–2.7	0.05	0.12	0.89	22.98	10.53	–3.10	0.00/13.8
B0.05n2.4		–2.4	0.12	0.32	0.86	22.77	13.81	–2.42	0.00/13.8
B0.05n2.1		–2.1	1.48	4.13	0.84	22.56	15.05	–1.98	0.00/13.8
B0.10n2.9	0.10	–2.9	0.18	0.46	0.91	23.17	8.77	–2.09	0.00/13.8
B0.20n2.9	0.20		0.52	1.36	0.90	23.12	10.92	–2.20	0.00/13.8
B0.50n2.9	0.50		25.93	53.81	1.54	27.60	18.33	–0.40	0.00/13.8
h159									
B0.00n0.0	0.00	0.0	0.40	1.03	0.68	21.02	9.31	–2.42	0.00/13.8
B0.05n2.9	0.05	–2.9	0.43	1.09	0.68	21.05	8.96	–1.75	0.00/13.8
B0.05n2.7		–2.7	0.27	0.69	0.67	20.93	10.23	–2.42	0.00/13.8
B0.05n2.4		–2.4	0.40	1.10	0.59	20.09	11.59	–2.20	0.00/13.8
B0.05n2.1		–2.1	2.08	6.06	0.65	20.73	15.12	–1.86	0.00/13.8
B0.10n2.9	0.10	–2.9	0.50	1.29	0.68	21.00	9.98	–1.75	0.00/13.8
B0.20n2.9	0.20		0.91	2.49	0.67	20.93	10.49	–2.20	0.00/13.8
B0.50n2.9	0.50		15.10	36.82	1.64	28.18	18.10	–1.19	0.00/13.8
h168									
B0.00n0.0	0.00	0.0	0.11	0.27	0.54	19.42	8.68	–2.76	0.00/13.8
B0.05n2.9	0.05	–2.9	0.66	1.79	2.88	34.01	9.60	–2.20	0.00/13.8
B0.05n2.7		–2.7	0.31	0.81	2.70	33.29	10.70	–2.31	0.00/13.8
B0.05n2.4		–2.4	0.32	0.88	1.14	24.93	11.90	–2.20	0.00/13.8
B0.05n2.1		–2.1	1.51	4.43	0.52	19.18	11.08	–1.98	0.00/13.8
B0.10n2.9	0.10	–2.9	0.70	1.92	2.68	33.20	10.15	–2.20	0.00/13.8
B0.20n2.9	0.20		1.31	3.67	2.31	31.61	12.15	–1.41	0.00/13.8
B0.50n2.9	0.50		18.36	40.09	1.43	26.94	18.34	–1.08	0.00/13.8
h177									
B0.00n0.0	0.00	0.0	0.18	0.47	0.52	19.26	8.35	–2.31	0.00/13.8
B0.05n2.9	0.05	–2.9	0.19	0.50	0.52	19.22	7.53	–2.54	0.00/13.8
B0.05n2.7		–2.7	0.07	0.17	0.51	19.07	8.02	–2.65	0.00/13.8
B0.05n2.4		–2.4	0.18	0.49	0.37	17.08	10.72	–2.09	0.00/13.8
B0.05n2.1		–2.1	1.14	3.18	0.68	21.06	13.11	–1.98	0.00/13.8
B0.10n2.9	0.10	–2.9	0.25	0.65	0.54	19.42	8.27	–2.31	0.00/13.8
B0.20n2.9	0.20		0.52	1.40	0.56	19.67	8.64	–2.20	0.00/13.8
B0.50n2.9	0.50		5.63	17.27	0.94	23.41	13.54	–1.19	0.00/13.8

M. Sanati et al.: Dwarf galaxies as a probe of Primordial Magnetic Fields

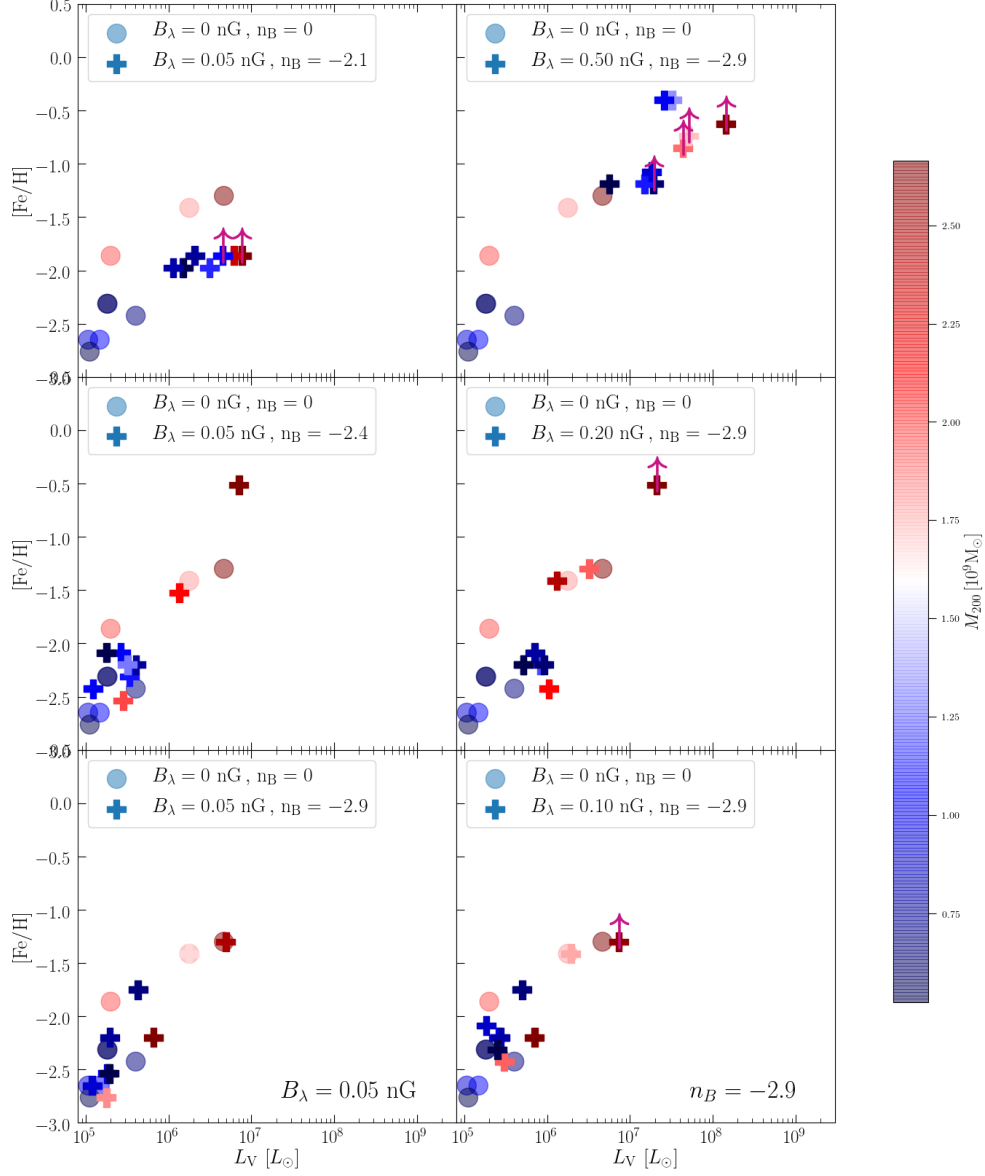


Fig. A.1. Mean metallicity versus stellar V-band luminosity. Each object corresponds to one model galaxy with the physical properties given in Table A.1 for which $[\text{Fe}/\text{H}]$ is computed as the median of the galaxy stellar metallicity distribution function. The color-coding shows the halo mass of each model galaxy. The purple arrows indicate models that did not reach $z = 0$ and are expected to have a slightly higher metallicity.

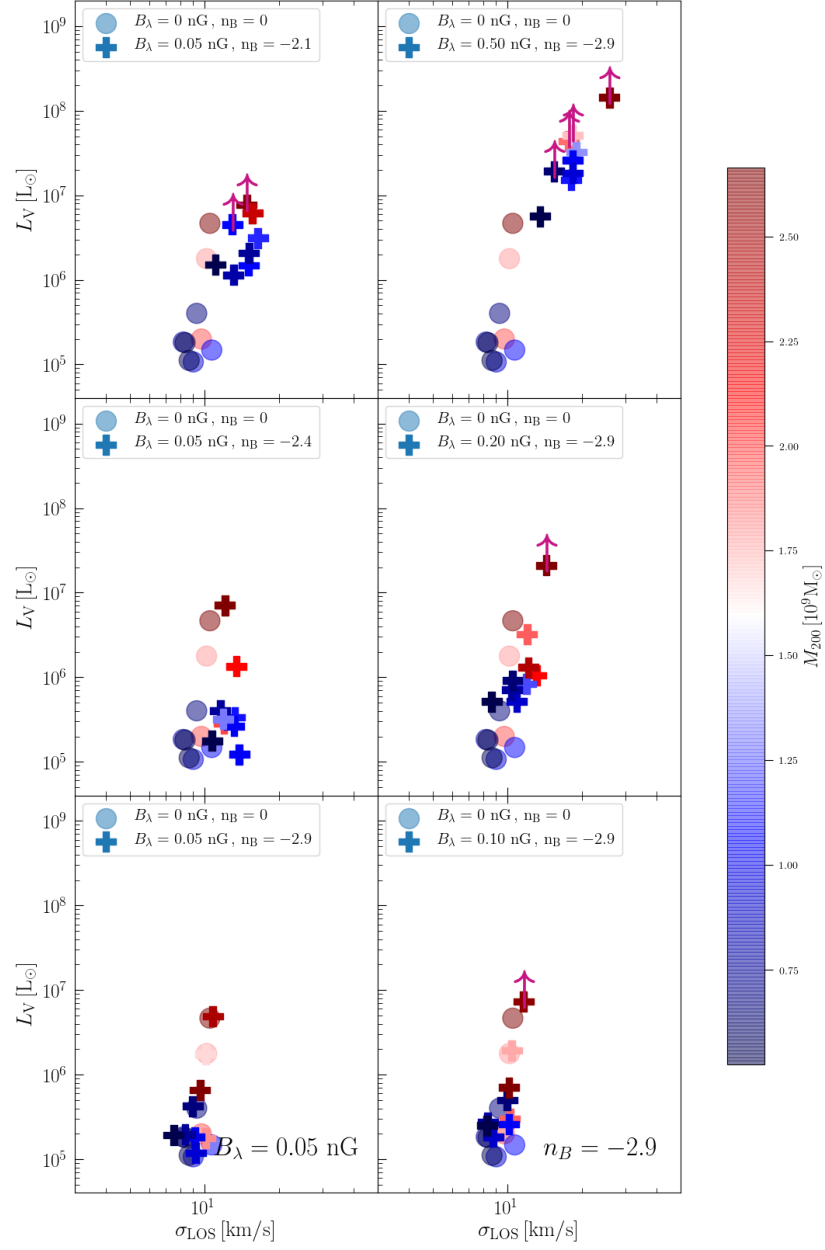


Fig. A.2. V-band luminosity as a function of line-of-sight velocity dispersion in each model galaxy with physical properties given in Table A.1 in each magnetic field model compared to the no-magnetic-field model. The color-coding shows the halo mass of each model galaxy. The purple arrows indicate models that did not reach $z = 0$ and are expected to have a slightly brighter luminosity.

Chapter 6

Dwarf galaxies in a primordially magnetized Universe

The next chapter corresponds to a first author paper to be submitted to Astronomy & Astrophysics Journal

Dwarf galaxies in a primordially magnetized Universe

Mahsa Sanati¹, Sergio Martin-Alvarez², Jennifer Schober¹, Yves Revaz¹

¹ Institute of Physics, Laboratory of Astrophysics, École Polytechnique Fédérale de Lausanne (EPFL), 1290 Sauverny, Switzerland
e-mail: mahsa.sanati@epfl.ch

² Institute of Astronomy and Kavli Institute for Cosmology, University of Cambridge, Madingley Road, Cambridge CB3 0HA, UK

Received: XXXX; accepted: YYYY

ABSTRACT

The true character of primordial magnetic fields (PMFs) in the first phases of galaxy formation still remains elusive. We address this challenge by exploring their impact on galaxy evolution via (i) their modification of the initial matter power spectrum, in opposition to (ii) the pressure support produced by magnetic fields in the interstellar medium (ISM) of galaxies, in order to find the dominant agent. We run zoom-in magneto-hydrodynamical simulations of twelve halos extracted from a Λ CDM cosmological box and follow their evolution down to redshift $z = 0$. Model galaxies are validated on the basis of global galaxy properties such as half light radius, V-band luminosity, mean metallicity and velocity dispersion profile. We identify the distinct effect of PMFs in shaping the evolution of low mass dwarfs due to their shallower gravitational potential contrary to that of more massive galaxies. The magnetic pressure decreases the stellar mass immensely, delays the onset of star formation, and even prevents the formation of stellar particles in small mass halos altogether. However, we show that the impact of PMFs in initiating the structure formation dominates the later contribution of magnetic energy to the ISM. Primordial fields speed up the formation of the first dark halos, leading to an earlier onset and a higher rate of star formation. In addition we show that magnetic fields of initial strength $B_i > 0.20$ nG serve as evidence for a pronounced growth of the magnetic energy, with a short saturation period. These trends are independent of the initial conditions, regardless of whether it is the classical Λ CDM or modified by PMFs, though the growth rate is steeper in the latter. Lastly, we introduce the present-time observable properties of dwarf galaxies as an indicator for the impact of PMFs.

Key words. Primordial magnetic fields, Magnetic Fields, Cosmology, Dwarf galaxy, Ultra faint dwarf galaxies, Galaxy evolution, Star Formation, Magnetohydrodynamical simulations

1. Introduction

From planets and stars (Stevenson 2010; Reiners 2012) to galaxies (Beck 2001; Beck & Wielebinski 2013) and galaxy clusters (Clarke et al. 2001; Govoni & Feretti 2004; Vogt & Enßlin 2005), magnetic fields have been observed on all cosmic scales. Radio spectropolarimetry observations reveal magnetic fields with a few micro-gauss strengths in local (Fletcher et al. 2011; Beck 2015a; Robishaw et al. 2008; McBride & Heiles 2013) and high redshift (Bernet et al. 2008; Mao et al. 2017) galaxies. However, understanding the origin of magnetic fields in galaxies and at large scales is still a challenge for modern astrophysics (see e.g. Kulsrud & Zweibel 2008).

A variety of theories have been proposed to explain the generation of magnetic fields from a cosmological source and their amplification by a dynamo in collapsed objects (Ichiki & Takahashi 2006; Ryu et al. 2008; Naoz & Narayan 2013) or the generation of magnetic fields from an astrophysical source (Widrow 2002; Hanayama et al. 2005; Safarzadeh 2018; Durrive & Langer 2015; Schober et al. 2013). Neronov & Vovk (2010) suggest a lower limit of $\sim 10^{-16}$ G (coherent on Mpc scales) for the magnetism in the intergalactic medium voids. The presence of fields in these relatively quiet environments is difficult to explain by turbulence alone and would perhaps favor a primordial origin.

Primordial magnetic fields are presumably generated in the process of phase transitions during the inflationary expansion phase (Turner & Widrow 1988a; Adshead et al. 2016; Domcke et al. 2019; Fujita & Durrer 2019), Hogan (1983) and Ratra

(1992a) suggest that a small fraction of energy released during the electroweak or quark-hadron transitions is converted to large scale magnetic fields. A primordial field, generated in the Early Universe, could be amplified during the collapse of density perturbations and explain the magnetic fields observed in galaxies (Kandus et al. 2011).

Current observational constraints of primordial magnetic fields have been obtained namely from the cosmic microwave background (CMB) anisotropies (Shaw & Lewis 2010; Planck Collaboration et al. 2015; Zucca et al. 2017; Paoletti et al. 2019), CMB spectral distortions (Jedamzik et al. 2000; Kunze & Komatsu 2014; Wagstaff & Banerjee 2015), Large-Scale Structures (Kahnishvili et al. 2010), the Sunyaev-Zel'dovich statistics (Tashiro et al. 2009), the two-point shear correlation function from gravitational lensing (Pandey & Sethi 2012), Lyman- α forest clouds (Pandey & Sethi 2013), and the reionization history of the Universe (Pandey et al. 2015). The above constraints limit the strength of the magnetic fields to the upper value of 47 pG for scale-invariant fields (Jedamzik & Saveliev 2019) and a few nG in more general states, coherent on 1 Mpc scales.

The uncertainty remains surrounding cosmic magnetic fields, motivates the question whether truly primordial fields can be detected and how their characteristics can be constrained. In this regard, numerical simulations are the perfect tool to disentangle between the primordial action of magnetic fields and its role in astrophysical processes at later times.

A primordial magnetic field may generate density perturbations in addition to the standard ones generated by inflation. The magnetically-produced perturbations can dominate the power-

law spectrum of the Lambda Cold Dark Matter (ΛCDM) on small length scales ($k \geq 10 h \text{ Mpc}^{-1}$). This modification to the matter power spectrum can affect the formation of small scale structures (Kim et al. 1996; Wasserman 1978b). As direct observational constraints do not reach scales smaller than those probed by the Lyman- α forest, we need to rely on dwarf galaxies to explore structure formation on yet smaller scales. The influence of primordial magnetic fields on the matter power spectrum, which predominantly modify the number and properties of dwarfs, could thus lead to a substantial revision of our understanding of the standard cosmological model.

The abundance and internal structure of dwarf galaxies can potentially shed new light on the long-standing tensions existing between ΛCDM and Local Group observations, namely, cusp/core (Navarro et al. 1996, 1997), missing satellites (Klypin et al. 1999; Moore et al. 1999), too-big-to-fail (Boylan-Kolchin et al. 2011, 2012), and satellite planes (Pawlowski & Kroupa 2013) (see Bullock & Boylan-Kolchin (2017) for a recent review).

As one of the main components in the interstellar medium (ISM) energy budget, magnetic fields play a part in the evolution of dwarf galaxies. The importance of magnetic fields is well recognized in various mechanisms happening in galaxies, in particular, concerning their effect on the star formation (Padoan & Nordlund 2011; Marinacci & Vogelsberger 2016; Zamora-Avilés et al. 2018), global morphological and dynamical properties of galaxies (Pillepich et al. 2018; Martin-Alvarez et al. 2020; Iffrig & Hennebelle 2017; Körtgen et al. 2019), and the evolution of galactic outflows (Grønnow et al. 2018). ISM observations at low redshift revealed the magnetic energy to be in equipartition with the turbulent, thermal and cosmic ray energies (Tabatabaei et al. 2008; Beck 2007, 2015b).

Using analytical models and cosmological simulations, respectively, Pandey et al. (2015) and Sanati et al. (2020) showed the impact of primordial magnetic fields on the history of reionization. In a recent study, Katz et al. (2021) presented a suite of cosmological radiation-magnetohydrodynamics simulations showing the impact of primordial magnetic fields on the galaxy formation during the epoch of reionization. Alternatively, Koh et al. (2021) studied the impact of magnetic fields on the formation of first stars. They showed that magnetic fields whose Alfvén velocity is higher than the speed of sound can completely suppress the collapse of minihalos $< 10^6 M_\odot$ hosting first stars.

Here we aim to unveil the impact of primordial magnetic fields on the global properties of dwarf galaxies. For that we follow the cosmological evolution of dwarf galaxies forming from the matter power spectrum altered by primordial magnetic fields. Simultaneously, we allow for the effect of magnetization on the structure and pressure support of the multi phase ISM. The goal of this paper is to study if the cosmological impact of primordial fields dominates over the interfere of magnetic fields in astrophysical processes rule the evolution of galaxies.

This paper is organized as follows. Section 2 recalls the theories explain the effect of inflationary-produced primordial magnetic fields on the ΛCDM matter power spectrum. Section 3 describes in details our numerical framework as well as the simulations performed. The results are presented in Section 4. We first discuss results on magneto-hydrodynamical (MHD) simulations where the matter power spectrum is of the classical ΛCDM paradigm. Then we present the results of including the effect of primordial fields. A brief conclusion is given in Section 5.

2. Impact of primordial magnetic fields on the density fluctuations

We consider the effect of primordial magnetic fields produced before recombination in the process of phase transitions. (ex. Turner & Widrow 1988b; Ratra 1992b; Boyarsky et al. 2012a). (e.g., Turner & Widrow 1988b; Ratra 1992b). It has been shown in the seminal works of Wasserman (1978a) and Kim et al. (1996) that after the recombination epoch, primordial magnetic fields may induce motions in the ionized baryons through the Lorentz force which drives compressional and rotational perturbations causing density fluctuations in the gas. These perturbations propagate down to the neutral gas and also to the dark matter through the gravitational coupling, and a direct impact on the total matter power spectrum is expected.

Characterizing this impact, however, is non-trivial and a large literature has been dedicated to describe it. Hereafter, without entering into too much detail, we briefly review the principal steps that allow us to determine the origin of the effect of primordial magnetic fields on the total matter power spectrum.

2.1. Primordial magnetic field

Following Wasserman (1978a), Kim et al. (1996), and Gopal & Sethi (2003), we first assume that the tangled magnetic field results from a statistically homogeneous and isotropic vector random process. The two-point correlation function of a non-helical field in Fourier space can then be expressed as

$$\langle \hat{B}_i(\mathbf{k}) \hat{B}_j^*(\mathbf{k}') \rangle = (2\pi)^3 \delta(\mathbf{k} - \mathbf{k}') \frac{P_{ij}(\mathbf{k}, \mathbf{k}')}{2} P_B(k), \quad (1)$$

where $P_{ij}(\mathbf{k}) = \delta_{ij} - \frac{k_i k_j}{k^2}$, $k = |\mathbf{k}|$ is the comoving wave number and $P_B(k)$ is the magnetic field power spectrum. Without further information on the exact origin of the primordial magnetic fields, it is usually assumed that its power spectrum follows a simple power law

$$P_B(k) = A k^{n_B} \quad (2)$$

where n_B is the slope index and A is the amplitude of the magnetic spectrum, which is defined through the variance of the magnetic field strength B_λ^2 on a scale $\lambda = 1 \text{ Mpc} \equiv k_\lambda^{-1}$, namely (Shaw & Lewis 2012):

$$A = \frac{(2\pi)^{n_B+5} B_\lambda^2}{2\Gamma(\frac{n_B+3}{2}) k_\lambda^{n_B+3}}. \quad (3)$$

With these definitions, n_B and B_λ fully characterize the primordial magnetic fields. They constitute our main free parameters.

2.2. Growth of perturbations

In the linearized Newtonian theory, the evolution of density fluctuations in the presence of primordial magnetic fields is described by the two following coupled equations for the baryonic fluid perturbation field $\delta_b(\mathbf{x}, t) = \delta\rho_b(\mathbf{x}, t)/\bar{\rho}_b$ and for the collisionless dark matter $\delta_{\text{DM}}(\mathbf{x}, t) = \delta\rho_{\text{DM}}(\mathbf{x}, t)/\bar{\rho}_{\text{DM}}$ (see, e.g., Subramanian & Barrow 1998; Sethi & Subramanian 2005):

$$\frac{\partial^2}{\partial t^2} \delta_b + \left[2H + \frac{4\rho_\gamma}{3\rho_b} n_e \sigma_T a \right] \frac{\partial}{\partial t} \delta_b = c_b^2 \nabla^2 \delta_b + 4\pi G a^2 [\rho_b \delta_b + \rho_{\text{DM}} \delta_{\text{DM}}] + \frac{S(\mathbf{x}, t)}{a^3} \quad (4)$$

Mahsa Sanati, Sergio Martin-Alvarez, Jennifer Schober, Yves Revaz: XXX

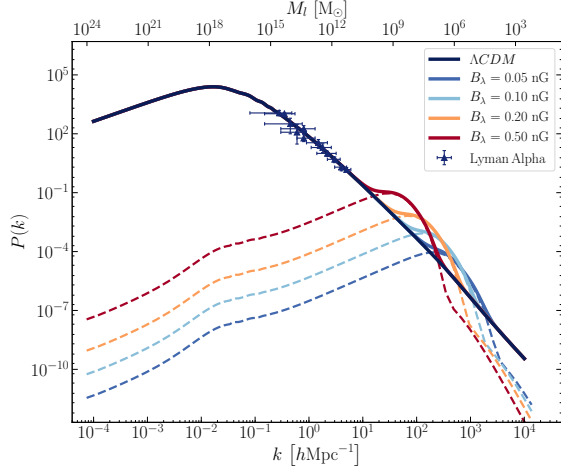


Fig. 1: Contribution of the magnetically induced power spectrum for a variety of magnetic field amplitudes (dashed colored lines) to the total matter power spectrum (solid colored lines). The unperturbed Λ CDM spectrum is shown as the dark blue solid line. The magnetic field spectral slope is kept constant at $n_B = -2.9$.

and

$$\frac{\partial^2}{\partial t^2} \delta_{\text{DM}} + 2H \frac{\partial}{\partial t} \delta_{\text{DM}} = 4\pi G a^2 [\rho_b \delta_b + \rho_{\text{DM}} \delta_{\text{DM}}]. \quad (5)$$

Here a is the scale factor, $H = \dot{a}/a$ the Hubble constant, ρ_b and ρ_γ the baryon and photon mass density, n_e the electron number density, σ_T the Thomson cross section for electron-photon scattering, and c_b the baryon sound speed. The magnetic field source term, S , represents normalized to the baryon density at the present time, $\bar{\rho}_b(t_0)$:

$$S(\mathbf{x}, t) = \frac{\nabla \cdot [\mathbf{B} \times (\nabla \times \mathbf{B})]}{4\pi \bar{\rho}_b(t_0)}. \quad (6)$$

The baryon pressure term $c_b^2 \nabla^2 \delta_b$ in Eq. 4 is sub-dominant with respect to the magnetic pressure as long as the background magnetic field is larger than 5×10^{-11} G (Subramanian & Barrow 1998) and may thus be ignored. The damping term involving the Thomson cross section corresponds to the radiation viscosity. Prior to recombination, this term leads to the damping of small-scale magnetic waves (Jedamzik et al. 1998; Subramanian & Barrow 1998), a physical process similar to Silk damping (Silk 1968). This induces a sharp cutoff of the magnetic field when entering the recombination epoch, and subsequently of its contribution in the total matter power spectrum.

We introduce the total matter density perturbation:

$$\delta_m(\mathbf{x}, t) = (\bar{\rho}_{\text{DM}} \delta_{\text{DM}} + \bar{\rho}_b \delta_b) / (\bar{\rho}_{\text{DM}} + \bar{\rho}_b). \quad (7)$$

We can then solve Eqs. 4 and 5 and get the time evolution of δ_m . The additional term in the evolution of δ_m , due only to the presence of the magnetic fields, is found to be (Sethi & Subramanian 2005):

$$\delta_m \sim \frac{3}{5} \frac{\Omega_b}{\Omega_m^2} \left[\frac{3}{2} \left(\frac{t}{t_{\text{rec}}} \right)^{2/3} + \left(\frac{t_{\text{rec}}}{t} \right) - \frac{5}{2} \right] S(\mathbf{x}, t_{\text{rec}}) t_{\text{rec}}^2, \quad (8)$$

where t_{rec} is the time at recombination and Ω_m and Ω_b are the matter and baryon density parameters.

The important point to get from the previous equations is that the spatial dependence of $\delta_m(\mathbf{x}, t)$ can be followed through the magnetic field source term $S(\mathbf{x}, t_{\text{rec}})$. We thus expect the total matter power spectrum to directly depend on the power spectrum of the magnetic field.

It is worth noting that the most significant evolution of the magnetic field takes place before recombination (Kahniashvili et al. 2013; Brandenburg et al. 2017a,b). During recombination the ionization degree drops to a tiny value. Afterward, the magnetic field is more or less frozen into the gas, i.e., it just passively follows the cosmic expansion, ensuring that the magnetic flux is conserved.

2.3. Impact on the total matter power spectrum

The modification of the total matter power spectrum due to the influence of magnetic fields was first addressed by Kim et al. (1996) and was extended by Gopal & Sethi (2003). The total matter power spectrum is the ensemble average of the density fluctuations in Fourier space, $P(k, t) = \langle \delta_m(k, t) \delta_m^*(k, t) \rangle$, that we can obtain from the evolution equation (Eq. 7) and introducing the ensemble average of the primordial magnetic fields, Eqs. 6 and 2.

After the decoupling of photons, the ionized matter density fluctuations are affected by the magnetic Alfvén waves if the crossing time, $\tau_A \sim 1/k v_A$, is smaller than the inverse Hubble rate (Banerjee & Jedamzik 2004), where v_A is the Alfvén velocity $v_A = B_\lambda / \sqrt{\mu_0 \rho_0}$, with μ_0 the permeability or magnetic constant. As the magnetic energy B_λ^2 scales with $P_B(k) k^3$, $\tau_A \sim \sqrt{\mu_0 \rho_0} k^{-(3+n_B)/2}$. For $n_B > -5$, the crossing time is then shorter for larger k , amplifying the perturbations faster on smaller scales. In the limit where $k \ll k_B$, with $k_B \equiv (v_A \sqrt{\pi/\rho_0 G})^{-1}$, the magnetic wave number above the Alfvén waves damp instabilities (the equivalent of the Jeans wave number), at the lowest order in k/k_{max} (i.e., $k_{\text{max}} \equiv k_B$), the solution for the total matter power spectrum is (Gopal & Sethi 2003)

$$P(k) \sim A k^{2n_B+7} + B k_{\text{max}}^{2n_B+3} k^4 + C k_{\text{max}}^{2n_B+1} k^6 + \dots, \quad (9)$$

which strongly depends on the magnetic slope index n_B . For the scale-invariant case, $n_B \equiv -3$, $P(k) \sim k$, and $\tau_A \sim k^{-1}$, thus small-scale perturbations are strongly amplified, as long as $\tau_A < 1/H(t)$, up to about k_B where they are sharply quenched (see Sect. 2.2).

2.4. Adopted total matter power spectrum

We generated the matter power spectrum using a modified version of the CAMB code which includes the effects of primordial magnetic fields (for details see Shaw & Lewis (2012)). In this version the non-linear effects of the magnetic Jeans length (magnetic pressure) and the damping due to the radiation viscosity (when the photon free streaming length is small) are both explicitly computed. As such, contrary to other studies, there is no need to artificially include a cutoff wave number.

Figure 1 displays the matter power spectrum due to the magnetic field (dashed lines) together with its contribution to the total matter power spectrum (plain lines). The dark blue continuous line corresponds to the unperturbed Λ CDM power spectrum. The dependence with respect to the magnetic field amplitude ($B_\lambda = 0.05, 0.10, 0.20, 0.50$ nG) is shown keeping the spectral

index constant ($n_B = -2.9$). The range of parameters explored is chosen in such a way that they impact the power spectrum without violating the existing constraints, as do those presented in Section 1.

It is worth mentioning that for the magnetic spectral index a range of both positive and negative values are suggested. In this study, we considered primordial magnetic fields generated during the inflation, which tend to have negative values for n_B , (Turner & Widrow 1988a; Ratra 1992a; Giovannini & Shaposhnikov 2000; Martin & Yokoyama 2008). However, positive values for n_B are also plausible in other magnetogenesis processes, like the electroweak phase transition (Grasso & Rubinstein 2001; Kandus et al. 2011; Durrer & Neronov 2013) and Higgs field gradients (Vachaspati 1991), or in the case of subsequent evolution of the primordial magnetic fields, for example via the chiral anomaly (Boyaarsky et al. 2012b; Rogachevskii et al. 2017; Schober et al. 2018).

As expected from Eq. 9, on large scales (small k), for $n_B = -2.9$ the slope is nearly 1. Small-scale structures are thus strongly magnetically amplified and reach an amplitude larger than the one induced by inflation alone. On very small scales, the power spectrum is sharply quenched owing to the magnetic pressure and radiation viscosity damping. The total power spectrum is thus characterized by a bump at the smallest amplified scales, $k \sim 10 - 1000 \text{ hMpc}^{-1}$, depending on the exact values of B_λ . In Fig. 1, we link the wave number and the mass contained within a sphere of comoving Lagrangian radius r_l at $z = 0$ by defining the mass scale M_l (the equivalent of the Jeans mass), assuming a background mean density given by the cosmological parameters (see e.g., Bullock & Boylan-Kolchin 2017):

$$M_l = \frac{4\pi}{3} r_l^3 \rho_m = \frac{\Omega_m H_0^2}{2G} r_l^3 = 1.71 \times 10^{11} M_\odot \left(\frac{\Omega_m}{0.3}\right) \left(\frac{h}{0.67}\right)^2 \left(\frac{r_l}{1 \text{ Mpc}}\right)^3 \quad (10)$$

The bumps precisely cover masses expected for the total mass of dwarf galaxies. Therefore, primordial magnetic fields could significantly influence the formation and properties of those objects.

3. Methods and simulations

We generate all the cosmological magneto-hydrodynamical simulations studied in this work employing our own modified version of the RAMSES code (Teyssier 2002; Fromang et al. 2006; Teyssier et al. 2006). In addition to the collisionless dark matter and stellar particles, RAMSES employs an adaptive mesh refinement octree grid to solve the evolution of gas. It treats the baryonic physics by including gas cooling, redshift-evolving UV-background heating, star formation and stellar feedback. We briefly summarize its essential elements below.

3.1. Numerical setup

Ideal MHD In its ideal MHD implementation, RAMSES uses a constrained transport method to solve the evolution of magnetic fields (Teyssier et al. 2006; Fromang et al. 2006). This method guarantees a null divergence of the magnetic field down to numerical precision and guarantees no spurious modifications of conserved quantities and emergence magnetohydrodynamical artifacts (?).

We model primordial magnetic fields through an ab-initio field, seeded uniformly and aligned with the z -axis of the computational domain, with strength B_λ . This choice of a uniform

field is common practice amongst MHD simulations (e.g., Vazza et al. 2014; Pakmor et al. 2017; Martin-Alvarez et al. 2018), but we note that smaller-scale perturbations for such strong initial fields may influence the magnetic field amplification and galaxy formation during the early stages of simulations.

Radiative cooling and heating processes We model the process of reionization using a UV background (Haardt & Madau 1996), which we initialize at $z = 10$. Additionally, we account for metal cooling above 10^4 K interpolating the corresponding CLOUDY tables (Ferland et al. 1998). Below temperatures of 10^4 K we follow fine structure metal cooling rates from Rosen & Bregman (1995). To account for the pre-enrichment by the Population III stars we assume a metallicity floor of $8.3 \cdot 10^{-4} Z_\odot$ for gas (Wise et al. 2012).

Star formation We model the process of star formation employing a magneto-thermo-turbulent (MTT) star formation prescription, presented in more detail in its hydrodynamical version by Kimm et al. (2017) and Trebitsch et al. (2017), and in its MHD version by Martin-Alvarez et al. (2020). As a brief summary of the model, in this MTT star formation we allow gas to be converted into stellar particles in cells at the highest level of refinement (Rasera & Teyssier 2006) where the gravitational pull overcomes the local MTT support and following a Schmidt law (Schmidt 1959). The efficiency of this conversion is a local quantity that depends on the local gas properties, following the multi-PN model (Padoan & Nordlund 2011) as presented by Federrath & Klessen (2012).

Stellar feedback Stellar particles are allowed to explode as mechanical supernovae feedback using the Kimm & Cen (2014) supernova implementation and assuming a Kroupa initial mass function (Kroupa 2001). Each supernova injects to its host cell and its immediate neighbours gas and metal mass with fractions of $\eta_{\text{SN}} = 0.213$ and $\eta_{\text{metal}} = 0.075$ respectively. In order to reproduce realistic dwarf galaxy properties, we calibrate the supernova feedback strength in our hydrodynamical simulations to a specific energy injection per SN of $\varepsilon_{\text{SN}} = E_{\text{SN}}/M_{\text{SN}} = 0.4 \cdot 10^{51} \text{ erg} / 9.568 M_\odot$. We have decreased the supernova progenitor mass, which leads to a larger number of supernovae events per stellar particle. As the energy ejected in each supernovae event is fixed, such progenitor mass reduction increases the total feedback energy released to the ISM. Therefore, by additionally decreasing the supernovae feedback energy, ε remains approximately unchanged. We do not account for any additional injection or removal of magnetic fields during star formation or supernova feedback.

3.2. Initial conditions

The initial conditions are generated with the MUSIC code (Hahn & Abel 2011), assuming the cosmology of Planck Collaboration et al. (2016) with $\Omega_\Lambda = 0.685$, $\Omega_m = 0.315$, $\Omega_b = 0.0486$, and $h = 0.673$. All simulations are started at redshift $z = 70$, ensuring that the rms variance of the initial density field, σ_8 , lies between 0.1 and 0.2 (Knebe et al. 2009; Oñorbe et al. 2015).

Using the zoom-in technique, we refine a ellipsoidal of size $\approx 0.85 \text{ cMpc}$ (co-moving Mpc) across, in the center of the cubic simulation box of volume $(5 \text{ cMpc})^3$. In this refined region, we achieve dark matter and stellar mass resolution of $m_{\text{DM}} \approx 4 \cdot 10^3 M_\odot$ and $m_\star = 382 M_\odot$, respectively. We gradually de-

Mahsa Sanati, Sergio Martin-Alvarez, Jennifer Schober, Yves Revaz: XXX

ID	B00	B05	B10	B20	B50	B05ps	B10ps	B20ps	B50ps
B_l [nG]	0	0.05	0.10	0.20	0.50	0.05	0.10	0.20	0.50
Power Spectrum	Λ CDM	-	-	-	-	Λ CDM+PMFs	-	-	-

Table 1: Parameters varying in the simulation runs. Columns are as follows: 1) Model ID. 2) Comoving strength of the initial primordial magnetic field. 3) Matter power spectrum used to generate the initial conditions. 4) The ratio between the feedback energy and the gas mass ejected in each supernovae event (See Section 3.1).

grade the resolution, from level 10 to 6 of MUSIC, outside the refined region. Throughout the course of the simulation, when either the total dark matter or gas mass inside a grid cell exceeds $8 m_{DM} \Omega_m / \Omega_b$, or it contains at least 8 dark matter particles, a parent grid cell is split into 8 equal children cells. With this adaptive refinement criteria, which allows to resolve dense and Jeans-unstable regions, we refine the grid to the minimum cell width of ~ 5 pc. The initial conditions match the perturbed range of the total matter power spectrum described in Section 2.4.

3.3. Set of simulations

We run eleven set of simulations as listed in Table 1. The first run has no magnetic fields and employs the classical matter power spectrum of the Λ CDM paradigm. In the second set of simulations, the strength of the primordial seed magnetic field is varied, but the matter power spectrum is unaffected. Then we explore different values for the amplitude of the primordial field, but also including its effect through the modification of the matter power spectrum.

All the simulations are designed to examine primordial magnetic fields with strengths allowed by current cosmological constraints (see Section 1). From Fig. 1 it appears that a stronger amplitude than the maximum one used in this work would affect the power spectrum for $k < 10 h\text{Mpc}^{-1}$. However, such a modification is ruled out by the observations of the Lyman- α forest (Tegmark & Zaldarriaga 2002; Pandey & Sethi 2013). The lowest amplitude used is at the border that the impact of primordial magnetic fields can modify structure formation (Shaw & Lewis 2010; Pandey et al. 2015; Sanati et al. 2020).

In the last set of simulations the supernovae feedback energy is fixed to zero. The arguments for this test is described in details in Section 4.2.

3.4. Extraction of the Observables, luminosity and metallicity

Galactic region Global galactic properties, such as gas mass and specific energies, are measured inside the *galactic region*. It is defined using the virial radius of the dark matter halo R_{200} at redshift $z = 0$. The galactic region is the spherical volume centered on the position of the galaxy with radius equal to the comoving evolution of $\sim 1.5 R_{200}(z = 0)$. This method is employed to adaptively increase the size of the studied region as the galaxy and its hosting dark matter halo grow in size. In order to obtain the centre of the galaxy, we tag the system by finding its position at redshift $z \sim 7$. From that point onwards, at each coarse time-step of RAMSES we re-compute the position of galaxy centre. To do this, we simply obtain the new center of mass of the most central ~ 20 stellar particles in the previous iteration. We use this approach to compute various galaxy properties on-the-fly, with time resolution equivalent to that of the coarse time-stepping of the simulation.

V-band Luminosity The galaxy V-band luminosity (L_V) is obtained by summing the luminosities of all stellar particles falling within the 90% of the halo light-radius. Their mass is converted into luminosity using the stellar population synthesis model of Vazdekis et al. (1996) computed with the revised Kroupa (2001) IMF. Where necessary, the luminosities are inter- and extrapolated in age and metallicity using a bivariate spline. We ignore dust absorption, as its role only becomes critical for intrinsic magnitudes brighter than $M_{AB} \sim -20$ (Ma et al. 2018).

Metallicity Because of the limited number of stars forming in dwarf galaxies, the choice of a representative *mean* [Fe/H] is not a trivial task. As the metallicity distribution is sparsely sampled computing the mode, the peak of the metallicity distribution function can lead to large uncertainties. In Sanati et al. (2022), a method is proposed to determine the mode based on a fitting analytical formula derived from a simple chemical evolution model. The error on [Fe/H] is taken at the maximum of the errors obtained by the different methods, peak and mode.

Velocity dispersion The line-of-sight (LOS) stellar velocity dispersion, σ_{LOS} , is calculated for seven different lines of sight inside a 1 kpc cylindrical radius. The value quoted for each galaxy represents the mean of these values.

4. Results

The setup of our simulations follows the evolution of twelve different spheroidal and ultra-faint dwarf galaxies with final luminosities $\sim 10^4 - 10^6 L_\odot$. Table 2 summarizes the main properties of model galaxies in our fiducial hydrodynamical model B00, at redshift $z = 0$. The galaxy halos are selected from dark matter only cosmological simulation in Revaz & Jablonka (2018). We re-simulate those halos using a zoom-in technique, including a full treatment of baryons described in Section 3. IDs are those of (Revaz & Jablonka 2018, see their Table 1). The seven other columns show the galaxy total V-band luminosity L_V , total stellar mass M_\star , virial mass M_{200} , virial radius R_{200} , mean stellar velocity dispersion σ_{LOS} and peak value of the metallicity distribution function [Fe/H].

4.1. Gas density

In the first set of simulations, the magnetic field is initialized to uniform values, as described in Section 3, and the matter power spectrum is that of the classical Λ CDM paradigm. These simulations are designed to explore the contribution of magnetic fields in shaping the internal structure and ISM of dwarf galaxies. Figure 2 shows the density-weighted projection of gas density in dwarf spheroidal h177 (see Table 2) at redshift $z = 9$ ($\sim 500\text{Myr}$). This corresponds to the intense phase of star formation in dwarf galaxies (Okamoto et al. 2012; Brown et al. 2014; Sacchi et al. 2021; Gallart et al. 2021). M_{gas} shows the gas mass averaged

Halo ID	L_V [$10^5 L_\odot$]	M_\star [$10^5 M_\odot$]	M_{200} [$10^9 M_\odot$]	R_{200} [kpc]	$r_{1/2}$ [kpc]	σ_{LOS} [km/s]	[Fe/H] [dex]
h063	10.63	26.92	3.08	45.3	0.36	9.2	-1.65
h187	4.81	12.47	1.50	35.6	0.31	8.2	-2.00
h111	3.61	9.76	1.61	36.4	0.81	8.8	-1.72
h113	3.40	8.78	1.48	35.5	0.33	7.7	-2.02
h159	2.56	7.08	0.97	30.8	0.90	7.3	-1.73
h134	2.39	6.11	1.35	34.4	0.48	7.0	-2.19
h177	1.62	4.51	0.78	28.6	0.28	6.6	-1.61
h152	1.56	4.10	0.94	30.5	0.25	6.8	-1.88
h190	1.56	4.18	0.66	27.0	0.21	6.7	-1.89
h259	0.78	2.03	0.50	24.8	0.17	6.1	-2.25
h249	0.68	1.82	0.51	24.9	0.22	5.3	-1.95
h277	0.19	0.51	0.52	25.0	0.18	4.9	-2.22

Table 2: Global properties of the 19 halos simulated when only Pop II stars are considered. The first column gives the halo ID following [Revez & Jablonka \(2018\)](#). L_V is the V-band luminosity and M_\star the stellar mass. M_{200} is the virial mass, i.e., the mass inside the virial radius R_{200} . σ_{LOS} is the line-of-sight velocity dispersion and [Fe/H] is the abundance ratio of iron with respect to hydrogen.

over the first 2 Gyr, before this system is completely depleted of gas. The gas mass is measured inside the galactic region (see Section 3.4) which is illustrated by white dashed circles. The magnetic field strength is increasing from left to right.

Magnetic fields may generate additional turbulence and pressure support in the ISM. These twofold effects are shown in Fig. 2. For illustration purpose, we remove B00 and compare all models with B05 with the lowest magnetic strength, which closely resemble the fiducial model. In B10, the pressure support, produced by a weak field of strength 0.10 nG, is unimportant. In this model, the role of magnetic fields in generating turbulence in the ISM is more dominant. For strong fields (B20 and B50), magnetic pressure along with the thermal pressure, acts against the gravitational field and prevents the collapse of gas. It may particularly affect the first stages of galaxy formation, i.e., for $z > 6$. The delay caused in the collapse of the first minihalos leads to the accumulation of gas and a stronger star formation burst. Thus the gravitational field in minihalos is less likely to retain the gas, when it is pushed out by the local stellar feedback. This effect is stronger in low mass dwarf galaxies due to the shallow potential well of their host halos. It leads to a reduction trend in the averaged gas mass with increasing B_λ .

In the second set of simulations, varying the strength of the magnetic field seeds, we additionally include its effect on the modification of the total matter power spectrum, Table 1. These simulations are designed to explore the net effect of magnetic fields through the altered matter power spectrum on the one hand, and the direct magnetically-produced turbulence and pressure, on the other hand.

In the bottom panels of Fig. 2, the amplitude of the primordial fields varies from $B_\lambda = 0.05$ to 0.50 nG. The first two columns correspond to models with a weak magnetism. The gas density maps in these two resemble their counterparts in the first row. Indeed, the impact of weak primordial fields on the matter power spectrum and consequently the buildup of galaxies is slim (see also [Sethi & Subramanian 2005](#); [Sanati et al. 2020](#); [Katz et al. 2021](#)). However, the averaged gas mass is slightly decreased. This is due to the additional perturbations generated by primordial magnetic fields. It causes the collapse of gas to be initiated earlier (approximately 100 Myr), and exhausted in the course of star formation.

Extending B_λ towards higher amplitudes, introduces considerable reformations in the main halo of the galaxy and the num-

ber of its subhalos. When $B_\lambda = 0.20$ nG, from Fig. 1 it appears that the additional perturbations generated by primordial magnetic fields mainly affect halos with the Jeans mass $M_J \leq 10^8 M_\odot$. This impact is projected in Fig. 2, where the number of subhalos in this mass range is noticeably enlarged. Compared to its counterpart in the first row, the gas mass of the main halo is decreased. Yet M_{gas} inside the galactic region, which also contains the satellites, remains approximately equal. The reduction trend in the averaged gas mass with increasing B_λ , formerly observed in the first set of simulations, still holds for B20ps.

When $B_\lambda = 0.50$ nG, from Fig. 1 it appears that the altered matter power spectrum influences the formation of halos with mass $M_J \approx 10^9 M_\odot$. Therefore, in this model, it is essentially the main halo of a dwarf galaxy which is affected. The last panel of Fig. 2 shows that here the gas mass is ~ 100 times higher than its counterpart emerged from the Λ CDM paradigm in the first row. Here, the strong gravitational potential of the central halo, can merge the satellite subhalos.

4.2. The evolution of energy components

In this section, we explore the co-evolution of main contributors to the ISM energy budget, as a dwarf galaxy evolves over time. The three panels in Fig. 3, respectively from left to right, represents the time evolution of the magnetic energy, internal energy and our estimate for the compressional evolution of the magnetic energy. For this plot we use dwarf spheroidal h177, but the outcomes are similar for other halos examined in this work (see Table 2). Note that the gas content within the galaxy halo, at different time steps, is subject to the natural mass growth due to accretions, mergers and outflows. Equally, computing the total energy over time is sensitive to the shape and volume of a galaxy. Therefore, for a fair comparison between different energy factors, we use specific energies

$$\varepsilon_x = \frac{E_x}{M_{\text{gas}}}, \quad (11)$$

as the ratio between the total energy E_x and the gas mass M_{gas} , inside the galactic region (see Section 3.4). The main amplifications of the magnetic energy is expected to occur before $z = 2$ ([Bernet et al. 2008](#)). After this redshift, magnetism is in equipartition with other energy components ([Wolfe et al. 1992](#); [Bernet et al. 2008](#)). Thus we truncate the time evolution of energies in this plot at 2 Gyr. Different lines represent models in Table 1, where the amplitude of B_λ varies from 0.05 – 0.50 nG. Color codes are the same as in Fig. 1. In the top row, the model galaxy is emerging from a classical matter power spectrum, while the strength of the magnetic field varies from $B_\lambda = 0.05$ to 0.50 nG. In the bottom row, the magnetically-induced perturbations by primordial fields are also included.

Magnetic energy In the most left panels, the growth of the specific magnetic energy ε_{mag} , is evaluated versus time. As expected, models which contain strong magnetization ($B_\lambda = 0.20$ and 0.50 nG) demonstrate a more pronounced growth. This trend is notable, both in the unperturbed Λ CDM and the magnetically-perturbed context, in the top and bottom row, respectively. When $B_\lambda = 0.50$ nG in particular, the magnetic energy experience a striking fast growth. This quick buildup of the final magnetic energy from the initial seeds is independent of the initial matter power spectrum, if it is the classical Λ CDM or modified by pri-

Mahsa Sanati, Sergio Martin-Alvarez, Jennifer Schober, Yves Revaz: XXX

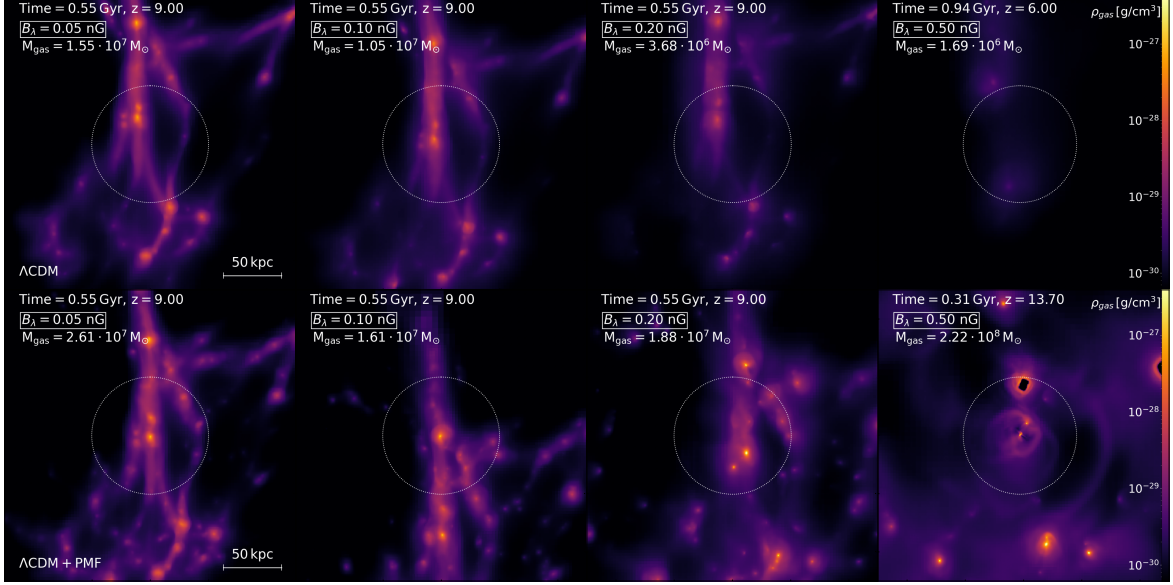


Fig. 2: Gas density projections of dwarf galaxy h111 (see Table 2) at redshift $z = 9$. The strength of the magnetic field is increasing from $B_\lambda = 0.05$ nG on the left to $B_\lambda = 0.50$ nG at the rightmost panels. The upper and lower rows respectively represent all the models in Λ CDM and Λ CDM+PMFs set of simulations (see Table 1). The white circle shows the galactic region (Section 3.4), which is traced in all time steps. The evolution of various galaxy quantities, such as its gas content, is evaluated inside this region with radius ~ 1.5 virial radius of the dark matter halo. Panels have physical sides and depth of 256 kpc. Gas mass represents the average mass of gas in the galactic region for snapshots in the first 2 Gyr.

mordial magnetic fields. However, the growth rate is steeper in models forming from the latter one.

The rate, with which the specific energy increases, correlates with the timescale of the raise, before the magnetic fields start to saturate. A faster growth of the fields is leading to an earlier saturation on time intervals as short as a few hundred Myrs. Both sets of runs, in the top and bottom panels, follow well this scaling. In models which contain a weaker magnetisation ($B_\lambda = 0.05$ and 0.10 nG), the magnetic energy amplification is sustained for slightly longer times.

Internal energy The middle panels show the specific internal energy ε_{int} , as a function of time. In the first setting (see Table 1), the internal energy is reducing progressively when B_λ is elevating from 0.05 to 0.50 nG. This is the direct imprint of the additional pressure support generated by magnetic fields. In these models, magnetism in the ISM prevents the collapse of gas clouds (see the discussion in Section 4.1). These low density gas thus stay cold, which through the course of simulations, leads the ε_{int} to be decreased when raising the amplitude of the magnetic field. The exception is the model with $B_\lambda = 0.10$ nG. As discussed in Section 4.1, here the turbulence that is magnetically generated in the ISM is more prominent than the pressure support produced by this weak field. Another striking feature here is the delay in the growth of internal energy when the magnetic field is of strength 0.20 and 0.50 nG. Indeed, the evolution of the internal energy closely correlates with the density and temperature in the ISM and thus follow the collapse of gas clouds. Therefore, the delay caused by strong fields in the formation of minihalos, affect the time that ε_{int} starts to buildup from its initial value.

Nonetheless, the impact of primordial fields, included in second simulation setup (see Table 1), presents a different trend in the bottom panel compared to one on the top. Here, the rate of energy growth is steeper for higher amplitude of B_λ . In particular, when $B_\lambda = 0.20$ and 0.50 nG the growth of the internal energy is remarkably rapid. This is explicitly because the evolution of dwarf galaxies follow a different track when their halo form out of a modified matter power spectrum. In these models, the formation of more massive minihalos leads to a higher pace of collapse. This in turn influences the pace with which the internal energy is growing. Primordial magnetic fields also accelerate the formation of the first minihalos in a galaxy. As the density increases in the collapse of these gas clouds, the temperature and consequently the internal energy increase with time. This prompts the buildup of specific energy to be initiated in timescales as early as several tens of Myr, when $B_\lambda = 0.50$ nG.

Compressional energy The most right panels show the evolution of the specific compressional energy $\varepsilon_{\text{comp}}$ versus time. This term is obtained from an isotropic adiabatic approximation of the gas collapse. In the initial phases of the formation of a galaxy, the amplitude of the magnetic field scales with the gas density as $B_\lambda^2 \propto \rho_{\text{gas}}^{4/3}$ (see e.g., Rieder & Teyssier 2017). This approximation is ruling the evolution of the frozen-in magnetic field lines, which follow the formation of cosmic structures, in the absence of amplification or decaying processes. For extracting this term in each time step of the simulation, we use

$$E_{\text{comp,cell}}(t) = \frac{d_{\text{cell}}^3}{\frac{4}{3}\pi r_{\text{gal}}^3(t_0)} \times \langle E_{\text{mag,gal}}(t_0) \rangle \times \left(\frac{\rho_{\text{gas,cell}}(t)}{\rho_{\text{gas,gal}}(t_0)} \right)^{4/3}, \quad (12)$$

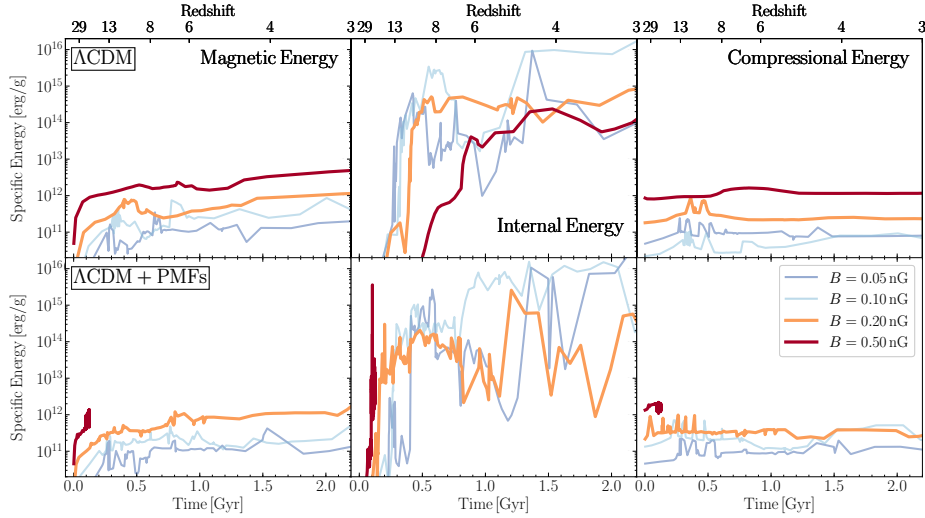


Fig. 3: Comparison of different energy components in the galactic region (white circle in Fig. 2). The upper and lower panels respectively represent all the models in the Λ CDM and the Λ CDM+PMFs set of simulations (see Table 1). Columns correspond from left to right to the time evolution of the specific term of magnetic energy, internal energy, and the estimate for the compressional part of the magnetic energy. The color-codes for B_i is the same as in Fig. 1.

where $\rho_{\text{gas,cell}}$ is the density of gas in each cell of size dx_{cell} . $\langle E_{\text{mag,gal}}(t_0) \rangle$ stands for the average of magnetic energy over the galactic region of radius r_{gal} , estimated at time t_0 when it is in the minimum state. It corresponds to the turnaround point between the expansion of initial perturbations and the beginning of their collapse. This moment, at which the magnetic energy reaches a minimum, marks the accumulation of the baryonic matter and the generation of the first stars in a forming galaxy. Eventually, the total compression term is derived by summing over all cells within the galactic region. It is then divided by the total gas mass in this region to obtain the specific energy. Figure 3 shows that the evolution of compressional energy in time, follows the same trend as the internal term. Expectedly, the growth in the gas density leads to an increase in the final value of $\varepsilon_{\text{comp}}$.

Comparing the growth of magnetic energy and compressional energy, we then explore the signatures of magnetic field amplification. Figure 4 shows the ratio between E_{mag} and E_{comp} as a function of time. As described, the compressional term shows the expected buildup of magnetic fields, when exclusively frozen in the collapse of matter into dark halos. The deviation of E_{mag} from E_{comp} points out the amplification of the magnetic fields inside the galactic region. This may occur through different processes functioning besides the adiabatic magnetic compression, namely the generation of a dynamo in the collapsing gas clouds.

Nevertheless, the deviation of E_{mag} in time from the adiabatic compression evolution can also be explained in the context of powerful supernova feedback events. The supernova shock evacuates the surroundings from gas, thus reducing the E_{comp} . Simultaneously, the supernova winds push the magnetic fields outwards, while keeping them in the galactic region. Therefore the $E_{\text{mag}}/E_{\text{comp}}$ ratio is increasing with time.

In order to unravel the origin of this deviation, we re-simulate h177 in model B20 and B50 (Table 1), deactivating the supernovae feedback. Figure 5 demonstrates this comparison. The

solid and dotted lines respectively corresponds to the runs where the supernovae feedback is set to the fiducial value of $E_{\text{SN}} = 0.40 \cdot 10^{51}$ erg and zero. The steeper growth of magnetic energy compared to the compressional energy, persist in runs with zero feedback. It suggests that the amplification of the magnetic fields is not generated in the process of the supernovae explosion. This reinforces the idea that magnetic fields initialized by a strong seed ($B_i = 0.20$ and 0.50 nG), may grow due to the dynamo amplification, as the galaxy evolves through the gas accretion, collapse of halos and mergers.

4.3. Star formation

In this section, we show the impact of primordial magnetic fields on the star formation history and final stellar mass of dwarf galaxies. From each zoom-in simulation, we first extract the halo corresponding to the reference halo in the fiducial model. Based on the position and particle IDs, we then extract the correspondent halo in other models. The physical quantities of each galaxy such as the stellar mass are computed inside the virial radius R_{200} of the extracted halo.

Figure 6 and 7 display the cumulative mass of stars forming in the first 2.5 Gyr. In each model, the solid line corresponds to the mean value of the stellar mass measured for all model galaxies, listed in Table 2. The dashed lines represents the low mass galaxies that fall in the ultra-faint regime. In the fiducial model B00, shown in dark blue, star formation is quenched in ultra-faint galaxies before 1 Gyr, and in more massive dwarfs before at most 1.5 Gyr.

In the first set of simulations, galaxies are magnetized with a uniform field in the Λ CDM paradigm (see Table 1). As discussed in Section 4.1, in these models, the magnetic pressure counterbalance the gravitational collapse of gas. Specifically in the first Gyr, this additional pressure support affects the star formation history. The delay it induces in the onset of star forma-

Mahsa Sanati, Sergio Martin-Alvarez, Jennifer Schober, Yves Revaz: XXX

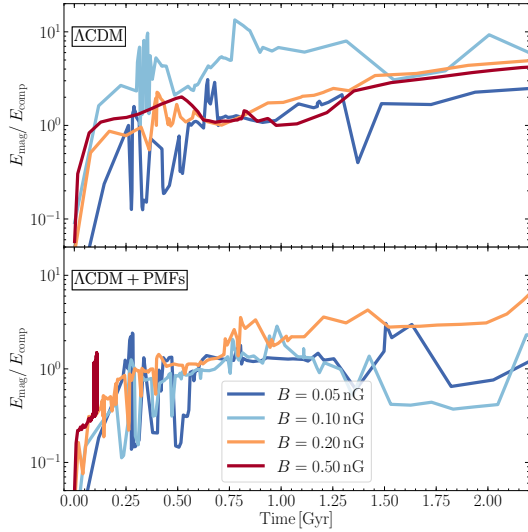


Fig. 4: Time evolution of the ratio of the magnetic energy to the compression energy in the galactic region (white circle in Fig. 2) for all the simulations in the first 2 Gyr. The upper and lower panels respectively corresponds to all the models in Λ CDM and Λ CDM+PMFs settings.

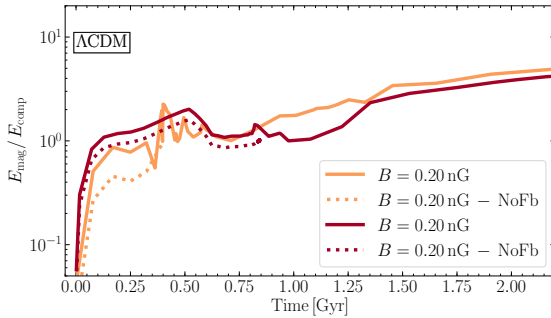


Fig. 5: The comparison of the ratio of the magnetic energy to the compression energy in dwarf galaxy h177 emerging from a Λ CDM matter power spectrum. The solid and dotted lines respectively corresponds to the runs with the fiducial value of supernovae feedback $E_{SNe} = 0.40 \cdot 10^{51}$ erg and zero.

tion is shown in Fig. 6. This feature is beheld for all amplitudes of magnetic field examined. The delay in the birth of first stars, in turn leads to an intense phase of star formation from the accumulated gas. It leads to the depletion of gas reservoir in minihalos and an earlier quench in dwarf galaxies. Especially in ultra-faint dwarfs, the period of forming stars may shrink to less than 500 Myrs.

Consistently, the rate of star formation and the final stellar mass is decreasing with increasing the magnetic field strength. In order to demonstrate this correlation quantitatively, in Fig. 8 we show the final stellar mass of dwarf galaxies as a function of B_λ . Each circle is representative for one galaxy at redshift $z = 0$, color-coded by the virial mass of its dark halo. For both ultra-faints and dwarf spheroidals, the final stellar mass is hardly

modified in the weak models ($B_\lambda = 0.05$ and 0.10 nG). However, the magnetic pressure generated by stronger fields ($B_\lambda = 0.20$ and 0.50 nG) may act strongly against the gravitational field and decrease the final stellar mass by almost one dex. This effect is more severe in low mass galaxies. $B_\lambda = 0.50$ nG may produce a strong pressure support, enough to completely hamper the collapse of minihalos. In our sample of twelve different dwarf galaxies, the density and temperature of gas in six halos remain below the Jeans polytrope to form stellar particles. To include these six halos in Fig. 8, their zero stellar mass is replaced by random values between 5 and $6 \times 10^3 M_\odot$. These halos are marked by sign *no stars* above them.

Using the second set of simulations we examine the primordial impact of magnetic fields on the star formation history of dwarf galaxies. Figure 7 is the same as Fig. 6, but for models which include magnetic fields through the altered matter power spectrum. One striking outcome of these models is an expedited onset of star formation. This stem from the influence of primordial fields in speeding up the formation of first dark halos. This persist for all amplitudes of magnetic field examined. However, it is milder in models with a weak primordial field. From Fig. 1 it appears that the region affected by weakly perturbed models ($B_\lambda = 0.05$ and 0.10 nG) contains halos with the Jeans mass $M_J \simeq 10^5 - 10^7 M_\odot$. In these models, this effect is secondary to the role magnetic fields play in boosting the counteracting pressure in the ISM. Thus the abundance of small minihalos is slightly increased in the weakly perturbed models, though the gas content in most of these minihalos is not sufficiently massive to form stars.

Raising the amplitude of primordial fields, the region of effect in the modified matter power spectrum is shifting towards more massive halos, Fig. 1. When $B_\lambda = 0.20$ nG, the abundance of subhalos with $M_J \sim 10^8 M_\odot$ increases. The gas content in minihalos of this mass range is in accord with the Jeans criteria to form stellar particles. When $B_\lambda = 0.50$ nG, the main halo of each dwarf galaxy grows in mass. A stronger gravitational field in this case affects the collapse of gas and the star formation history. Contrary to lower amplitudes of B_λ , here the primordial effect of magnetic fields dominates its role in the ISM. The net effect is to accelerate the formation of first minihalos. Figure 7 shows that in these two strongly perturbed models the star formation is initiated at extremely high redshifts. For $B_\lambda = 0.20$ and 0.50 nG, galaxies on average start to form stars respectively at redshift $z \sim 42$ and $z \sim 100$. These two are in disagreement with the constraints that are observationally obtained for the history of reionization (Bolton & Haehnelt 2007; Loeb & Haiman 1997; Fan et al. 2000; Hu et al. 1999).

Along this line, in the evolution of dwarf galaxies, magnetic pressure plays a less important role in models which are strongly perturbed by primordial fields. This effect, which persist till the end of the star forming phase, is shown in Fig. 8. Despite the steady additional pressure against the gravitational collapse, a higher number of minihalos, with more massive gas contents, lead to a higher stellar mass at redshift $z = 0$. This imprint is more striking in low mass dwarf galaxies which do not form stars in model B50. The inclusion of primordial fields in these models leads to the formation of bright dwarf galaxies, comparable to those in the fiducial model.

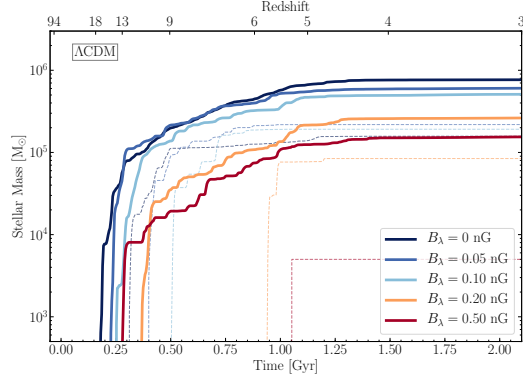


Fig. 6: Cumulative stellar mass during the first 2 Gyr for different models with magnetic field strength varying from $B_\lambda = 0.05$ to $B_\lambda = 0.50$ nG, compared with the model without magnetic field. Solid lines show the mean stellar mass of all galaxies, and dashed lines show the mean stellar mass in the UFD models.

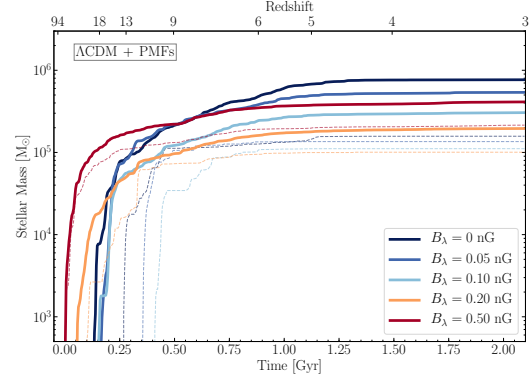


Fig. 7: Same as Fig. 6 but in addition to initial seeds of magnetic field, the contribution of magnetic spectrum in the Λ CDM matter power spectrum is also considered in the initial conditions.

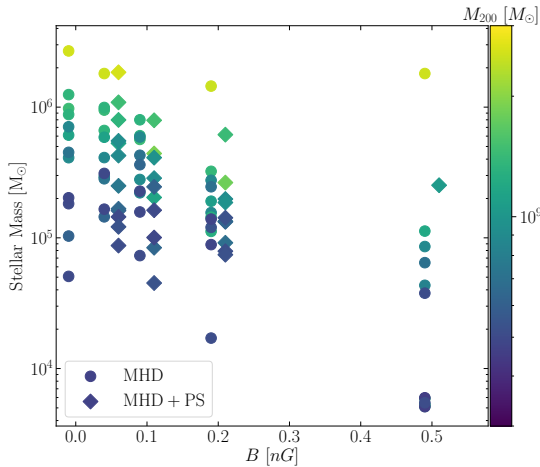


Fig. 8: Some suggestions that come to mind (you can ignore them) are to separate this figure into two panels, one of top of each other, showing your circles in one and diamonds in the other. Additionally, if the trend is monotonic (or almost) with B strength, maybe you can also join the points corresponding to the same galaxy, so we can see visually how M_{star} decreases (?) with B . Stellar mass of each galaxy at redshift $z = 0$ color-coded by the virial mass of the dark halo, is demonstrated for varying magnetic field strengths. Each triangle represents one galaxy simulated in the MHD suite (MHD model). In the simulation of galaxies shown as squares (MHD + PS model), in addition to magneto-hydrodynamics the contribution of primordial fields in the matter power spectrum is also considered. The stellar mass of six halos which do not form any stars is shown at $M_\star < 10^4 M_\odot$ instead of $0 M_\odot$.

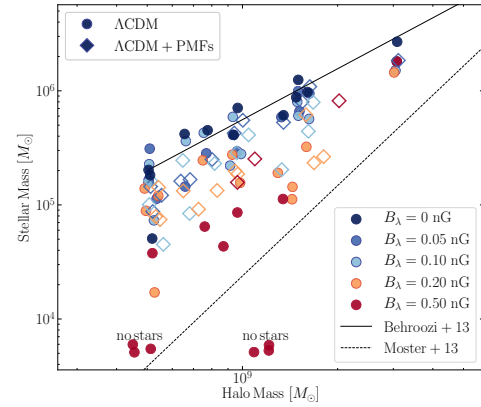


Fig. 9: Stellar mass to halo mass at redshift $z = 0$ is compared to abundance matching relation given in Behroozi et al. (2013) and Moster et al. (2013) in solid and dashed lines, respectively. In order to include six halos which do not form any stars in the plot, their stellar masses are shown at $M_\star \sim 10^3 M_\odot$.

4.4. Scaling relations

In this section, we explore the impact of primordial magnetic fields on the global properties of dwarf galaxies, namely, the V-band stellar luminosity L_V , the stellar mass M_\star , the virial mass M_{200} , the stellar LOS velocity dispersion σ_{LOS} , and the mode of the stellar metallicity distribution function $[\text{Fe}/\text{H}]$. The method for calculating each quantity is described in Section 3.4.

4.4.1. Stellar mass-halo mass

Figure 9 shows the stellar mass as a function of halo mass for our simulated galaxies at redshift $z = 0$. We include the results from abundance matching by Behroozi et al. (2013) and Moster et al. (2013), as solid and dashed lines, respectively. Both are extrapolated to $5 \cdot 10^8 M_\odot$, in order to include the mass range

Mahsa Sanati, Sergio Martin-Alvarez, Jennifer Schober, Yves Revaz: XXX

of dwarf galaxies. In the fiducial model, the final stellar masses are between $\sim 10^4 - 10^6 M_\odot$. All galaxies in this model are well within the expected values for the final halo mass, between $5 \cdot 10^8 - 5 \cdot 10^9 M_\odot$. Our feedback prescription does not include stellar winds, local radiation from young stars, photo-electric heating, and cosmic rays. These energetic sources, besides supernovae, may decrease the final stellar mass of our galaxies.

Halos in the first set of simulations, emerging from a Λ CDM paradigm, are shown in colored circles. Magnetism of low amplitudes ($B_\lambda = 0.05$ and 0.10 nG) does not dramatically influence their location compared to the fiducial model. The reverse scaling of the stellar mass with the strength of the field, observed in Section 4.3 for magnetism of higher amplitudes, persists in this relation as well. For a given halo mass, the final stellar mass is decreasing with increasing B_λ . Low mass halos which do not form stars in the extreme model, where $B_\lambda = 0.50$ nG (see Section 4.3 for a detailed discussion), are marked by the sign *no stars*. To include these halos in the plot, their zero stellar mass is replaced by a random value between 5 and $6 \times 10^3 M_\odot$.

Halos in the second set of simulations, emerging from a modified Λ CDM paradigm, are shown in colored diamonds. The global properties of galaxies are predicted to undergo only minor changes in the weakly perturbed models (Sanati et al. 2020; Katz et al. 2021). When $B_\lambda = 0.05$ and 0.10 nG, all halos closely resemble their counterparts in the fiducial model. However, the final stellar mass in the strongly perturbed models recurrently show that the primordial impact of magnetic fields dominates over the impact of magnetic pressure in the ISM. Galaxies which do not form stars in the $B0.50$ model, evolve into bright dwarfs with $M_\star > 10^3 M_\odot$, when the primordial fields are introduced through the matter power spectrum. The impact of this latter on the formation and gas content of halos is stronger than the pressure support produced by magnetic fields, affecting the gas collapse in the ISM.

Since the abundance matching relation is not well constrained in the regime of dwarf galaxies, none of the models is ruled out through this comparison. It is indeed likely that the same halo mass supports orders of magnitude differences in the stellar mass depending on the environmental effects and specific history of each dwarf galaxy. This may lead to a large scatter in this low mass regime.

4.4.2. Luminosity-velocity dispersion

Figure 10 shows the V-band luminosity L_V versus the LOS velocity dispersion for each galaxy at redshift $z = 0$. We compare those with the observed galaxy sample obtained from the Local Group and Nearby Dwarf Galaxies data base of McConnachie (2012), which are represented by grey squares and triangles respectively for the Milky Way and Andromeda satellites.

As discussed in Section 4.4.1, increasing B_λ in the first set of simulations, the final stellar mass decreases for a given halo mass. Therefore, in models with a strong field, systems are significantly fainter than their analogues in the fiducial model. When $B_\lambda = 0.20$ and 0.50 nG, the final luminosity of dwarfs is reduced by $0.5 - 1.0$ dex, in comparison to the model without magnetic fields. Due to a lower star formation rate in these models, the dynamical components, i.e. the LOS velocity dispersion, in each halo are also slightly decreased.

With the inclusion of primordial magnetic fields through the matter power spectrum, the first minihalos start clumping and accreting gas earlier. This in turn produce a deeper potential well and prevents the gas reservoir to be pushed out by the UV-background and local supernovae feedback. It mainly influences

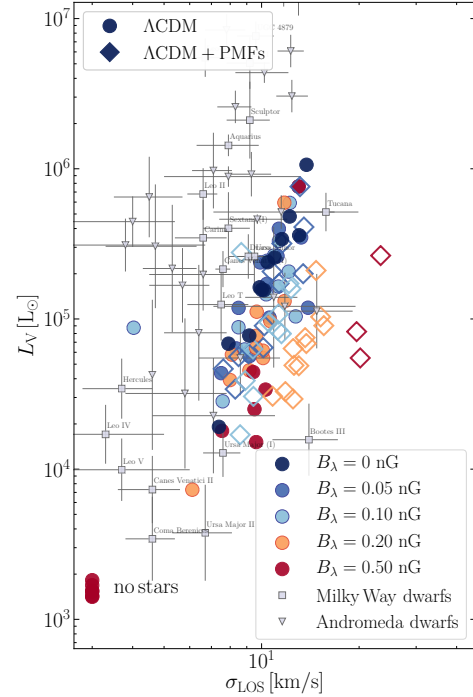


Fig. 10: V-band luminosity as a function of line-of-sight velocity dispersion in each model galaxy is compared to the observational data of Milky Way and M31 satellites in black squares and triangles, respectively. In order to include six halos which do not form any stars in the plot, their luminosities are shown at $L_V \sim 10^3 L_\odot$. There's a very interesting change in correlation (or the offset) between L and σ with B . Maybe it'd be useful to have this plot shown in three panels. One as presented here, and two additional ones, just showing either circles or diamonds. In those latter two, you could also maybe plot a line for the power-law correlation at each B .

the evolution of low mass dwarf galaxies. Contrary to the fiducial model, where the star formation is quenched during the epoch of reionization, in models with a strong primordial field, the star forming phase is more extended. Due to this latter, simulated dwarfs grow into more massive and brighter galaxies at redshift $z = 0$, with a younger stellar population. Therefore, not only the luminosity, but also the dynamics of the simulated galaxies are influenced. In the strongly perturbed models, the LOS velocity dispersion of each halo is extremely larger than its counterpart in the fiducial model.

4.4.3. Metallicity-Luminosity

Figure 11 shows the metallicity (traced by $[\text{Fe}/\text{H}]$) as a function of V-band luminosity for each simulated galaxy. Our observational sample is the same as in Fig. 10, which are represented by grey squares. Here our sample includes only confirmed ultra-faint dwarfs that benefit from medium resolution spectroscopy with metallicity derived either from spectral synthesis or Calcium triplet (CaT) calibration. In the fiducial model B00, the

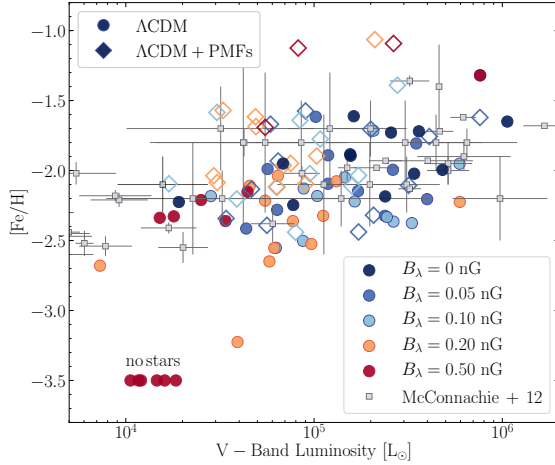


Fig. 11: Mean metallicity vs. stellar V-band luminosity. Each object correspond to one model galaxy for which $[\text{Fe}/\text{H}]$ is computed as the median of the galaxy stellar metallicity distribution function. Milky Way and Andromeda satellites are identified with black squares. In order to include six halos which do not form any stars in the plot, their luminosities are shown at $L_V \sim 10^3 L_\odot$.

mode of the stellar metallicity distribution function for all simulated galaxies lies between -1.5 and -2.5 . Their total stellar luminosities are within $10^4 - 10^5 L_\odot$, in a good agreement with the observational data.

Each colored circle represents a dwarf galaxy forming from the first simulation setting (see Table 1). Here with introducing the magnetic fields, as expected from a reduced rate of star formation (see Section 4.3), the final metallicity deviates towards lower values. In these models, nucleosynthesis yields, produced by a less abundant stellar population, are less efficient to metal-enrich the ISM. This in turn affects the cooling and star formation rate. Thus the simulated galaxies eventually become fainter and more metal-poor. Here the presence of a strong field ($B_\lambda = 0.50 \text{ nG}$) is driving the dwarf spheroidal models toward the ultra-faint regime with $L_V < 10^5 L_\odot$.

Colored diamonds represent dwarf galaxies which form from the second simulation setting (see Table 1). Here the imprint of primordial fields essentially compensates over the contribution of magnetic fields in the energy budget. This latter angles off both the luminosity and metallicity of dwarf models. For $B_\lambda = 0.50 \text{ nG}$, the $z = 0$ properties of simulated galaxies are representations of brighter and more metal-rich dwarfs than those in the fiducial model. The high $[\text{Fe}/\text{H}]$ of these luminous dwarfs deviate from the observed metallicity-luminosity relation in the Local Group.

4.4.4. Size-Luminosity

Figure 12 shows the stellar half-light radius ($r_{1/2}$) as a function of the V-band luminosity (L_V) at redshift $z = 0$. As in Fig. 11, Local Group dwarfs, compiled from McConnachie (2012), are illustrated in gray squares with error bars. Galaxies simulated in the fiducial model, cover a wide range in luminosity and size, in

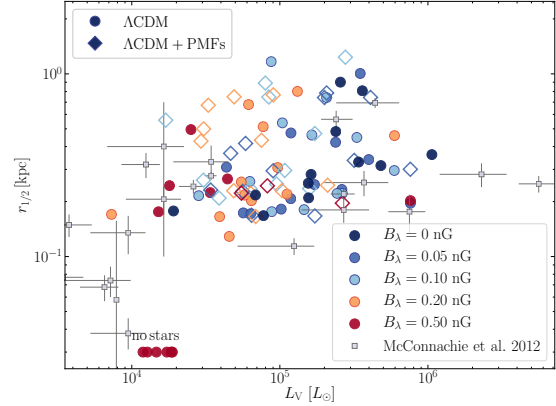


Fig. 12: Half-light radius as a function of V-band luminosity of each model galaxy at redshift $z = 0$ is compared to Milky Way and M31 satellites in black squares, given by McConnachie (2012). In order to include six halos which do not form any stars in the plot, their luminosities are shown at $L_V \sim 10^3 L_\odot$.

accordance with the observed dwarfs. The half light sizes in this model spread between $170 - 900 \text{ pc}$.

Galaxies in the first set of simulations (see Table 1) are shown in colored circles. As discussed in Section 4.4.2, the pressure support produced by magnetic fields affect the kinematics of dwarf galaxies. The LOS velocity dispersion is decreasing with increasing the amplitude of the magnetic field. In these models, stellar populations may form in a more concentrated manner. Thus the size of the simulated galaxies shrink, due to a lower rate of dynamical perturbations. This effect is more visible when the magnetic field is stronger, i.e., for $B_\lambda = 0.20$ and 0.50 nG . In the low mass dwarfs, the smaller size joined with the lower V-band luminosity at redshift $z = 0$ deviates model galaxies from their fiducial counterparts.

Colored diamonds show simulated dwarfs in the second set of simulations. In these models, stellar populations are more dispersed in the halo of each galaxy. This is the direct imprint of the primordial fields, increasing the stellar LOS velocity dispersion of dwarfs. This effect is specially visible when $B_\lambda = 0.20$ and 0.50 nG . In these models, the half light sizes of the simulated galaxies are increased. The combination of this latter with the enlarged V-band luminosity at redshift $z = 0$ result in the formation of galaxies incompatible with observations.

In summary, the $z = 0$ properties of halos emerging from our fiducial model, provide a good representation of dwarf galaxies in the Local Group. Their luminosities, sizes, metallicities and kinematics are well reproduced by our simulations in B00. We base our predictions for the impact of the magnetic fields on this reassuring finding. As regards to our results, we can confirm that primordial magnetic fields with strengths $B_\lambda > 0.10 \text{ nG}$ significantly impact the physical observables of dwarf galaxies.

Mahsa Sanati, Sergio Martin-Alvarez, Jennifer Schober, Yves Revaz: XXX

5. Discussion & Conclusions

We have studied the impact of primordial magnetic fields on the formation and evolution of dwarf galaxies. We performed cosmological zoom-in magneto-hydrodynamical simulations from redshift $z = 200$ to zero of twelve halos hosting dwarfs with V-band luminosities between $\sim 10^4 - 10^6 L_\odot$. All simulations are generated using our modified version of the constrained transport MHD `RAMSES` code. We employed two different simulation setups. In the first, a uniform magnetic field is initialized with a given strength and the matter power spectrum is that of the classical Λ CDM paradigm. In the second, in addition to varying the strength of magnetic fields, we include the effect of a Gaussian random primordial field on the matter distribution through the modification of the total matter power spectrum. The former is designed to study the direct impact of magnetism on the ISM of small mass galaxies, while the latter is useful to explore the net effect of magnetic fields through the altered matter power spectrum on the one hand, and the direct magnetically-produced turbulence and pressure support, on the other hand.

Depending on the amplitude, each magnetic field model affects a distinct mass range of dark matter halos hosting dwarf galaxies. All the primordial magnetic fields examined in our models are of strength allowed by cosmological constraints (listed in section 1). We varied the amplitude of the magnetic field in the range $B_\lambda = 0.05 - 0.50$ nG, while keeping the spectral index constant at $n_B = -2.9$. Our main results can be summarized as follows:

- In a Λ CDM cosmological framework, magnetic fields of initial strength $B_\lambda \geq 0.10$ nG, have a non-negligible contribution in shaping the evolution of dwarf galaxies. The magnetically-produced pressure support not only delays the collapse of gas clouds, but in the presence of strong fields prevents the formation of minihalos altogether.
- In a cosmological setup evolved from a Λ CDM+PMFs initial conditions, the main halo of a dwarf galaxy and the number of its subhalos are influenced. When halos, that are affected by primordial fields, are in the Jeans mass range $M_J \leq 10^8 M_\odot$, the gas is distributed in the higher number of these low mass subhalos. While if the halo mass range affected, contains the Jeans mass of the main halo of a dwarf galaxy $M_J \approx 10^9 M_\odot$, the gas content in the central halo is increased. This strong gravitational potential can merge the satellite subhalos.
- After the delay caused by magnetic pressure in the birth of first stars, the gravitational field of low mass dark halos is unlikely to retain the gas, when it is pushed out by the UV-radiation during the epoch of reionization. This leads to the depletion of gas reservoir in minihalos and an earlier quench of star formation. In our sample of twelve different dwarf galaxies, the density and temperature of gas in six halos remain below the MTT criteria to form stellar particles. Nonetheless, the primordial magnetic fields speed up the formation of the first dark matter minihalos, leading to an earlier and higher rate of star formation.
- The observable properties of dwarf galaxies at redshift $z = 0$ showcase the impact of magnetic fields on their star formation history and kinematics. In general, the imprint of primordial fields essentially dominates over the contribution of magnetic fields in the energy budget. Dwarf galaxies, forming in a Universe with a strong primordial magnetic field, on average are $\sim 80\%$ brighter and have a $\sim 50\%$ higher velocity dispersion than galaxies of similar halo mass forming in the simulations with the same B_λ but a different initial

condition (Λ CDM power spectrum in this case). Due a more extended and more efficient star formation, the $z = 0$ dwarfs are representations of luminous and metal-rich incompatible with the observed Local Group scaling relations.

- Simulations which contain a strong magnetization ($B_\lambda = 0.20$ and 0.50 nG) serve as evidence for a pronounced growth of the magnetic energy. This steep increase leads to the timescale of the magnetic field saturation to be as short as a few hundreds of Myr. These trends are independent of the initial matter power spectrum, regardless of whether it is the classical Λ CDM or modified by primordial magnetic fields. However, the growth rate is steeper in models forming from the latter one.
- In our simulations, the buildup of magnetic energy in time deviates from the evolution of magnetic fields in an adiabatic spherical collapse, or compressional amplification. This latter is not driven by the supernovae feedback, suggesting that the amplification of the magnetic energy is not provoked in the course of the supernovae explosion. Therefore, it supports the growth of magnetic fields initialized by a strong seed ($B_\lambda = 0.20$ and 0.50 nG) due to the dynamo amplification.

In summary the main conclusion of this paper is that the impact of primordial magnetic fields in initiating the structure formation dominates their later-time contribution in generating turbulence and pressure support in the ISM. Although this latter have a severe impact on the physical properties of the small mass dwarf galaxies, primordial fields through the modifications of the matter power spectrum dramatically impact the initial stages of the formation of dwarf galaxies.

Acknowledgements.

References

- Adshad, P., Giblin, John T., J., Scully, T. R., & Sfakianakis, E. I. 2016, *J. Cosmology Astropart. Phys.*, 2016, 039
- Banerjee, R. & Jedamzik, K. 2004, *Phys. Rev. D*, 70, 123003
- Beck, R. 2001, *Space Sci. Rev.*, 99, 243
- Beck, R. 2007, *A&A*, 470, 539
- Beck, R. 2015a, *A&A Rev.*, 24, 4
- Beck, R. 2015b, *A&A*, 578, A93
- Beck, R. & Wielebinski, R. 2013, *Magnetic Fields in Galaxies*, ed. T. D. Oswalt & G. Gilmore, Vol. 5, 641
- Behroozi, P. S., Wechsler, R. H., & Conroy, C. 2013, *ApJ*, 770, 57
- Bernert, M. L., Miniati, F., Lilly, S. J., Kronberg, P. P., & Dessauges-Zavadsky, M. 2008, *Nature*, 454, 302
- Bolton, J. S. & Haehnelt, M. G. 2007, *MNRAS*, 382, 325
- Boyarsky, A., Fröhlich, J., & Ruchayskiy, O. 2012a, *Phys. Rev. Lett.*, 108, 031301
- Boyarsky, A., Fröhlich, J., & Ruchayskiy, O. 2012b, *Phys. Rev. Lett.*, 108, 031301
- Boylan-Kolchin, M., Bullock, J. S., & Kaplinghat, M. 2011, *MNRAS*, 415, L40
- Boylan-Kolchin, M., Bullock, J. S., & Kaplinghat, M. 2012, *MNRAS*, 422, 1203
- Brandenburg, A., Kahnishvili, T., Mandal, S., et al. 2017a, *Phys. Rev. D*, 96, 123528
- Brandenburg, A., Schober, J., Rogachevskii, I., et al. 2017b, *ApJ*, 845, L21
- Brown, T. M., Tumlinson, J., Geha, M., et al. 2014, *ApJ*, 796, 91
- Bullock, J. S. & Boylan-Kolchin, M. 2017, *ARA&A*, 55, 343
- Clarke, T. E., Kronberg, P. P., & Böhringer, H. 2001, *ApJ*, 547, L111
- Domcke, V., von Harling, B., Morgante, E., & Mukaida, K. 2019, *J. Cosmology Astropart. Phys.*, 2019, 032
- Durrer, R. & Neronov, A. 2013, *A&A Rev.*, 21, 62
- Durrive, J. B. & Langer, M. 2015, *MNRAS*, 453, 345
- Fan, X., White, R. L., Davis, M., et al. 2000, *AJ*, 120, 1167
- Federrath, C. & Klessen, R. S. 2012, *Astrophysical Journal*, 761, 156
- Ferland, G. J., Korista, K. T., Verner, D. A., et al. 1998, *Publications of the Astronomical Society of the Pacific*, 110, 761
- Fletcher, A., Beck, R., Shukurov, A., Berkhuijsen, E. M., & Horellou, C. 2011, *MNRAS*, 412, 2396

- Fromang, S., Hennebelle, P., & Teyssier, R. 2006, *A&A*, 457, 371
- Fromang, S., Hennebelle, P., & Teyssier, R. 2006, *Astronomy & Astrophysics*, 457, 371
- Fujita, T. & Durrer, R. 2019, *J. Cosmology Astropart. Phys.*, 2019, 008
- Gallart, C., Monelli, M., Ruiz-Lara, T., et al. 2021, *ApJ*, 909, 192
- Giovannini, M. & Shaposhnikov, M. 2000, *Phys. Rev. D*, 62, 103512
- Gopal, R. & Sethi, S. K. 2003, *Journal of Astrophysics and Astronomy*, 24, 51
- Govoni, F. & Ferretti, L. 2004, *International Journal of Modern Physics D*, 13, 1549
- Grasso, D. & Rubinstein, H. R. 2001, *Phys. Rep.*, 348, 163
- Grønnow, A., Tepper-García, T., & Bland-Hawthorn, J. 2018, *ApJ*, 865, 64
- Haardt, F. & Madau, P. 1996, *The Astrophysical Journal*, 461, 20
- Hahn, O. & Abel, T. 2011, *MNRAS*, 415, 2101
- Hanayama, H., Takahashi, K., Kotake, K., et al. 2005, *ApJ*, 633, 941
- Hogan, C. J. 1983, *Physics Letters B*, 133, 172
- Hu, E. M., McMahon, R. G., & Cowie, L. L. 1999, *ApJ*, 522, L9
- Ichiki, K. & Takahashi, K. 2006, *Astronomical Herald*, 99, 568
- Iffrig, O. & Hennebelle, P. 2017, *A&A*, 604, A70
- Jedamzik, K., Katalinić, V., & Olinto, A. V. 1998, *Phys. Rev. D*, 57, 3264
- Jedamzik, K., Katalinić, V., & Olinto, A. V. 2000, *Phys. Rev. Lett.*, 85, 700
- Jedamzik, K. & Saveliev, A. 2019, *Phys. Rev. Lett.*, 123, 021301
- Kahnishvili, T., Tevzadze, A. G., Brandenburg, A., & Neronov, A. 2013, *Phys. Rev. D*, 87, 083007
- Kahnishvili, T., Tevzadze, A. G., Sethi, S. K., Pandey, K., & Ratra, B. 2010, *Phys. Rev. D*, 82, 083005
- Kandus, A., Kunze, K. E., & Tsagas, C. G. 2011, *Phys. Rep.*, 505, 1
- Katz, H., Martin-Alvarez, S., Rosdahl, J., et al. 2021, *MNRAS*, 507, 1254
- Kim, E.-J., Olinto, A. V., & Rosner, R. 1996, *ApJ*, 468, 28
- Kimm, T. & Cen, R. 2014, *Astrophysical Journal*, 788, 121
- Kimm, T., Katz, H., Haehnelt, M., et al. 2017, *Monthly Notices of the Royal Astronomical Society*, 466, stx052
- Klypin, A., Kravtsov, A. V., Valenzuela, O., & Prada, F. 1999, *ApJ*, 522, 82
- Knebe, A., Wagner, C., Knollmann, S., Dieckhoff, T., & Krause, F. 2009, *ApJ*, 698, 266
- Koh, D., Abel, T., & Jedamzik, K. 2021, *ApJ*, 909, L21
- Körtgen, B., Banerjee, R., Pudritz, R. E., & Schmidt, W. 2019, *MNRAS*, 489, 5004
- Kroupa, P. 2001, *Monthly Notices of the Royal Astronomical Society*, 322, 231
- Kulsrud, R. M. & Zweibel, E. G. 2008, *Reports on Progress in Physics*, 71, 046901
- Kunze, K. E. & Komatsu, E. 2014, *JCAP*, 01, 009
- Loeb, A. & Haïman, Z. 1997, *ApJ*, 490, 571
- Ma, X., Hopkins, P. F., Garrison-Kimmel, S., et al. 2018, *Monthly Notices of the Royal Astronomical Society*, 478, 1694
- Mao, S. A., Carilli, C., Gaensler, B. M., et al. 2017, *Nature Astronomy*, 1, 621
- Marinacci, F. & Vogelsberger, M. 2016, *MNRAS*, 456, L69
- Martin, J. & Yokoyama, J. 2008, *J. Cosmology Astropart. Phys.*, 2008, 025
- Martin-Alvarez, S., Devriendt, J., Slyz, A., & Teyssier, R. 2018, *Monthly Notices of the Royal Astronomical Society*, 479, 3343
- Martin-Alvarez, S., Slyz, A., Devriendt, J., & Gómez-Guijarro, C. 2020, *MNRAS*, 495, 4475
- Martin-Alvarez, S., Slyz, A., Devriendt, J., & Gómez-Guijarro, C. 2020, *Monthly Notices of the Royal Astronomical Society*, 495, 4475
- McBride, J. & Heiles, C. 2013, *ApJ*, 763, 8
- McConnachie, A. W. 2012, *AJ*, 144, 4
- Moore, B., Ghigna, S., Governato, F., et al. 1999, *ApJ*, 524, L19
- Moster, B. P., Naab, T., & White, S. D. M. 2013, *MNRAS*, 428, 3121
- Naoz, S. & Narayan, R. 2013, *Phys. Rev. Lett.*, 111, 051303
- Navarro, J. F., Frenk, C. S., & White, S. D. M. 1996, *ApJ*, 462, 563
- Navarro, J. F., Frenk, C. S., & White, S. D. M. 1997, *ApJ*, 490, 493
- Neronov, A. & Vovk, I. 2010, *Science*, 328, 73
- Oñorbe, J., Boylan-Kolchin, M., Bullock, J. S., et al. 2015, *MNRAS*, 454, 2092
- Okamoto, S., Arimoto, N., Yamada, Y., & Onodera, M. 2012, *ApJ*, 744, 96
- Padoan, P. & Nordlund, Å. 2011, *ApJ*, 730, 40
- Padoan, P. & Nordlund, A. 2011, *Astrophysical Journal*, 730, 40
- Pakmor, R., Gómez, F. A., Grand, R. J. J., et al. 2017, *Monthly Notices of the Royal Astronomical Society*, 469, 3185
- Pandey, K. L., Choudhury, T. R., Sethi, S. K., & Ferrara, A. 2015, *MNRAS*, 451, 1692
- Pandey, K. L. & Sethi, S. K. 2012, *ApJ*, 748, 27
- Pandey, K. L. & Sethi, S. K. 2013, *ApJ*, 762, 15
- Paoletti, D., Chluba, J., Finelli, F., & Rubiño-Martín, J. A. 2019, *MNRAS*, 484, 185
- Pawlowski, M. S. & Kroupa, P. 2013, *MNRAS*, 435, 2116
- Pillepich, A., Springel, V., Nelson, D., et al. 2018, *MNRAS*, 473, 4077
- Planck Collaboration, Adam, R., Aghanim, N., et al. 2016, *A&A*, 596, A108
- Planck Collaboration, Ade, P. A. R., Aghanim, N., et al. 2015, *A&A*, 582, A29
- Rasera, Y. & Teyssier, R. 2006, *Astronomy & Astrophysics*, 445, 1
- Ratra, B. 1992a, *ApJ*, 391, L1
- Ratra, B. 1992b, *ApJ*, 391, L1
- Reiners, A. 2012, *Living Reviews in Solar Physics*, 9, 1
- Revaz, Y. & Jablonka, P. 2018, *A&A*, 616, A96
- Rieder, M. & Teyssier, R. 2017, *MNRAS*, 472, 4368
- Robishaw, T., Quataert, E., & Heiles, C. 2008, *ApJ*, 680, 981
- Rogachevskii, I., Ruchayskiy, O., Boyarsky, A., et al. 2017, *ApJ*, 846, 153
- Rosen, A. & Bregman, J. N. 1995, *The Astrophysical Journal*, 440, 634
- Ryu, D., Kang, H., Cho, J., & Das, S. 2008, *Science*, 320, 909
- Sacchi, E., Richstein, H., Kallivayalil, N., et al. 2021, *ApJ*, 920, L19
- Safarzadeh, M. 2018, *MNRAS*, 479, 315
- Sanati, M., Jeanquartier, F., Revaz, Y., & Jablonka, P. 2022, *arXiv e-prints*, arXiv:2206.11351
- Sanati, M., Revaz, Y., Schober, J., Kunze, K. E., & Jablonka, P. 2020, *arXiv e-prints*, arXiv:2005.05401
- Schmidt, M. 1959, *The Astrophysical Journal*, 129, 243
- Schober, J., Rogachevskii, I., Brandenburg, A., et al. 2018, *ApJ*, 858, 124
- Schober, J., Schleicher, D. R. G., & Klessen, R. S. 2013, *A&A*, 560, A87
- Sethi, S. K. & Subramanian, K. 2005, *MNRAS*, 356, 778
- Shaw, J. R. & Lewis, A. 2010, *Phys. Rev. D*, 81, 043517
- Shaw, J. R. & Lewis, A. 2012, *Phys. Rev. D*, 86, 043510
- Silk, J. 1968, *ApJ*, 151, 459
- Stevenson, D. J. 2010, *Space Sci. Rev.*, 152, 651
- Subramanian, K. & Barrow, J. D. 1998, *Phys. Rev. Lett.*, 81, 3575
- Tabatabaei, F. S., Krause, M., Fletcher, A., & Beck, R. 2008, *A&A*, 490, 1005
- Tashiro, H., Silk, J., Langer, M., & Sugiyama, N. 2009, *MNRAS*, 392, 1421
- Tegmark, M. & Zaldarriaga, M. 2002, *Phys. Rev. D*, 66, 103508
- Teyssier, R. 2002, *Astronomy & Astrophysics*, 385, 337
- Teyssier, R., Fromang, S., & Dormy, E. 2006, *Journal of Computational Physics*, 218, 44
- Teyssier, R., Fromang, S., & Dormy, E. 2006, *Journal of Computational Physics*, 218, 44
- Trebitsch, M., Blaizot, J., Rosdahl, J., Devriendt, J., & Slyz, A. 2017, *Monthly Notices of the Royal Astronomical Society*, 470, 224
- Turner, M. S. & Widrow, L. M. 1988a, *Phys. Rev. D*, 37, 2743
- Turner, M. S. & Widrow, L. M. 1988b, *Phys. Rev. D*, 37, 2743
- Vachaspati, T. 1991, *Physics Letters B*, 265, 258
- Vazdekis, A., Casuso, E., Peletier, R. F., & Beckman, J. E. 1996, *ApJS*, 106, 307
- Vazza, F., Brüggemann, M., Gheller, C., & Wang, P. 2014, *Monthly Notices of the Royal Astronomical Society*, 445, 3706
- Vogt, C. & Enßlin, T. A. 2005, *A&A*, 434, 67
- Wagstaff, J. M. & Banerjee, R. 2015, *Phys. Rev. D*, 92, 123004
- Wasserman, I. 1978a, *ApJ*, 224, 337
- Wasserman, I. M. 1978b, PhD thesis, HARVARD UNIVERSITY.
- Widrow, L. M. 2002, *Reviews of Modern Physics*, 74, 775
- Wise, J. H., Turk, M. J., Norman, M. L., & Abel, T. 2012, *ApJ*, 745, 50
- Wolfe, A. M., Lanzetta, K. M., & Oren, A. L. 1992, *ApJ*, 388, 17
- Zamora-Avilés, M., Vázquez-Semadeni, E., Körtgen, B., Banerjee, R., & Hartmann, L. 2018, *MNRAS*, 474, 4824
- Zucca, A., Li, Y., & Pogosian, L. 2017, *Phys. Rev. D*, 95, 063506

Chapter 7

First stars in the faintest dwarf galaxies

The next chapter corresponds to a first author paper published during my PhD thesis in Astronomy & Astrophysics Journal [AA/2022/44309](#)

How much metal did the first stars provide to the ultra-faint dwarfs?

Mahsa Sanati¹, Fabien Jeanquartier¹, Yves Revaz¹, Pascale Jablonka^{1,2}

¹ Institute of Physics, Laboratory of Astrophysics, École Polytechnique Fédérale de Lausanne (EPFL), 1290 Sauverny, Switzerland
e-mail: mahsa.sanati@epfl.ch

² GEPI, CNRS UMR 8111, Observatoire de Paris, PSL University, 92125 Meudon, Cedex, France

Received: XXXX; accepted: YYYY

ABSTRACT

Numerical simulations of dwarf galaxies have so far failed to reproduce the observed metallicity-luminosity relation, down to the regime of ultra-faint dwarfs (UFDs). We address this issue by exploring how the first generations of metal-free stars (Pop III) could help increase the mean metallicity ([Fe/H]) of those small and faint galaxies. We ran zoom-in chemo-dynamical simulations of 19 halos extracted from a Λ Cold Dark Matter (CDM) cosmological box and followed their evolution down to redshift $z = 0$. Models were validated not only on the basis of galaxy global properties, but also on the detailed investigation of the stellar abundance ratios ([α /Fe]). We identified the necessary conditions for the formation of the first stars in mini-halos and derived constraints on the metal ejection schemes. The impact of Pop III stars on the final metallicity of UFDs was evaluated by considering different stellar mass ranges for their initial mass function (IMF), the influence of pair-instability supernovae (PISNe), and their energetic feedback, as well as the metallicity threshold that marks the transition from the first massive stars to the formation of low-mass long-lived stars. The inclusion of Pop III stars with masses below $140 M_{\odot}$, and a standard IMF slope of -1.3 does increase the global metallicity of UFDs, although these are insufficient to resolve the tension with observations. The PISNe with progenitor masses above $140 M_{\odot}$ do allow the metal content of UFDs to further increase. However, as PISNe are very rare and sometimes absent in the faintest UFDs, they have a limited impact on the global faint end of the metallicity-luminosity relation. Despite a limited number of spectroscopically confirmed members in UFDs, which make the stellar metallicity distribution of some UFDs uncertain, our analysis reveals that this is essentially the metal-rich tail that is missing in the models. The remaining challenges are thus both observational and numerical: (i) to extend high-resolution spectroscopy data samples and confirm the mean metallicity of the faintest UFDs; and (ii) to explain the presence of chemically enriched stars in galaxies with very short star formation histories.

Key words. galaxies: dwarf, ultra-faint dwarf galaxies - stars: Population III, pair-instability supernovae, galaxies: abundances, chemical evolution - methods: numerical

1. Introduction

Ultra-faint dwarf galaxies (UFDs) are the faintest galaxies known, with V-band luminosities fainter than $L_V = 10^5 L_{\odot}$, $M_V < -7.7$ (see Simon 2019, for a recent review). Some of them are as faint as a few hundred solar luminosities and may be as compact as faint globular clusters. Ultra-faint dwarfs are also the most dark-matter-dominated galactic systems and, as such, they constitute fundamental probes of the cosmological model (Bullock & Boylan-Kolchin 2017).

Semi-analytical and hydro-dynamical numerical simulations have shown that UFDs are compatible with the first galaxies formed in mini-halos before the epoch of reionization (e.g., Ricotti & Gnedin 2005; Wyithe & Loeb 2006; Salvadori & Ferrara 2009a,b; Bovill & Ricotti 2009; Wheeler et al. 2019; Rodríguez Wimberly et al. 2019). These metal poor systems (Muñoz et al. 2006; Martin et al. 2007; Simon & Geha 2007; Kirby et al. 2008) had indeed formed the bulk of their stellar mass ($\geq 80\%$) by $z \sim 6$, as revealed by deep ground- and space-based color-magnitude diagrams (Okamoto et al. 2012; Brown et al. 2014; Sacchi et al. 2021; Gallart et al. 2021). Therefore, their properties offer a unique insight into the physics at work in the early Universe.

One might think that these small systems, with very short star formation histories, would be the product of simple physical processes. This is not the case. They do challenge numerical simulations, which struggle to reproduce their properties. Their small size, low mass, and shallow gravitational potential

makes them extremely sensitive to the numerical implementation of the physical processes; they require high resolution, and they are critically sensitive to a correct and well controlled treatment of the first generations of stars, whose chemical signatures should be more salient than in more massive systems (e.g., Ji et al. 2015).

Along this line, one of the most striking obstacles faced by numerical simulations is the reproduction of the observed luminosity-metallicity relation in UFDs. As described in detail in Sec. 2, all hydro-dynamical models systematically predict too low a stellar metallicity at a given luminosity, compared to the observations, or in other words, too steep a slope of the [Fe/H]- L_V relation (Jeon et al. 2017; Macciò et al. 2017; Escala et al. 2018; Wheeler et al. 2019; Agertz et al. 2020; Applebaum et al. 2020; Jeon et al. 2021; Prugnet et al. 2022). The question arises whether the models are so far missing an important source of metals, and/or whether the nucleosynthesis products are too diluted in the interstellar medium (ISM) after the supernovae explosions.

The pair-instability supernovae (PISNe), first introduced by Barkat et al. (1967), are, in theory, an outstanding source of metals, and hence worth considering in the context of UFDs. These supernovae result from an instability induced by the production of free electron-positron pairs in metal-free stars with masses larger than $140 M_{\odot}$. This instability leads to a complete disruption of the star, releasing a large amount of heavy elements.

Article number, page 1 of 17

Since UFDs cease forming stars shortly after cosmic reionization, PISNe could significantly influence their chemical evolution as part of the first (population III, hereafter Pop III) stars, pre-enriching the ISM. The influence of Pop III stars in UFDs has hardly been investigated so far. They are either included in the semi-analytical approach of [Salvadori & Ferrara \(2009a\)](#), or in the hydro-dynamical simulations of [Jeon et al. \(2017\)](#), where their specific influence has not been documented.

No metal-free stars have yet been observed, suggesting that Pop III stars were sufficiently massive to either collapse into black holes or to explode as a supernovae. In the latter case, they could leave their nucleosynthesis imprints in the next generations of low-mass long-lived stars (population II, hereafter Pop II) that are observed today. However, the physical conditions under which they are formed and their detailed properties are still unsettled. This leaves wide open questions about the time frame of their formation in the cosmic history ([Bromm & Larson 2004](#); [Yoshida et al. 2012](#); [Hummel et al. 2012](#); [Magg et al. 2016](#)), the mass of the halos in which they were hosted, and their external enrichment from neighboring halos (see e.g., [Skinner & Wise 2020](#); [Schauer et al. 2020](#); [Graziani et al. 2017](#); [Hicks et al. 2021](#)), as well as their initial mass function (IMF, see e.g., [Machida 2008](#); [Turk et al. 2009](#); [Stacy et al. 2010](#); [Clark et al. 2011](#); [Maeder & Meynet 2012](#); [de Bannassuti et al. 2017](#); [Chon et al. 2021, 2022](#)). Chemo-dynamical cosmological zoom-in simulations of UFDs can test different Pop III models and verify their compatibility with the stellar abundance ratios observed in Pop II stars.

The goal of this paper is to precisely track down the conditions under which the global metal content of the model UFDs, traced by their iron abundance, can be increased at fixed stellar mass and/or luminosity. This involves investigating: i) the physical conditions of star formation; ii) the possible strong Fe contributors among the very first stars; iii) the IMF of the first stars; iv) how metals are released and mixed in the ISM; and v) the impact of the supernovae feedback energy. Just as in our previous works, we discriminate between different scenarios not only on the grounds of global galaxy properties (e.g., $\langle [\text{Fe}/\text{H}] \rangle$, luminosities, and mass) but also on their detailed stellar abundance ratios, stellar metallicity distributions, and velocity dispersions.

The paper is organized as follows. In Sec. 2, we review in detail the discrepancies between the observed and simulated luminosity-metallicity relations, and the different scenarios that have been suggested to address this issue. In Sec. 3, we present our numerical methods, introduce in particular our treatment of the Pop III stars, and describe the entire set of simulations. In Sec. 4, we discuss the conditions from the formation of high-mass and low-mass stars, the IMF of Pop III stars, and their explosion energy, as well as their impact on the relation between stellar metallicity and luminosity, with and without PISNe. We also compare the α -elements abundance ratios, as well as the metallicity distribution function in models and observations. Our conclusions are presented in Sec. 5.

2. The challenge of the luminosity-metallicity relation

Similarly to more massive galaxies, dwarf galaxies fall on the scaling relations. Among those, the metallicity-luminosity relation was first observed by [Lequeux et al. \(1979\)](#) for irregular and blue compact galaxies, and subsequently confirmed by many authors, extending both to dwarf galaxies or more distant spirals (see e.g., [Skillman et al. 1989](#); [Garnett 2002](#); [Tremonti et al.](#)

[2004](#)). Basically, dwarf galaxies brighter than $L_V > 10^5 L_\odot$ synthesize a larger quantity of metals, which are further locked in the next generation of stars. This is relatively well reproduced by the models. However, in the faint (UFD) regime, the observed dispersion in stellar metallicity at fixed luminosity increases ([Simon 2019](#)), and the slope of the observed relation is less steep than the models, with too low a $[\text{Fe}/\text{H}]$ at a given luminosity. This common feature remains despite a variety of numerical schemes and stellar feedback recipes ([Agertz et al. 2020](#)). While this systematic deviation drew attention only recently, in particular with the recent improvements in numerical resolution, it was already mentioned in past studies ([Bovill & Ricotti 2009](#), see their Fig. 3).

This discrepancy is illustrated in Fig. 1, where Local Group dwarfs and UFDs are compared to the available hydro-simulations from [Jeon et al. \(2017\)](#), [Macciò et al. \(2017\)](#), [Revaz & Jablonka \(2018\)](#), [Escala et al. \(2018\)](#), [Wheeler et al. \(2019\)](#), [Agertz et al. \(2020\)](#), [Applebaum et al. \(2020\)](#), and [Prgomet et al. \(2022\)](#). This figure includes a set of UFDs not published in [Revaz & Jablonka \(2018\)](#) but obtained with exactly the same physical model. The observed galaxy sample was obtained thanks to the continuously updated *Local Group and Nearby Dwarf Galaxies* database¹ of [McConnachie \(2012\)](#) and are represented by gray squares. It should be noted that our sample includes only confirmed UFDs that benefit from medium resolution spectroscopy with metallicity derived either from spectral synthesis or Calcium triplet (CaT) calibration.

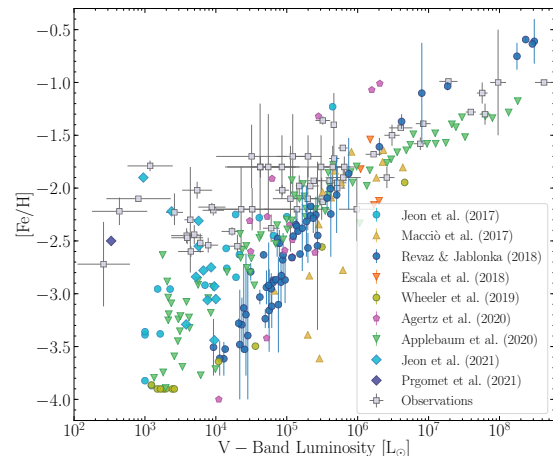


Fig. 1. Comparison of the luminosity-metallicity relation for dwarf galaxies and UFDs, between Local Group observations and simulations. The gray squares represent our Local Group sample (see text for details). Colored points stand for different simulations published with the references given at the bottom of the figure. We extended our own work ([Revaz & Jablonka 2018](#)) with the results of unpublished galaxies in the UFD regime. Error bars for the stellar metallicity in our simulated galaxies were calculated by comparing the results obtained with the mean, the median, and the mode acquired with several binning choices. See Sec. 3.6 for more details on the method used.

Several explanations are proposed for the origin of the tension between models and observations. [Bovill & Ricotti \(2011\)](#) suggest that the observed dwarfs may be a subset of bright pri-

¹ http://www.astro.uvic.ca/~alan/Nearby_Dwarf_F_Database.html

mordial fossils that have been stripped of 90% - 99% of their stars. Indeed, tidal stripping could remove stars from a dwarf galaxy, subsequently reducing its luminosity without affecting its metallicity. However, only dwarf galaxies with a very small pericenter will lose an appreciable fraction of their stars (Peñarrubia et al. 2008). Moreover, stripping would induce an expansion of the stellar component, in contradiction with UFDs having a very small half-light radius. Environmental pre-enrichment by the host galaxy was suggested by Wheeler et al. (2019). Applebaum et al. (2020) mention, however that in a Milky Way-like environment, dwarf galaxies that have never been harassed or stripped show comparable metallicities with respect to the dwarf satellites. They suggest instead that their simulated dwarfs are simply under-producing iron and that the tension can be solved by increasing the contribution to the iron abundance of Type Ia supernovae (SNIa). This, however, requires either reducing the SNIa explosion timescale, or extending the star formation history of UFDs beyond two Gyr, in contradiction with current observations.

Prgomet et al. (2022) looked into the impact of a metallicity-dependent IMF on the stellar mass and metallicity of their simulated dwarf galaxies. They examined the effect of a top-heavy IMF for metal-poor stars. They show that the largest number of massive stars exploding as core-collapse supernovae (CCSNe), decreases the final luminosity of the system through enhanced stellar feedback, while it increases the metallicity. Unfortunately, the boosted SNe feedback also leads to highly diffuse systems with a half-light radius of ~ 0.5 dex larger than the observed values.

Gandhi et al. (2022) suggest boosting the iron production by using a metallicity-dependent SNIa rate. However, because the number of SNIa is low in UFDs, the resulting model does not exceed $[\text{Fe}/\text{H}] \cong -3$, which is still below the observed metallicities.

Alternatively, Revaz & Jablonka (2018) suggest that Pop III stars could play a role in reconciling observations with simulations, a feature worth exploring in hydro-codes. Indeed, hydro-codes self-consistently treat the formation of galaxies, in particular the merger history of sub-halos that may have been enriched independently. Moreover, they properly account for the ejecta of polluted gas and its recycling after re-accretion on the same halo it originates, or on different ones.

3. Methods and simulations

We performed a set of 19 zoom-in Λ Cold Dark Matter (CDM) cosmological simulations of dwarf and UFD galaxies with a final luminosity between $2 \cdot 10^3$ to $3 \cdot 10^5 L_\odot$. We selected galaxy halos from different regions in the dark-matter-only (5 Mpc)³ cosmological volume used in Revaz & Jablonka (2018). Those regions were identified to form a dark halo with a mass typical of a UFD at redshift $z = 0$. We re-simulated those halos using a zoom-in technique including a full treatment of baryons that we describe below. The initial conditions were obtained with the MUSIC code (Hahn & Abel 2011). Compared to our previous studies of dwarf galaxies (e.g., Revaz & Jablonka 2018; Harvey et al. 2018; Hausammann et al. 2019; Sanati et al. 2020), simulations in this work were run with a factor of eight enhancement in resolution for the gas and dark matter, and a factor of 16 for the stars. This was essential to resolve the Pop III host halos with masses between 10^6 and $10^7 M_\odot$, and to guarantee that UFDs with a luminosity as low as a few $10^3 L_\odot$ were populated with at least ten stellar particles. In the refined region (the so-called Lagrangian region), we achieved a dark matter, gas, and stellar

mass resolution of $4172 M_\odot$, $761 M_\odot$, and $380 M_\odot$, respectively. The resolution was gradually degraded from level 10 to 6 outside². The initial Lagrangian region was an ellipsoidal of size of about 1.3 Mpc across, to enclose all the particles that eventually ended up within the target halo at redshift $z = 0$ (Oñorbe et al. 2014a). It is important to note that we limited our stellar resolution to $380 M_\odot$ to ensure a proper IMF sampling up to the most massive stars in the mass range $[140 - 300] M_\odot$ considered in this work (see Sec. 3.3 and 3.2).

We used the cosmology of the Planck Collaboration et al. (2016) with $\Omega_\Lambda = 0.685$, $\Omega_m = 0.315$, $\Omega_b = 0.0486$, $H_0 = 67.3 \text{ km s}^{-1} \text{ Mpc}^{-1}$, $n_s = 0.9603$, and $\sigma_8 = 0.829$. All simulations were started at redshift $z = 70$, ensuring that the rms variance of the initial density field, σ_8 , lied between 0.1 and 0.2 (Knebe et al. 2009; Oñorbe et al. 2014b), and ran till redshift $z = 0$.

All galaxies in this work were evolved in a cosmological context but without taking into account any interaction with a Milky Way-like system. Such an interaction might potentially influence the star formation history of UFDs. However, there is no clear observational evidence that the star formation histories of the Local Group satellites depend on such interactions with the Milky Way (Dixon et al. 2018).

3.1. Numerical setup

The simulations were run with GEAR (Revaz & Jablonka 2012; Revaz et al. 2016; Revaz & Jablonka 2018), a fully parallel chemo-dynamical Tree/Smoothed Particle Hydrodynamics (SPH) code based on GADGET-2 (Springel 2005). In addition to the collision-less dark matter, GEAR treats the baryonic physics by including gas cooling, redshift-dependent UV-background heating, star formation, and stellar feedback. We briefly summarize its essential elements below.

Radiative cooling Gas cooling is computed using the GRACKLE library (Smith et al. 2017). In addition to primordial gas cooling, it includes metal-line cooling scaled according to the gas metallicity. GRACKLE also includes UV-background radiation based on the prediction from Haardt & Madau (2012). Hydrogen self-shielding against the ionizing radiation is incorporated by suppressing the UV-background heating for gas densities above $n_{\text{H}} = 0.007 \text{ cm}^{-3}$ (Aubert & Teyssier 2010). It should be noted that while GRACKLE includes H_2 and dust, we did not consider those species in our model. At the current resolution of our simulations, the maximal density reached by the gas is about 100 atom/cm^3 , below the regime where dust starts to play a major role as a coolant (see e.g., Omukai et al. 2005). Moreover, with such resolution, at a density of $n_{\text{H}} = 1 \text{ atom/cm}^3$ the Jeans length is not resolved for gas with a temperature below 100 K. In this regime, as described below, we relied on the pressure-floor method, and thus did not solve the very dense and cold gas in a fully self-consistent way. The lack of H_2 cooling could slightly delay the formation of the first stars. The impact on our results was nevertheless very mitigated by the very large variety of star formation histories that our models sampled. We leave further improvements to our models, containing the treatment of dust and its impact on the cooling process (e.g., as done in Bekki 2015; McKinnon et al. 2017; Aoyama et al. 2019; Chikaki et al. 2020) for future studies. Also, it is worth mentioning

² One resolution level l corresponds to $N = (2^l)^3$ particles in the full cosmological box. The particle mass is thus decreased by a factor of two between two levels.

that while the cosmic UV-background radiation was included, our physical model did not include ionizing photons emitted from the in situ massive stars.

Star formation Star formation is modeled using the stochastic prescription proposed by Katz (1992) and Katz et al. (1996) that reproduces the Schmidt law (Schmidt 1959). This classical recipe is supplemented by a modified version of the Jeans pressure floor through adding a nonthermal term in the equation of state of the gas. The purpose of this modification is to avoid any spurious gas fragmentation (Truelove et al. 1997; Bate & Burkert 1997; Owen & Villumsen 1997). In dense regions where the system is dominated by unresolved physics, we adopted a star formation density threshold based on the Jeans polytrope, directly correlating the SPH smoothing length with density:

$$\rho_{\text{SFR},i} = \frac{\pi}{4} G^{-1} N_{\text{Jeans}}^{-2/3} h_i^{-2} \left(\gamma \frac{K_B}{\mu m_H} T + \sigma_i^2 \right). \quad (1)$$

Here G is the universal gravitational constant and γ the adiabatic index of the gas fixed to 5/3. h_i and ρ_i are the SPH smoothing length and density, respectively. σ_i is the velocity dispersion of the gas particle i , summed over the neighboring particles in the Jeans mass. N_{Jeans} is the ratio between the Jeans mass and the SPH mass resolution of particle i , and is fixed to ten. T corresponds to the gas temperature. In this work, we supplemented this temperature-dependent threshold with a constant density threshold $\rho_{\text{SFR},c}$, which prevents stars from forming in the cold low-density gas regions. The importance of this threshold and its value is discussed in Sec. 4.1. Above $\max(\rho_{\text{SFR},c}, \rho_{\text{SFR},i})$, stars may form with a star formation efficiency of 1%.

Depending on the metallicity of the gas particle from which it will form, the stellar particle is composed of either Pop II or Pop III stars. Pop III stars only form from gas particles with $[\text{Fe}/\text{H}]$ lower than a critical value, $[\text{Fe}/\text{H}]_c$. Above this gas metallicity, only Pop II stars will form. For our fiducial model, we set $[\text{Fe}/\text{H}]_c$ equal to -5 , as above this metallicity fine-structure line cooling of atomic carbon and oxygen (Bromm & Loeb 2003), but also dust grain emission (Omukai et al. 2005), lead to gas fragmentation and the formation of low-mass stars. As presented below, we assumed Pop III stars to be massive stars. Thus, in our model, all stars more metal poor than $[\text{Fe}/\text{H}]_c$ explode in a few Myrs, and will be absent at redshift $z = 0$. In Sec. 4.6.1, we discuss the impact of modifying $[\text{Fe}/\text{H}]_c$. Because $[\text{Fe}/\text{H}]_c$ is not reached in all gas particles at the same time, these Pop II and Pop III stars can potentially coexist at a given time step.

3.2. Initial mass function

Pop III stars are predicted to have specific IMF and yields (e.g., Iwamoto 2005; Heger & Woosley 2010; Bromm 2013), and we thus updated GEAR with the capability to fully distinguish the properties of Pop II and Pop III stars. In our approach, each stellar particle represents a single stellar population (SSP) that is associated with its own IMF and stellar yields.

For both Pop II and Pop III stars, the IMF is described by the probability function $\Phi(m)$, where $\Phi(m) dm$ gives the fraction of stars born in the mass range $[m, m + dm]$. In our implementation, $\Phi(m)$ is defined by a set of power laws with the slope $\alpha(m)$ depending on the mass interval :

$$\Phi(m) = \frac{m^{\alpha(m)}}{\beta}, \quad (2)$$

with β the normalization constant that ensures the integral of $\Phi(m)$ over the entire mass range considered to be one.

Pop II: We used the revised IMF of Kroupa (2001), including systematic bias due to unresolved binaries in observations, previously implemented in GEAR with

$$\alpha(m) = \begin{cases} 0.7, & \text{if } m \in [0.05 \text{ M}_\odot, 0.08 \text{ M}_\odot] \\ -0.8, & \text{if } m \in [0.08 \text{ M}_\odot, 0.50 \text{ M}_\odot] \\ -1.7, & \text{if } m \in [0.50 \text{ M}_\odot, 1.00 \text{ M}_\odot] \\ -1.3, & \text{if } m \in [1.00 \text{ M}_\odot, 50.0 \text{ M}_\odot] \end{cases}. \quad (3)$$

The minimal and maximal stellar masses were set to 0.05 and 50 M_\odot , respectively.

Pop III: Adopting a different IMF for Pop III than that of Pop II stars was motivated by the fact that no metal-free star has been observed so far, an indication that there are no, or very few, long-lived primordial low-mass stars. It is thus expected that the majority of Pop III stars are massive enough to explode as CCSNe and disappear (Larson 1998; Bromm et al. 1999; Karlsson et al. 2008). For Pop III stars, we adopted a simple power-law IMF with a unique slope $\alpha = -1.3$, similar to the one of the most massive Pop II stars. The minimal mass M_{min} was set to 13 M_\odot . It is worth mentioning that M_{min} was above the lower supernova mass limit. The maximal mass M_{max} , when PISNe were not considered, was set to 140 M_\odot . When PISNe were included, M_{max} was set to 300 M_\odot .

3.3. Stellar feedback: Yields and energy

The stellar lifetimes were mass- and metallicity-dependent, following Kodama & Arimoto (1997) (private communication). At each time step, the exploding supernovae were randomly selected following the random discrete IMF sampling scheme of Revaz et al. (2016), in which the IMF was considered as a probability distribution. We calculated the number of potentially exploding supernovae $N_{\text{SN},i}(t, \Delta t)$ at each time step. For each stellar particle i , this number depended on the lifetimes of stars it contained. The integer part of $N_{\text{SN},i}(t, \Delta t)$ was assumed to explode as supernovae. The remaining fractional value was compared to a random variable χ between zero and one. If the fractional part was above χ , the number of exploding supernovae was increased by one, otherwise, the number of dying stars was equal to the integer part.

As to the massive stars that lead to supernovae explosion, our previous works (Revaz & Jablonka 2012; Nichols et al. 2014, 2015; Revaz et al. 2016; Revaz & Jablonka 2018; Harvey et al. 2018; Hausammann et al. 2019; Sanati et al. 2020), only included CCSNe, with the yields of Tsujimoto et al. (1995), for stellar masses up to 70 M_\odot . We had not yet considered zero metallicity stars. Therefore, for the purpose of the present study, for which we do need Pop III stars, we introduced the metallicity-dependent yields of N13, from $[\text{M}/\text{H}] = -\infty$ to 0.4. Figure 2 summarizes the yields and feedback energies of Pop II and Pop III stars, as considered in this study and further described below.

Pop II: As indicated above, we used the yield tables of N13, taking into account the analysis and conclusions of Kobayashi et al. (2020). The N13 yields were provided at $[\text{M}/\text{H}] = -\infty, -1.3, -0.7, -0.4, 0, 0.4$. As GEAR only treats metallicity-independent yields, we interpolated the N13 tables at $[\text{M}/\text{H}] =$

M. Sanati et al: Ultra-faint dwarfs - enrichment from first stars

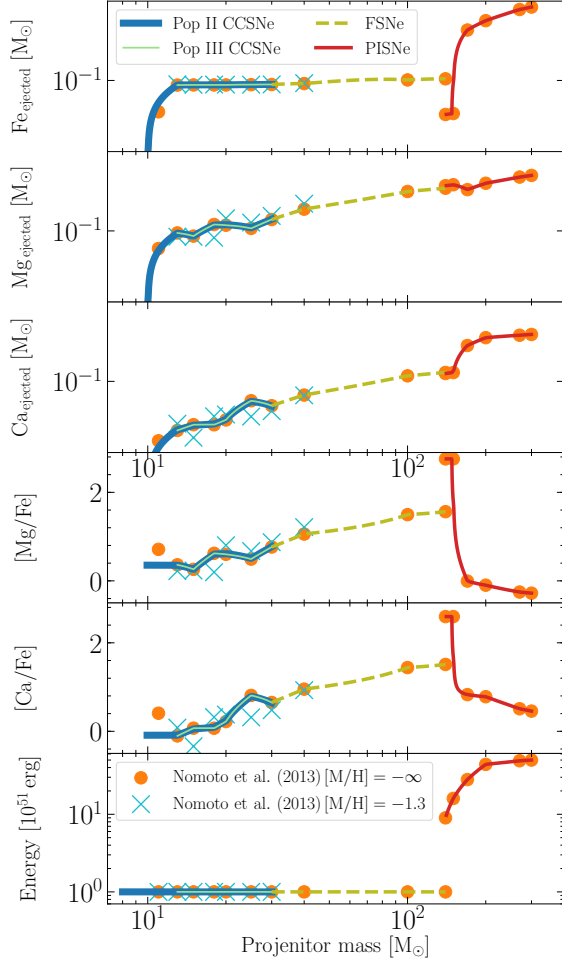


Fig. 2. Comparison of the yields of iron, magnesium, and calcium as a function of stellar masses from N13. The corresponding abundance ratios $[Mg/Fe]$ and $[Ca/Fe]$, and the supernovae explosion energies are also shown. The N13 table values for stars with $M_{\text{proj}} < 30 M_{\odot}$ at $[M/H]^3 = -\infty$ and -1.3 are shown with orange circles and blue crosses, respectively. The thick blue and thin green curves respectively show the adopted, interpolated values used in this work for the Pop II and Pop III stars. The dashed yellow lines indicate the mass ranges of stars ending as FSNe. The red curves show the yields and energies for PISNe with $M_{\text{proj}} > 140 M_{\odot}$ examined in this work from N13.

-2.5 , which globally corresponds to the average stellar metallicity of UFDs. The result of this interpolation is seen with thick blue lines in Fig. 2. Below $40 M_{\odot}$ the values of the N13 table for the two lowest metallicities, $[M/H] = -\infty$ and $[M/H] = -1.3$, are shown with orange circles and blue crosses, respectively. The proximity of these two sets of values (barely visible for the iron ejecta) supports our interpolation.

As in Kobayashi et al. (2020), only supernovae progenitors less massive than $30 M_{\odot}$ contribute to the chemical enrichment. Above this mass, models predict that the formation of supernova progenitors is quite unlikely (Smartt 2009). We thus ignored the

explosion of the stars that are referred to as failed supernovae (FSNe) in the text. For all Pop II CCSNe with mass less than $30 M_{\odot}$ the energy released per explosion was fixed to the fiducial value of 10^{51} erg.

SNela: Stars with initial masses between 3 and $8 M_{\odot}$ can be progenitors of SNeIa, following the model of binary systems of Kobayashi et al. (2000). The SNeIa yields were taken from Tsujimoto et al. (1995). Their explosion energy was fixed to 10^{51} erg.

Pop III: The yields and energies of Pop III stars are those of the metal-free ($[M/H] = -\infty$) stars provided by N13. In the mass range 13 to $30 M_{\odot}$, shown with thin green lines in Fig. 2, Pop III stars explode as CCSNe with feedback energy 10^{51} erg. As the uncertainties in the physics of black hole formation from the first massive stars obscure the upper limit of CCSNe, for Pop III with initial masses between 30 and $140 M_{\odot}$ (dashed yellow lines), we examined two different final fates: (i) normal CCSNe with nucleosynthesis yields from N13, and (ii) FSNe that, according to Kobayashi et al. (2020), end as black holes. In this latter case, no energy nor yields are ejected.

In the PISNe regime for stars above $140 M_{\odot}$, yields were also taken from the N13 table, corresponding to the model predictions of Umeda & Nomoto (2002). In this mass regime, shown with red lines, supernova energy varies from 9 to $50 \cdot 10^{51}$ erg for the most massive stars with $300 M_{\odot}$.

3.4. Stellar feedback

Exploding supernovae release both synthesized chemical elements and energy into the ISM. In particle-based codes, this is modeled by distributing these quantities on the neighboring particles, whose definition and identification are not trivial. We describe here the two methods implemented in GEAR and discuss their advantages and drawbacks. The impact of these schemes, as well as their parameters, are studied in Sec. 4.1.

Injecting into the SPH kernel The standard method consists in releasing the ejecta into the effective number of neighboring particles, N_{eff} , which is determined by the implemented SPH scheme. In the modern conservative formulation of SPH (Springel & Hernquist 2002; Price 2012; Springel 2010; Hopkins 2013) as used by GEAR, a differentiable relation between the volume of a particle (or equivalently its density) and its smoothing length is required. The most natural one is to consider that mass in the kernel volume of a particle remains constant, equal to \bar{N}_{ngb} times the mass m_i of particle i . The parameter \bar{N}_{ngb} (fixed to 50) sets the average number of neighboring particles defined by:

$$\frac{4}{3} \pi h_i^3 \rho_i = m_i \bar{N}_{\text{ngb}}, \quad (4)$$

where the smoothing length h_i and density ρ_i of particle i are related to the volume V_i by $\rho_i = m_i/V_i$. Defining V_i through the summation over neighboring particles, via the kernel function W :

$$V_i = \frac{1}{\sum_{j=1}^{N_{\text{eff}}} W(|\mathbf{r}_i - \mathbf{r}_j|, h_i)}, \quad (5)$$

³ $[M/H] = \log_{10} \left(\frac{M_{\text{metals}}}{M_{\text{H}}} \right)_{\star} - \log_{10} \left(\frac{M_{\text{metals}}}{M_{\text{H}}} \right)_{\odot}$

⁴ It should be noted that there are different possibilities to express V_i . See Hopkins (2013).

Table 1. Parameters of the simulations. Columns are as follows: 1) Model description and ID. 2) Mass range of Pop II and Pop III stars. 3) IMF slopes. 4) Mass range of Pop II and Pop III stars that fall into a CCSNe, for which a feedback energy of 10^{51} erg is assumed. 5) Mass range of Pop II and Pop III stars that fail to explode and fall into black holes. 6) Mass range of Pop III stars forming PISNe and the feedback energy released after their explosion. 7) Critical gas metallicity below which only Pop III stars form. Above this metallicity only Pop II stars form. 8) Density threshold in gas clouds, $\rho_{\text{SFR,c}}$, required for the onset of star formation. 9) Radius, R_{ejecta} , around each supernova in which metals are ejected.

(1) Model description Model ID	(2) Mass range [M_{\odot}] Pop II Pop III	(3) IMF slope(α) Pop II Pop III	(4) CCSNe Pop II Pop III	(5) FSNe Pop II Pop III	(6) PISNe M [M_{\odot}] E [10^{51} erg]	(7) Critical metallicity [Fe/H] _c	(8) Density threshold $\rho_{\text{SFR,c}}$ [atom/cm ³]	(9) Metal ejection radius R_{ejecta} [pc]
Models with only Pop II stars								
PopII	[0.05, 50]	[0.7, -0.8, -1.7, -1.3]	[8, 30]	[30, 50]	-	-	5	300
Models with Pop III stars								
PopII+PopIII (CCSNe)	[0.05, 50] [13, 140]	[0.7, -0.8, -1.7, -1.3] -1.3	[13, 30] [13, 140]	[30, 50] -	-	-5	5	300
Models with Failed SNe								
PopII+PopIII (CCSNe+FSNe)	[0.05, 50] [13, 140]	[0.7, -0.8, -1.7, -1.3] -1.3	[13, 30] [13, 30]	[30, 50] [30, 140]	-	-5	1, 5	h_i , 300
Models with PISNe								
PopII+PopIII (CCSNe+FSNe)+PISNe	[0.05, 50] [13, 300]	[0.7, -0.8, -1.7, -1.3] -1.3	[13, 30] [13, 30]	[30, 50] [30, 140]	[140, 300] [9, 50]	-5	5	300
Models with decreasing PISNe feedback energy								
PopII+PopIII (CCSNe+FSNe)+PISNe(E_{51})	[0.05, 50] [13, 300]	[0.7, -0.8, -1.7, -1.3] -1.3	[13, 30] [13, 30]	[30, 50] [30, 140]	[140, 300] 1	-5	5	300
Models with increasing critical metallicity								
PopII+PopIII (CCSNe+FSNe)+PISNe(Z-4)	[0.05, 50] [13, 300]	[0.7, -0.8, -1.7, -1.3] -1.3	[13, 30] [13, 30]	[30, 50] [30, 140]	[140, 300] [9, 50]	-4	5	300

one can explicitly express \bar{N}_{ngb} :

$$\bar{N}_{\text{ngb}} = \frac{4}{3} \pi h_i^3 \sum_{j=1}^{N_{\text{eff}}} W(|\mathbf{r}_i - \mathbf{r}_j|, h_i). \quad (6)$$

This latter relation shows that the effective number of neighboring particles N_{eff} is different from the fixed parameter \bar{N}_{ngb} , and that N_{eff} strongly depends on the distribution of the neighboring particles through $W(|\mathbf{r}_i - \mathbf{r}_j|, h_i)$. We thus expect this number to be different for each time ejection event.

A particular case worth mentioning is when two supernovae explode subsequently in the same region. In this case, the second supernova explodes in the Sedov cavity created by the first explosion. Assuming an initial homogeneous ISM, for the first explosion, the SPH scheme will find $N_{\text{eff}} \cong \bar{N}_{\text{ngb}}$, while for the second supernova, N_{eff} will largely exceed \bar{N}_{ngb} . Indeed, as neighboring particles can only be found at larger distances, each one of them will have a low $W(|\mathbf{r}_i - \mathbf{r}_j|, h_i)$. In this case, a large number of particles have to be considered in the sum of Eq. 6, in order to guarantee the convergence toward \bar{N}_{ngb} . Consequently, this scheme can potentially cause the ejection of metals into unrealistic and uncontrolled distances. Moreover, it is strongly resolution dependent as h_i scales with the spatial resolution. We further discuss the consequences of using this scheme in Sec. 4.1.

Injecting into a constant volume An alternative to the previous scheme is to distribute the ejecta among particles that reside in a constant volume. This volume is defined by a sphere of radius R_{ejecta} around the exploding star. In addition to avoiding the bias of ejecting into the SPH volume, the method is motivated by reproducing the effective extent of a supernova explosion. The adiabatic supernova explosion in a homogeneous medium must follow the Sedov-Taylor solution (Sedov 1959; Taylor 1950). The mean pressure \bar{P} within the blast wave falls off rapidly with radius. This means that the expansion of the supernova shock must follow a power law that, at the end of the blast wave phase, using typical values for supernova explosions, is approximately equal to:

$$R_{\text{ejecta}} \approx 300 \text{ pc} \left(\frac{E}{10^{51} \text{ erg}} \right)^{1/3} \left(\frac{\bar{P}}{4 \times 10^{-13} \text{ dyne cm}^{-2}} \right)^{-1/3}, \quad (7)$$

where we assume that an amount of energy E is instantaneously ejected into the ambient medium of uniform density ρ , characterized by the adiabatic index $\gamma = \frac{5}{3}$ (Ostriker & McKee 1988). We thus supplemented GEAR with the possibility to eject metals in a constant physical volume (not a comoving volume) using R_{ejecta} that we chose to be 300 pc.

Delayed cooling and mixing In both schemes mentioned above, deposited energy and metals are weighted by the kernel $W(|\mathbf{r}_i - \mathbf{r}_j|, h_i)$. To avoid an instantaneous radiation of the injected energy, we used the delayed cooling method, which consists in disabling gas cooling for a short period of time (Stinson et al. 2006), here taken as 5 Myr. Only a fraction ϵ of the supernova energy is deposited into the ISM. We assumed $\epsilon = 0.2$, and hence $\sim 20\%$ of the released energy impacted the ISM effectively. The released chemical elements were further mixed in the ISM using the Smooth metallicity scheme (Okamoto et al. 2005; Tornatore et al. 2007; Wiersma et al. 2009). In short, the chemical abundance of a gas particle results from the convolution of the metal content of its neighbors.

3.5. Models

We explored the impact of the different parameters listed in Table 1. The stellar range of properties, as well as the model ID are provided in the first column.

Models including only Pop II stars are our references, hereafter denoted as PopII. The mass range of Pop II and Pop III stars is given in the second column. As described in Sec. 3.2, the IMF slope of the Pop II stars changes with the stellar mass range (Kroupa 2001). For the Pop III stars, we adopted a fixed slope of -1.3 , similar to the most massive of the Pop II stars.

The mass range of CCSNe is shown in the fourth column. In PopIII (CCSNe), all Pop III stars explode as a normal CCSNe, while in PopIII (CCSNe+FSNe), stars in mass range [30 – 140] M_{\odot} fail to explode and end as black holes. The mass range of these FSNe (see Sec. 3.3), ejecting no energy nor yields, is given in the fifth column.

For massive Pop III stars ([140 – 300] M_{\odot}) exploding as PISNe, we explored the two feedback energy prescriptions in-

licated in the sixth column: (i) in our reference PISNe model, the highly energetic feedback increases from 9 to $50 \cdot 10^{51}$ erg, according to the initial mass of the star (see N13, for more details); (ii) in the PISNe(E₅₁) model, we explored a less energetic feedback. In this model, the supernova energy is independent of the progenitor mass and equal to the energy ejected by the normal CCSNe (i.e., 10^{51} erg).

The critical gas metallicity $[\text{Fe}/\text{H}]_c$, below which only the first massive and metal-free stars may form, is shown in the seventh column. When the metallicity of gas is higher than this critical value, low-mass long-lived Pop II stars can form. In model PISNe(Z-4), we increased $[\text{Fe}/\text{H}]_c$ from -5, of our reference PISNe model, to -4.

In model PopIII(CCSNe+FSNe), we explored the impact of the gas density threshold, $\rho_{\text{SFR},c}$, required for the onset star formation. In this model we also explored the radius R_{ejecta} around each supernova in which metals were ejected (see Sec. 3.4). These two parameters are given in columns eight and nine. In all other models, these parameters were fixed to 5 atom/cm³ and 300 pc, respectively.

3.6. Extraction of the observables, luminosity and metallicity

Both the galaxy luminosity and metallicity were extracted from the low-mass long-lived stars traced by the Pop II stellar particles. All Pop III stars explode, and therefore do not contribute to the final stellar mass budget, luminosity, or metallicity of their host galaxy. The line-of-sight (LOS) stellar velocity dispersion, σ_{LOS} , was calculated for seven different lines of sight inside a 1 kpc cylindrical radius. The value quoted for each galaxy represents the mean of these values.

The galaxy V-band luminosity (L_V) was obtained by computing the luminosity of individual Pop II stellar particles located within the 90% of the halo's light radius. Their mass was converted into luminosity using the stellar population synthesis model of Vazdekis et al. (1996), computed with the revised Kroupa (2001) IMF. Where necessary, the luminosities were inter- and extra-polated in age and metallicity using a bivariate spline. We ignored dust absorption, as the stellar metallicity of galaxies studied here were $[\text{Fe}/\text{H}] < -2$. Indeed, at these low metallicities, the dust-to-gas ratio was lower than 10^{-5} (see e.g., Fig. 1 in Hirashita 2015).

Because of the limited number of stars formed in UFDs, the choice of a representative "mean" $[\text{Fe}/\text{H}]$ is not a trivial task. As the metallicity distribution is sparsely sampled computing the mode, the peak of the metallicity distribution function can lead to large uncertainties. In Appendix A, we propose a method to determine the mode based on a fitting analytical formula derived from a simple chemical evolution model. The error on $[\text{Fe}/\text{H}]$ was taken at the maximum of the errors obtained by the different methods, peak and mode. All chemical abundances were calculated with respect to the solar abundances of Anders & Grevesse (1989).

4. Results

Table 2 summarizes the main properties of the simulated halos at $z = 0$ for our fiducial model, which includes only Pop II stars. The halo IDs are those of Revaz & Jablonka (2018, see their Table 1), while the simulations were run with the physics described in this paper. Table 2 provides the galaxy total V-band luminosity L_V , total stellar mass M_* , virial mass M_{200} , virial radius R_{200} , mean stellar velocity dispersion σ_{LOS} , and the peak value of the

stellar metallicity distribution function $[\text{Fe}/\text{H}]$. The halo h177 hosts a Sextans-like classical dwarf galaxy (see next section). The other 18 halos host dwarf galaxies with luminosities equal to or lower than $10^5 L_\odot$ and are considered to be UFDs.

Table 2. Global properties of the 19 halos simulated when only Pop II stars are considered. The first column gives the halo ID following Revaz & Jablonka (2018). L_V is the V-band luminosity and M_* the stellar mass. M_{200} is the virial mass, i.e., the mass inside the virial radius R_{200} . $r_{1/2}$ is the half-light radius, σ_{LOS} is the line-of-sight velocity dispersion, and $[\text{Fe}/\text{H}]$ is the peak value of the metallicity distribution function.

Halo ID	L_V [$10^5 L_\odot$]	M_* [$10^5 M_\odot$]	M_{200} [$10^9 M_\odot$]	R_{200} [kpc]	$r_{1/2}$ [kpc]	σ_{LOS} [km/s]	$[\text{Fe}/\text{H}]$ [dex]
h177	3.07	10.28	0.51	25.9	0.26	5.7	-1.97
h063	1.41	3.73	2.41	41.8	0.51	6.4	-2.31
h190	1.31	3.62	0.47	24.2	0.28	4.8	-2.15
h187	1.04	2.86	0.43	23.4	0.25	5.3	-2.27
h166	0.71	1.92	0.64	26.9	0.22	5.0	-2.36
h112	0.63	1.68	1.18	32.9	0.43	6.9	-2.79
h152	0.53	1.42	0.80	28.9	0.38	6.4	-2.82
h113	0.41	1.08	1.14	32.5	0.53	7.4	-3.07
h184	0.30	0.81	0.61	26.4	0.28	4.8	-2.69
h245	0.17	0.45	0.39	22.7	0.32	6.0	-3.24
h259	0.20	0.53	0.39	22.7	0.21	5.1	-2.74
h226	0.15	0.38	0.44	23.6	0.25	4.8	-2.87
h277	0.10	0.26	0.36	22.2	0.42	5.3	-3.03
h249	0.07	0.18	0.39	22.8	0.28	5.7	-3.18
h315	0.05	0.14	0.33	21.6	0.51	5.6	-3.16
h323	0.05	0.13	0.27	20.1	0.21	4.0	-3.07
h170	0.05	0.13	0.62	26.5	0.41	5.0	-3.56
h273	0.04	0.09	0.39	22.7	0.32	4.1	-3.53
h291	0.02	0.04	0.33	21.4	0.18	5.5	-3.69

4.1. Model calibration and validation

While in Revaz & Jablonka (2018) we could successfully reproduce the observed properties of the Local Group classical dwarf galaxies, in the present study, not only did we use different nucleosynthesis tables, but we also increased the effective resolution of the simulations by one order of magnitude. Therefore, before taking up the challenge of UFDs, we first needed to calibrate our physical reference model. To this end, we focused on the halo h177, representative of a Sextans-like galaxy. Indeed Sextans is one the least massive classical dwarf galaxies and it benefits from extensive medium- and high-resolution spectroscopy, including abundance ratios over a wide metallicity range. This enables a proper and detailed comparison with the models.

Compared to Revaz & Jablonka (2018), the supernova efficiency was increased by a factor of two, from $\epsilon = 0.1$ to 0.2. With this setting, our Sextans-like model h177 had a total V-band luminosity of about $3 \cdot 10^5 L_\odot$, only 25% lower than the observed value (McConnachie 2012). Star formation fully ended after 3 Gyr, in agreement with the star formation history derived from color magnitude diagrams (Lee et al. 2003, 2009; Bettinelli et al. 2018). The peak metallicity (-1.97) and the velocity dispersion (~ 6 km/s) were both in agreement with the values derived from the Calcium triplet (Battaglia et al. 2011).

In a Λ CDM cosmological framework, dwarf galaxies, and particularly UFDs, are dominated by metal-poor stars, which form in clumps in the initial mini-halos. After a few hundred Myrs, these clumps merge and form the final galaxy. This sequence is shown in Fig. 3, which displays the build-up history of h177 from 190 to 430 Myr, a period that corresponds to the first intense phase of the star formation in this system. For illustration purposes, we show here the model PopII+PopIII(CCSNe+FSNe), which includes Pop III stars,

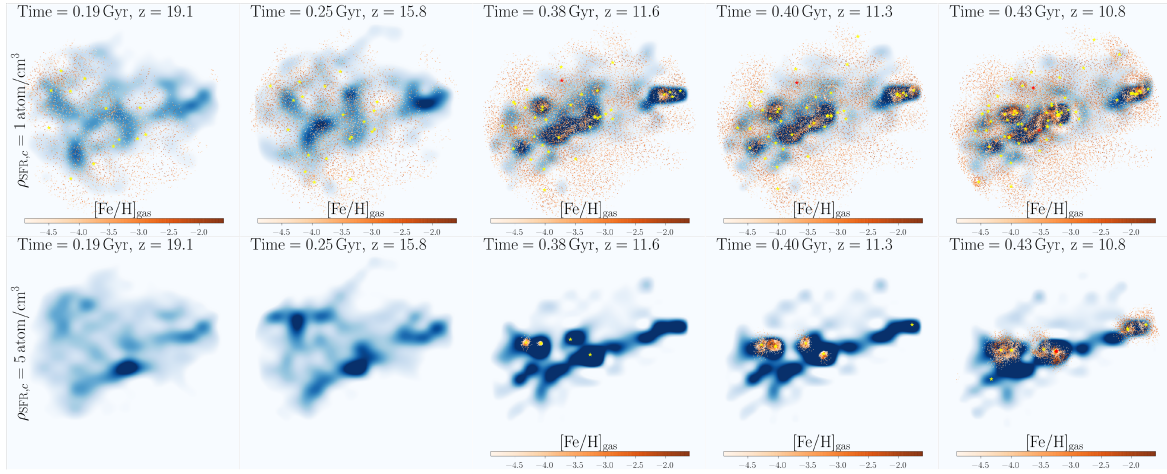


Fig. 3. Metal enrichment of the Sextans-like model galaxy, h177, from 190 to 430 Myr. The surface density of gas is color-coded in blue. After each supernova explosion, shown in yellow and red for Pop III and Pop II stars, respectively, yields were ejected, using the SPH kernel scheme. The metallicity of gas, color-coded in orange, was determined by the amount of Fe received from the supernovae ejecta. The star formation density threshold $\rho_{\text{SFR},c}$ was set to 1 and 5 atom/cm³ in the top and bottom panels, respectively.

but the sequence is identical in all models. The surface density of the gas is color-coded in blue. The Pop III and Pop II stars are respectively shown by yellow and red symbols. The hierarchical assembly of the dwarf is clearly seen; UFDs follow the same hierarchical pattern.

From Fig. 3, it is easy to understand that, besides the supernovae feedback energy, two other parameters are crucial to the evolution of the model dwarfs: the density threshold, $\rho_{\text{SFR},c}$, above which stars form, and the size of the regions over which the supernovae ejecta are distributed. These two parameters are constrained by considering the trend and dispersion of the stellar abundance ratios, considering the α -elements Mg and Ca, as a function of metallicity ([Fe/H]).

The star formation density threshold In our previous studies, star formation was enabled when the gas density of particle i was larger than $\rho_{\text{SFR},i}$ (defined by Eq. 1). Indeed, while the probability is low, in principle, it is possible that stars form from low-density gas (i.e., lower than 1 atom/cm³). Together with the gas surface density, Fig. 3 traces the metallicity of the gas ([Fe/H]_{gas}) in orange. This allows us to follow the regions that are enriched by the supernovae ejecta.

In the top panel of Fig. 3, $\rho_{\text{SFR},c}$ is set to 1 atom/cm³ (1.67×10^{-24} g/cm³). Star formation starts at ~ 100 Myr in mini-halos of low gas density. Because their reservoir of gas is small, only one generation of stars can occur in each of the mini-halos. Metals ejected by Pop III stars are dispersed over large regions, of up to ~ 500 pc h^{-1} physical radii. Consequently, only a small fraction of these metals are locked into the second generation of stars.

Not only this, but random sampling of IMF in each mini-halo naturally leads to a various amount of metals released in different mini-halos. The fact that mixing is very inefficient between them results in a large scatter in the abundance ratios ([Mg/Fe], [Ca/Fe]) at a fixed metallicity, above the dispersion measured in the observations.

In the bottom panel of Fig. 3, $\rho_{\text{SFR},c}$ is set to 5 atom/cm³ (8.36×10^{-24} gr/cm³), that is to say five times the value used in

the simulation shown in the top panel. One immediate impact is the delayed onset of star formation by about ~ 200 Myr, as gas particles need time to merge and sufficiently increase the gas density.

Another consequence of the increase in $\rho_{\text{SFR},c}$ is that, being more massive, the gas reservoirs enable the formation of more than one generation of stars in each of the mini-halos. The ejecta of the Pop III stars increase the metallicity of the gas to about [Fe/H] = -3 , then multiple Pop II stars form from this enriched gas in the same mini-halo, inheriting the chemical imprints of the Pop III stars. Because star formation is more spatially concentrated and the number of gas particles higher, the dilution of the metals in the ISM is reduced. Thus, in order to avoid the dispersion of metals in a large unrealistic volume, such as occurs with $\rho_{\text{SFR},c} = 1$ atom/cm³, we set the star formation density threshold to 5 atom/cm³. This choice resulted from our investigation of a range of values, from 2 to 10 atom/cm³, and best reproduced the observed scatter in [Mg/Fe] and [Ca/Fe].

Spatial extent of the ejection of metals As mentioned above, the extent of the region polluted by the supernova ejecta impacts the chemical abundance pattern of the gas particles, later imprinted in the stars. This includes metallicity and abundance ratios. We investigated two ejection schemes with the aim of reproducing the observed galaxy stellar metallicity distributions, as well as the trends and scatter of the α -element abundance ratios with metallicity.

We performed a statistical analysis of the properties of the regions reached by the supernovae explosions. The size of the polluted region R_{ejecta} is defined as the distance to the furthest particle receiving the supernova ejecta. Figure 4 presents the 2D histogram of R_{ejecta} and time, during the first 1.2 Gyr of evolution of the halo h177. Each point of the diagram corresponds to the number of supernova explosions, which at a given time enriched the ISM up to R_{ejecta} . Blue corresponds to the case where the metals were ejected into the SPH kernel, while red stands for the case where the ejecta were distributed in a volume of constant *maximum* radius of 300 pc (see Sec. 3.4 for the details of

M. Sanati et al: Ultra-faint dwarfs - enrichment from first stars

both methods). Before applying any additional constraints to the metal ejection schemes, the SPH radius was generally smaller than 100 pc, with the consequence that a large part of the gas particles were left in their pristine state, slowing down the metal enrichment of the ISM. Therefore, from the point of view of the galaxy mean metallicity, increasing the diffusion radius of the metals is more efficient. As to the abundance ratios, the general trend of $[\alpha/\text{Fe}]$ versus $[\text{Fe}/\text{H}]$ was successfully reproduced by both implementations, in particular the position of the so-called knee, which indicates the time when the SNeI ejecta significantly contribute to the metal content of the ISM.

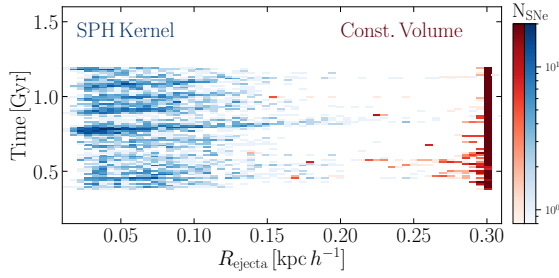


Fig. 4. Comparison between the two different methods for metal ejection implemented in GEAR. Injection into the SPH kernel and into a constant volume, as described in Sec. 3.4, are shown in blue and red, respectively, for the Sextans-like model h177. Both models are plotted as the 2D histogram of the extent of the polluted region R_{ejecta} , and the time at which the explosion occurs, limited to the first ~ 1 Gyr of the simulation. Pixels are color-coded by the number of supernova events. In each event, R_{ejecta} is defined as the distance to the furthest particle that receives the supernova remnants.

Generally, the size of the polluted regions are much smaller in the SPH kernel ejection scheme than in the constant volume method. In dense gas clouds, where the N_{ngb} neighboring particles are found at small distances, R_{ejecta} may be as small as $10 \text{ pc } h^{-1}$. As expected, in the constant volume ejection scheme, the size of the maximum polluted region is 300 pc on average. This radius can occasionally be smaller in cases of very isolated gas clouds.

The small ejecta radii induced by the SPH scheme leads to less efficient metal mixing and consequently larger scatter in the abundance ratios of α -elements, as seen in Fig. 5, which displays the stellar $[\text{Mg}/\text{Fe}]$ and $[\text{Ca}/\text{Fe}]$ as a function of $[\text{Fe}/\text{H}]$. The two settings for metal ejection, the SPH kernel and the constant volume (see Table 1), are shown in blue and green, respectively. For the sake of a fair comparison with the observations, we added random uncertainties to the model abundances, following a normal distribution with a standard deviation of 0.1 dex. Using the same yields, Kobayashi et al. (2020) semi-analytical models produce a $[\text{Mg}/\text{Fe}]$ plateau 0.2 dex higher than the observations. This small difference is interpreted as uncertainties in the stellar yields. We therefore shifted our model $[\text{Mg}/\text{Fe}]$ by -0.2 dex in all subsequent figures involving abundance ratios. Figure 5 shows that the scatter induced by the SPH scheme leads to a larger scatter than observed⁵. We therefore adopted a constant R_{ejecta} for our simulations as it leads to an improved chemical mixing.

⁵ It should be noted that the dispersion in the observed $[\text{Mg}/\text{Fe}]$ is larger than in the observed $[\text{Ca}/\text{Fe}]$ simply because the number of lines used for the derivation of the magnesium was much smaller than for the calcium.

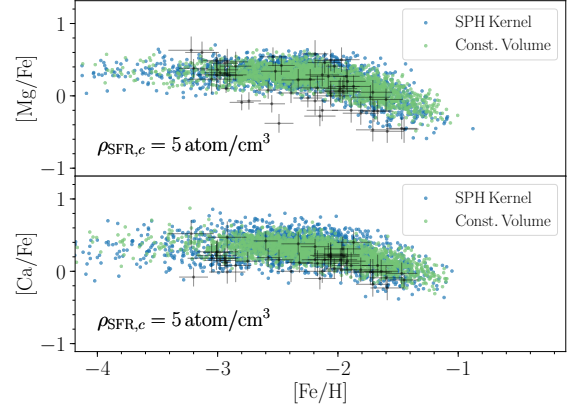


Fig. 5. $[\text{Mg}/\text{Fe}]$ and $[\text{Ca}/\text{Fe}]$ versus $[\text{Fe}/\text{H}]$ for stars formed in the two different methods for metal ejection, compared to the observed stars. Metal ejection into the SPH kernel and into a constant volume are shown in blue and green, respectively. Observational values for Sextans stars are shown with black dots and error bars. The data were taken from Shetrone et al. (2001), Kirby et al. (2010), Tafelmeyer et al. (2010), Thaler et al. (2020), and Lucchesi et al. (2020).

4.2. New yields for Pop II stars

Compared to our previous work, the resolution, the yields, and the injection scheme changed. In a first step, we simulated our galaxy models (see Table 2) considering only Pop II stars and checked the impact of our updates on the luminosity-metallicity relation. Our new galaxy models (PopII) are displayed in blue in Fig. 1). Compared to the old ones (shown also by blue circles in Fig. 1), the differences are small. With the new simulation setting, our Sextans model h177 ($L_V = 3 \cdot 10^5 L_\odot$, $[\text{Fe}/\text{H}] = -1.97$), is perfectly superimposed with its counterpart simulated in Revaz & Jablonka (2018). At low luminosities, in the UFD regime, the strong deviation with respect to the observations remains. Our faintest dwarfs with luminosities of a few $10^3 L_\odot$ have a $[\text{Fe}/\text{H}]$ value as low as -3.5 , about one dex below the observed relation. The new simulation setting slightly reshuffles the stellar luminosity and metallicity of our faintest dwarfs when studied individually, on a one to one basis. This underlines the great sensitivity of those objects to any kind of perturbations. Similar changes would have been expected by, for example, a modification to the random seed used in the stochastic star formation recipe (see e.g., Revaz et al. 2016; Keller et al. 2019).

From this first experiment, it stands out that using a higher resolution, but also an updated injection scheme and new yields for Pop II stars, do not solve the under-prediction of stellar metallicity at low luminosity. This first set of simulations with only Pop II stars is considered as our reference model PopII (see Table 1).

4.3. Pop III stars - without PISNe

Looking for the impact of Pop III stars in the evolution of the UFDs, we first considered them up to $140 M_\odot$ (i.e., excluding PISNe). Pop III stars with initial masses between 13 and $30 M_\odot$ explode as CCSNe. For stars with masses between 30 to $140 M_\odot$, we considered two possibilities: (i) these stars are FSNe (i.e. they do not release any metal nor energy). This is the PopIII(CCSNe+FSNe) model in Table 1 (Kobayashi et al.

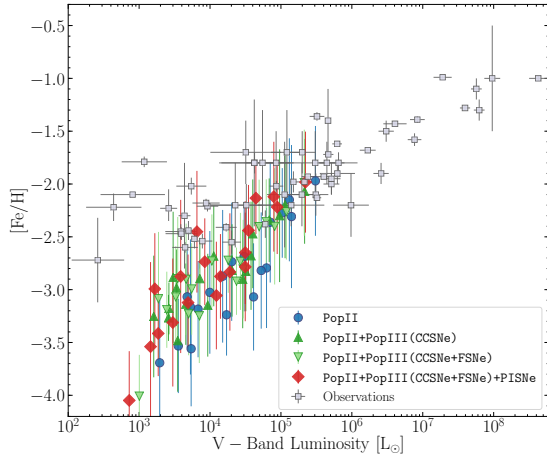


Fig. 6. Comparison of the luminosity-metallicity relation for dwarfs and UFDs, between Local Group observations and simulations. The gray squares represent our Local Group sample (see text for details). Colored points stand for different simulations described in Table 1: The reference PopII model is in blue points, model PopIII(CCSNe) including yields from both massive and low-mass Pop III stars is in dark green triangles, model PopIII(CCSNe+FSNe) including yields from only low-mass Pop III stars is in light green triangles, and model PISNe including yields from PISNe is in red diamonds. Error bars are computed following the method discussed in Sec. 3.6.

2020). (ii) they explode as normal CCSNe with the nucleosynthesis yields of N13. Even if unlikely, this hypothesis was considered to check how much the released mass of metals can be increased in this stellar mass range. This is the PopIII(CCSNe) model in Table 1.

The impact of Pop III on the luminosity-metallicity relation is presented in Fig. 6. Light- and dark-green triangles stand for the PopIII(CCSNe) and PopIII(CCSNe+FSNe) models, respectively. Two effects explain the shift of the relation: on the one hand, Pop III stars explode in a few Myrs, and therefore do not contribute to the final stellar mass budget of their host galaxy. Compared to the PopII only model, the total luminosity is reduced by $\sim 30\%$. On the other hand, the IMF of Pop III stars starts at $13 M_{\odot}$, strongly increasing the number of supernovae formed per unit of stellar mass. They can all potentially contribute to the metal enrichment. In contrast, in the case of the PopII model, a large fraction is locked in low-mass stars ($[0.05 - 8] M_{\odot}$), which do not contribute to the chemical enrichment of their host galaxy.

To illustrate this point, Table 3 provides the number supernovae that explode for $1000 M_{\odot}$ of stars formed, as well as the amount of iron produced by each type of supernovae. While on average only seven CCSNe are present in the PopII model, this number rises to 26 for model PopIII(CCSNe+FSNe) and to 33 for PopIII(CCSNe). This increases in the number of supernovae boosts the released mass of iron. It is multiplied by 6.6 in PopIII(CCSNe+FSNe) and by nine in PopIII(CCSNe), as compared to PopII.

While the tension with observations is mitigated, thanks to the decrease in galaxy luminosity and the increase in metallicity, $[Fe/H]$ still deviates by one dex, for luminosities below $5 \cdot 10^4 L_{\odot}$.

Table 3. Total number of supernova events, number of PISNe, and their corresponding iron ejection mass for the different IMFs used in this work. All quantities were computed for $1000 M_{\odot}$ of stars formed.

Model ID	#SNe ¹ / #PISNe ²	Fe Total ³ / Fe PISNe ⁴	Fe Boost ⁵
PopII	7.4/0	0.29/0	1
PopIII(CCSNe)	33.2/0	2.6/0	9.0
PopIII(CCSNe+FSNe)	26.7/0	1.9/0	6.6
PopIII(CCSNe+FSNe)+PISNe	23.2/0.83	7.7/6.2	26.6

¹ Total number of supernovae (CCSNe and PISNe) for $1000 M_{\odot}$

² Number of PISNe for $1000 M_{\odot}$ of stars

³ Total iron mass ejected from CCSNe and PISNe per $1000 M_{\odot}$ of stars

⁴ Iron mass ejected from PISNe per $1000 M_{\odot}$ of stars

⁵ Ratio of the total mass of ejected iron in each model compared to the Pop II, which contains no Pop III stars

4.4. Pop III stars - including PISNe

We next introduced very massive Pop III stars in our simulations, which explode as PISNe. To do so, we extended the maximal mass of the Pop III IMF from 140 to $300 M_{\odot}$. The impact of PISNe on the luminosity-metallicity relation is shown by the red diamonds in Fig. 6. While there are still few faint galaxies that lie slightly below the observed relation, with some having $[Fe/H] \leq -3$, there is a general improvement, arising from: (i) an increase in metallicity, and (ii) a decrease in luminosity.

First, as seen in the top panel of Fig. 2, stars with masses above $140 M_{\odot}$ provide the largest masses of iron (up to 100 times higher than the normal CCSNe). Table 3 shows that an IMF including PISNe generates 26 times more Fe than in PopII, and three times more than in PopIII(CCSNe), with PISNe contributing to about 80% of this amount. Second, because Pop III stars dominate the UFD population but do not contribute to the total final mass budget, the luminosity of the PISNe model is again 0.2 dex lower than that of PopII, similar to the Pop III models without PISNe. The higher the fraction of Pop III relative to Pop II stars, the more these two effects impact the final luminosity and metallicity of the galaxy. They are particularly significant for the faintest dwarf galaxies, which have shorter star formation histories, as seen in Fig. 6. However, as PISNe may be extremely rare, even nonexistent in systems forming few stars, the metallicity is not increased at the faintest end (i.e., at a luminosity of about $10^3 L_{\odot}$). Figure 7 quantifies the origin of the iron content of each stellar particle in the PISNe model. In order to do so, the gas particles from which each of the stellar particle form were identified and their pollution history was analyzed. This was done thanks to a logger module that records on-the-fly the time at which a gas particle received metals from a supernova, allowing us to distinguish between CCSNe and PISNe sources.

Figure 7 shows the iron mass fraction originating from PISNe as a function of galaxy luminosity. The color code shows the relative number of PISNe. The trend is very clear. In the faintest systems, up to 4% of supernovae are PISNe, while the same value drops below 1% for the brightest systems. This means that the iron production by PISNe is dominant (up to 90%) in the total iron budget of the faint galaxies, while this value drops down to 30% for a Sextans-like galaxy. Indeed, Sex-

tans and more massive dwarf galaxies are dominated by in situ star formation. Thus, after a short period of Pop III star formation, the galaxy is dominated by Pop II stars (see Fig. 11). On the contrary, in UFDs, as mentioned in Sec. 4.1, the first stars form in isolated small mini-halos. Due to their shallow gas reservoir, only a few stars can form in the same mini-halo. The gas metallicity stays below the metallicity threshold for the onset of the formation of Pop II stars up to 1 Gyr. As a consequence, Pop III, and in particular PISNe, have a strong impact on the metallicity and luminosity of the faintest UFDs.

There are two notable exceptions to this general rule: the halo h291 with $L_V \approx 7 \cdot 10^2 L_\odot$ does not experience any PISNe explosion, and h273 with $L_V \approx 2 \cdot 10^3 L_\odot$ has only one PISNe exploding in an isolated sub-halo. Indeed, for UFDs with luminosities below $10^4 L_\odot$, the expected number of PISNe is very low (see Table 3). This is confirmed by our models that, on average, form fewer than five PISNe per UFD. Thus, due to this stochasticity, PISNe induce a large scatter in the luminosity-metallicity relation rather than a shift toward a higher [Fe/H]. Consequently, PISNe cannot be counted as a reliable source of metals in these systems. This also underlines the importance of examining a large sample of UFDs, as done in this study.

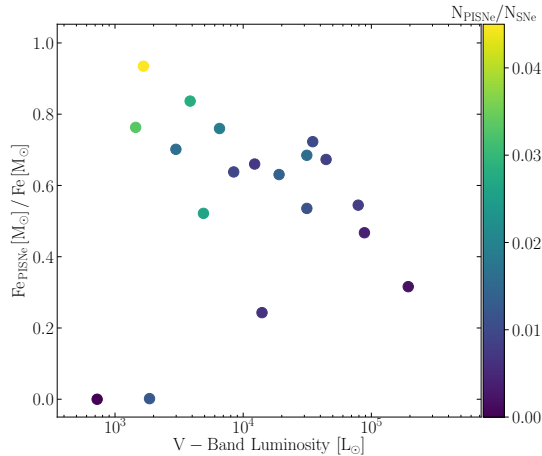


Fig. 7. Fe released by PISNe compared to the total Fe produced in all CCSNe and PISNe events. Each point represents one model galaxy, color-coded by the ratio between the number of stars forming PISNe and the total number of stars ending up as supernovae.

4.5. Abundance ratios

Our simulations allowed us to assess the impact of the different types of first stars on the galaxy mean properties (e.g., [Fe/H], L_V), as well as their influence on the chemical abundance ratios of long-lived low-mass stars. This was done in comparison with the observations, compiling all existing chemical abundance studies with available abundance ratios from high or medium spectroscopic resolution.

Figure 8 presents the [Mg/Fe] and [Ca/Fe] stellar abundance ratios as a function of [Fe/H] for our Sextans model (h177) and different prescriptions listed in Table 1. These two α -elements are particularly well documented for the Sextans dSph, handling both nucleosynthesis and star formation timescales. In Figs. 9 and 10, for our UFD models, we restricted the comparison with

observations to Mg. This is indeed the element that has been most often determined in these faint systems. However, only a handful of stars in each individual UFD benefit from detailed chemical analysis (the maximum being Bootes with 13 stars). Therefore, we drew the comparison of our 18 UFD models with the combination of the existing observations of 68 stars in 14 UFDs. Both simulations and observations were, however, split in two luminosity intervals, with $L_V > 10^4 L_\odot$ and $L_V < 10^4 L_\odot$. In Figs. 8, 9, and 10, the model probability distributions are shown in blue, while the observations are displayed with gray points. The black and red contours delineate the regions encompassing 30, 60, and 90% of the stars, in the models and observations, respectively. In Fig. 8 it is indeed puzzling that a clump of stars exists at [Fe/H] ≈ -3 . However, with the sparsity of data in this low metallicity range, it is not clear if this clump has a physical origin. On the contrary, our models containing a higher number of stars lead to a more continuous distribution.

All models of the h177 halo feature the same general trend with increasing metallicity, starting with a super solar $[\alpha/\text{Fe}]$ plateau below [Fe/H] ~ -2 , followed by a knee and a descending branch down to subsolar $[\alpha/\text{Fe}]$ values, under the influence of the iron-rich Type Ia supernova ejecta. This is the consequence of a relatively extended star formation history, over 3 Gyr, imprinted in the Pop II stars, which constitute up to 98% of the total stellar populations in these massive systems (as shown in Fig. 11). However, some differences between the models are noticeable, which stem from the specific nucleosynthesis of each type of Pop III stars, but also the total number of supernova explosions and feedback energy. In particular, keeping as reference the PopII model, the highest concentration of stellar particles is located at lower [Fe/H] values, by about 0.2 dex for the PopIII (CCSNe) model. Moreover, a small but still significant fraction of the population has higher [Ca/Fe] than in the observations at [Fe/H] < -2 , suggesting that it is indeed unlikely that stars in the mass range 30 to $140 M_\odot$ contributed to the galaxy chemical enrichment, in agreement with the FSNe mass range of Kobayashi et al. (2020).

Figures 9 and 10 enable a deeper assessment of the impact of the Pop III stars in the evolution of UFDs above and below $10^4 L_\odot$, respectively. In both luminosity ranges, the main change in the chemical evolution of UFDs is the shift of the metallicity peak toward higher values, as seen in Fig. 6. For the brightest UFDs, the tail of the distribution of stars at [Fe/H] ≤ -3.5 also disappears. Pop III stars remain influential in these bright UFDs, still accounting for 38% of all stars formed (see Fig. 11), but the choice of the type of Pop III has little influence on the position of the [Fe/H] peak and the distribution in both [Mg/Fe] and [Fe/H] around it. Indeed, in these systems, the global galaxy evolution is dominated by the Pop II stars. This explains the limited sensitivity to the specific nature (CCSNe, FSNe or PISNe) and mass range of the first stars. However, PISNe, which on average produce less magnesium than iron, induce a decrease in [Mg/Fe] and the formation of metal-rich α -poor stars, accentuating the subsolar [Mg/Fe] branch to a level that does not appear to be supported by the observations.

The faintest UFDs, for which Pop III stars contribute to 86% of the full population (see Fig. 11), are more sensitive to the nature of the first stars, with the [Fe/H] distribution becoming slightly more peaked. The tail of the [Fe/H] distribution below -3.5 remains, irrespective of the Pop III nucleosynthesis prescription. More importantly, the intrinsic chemical evolution of these systems hardly exceeds [Fe/H] ~ -2.5 , contrary to the observations, which seem to extend much beyond. Given the extremely short star formation history of these systems, it is very

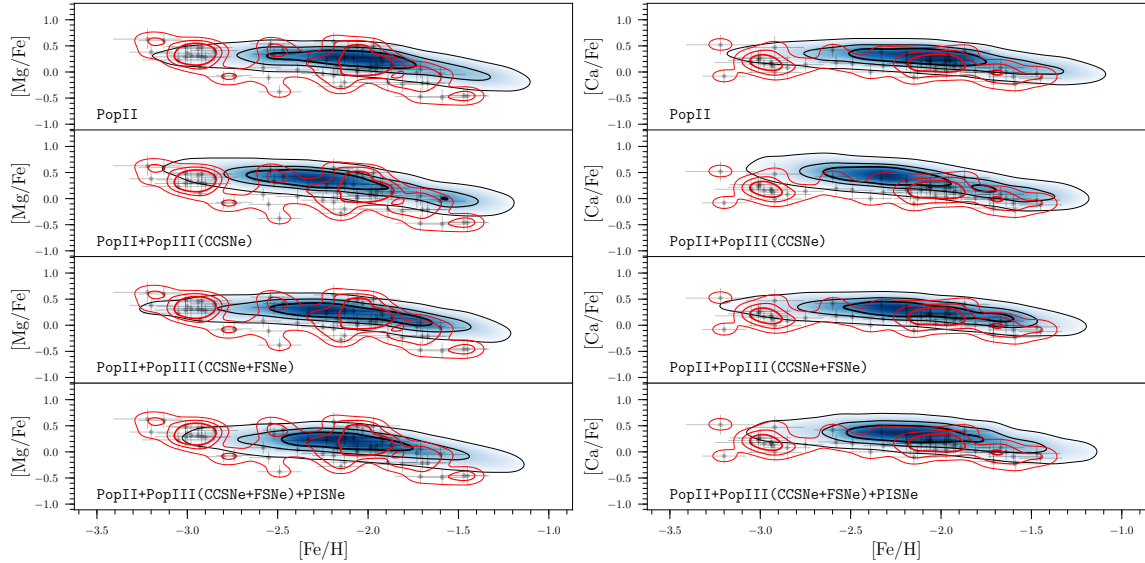


Fig. 8. $[\text{Mg}/\text{Fe}]$ and $[\text{Ca}/\text{Fe}]$ abundance ratios as a function of $[\text{Fe}/\text{H}]$ for the dwarf spheroidal model (h177). The stellar distribution in blue is compared to the Sextans observations, shown as gray points with error bars. For both simulations and observations, we added contours, shown in black and red, respectively, which represent the regions encompassing 30, 60, and 90% of the stars. The observational data are the same as in Fig. 5.

difficult to see how their intrinsic evolution alone could ever reach metallicities as high as -1 . Further comparison with the observations, based on the stellar metallicity distribution, is conducted in Sec. 4.6.3.

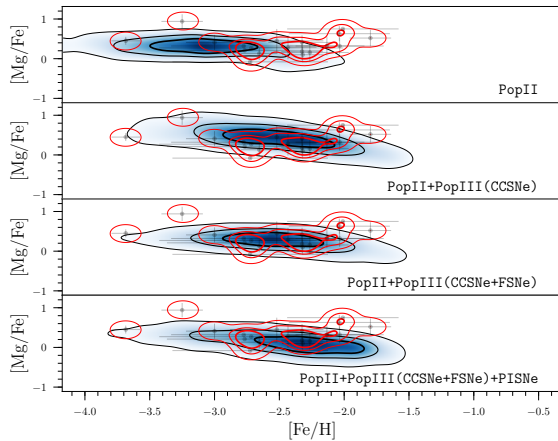


Fig. 9. $[\text{Mg}/\text{Fe}]$ vs. $[\text{Fe}/\text{H}]$ for the UFDs with luminosities larger than $10^4 L_{\odot}$, for the models (in blue) and the observations (in gray). Contours, in black for the models and in red for the observations, represent the regions encompassing 30, 60, and 90% of the stars. The data contain a total of 19 stars from Bootes I (Gilmore et al. 2013; Feltzing et al. 2009; Norris et al. 2010b; Ishigaki et al. 2014) and Hercules (Koch et al. 2008; Vargas et al. 2013; François et al. 2016).

4.6. Robustness of the results

We checked the robustness of our results with respect to different model parameters that could potentially affect our conclusions, specifically the gas metallicity threshold $[\text{Fe}/\text{H}]_c$ and the feedback energy of PISNe, which are uncertain. Then we looked into the comparison of the observed and model stellar metallicity distributions, in order to help provide deeper insight into the resisting shift between their corresponding $[\text{Fe}/\text{H}]$.

4.6.1. Metallicity threshold $[\text{Fe}/\text{H}]_c$

We re-simulated the PISNe model, increasing $[\text{Fe}/\text{H}]_c$ from the fiducial value of -5 to -4 . Increasing $[\text{Fe}/\text{H}]_c$ leads to an increased number of Pop III stars and consequently a potential increase in the final metallicity of UFDs, given that Pop III stars can provide up to three times more iron than Pop II stars (Sec. 4.3). Figure 12 compares the final metallicity of the $[\text{Fe}/\text{H}]_c = -5$ (red diamonds) and $[\text{Fe}/\text{H}]_c = -4$ (blue triangles) models as a function of metallicity. For the vast majority of the models, the impact was very limited. It was the strongest for the faintest systems such as h291 and h273, because the probability of PISNe explosions is very low in these low-mass systems (Sec. 4.4), and the addition of even one single event is very significant. Nevertheless, increasing $[\text{Fe}/\text{H}]_c$ does not lead to the monotonic upward shift of the global L_V - $[\text{Fe}/\text{H}]_c$ relation, which would make the models and observations overlap.

4.6.2. PISNe energy

As introduced in Sec. 4.4, the energy of PISNe strongly increases with the progenitor mass, from 9 to $50 \cdot 10^{51}$ erg (see Fig. 2). Between zero and five PISNe can explode in faint UFDs ($L_V < 10^4 L_{\odot}$), and up to 15 in brighter ones. Thus, in extreme

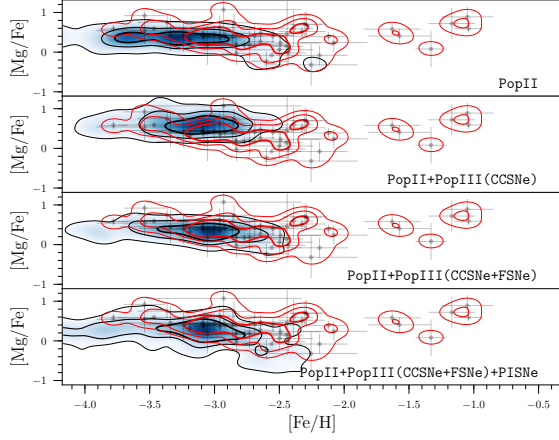


Fig. 10. $[\text{Mg}/\text{Fe}]$ vs. $[\text{Fe}/\text{H}]$ for the UFDs with luminosities lower than $10^4 L_\odot$, for the models (in blue) and the observations (in gray). Contours, in black for the models and in red for the observations, represent the regions encompassing 30, 60, and 90% of the stars. The data contain a total of 49 stars from Bootes II (Ji et al. 2016d; Koch et al. 2009; François et al. 2016), Canes Venatici II (François et al. 2016; Vargas et al. 2013), Grus I (Ji et al. 2019), Horologium (Nagasawa et al. 2018), Leo IV (Simon et al. 2010; François et al. 2016), Reticulum II (Ji et al. 2016c,a; Roederer et al. 2016; Ji & Frebel 2018), Segue I (Norris et al. 2010a; Vargas et al. 2013; Frebel et al. 2014), Segue II (Kirby et al. 2013), Triangulum II (Venn et al. 2017; Kirby et al. 2017; Ji et al. 2019), Tucana II (Ji et al. 2016b; Chiti et al. 2018), Tucana III (Hansen et al. 2017), and Ursa Major II (Frebel et al. 2010; Vargas et al. 2013).

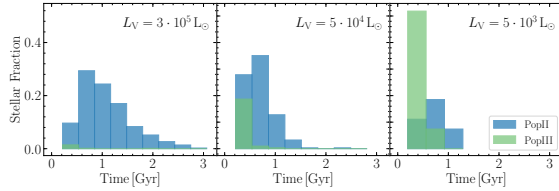


Fig. 11. Fraction of formed Pop II (in blue) and Pop III (in green) stars. Each panel corresponds to one halo, with its total luminosity indicated on the upper right side of the panel. The left panel shows our Sextans-like model, h177, with $L_V \sim 3 \cdot 10^5 L_\odot$. The middle panel shows h152 ($L_V \sim 0.5 \cdot 10^5 L_\odot$), representative of medium-mass UFDs. The right panel displays h323, representative of low-mass UFDs ($L_V \sim 0.05 \cdot 10^5 L_\odot$), with quenched star formation after 1 Gyr.

cases, more than 10^{53} erg can be released in the ISM, limiting the star formation activity in the early stages of the galaxy evolution. We re-simulated the PISNe model, decreasing the energy of PISNe explosions to a constant value of 10^{51} erg, corresponding to the standard CCSNe feedback energy. In Fig. 12 the orange circles represent the PISNe(E_{51}) model with 10^{51} erg feedback, while the red diamonds show our fiducial PISNe model. The net effect of the reduction of the feedback energy is that there is no system below $10^3 L_\odot$ formed anymore, most likely because star formation was less hampered by the PISNe explosions. Similar to increasing $[\text{Fe}/\text{H}]_c$, while the metallicities slightly increased at a fixed luminosity, this was not in a sufficiently large amount to make the observed and modeled relations match.

4.6.3. UFD metallicity distribution functions

The challenge of reproducing the UFDs called for an even closer look at the structure of the models, but also at the status of the observations and in particular at how well they sample the properties of these galaxies. To this end, Fig. 13 compares the metallicity distribution function (MDF) of the PISNe(Z-4) model, chosen because it is the closest to the observed metallicity-luminosity relation in Fig. 12, with the observed distributions derived from the calcium triplet, in three luminosity intervals. The stellar samples were taken from the references in Battaglia et al. (2022) and McConnachie (2012).

The observed MDF of each galaxy is displayed in blue. The number of spectroscopically confirmed galaxy members used in these MDFs is provided. The blue horizontal lines indicate the full metallicity ranges. The red points locate the mean $[\text{Fe}/\text{H}]$ values. For the faintest systems, with fewer than ten member stars, we indicate the median $[\text{Fe}/\text{H}]$ value with purple triangles. Although the number of member stars with available spectroscopic metallicities is fewer than 20 in most of the UFDs, it is already clear that they show a large variety of properties and a wide spread in metallicities up to more than 2 dex. The MDFs of the simulated galaxies are shown in red and their full metallicity ranges are indicated with solid red lines. The MDF peaks are shown with orange points. They are calculated in Appendix A.

As expected, the number of spectroscopically confirmed members decreases with the luminosity of the galaxies, with the consequence that the metallicity distributions may not be fully sampled. They are, in any case, very fragmented, making the position of their mean values rather uncertain. Less expected is that the low-metallicity tail, at $[\text{Fe}/\text{H}] \leq -3$, seems to gradually disappear toward less massive systems. Conversely, the high-metallicity tail of the distributions remains. The question arises as to whether this apparent bias is simply a reflection of incomplete sampling or of different intrinsic evolution. In contrast, by their very nature, the models include all stellar populations. They keep the majority of the metal-poor population regardless of the mass and/or luminosity of the galaxy, whereas the full

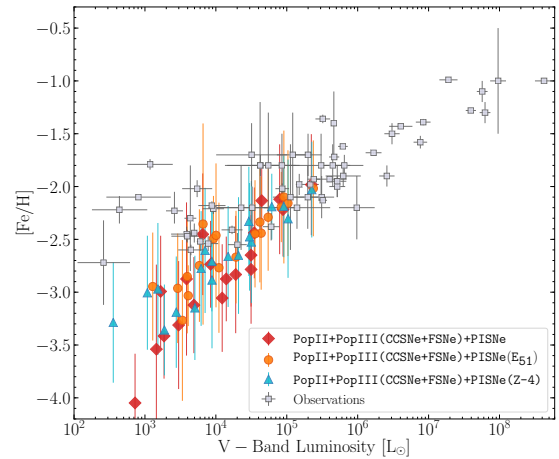


Fig. 12. Tests of different prescriptions. The PISNe model is shown by the same red diamonds as in Fig. 6. Models with a fixed value of $1 \cdot 10^{51}$ erg are shown as orange circles. Models with a critical metallicity of -4 are displayed with blue triangles.

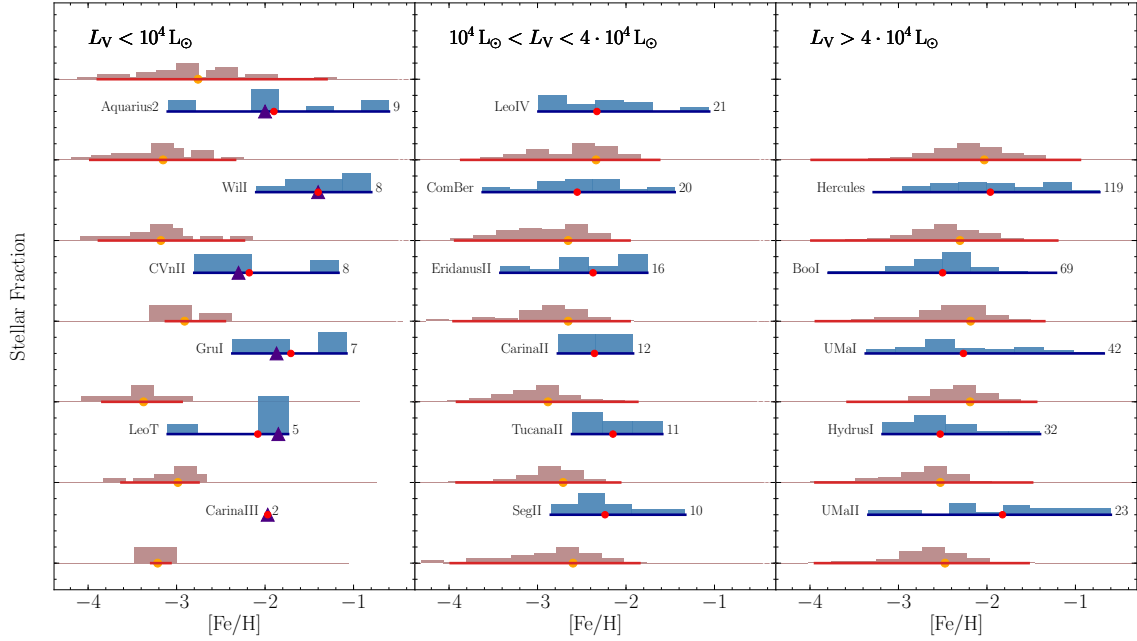


Fig. 13. Comparison of the metallicity distribution functions of the PISNe(Z-4) model (in red) and a set of observed galaxies (in blue) in three luminosity ranges. The solid red and blue horizontal lines indicate the full extent of the stellar metallicity distributions in the simulations and observations, respectively. The orange points show the mode of the [Fe/H] model distribution (see Appendix A). The purple triangles and red points represent, respectively, the median and mean of metallicities for each observed galaxy. The number of the spectroscopically confirmed member stars with metallicity estimates is indicated.

range of metallicity covered depends on the extent of the star formation history. As commented in the previous section, there are few stellar particles above $[\text{Fe}/\text{H}] = -2$, and only in one case do we reach $[\text{Fe}/\text{H}] = -1$. In summary, it appears from this analysis that we are facing two limits, one observational, with the sampling of UFD properties still partial, but also a numerical limit with the challenge of reproducing systems that, despite very short star formation histories, contain stars as chemically enriched as in more massive systems.

5. Conclusions and discussion

Despite their many successes in recent years, the cosmological simulations of dwarf galaxies still fail at the smallest scales. Specifically, in the UFD regime, hydrodynamical models predict a steeper metallicity-luminosity relation than the one observed. Below $10^5 L_\odot$, the galaxy mean metallicities can be as much as 2 dex too low at a given luminosity. In order to tackle this issue and understand how very faint galaxies acquire their metals, we studied the impact of Pop III stars on the metallicity evolution of UFDs. To this end, we performed cosmological zoom-in chemo-dynamical simulations from redshift 70 to zero of 19 halos hosting dwarfs with V-band luminosities between $2 \cdot 10^3$ to $3 \cdot 10^5 L_\odot$. The most massive of these halos is a Sextans-like spheroidal dwarf galaxy, while the eighteen others are fully in the UFD regime, with luminosities equal or below $10^5 L_\odot$. We validated our models by reproducing both the global properties and the α -elements trend of the Sextans dwarf galaxy. We checked the robustness of our results with respect to model-dependent parameters or poorly constrained physics. In particu-

lar, we looked into the effect of the critical metallicity, $[\text{Fe}/\text{H}]_c$, which defines the transition from Pop III to Pop II stars. We also looked into the energy release from PISNe to see how it could affect the UFD build-up and physical properties.

Our main conclusions can be summarized as follows:

- In a Λ CDM cosmological framework, dwarf galaxies, and particularly UFDs, are dominated by metal-poor stars, which form in clumps hosted by the initial mini-halos. After a few hundred Myrs, these clumps merge and form the final galaxy.
- The evolution of UFDs is strongly influenced by Pop III stars. On average, 38% of all stars formed from gas at $[\text{Fe}/\text{H}] < -5$. In small mass UFDs, for which star formation is completely quenched after 1 Gyr, this fraction rises to 86%.
- Assuming a Kroupa-like IMF for Pop III stars, one with a slope of -1.3 , as is usually considered for the massive stars, the main change in the chemical evolution of the dwarf galaxies due to the contribution of the first stars' nucleosynthesis is the upward shift of the peak of their final metallicity distributions. The nature of these first stars, which end up as CCSNe, FSNe or PSINe, is of secondary importance.
- Pop III stars with masses lower than $140 M_\odot$ can increase the production of iron by up to a factor of six per $1000 M_\odot$ of stars formed. This increase is, however, still insufficient to match the observed metallicity-luminosity relation.
- PISNe, with progenitor masses between $140 M_\odot$ and $300 M_\odot$, increase the production of iron by a factor of 26 per $1000 M_\odot$ of stars formed. However, PISNe are rare events and occasionally absent in the faintest UFDs. Therefore, they have a limited impact on the global $L_V - [\text{Fe}/\text{H}]$ relation.

M. Sanati et al: Ultra-faint dwarfs - enrichment from first stars

The analysis of the galaxy metallicity distributions and trends of the stellar particle abundance ratios as a function of $[\text{Fe}/\text{H}]$ provides further insight into the impact of Pop III stars:

- For the brightest UFDs, above $L_V = 10^4 L_\odot$, the tail of the distribution of stars at $[\text{Fe}/\text{H}] \leq -3.5$ disappears, while it remains for the fainter ones. None of the $L_V \geq 10^4 L_\odot$ model UFDs contain stellar particles above $[\text{Fe}/\text{H}] = -2.5$, contrary to the observations. It remains a clear challenge to produce very small mass systems whose intrinsic evolution can create stars up to $[\text{Fe}/\text{H}] = -1$ on timescales smaller than ~ 1 Gyr.
- Because PISNe release less magnesium than iron, low-mass long-lived stars formed from gas enriched by their ejecta can have subsolar $[\text{Mg}/\text{Fe}]$. These seems to be outnumbered at $[\text{Fe}/\text{H}] \geq -2.5$ compared to the observations of UFDs.
- The analysis of the model abundance ratios rules out any significant contribution from Pop III stars in the $30 M_\odot$ to $140 M_\odot$ mass range. Indeed, they predict, for all dwarf galaxies, supersolar $[\text{Ca}/\text{Fe}]$ and $[\text{Mg}/\text{Fe}]$ ratios, in contradiction with the observations.
- From an observational point of view, the number of known, spectroscopically confirmed members, with metallicity estimates and/or detailed chemical abundances, is still limited for all UFDs. It decreases even more with galaxy luminosity. As a consequence, the observed stellar metallicity distributions can be still very fragmented, making the position of their mean values uncertain. Moreover the low-metallicity tail, at $[\text{Fe}/\text{H}] \leq -3$, seems to gradually disappear toward less massive systems.

Challenges to be taken up are thus both observational and numerical, with the need to reproduce systems that, despite very short star formation histories, contain stars as chemically enriched as in more massive ones.

Acknowledgements. We are grateful to Nicolas Longeard for kindly sharing with us some of the spectroscopic members used in the metallicity histograms presented in this paper. We would like to thank Georges Meynet and Chiaki Kobayashi for very useful discussions. We acknowledge the support by the International Space Science Institute (ISSI), Bern, Switzerland, for supporting and funding the international team “First stars in dwarf galaxies”. This work was supported by the Swiss Federal Institute of Technology in Lausanne (EPFL) through the use of the facilities of its Scientific IT and Application Support Center (SC-ITAS). The data reduction and galaxy maps have been performed using the parallelized Python `pNbody` package (<http://lastro.epfl.ch/projects/pNbody/>).

References

- Agertz, O., Pontzen, A., Read, J. L., et al. 2020, *MNRAS*, 491, 1656
- Anders, E. & Grevesse, N. 1989, *Geochim. Cosmochim. Acta*, 53, 197
- Aoyama, S., Hirashita, H., Lim, C.-F., et al. 2019, *MNRAS*, 484, 1852
- Applebaum, E., Brooks, A. M., Christensen, C. R., et al. 2020, *arXiv e-prints*, arXiv:2008.11207
- Aubert, D. & Teyssier, R. 2010, *ApJ*, 724, 244
- Barkat, Z., Rakavy, G., & Sack, N. 1967, *Phys. Rev. Lett.*, 18, 379
- Bate, M. R. & Burkert, A. 1997, *MNRAS*, 288, 1060
- Battaglia, G., Taibi, S., Thomas, G. F., & Fritz, T. K. 2022, *A&A*, 657, A54
- Battaglia, G., Tolstoy, E., Helmi, A., et al. 2011, *MNRAS*, 411, 1013
- Bekki, K. 2015, *MNRAS*, 449, 1625
- Bettinelli, M., Hidalgo, S. L., Cassisi, S., Aparicio, A., & Piotto, G. 2018, *MNRAS*, 476, 71
- Bovill, M. S. & Ricotti, M. 2009, *ApJ*, 693, 1859
- Bovill, M. S. & Ricotti, M. 2011, *ApJ*, 741, 17
- Bromm, V. 2013, *Reports on Progress in Physics*, 76, 112901
- Bromm, V., Coppi, P. S., & Larson, R. B. 1999, *ApJ*, 527, L5
- Bromm, V. & Larson, R. B. 2004, *ARA&A*, 42, 79
- Bromm, V. & Loeb, A. 2003, *Nature*, 425, 812
- Brown, T. M., Tumlinson, J., Geha, M., et al. 2014, *ApJ*, 796, 91
- Bullock, J. S. & Boylan-Kolchin, M. 2017, *ARA&A*, 55, 343
- Chiaki, G., Wise, J. H., Marassi, S., et al. 2020, *MNRAS*, 497, 3149
- Chiti, A., Frebel, A., Ji, A. P., et al. 2018, *ApJ*, 857, 74
- Chon, S., Omukai, K., & Schneider, R. 2021, *MNRAS*, 508, 4175
- Chon, S., Ono, H., Omukai, K., & Schneider, R. 2022, *MNRAS*, 514, 4639
- Clark, P. C., Glover, S. C. O., Smith, R. J., et al. 2011, *Science*, 331, 1040
- de Bannassuti, M., Salvadori, S., Schneider, R., Valiante, R., & Omukai, K. 2017, *MNRAS*, 465, 926
- Dixon, K. L., Iliev, I. T., Gottlöber, S., et al. 2018, *MNRAS*, 477, 867
- Escala, I., Wetzel, A., Kirby, E. N., et al. 2018, *MNRAS*, 474, 2194
- Feltzing, S., Eriksson, K., Kleyna, J., & Wilkinson, M. I. 2009, *A&A*, 508, L1
- François, P., Monaco, L., Bonifacio, P., et al. 2016, *A&A*, 588, A7
- Frebel, A., Simon, J. D., Geha, M., & Willman, B. 2010, *ApJ*, 708, 560
- Frebel, A., Simon, J. D., & Kirby, E. N. 2014, *ApJ*, 786, 74
- Gallart, C., Monelli, M., Ruiz-Lara, T., et al. 2021, *ApJ*, 909, 192
- Gandhi, P. J., Wetzel, A., Hopkins, P. F., et al. 2022, *MNRAS*, 511, 10477
- Garnett, D. R. 2002, *ApJ*, 581, 1019
- Gilmore, G., Norris, J. E., Monaco, L., et al. 2013, *ApJ*, 763, 61
- Graziani, L., de Bannassuti, M., Schneider, R., Kawata, D., & Salvadori, S. 2017, *MNRAS*, 469, 1101
- Haardt, F. & Madau, P. 2012, *ApJ*, 746, 125
- Hahn, O. & Abel, T. 2011, *Monthly Notices of the Royal Astronomical Society*, 415, 2101
- Hansen, T. T., Simon, J. D., Marshall, J. L., et al. 2017, *ApJ*, 838, 44
- Harvey, D., Revaz, Y., Robertson, A., & Hausammann, L. 2018, *MNRAS*, 481, L89
- Hausammann, L., Revaz, Y., & Jablonka, P. 2019, *A&A*, 624, A11
- Heger, A. & Woosley, S. E. 2010, *ApJ*, 724, 341
- Hicks, W. M., Wells, A., Norman, M. L., et al. 2021, *ApJ*, 909, 70
- Hirashita, H. 2015, *MNRAS*, 447, 2937
- Hopkins, P. F. 2013, *MNRAS*, 428, 2840
- Hummel, J. A., Pawlik, A. H., Milosavljević, M., & Bromm, V. 2012, *ApJ*, 755, 72
- Ishigaki, M. N., Aoki, W., Arimoto, N., & Okamoto, S. 2014, *A&A*, 562, A146
- Iwamoto, N. 2005, *Science*, 309, 451
- Jeon, M., Besla, G., & Bromm, V. 2017, *ApJ*, 848, 85
- Jeon, M., Bromm, V., Besla, G., Yoon, J., & Choi, Y. 2021, *Monthly Notices of the Royal Astronomical Society*, 502, 1
- Ji, A. P. & Frebel, A. 2018, *ApJ*, 856, 138
- Ji, A. P., Frebel, A., & Bromm, V. 2015, *Monthly Notices of the Royal Astronomical Society*, 454, 659
- Ji, A. P., Frebel, A., Chiti, A., & Simon, J. D. 2016a, *Nature*, 531, 610
- Ji, A. P., Frebel, A., Ezzeddine, R., & Casey, A. R. 2016b, *ApJ*, 832, L3
- Ji, A. P., Frebel, A., Simon, J. D., & Chiti, A. 2016c, *ApJ*, 830, 93
- Ji, A. P., Frebel, A., Simon, J. D., & Geha, M. 2016d, *ApJ*, 817, 41
- Ji, A. P., Simon, J. D., Frebel, A., Venn, K. A., & Hansen, T. T. 2019, *ApJ*, 870, 83
- Karlsson, T., Johnson, J. L., & Bromm, V. 2008, *ApJ*, 679, 6
- Katz, N. 1992, *ApJ*, 391, 502
- Katz, N., Weinberg, D. H., & Hernquist, L. 1996, *ApJS*, 105, 19
- Keller, B. W., Wadsley, J. W., Wang, L., & Kruijssen, J. M. D. 2019, *MNRAS*, 482, 2244
- Kirby, E. N., Boylan-Kolchin, M., Cohen, J. G., et al. 2013, *ApJ*, 770, 16
- Kirby, E. N., Cohen, J. G., Simon, J. D., et al. 2017, *ApJ*, 838, 83
- Kirby, E. N., Guhathakurta, P., Simon, J. D., et al. 2010, *The Astrophysical Journal Supplement Series*, 191, 352
- Kirby, E. N., Simon, J. D., Geha, M., Guhathakurta, P., & Frebel, A. 2008, *ApJ*, 685, L43
- Knebe, A., Wagner, C., Knollmann, S., Diekershoff, T., & Krause, F. 2009, *ApJ*, 698, 266
- Kobayashi, C., Karakas, A. I., & Lugaro, M. 2020, *ApJ*, 900, 179
- Kobayashi, C., Tsujimoto, T., & Nomoto, K. 2000, *ApJ*, 539, 26
- Koch, A., McWilliam, A., Grebel, E. K., Zucker, D. B., & Belokurov, V. 2008, *ApJ*, 688, L13
- Koch, A., Wilkinson, M. I., Kleyna, J. T., et al. 2009, *ApJ*, 690, 453
- Kodama, T. & Arimoto, N. 1997, *A&A*, 320, 41
- Kroupa, P. 2001, *Monthly Notices of the Royal Astronomical Society*, 322, 231
- Larson, R. B. 1998, *MNRAS*, 301, 569
- Lee, M. G., Park, H. S., Park, J.-H., et al. 2003, *AJ*, 126, 2840
- Lee, M. G., Yuk, I.-S., Park, H. S., Harris, J., & Zaritsky, D. 2009, *ApJ*, 703, 692
- Lequeux, J., Peimbert, M., Rayo, J. F., Serrano, A., & Torres-Peimbert, S. 1979, *A&A*, 500, 145
- Lucchesi, R., Lardo, C., Primas, F., et al. 2020, *A&A*, 644, A75
- Macciò, A. V., Frings, J., Buck, T., et al. 2017, *MNRAS*, 472, 2356
- Machida, M. N. 2008, *ApJ*, 682, L1
- Maeder, A. & Meynet, G. 2012, *Reviews of Modern Physics*, 84, 25
- Magg, M., Hartwig, T., Glover, S. C. O., Klessen, R. S., & Whalen, D. J. 2016, *MNRAS*, 462, 3591
- Martin, N. F., Ibata, R. A., Chapman, S. C., Irwin, M., & Lewis, G. F. 2007, *MNRAS*, 380, 281

- McConnachie, A. W. 2012, *The Astronomical Journal*, 144, 4
- McKinnon, R., Torrey, P., Vogelsberger, M., Hayward, C. C., & Marinacci, F. 2017, *MNRAS*, 468, 1505
- Muñoz, R. R., Carlin, J. L., Frinchaboy, P. M., et al. 2006, *ApJ*, 650, L51
- Nagasawa, D. Q., Marshall, J. L., Li, T. S., et al. 2018, *ApJ*, 852, 99
- Nichols, M., Revaz, Y., & Jablonka, P. 2014, *A&A*, 564, A112
- Nichols, M., Revaz, Y., & Jablonka, P. 2015, *A&A*, 582, A23
- Nomoto, K., Kobayashi, C., & Tominaga, N. 2013, *ARA&A*, 51, 457
- Norris, J. E., Wyse, R. F. G., Gilmore, G., et al. 2010a, *ApJ*, 723, 1632
- Norris, J. E., Yong, D., Gilmore, G., & Wyse, R. F. G. 2010b, *ApJ*, 711, 350
- Oñorbe, J., Garrison-Kimmel, S., Maller, A. H., et al. 2014a, *MNRAS*, 437, 1894
- Oñorbe, J., Garrison-Kimmel, S., Maller, A. H., et al. 2014b, *MNRAS*, 437, 1894
- Okamoto, S., Arimoto, N., Yamada, Y., & Onodera, M. 2012, *ApJ*, 744, 96
- Okamoto, T., Eke, V. R., Frenk, C. S., & Jenkins, A. 2005, *MNRAS*, 363, 1299
- Omukai, K., Tsuribe, T., Schneider, R., & Ferrara, A. 2005, *ApJ*, 626, 627
- Ostriker, J. P. & McKee, C. F. 1988, *Reviews of Modern Physics*, 60, 1
- Owen, J. M. & Villumsen, J. V. 1997, *ApJ*, 481, 1
- Pagel, B. E. J. 1997, *Nucleosynthesis and Chemical Evolution of Galaxies*
- Peñarrubia, J., Navarro, J. F., & McConnachie, A. W. 2008, *ApJ*, 673, 226
- Planck Collaboration, Ade, P. A. R., Aghanim, N., et al. 2016, *Astronomy & Astrophysics*, 594, A13
- Prgomet, M., Rey, M. P., Andersson, E. P., et al. 2022, *MNRAS*[arXiv:2107.00663]
- Price, D. J. 2012, *Journal of Computational Physics*, 231, 759
- Revaz, Y., Arnaudon, A., Nichols, M., & Jablonka, P. 2016, *Astronomy & Astrophysics*, 588, A21
- Revaz, Y. & Jablonka, P. 2012, *Astronomy & Astrophysics*, 538, A82
- Revaz, Y. & Jablonka, P. 2018, *Astronomy & Astrophysics*, 616, A96
- Ricotti, M. & Gnedin, N. Y. 2005, *The Astrophysical Journal*, 629, 259
- Rodriguez Wimberly, M. K., Cooper, M. C., Fillingham, S. P., et al. 2019, *MNRAS*, 483, 4031
- Roederer, I. U., Mateo, M., Bailey, John I., et al. 2016, *AJ*, 151, 82
- Sacchi, E., Richstein, H., Kallivayalil, N., et al. 2021, *ApJ*, 920, L19
- Salvadori, S. & Ferrara, A. 2009a, *MNRAS*, 395, L6
- Salvadori, S. & Ferrara, A. 2009b, *MNRAS*, 395, L6
- Sanati, M., Revaz, Y., Schober, J., Kunze, K. E., & Jablonka, P. 2020, arXiv e-prints, arXiv:2005.05401
- Schauer, A. T. P., Glover, S. C. O., Klessen, R. S., & Clark, P. 2020, arXiv e-prints, arXiv:2008.05663
- Schmidt, M. 1959, *ApJ*, 129, 243
- Sedov, L. I. 1959, *Similarity and Dimensional Methods in Mechanics*
- Shetrone, M.-D., C-t, P., & Stetson, P.-B. 2001, *Publications of the Astronomical Society of the Pacific*, 113, 1122
- Simon, J. D. 2019, *Annual Review of Astronomy and Astrophysics*, 57, 375
- Simon, J. D., Frebel, A., McWilliam, A., Kirby, E. N., & Thompson, I. B. 2010, *ApJ*, 716, 446
- Simon, J. D. & Geha, M. 2007, *ApJ*, 670, 313
- Skillman, E. D., Kennicutt, R. C., & Hodge, P. W. 1989, *ApJ*, 347, 875
- Skinner, D. & Wise, J. H. 2020, *MNRAS*, 492, 4386
- Smartt, S. J. 2009, *ARA&A*, 47, 63
- Smith, B. D., Bryan, G. L., Glover, S. C. O., et al. 2017, *MNRAS*, 466, 2217
- Springel, V. 2005, *Monthly Notices of the Royal Astronomical Society*, 364, 1105
- Springel, V. 2010, *ARA&A*, 48, 391
- Springel, V. & Hernquist, L. 2002, *MNRAS*, 333, 649
- Stacy, A., Greif, T. H., & Bromm, V. 2010, in *American Institute of Physics Conference Series*, Vol. 1294, *First Stars and Galaxies: Challenges for the Next Decade*, ed. D. J. Whalen, V. Bromm, & N. Yoshida, 289–290
- Stinson, G., Seth, A., Katz, N., et al. 2006, *MNRAS*, 373, 1074
- Tafelmeyer, M., Jablonka, P., Hill, V., et al. 2010, *A&A*, 524, A58
- Taylor, G. 1950, *Proceedings of the Royal Society of London Series A*, 201, 159
- Theler, R., Jablonka, P., Lucchesi, R., et al. 2020, *A&A*, 642, A176
- Tornatore, L., Borgani, S., Dolag, K., & Matteucci, F. 2007, *MNRAS*, 382, 1050
- Tremonti, C. A., Heckman, T. M., Kauffmann, G., et al. 2004, *ApJ*, 613, 898
- Truelove, J. K., Klein, R. I., McKee, C. F., et al. 1997, *ApJ*, 489, L179
- Tsujimoto, T., Nomoto, K., Yoshii, Y., et al. 1995, *Monthly Notices of the Royal Astronomical Society*, 277, 945
- Turk, M. J., Abel, T., & O'Shea, B. 2009, *Science*, 325, 601
- Umeda, H. & Nomoto, K. 2002, *ApJ*, 565, 385
- Vargas, L. C., Geha, M., Kirby, E. N., & Simon, J. D. 2013, *ApJ*, 767, 134
- Vazdekis, A., Casuso, E., Peletier, R. F., & Beckman, J. E. 1996, *ApJS*, 106, 307
- Venn, K. A., Starkenburg, E., Malo, L., Martin, N., & Laevens, B. P. M. 2017, *MNRAS*, 466, 3741
- Wheeler, C., Hopkins, P. F., Pace, A. B., et al. 2019, *Monthly Notices of the Royal Astronomical Society*, 490, 4447
- Wiersma, R. P. C., Schaye, J., Theuns, T., Dalla Vecchia, C., & Tornatore, L. 2009, *MNRAS*, 399, 574
- Wyithe, J. S. B. & Loeb, A. 2006, *Nature*, 441, 322
- Yoshida, N., Hosokawa, T., & Omukai, K. 2012, *Progress of Theoretical and Experimental Physics*, 2012, 01A305

Appendix A: Determining [Fe/H] for simulated galaxies

Properly attributing a stellar metallicity to each simulated dwarf galaxy is essential in this work. Knowing the metallicity of each stellar particle, the dwarf metallicity is usually computed by taking the mean, the median, or the mode of the MDF. By taking the mean or the median, one would, however, strongly underestimate the system metallicity, owing to the presence of stars with very low metallicity in simulations that contain only Pop II stars. Taking the mode is more appropriate but this may be hardly determined in noisy MDFs. Increasing the number of metallicity bins will help, although at the expense of the precision.

We used a method where the galaxy stellar metallicity is derived from the mode of a fit to the MDF. The fitting function was chosen as the MDF predicted by a simple chemical evolution model that assumes an instantaneous recycling (see [Pagel 1997](#)):

$$\frac{dN}{d[\text{Fe}/\text{H}]} \propto 10^{[\text{Fe}/\text{H}]} \exp\left(-\frac{10^{[\text{Fe}/\text{H}]}}{p}\right). \quad (\text{A.1})$$

Here, p is a free parameter that is related to the position of the MDF mode by the relation $[\text{Fe}/\text{H}]_{\text{mode}} = p \ln(10)$. Fig. A.1 illustrates the application of the method on three different dwarfs. It demonstrates its ability to derive a reliable mode, even if the histogram is noisy or if a large peak is found outside the main range of the MDF.

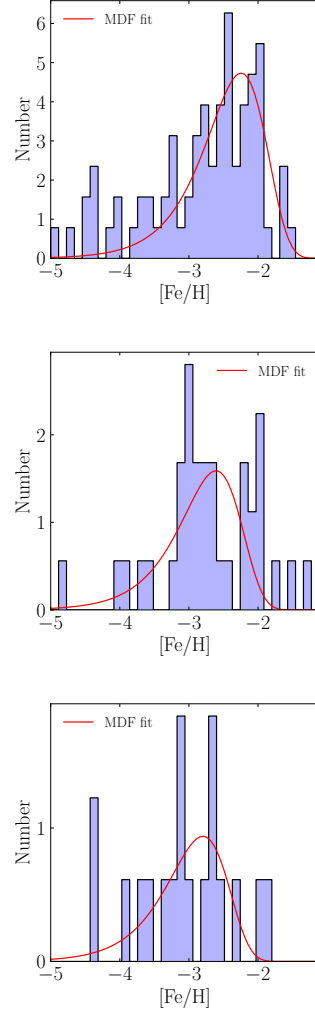


Fig. A.1. Application of the fitting method on three UFDs of decreasing luminosity (from left to right, $L_V = 3.9 \cdot 10^4 L_\odot$, $L_V = 1.9 \cdot 10^4 L_\odot$, and $L_V = 1.0 \cdot 10^4 L_\odot$). The MDF fit given by Eq. A.1 is displayed in red.

Chapter 8

Conclusions & Prospects

In the last chapters I have presented the papers I have written as first-author over the course of my PhD. In the following, I briefly review the main findings of these studies. In the end, I present an outlook on the continuation of this research I foresee.

8.1 Summary

The main focus of the study described in Chapter 5 is to answer the following question: How did the cosmology in the early-Universe, in particular primordial magnetic fields, impact the formation and evolution of the first galaxies? For that, I introduced the modified multi-scale initial conditions generated for this study, which is a realistic representation of the cosmological and galactic scales at high redshifts. The formation and evolution of dark matter halos and galaxies inhabiting them is then followed from this initial stage to redshift $z = 0$, and compared to the present-day dwarf satellites orbiting around the MW and M31.

Each type of simulation in this study reveals a unique aspect regarding the impact of primordial magnetic fields. The main finding from dark matter only simulations, is a higher number of substructures, which means more potential hosts for dwarfs. This is translated as a boosted number of dark halos around the MW able to form a satellite galaxy. Hydro-dynamical simulations, on the other hand, reveal the dynamical properties of stellar populations in each galaxy. The main finding of these simulations is an earlier onset of star formation, induced by primordial magnetic fields. The combination of the latter with a higher rate of forming stars leads to a large amount of ionizing photons at high redshifts.

The primary conclusion of this study is that strong magnetic fields characterized by a high amplitude ($B_\lambda = 0.20, 0.50$ nG with $n_B = -2.9$) or by a steep initial power spectrum

slope ($n_B = -2.1, -2.4$, with $B_\lambda = 0.05$ nG) induce perturbations in the mass scales from 10^7 to $10^9 M_\odot$. In this context emerging galaxies see their star formation rate strongly boosted. They become more luminous and metal rich than their counterparts without primordial magnetic fields. Such strong fields are ruled out by their inability to reproduce the observed scaling relations of dwarf galaxies. Besides overproducing luminous satellites in the Local Group, they predict dwarf galaxies to be at the origin of an unrealistically early reionization of the Universe. While, weaker magnetic fields impacting the primordial density field at corresponding masses $\lesssim 10^6 M_\odot$, produce a large number of dark minihalos orbiting dwarfs, these are however out of reach for current lensing observations.

This study thus introduced the novel approach of realistic galactic cosmological simulations for constraining the properties of primordial magnetic fields, which then inspired further research in this domain.

Following this study, a remaining question was the net effect of primordial magnetic fields on structure formation, as opposed to the direct impact of magnetic pressure on the ISM of galaxies. In Chapter 6, I introduced the simulation setup required to address both aspects, simultaneously. The magnetic field is uniformly initialized with a given strength, and the cosmology is imposed by the standard Λ CDM paradigm. This is then compared to the second setup which includes the effect of primordial fields through modifying the classical cosmology.

The main finding of the first setup is that magnetic fields of initial strength $B_\lambda \geq 0.10$ nG, have a non-negligible contribution in shaping the evolution of dwarf galaxies. The reason is the shallower gravitational potential in low mass dwarfs, contrary to that of more massive galaxies. Thus this additional pressure, not only decreases the stellar mass immensely, but also delays the onset of star formation. A strong field, when present, may even prevent the formation of stellar particles in small mass halos altogether.

The unique aspect of the second setup is that the primordial impact of magnetic fields is equally considered as its later-time contribution in the ISM energy budget. Depending on the strength of the field, the main halo of a dwarf galaxy or the number of its subhalos are influenced. When the affected mass range is comparable to a dwarf halo, a stronger gravitational potential may merge the satellite subhalos and further increase the mass content of the forming galaxy. In general, primordial fields speed up the formation of the first dark halos, leading to an earlier and higher rate star formation.

One interesting outcome of this study was introducing the present-time observable properties of dwarf galaxies as an indicator for the impact of magnetic fields. In a Universe with a strong primordial magnetic field, dwarf galaxies are on average $\sim 80\%$ brighter and have a $\sim 50\%$ higher velocity dispersions than those of a similar halo mass forming in a standard cosmology.

The main conclusion of this study is that the impact of primordial magnetic fields in initiating the structure formation dominates its later impact in increasing the turbulence and pressure support in the ISM. In addition, we showed that simulations with a strong magnetization ($B_\lambda = 0.20$ and 0.50 nG) serve as evidence for a pronounced growth of the magnetic energy. This steep increase leads to the timescale of the magnetic field saturation to be as short as a few hundreds of Myr. These trends are independent of the initial conditions, regardless of whether it is the classical Λ CDM or modified by primordial magnetic fields. However, the growth rate is steeper in models forming from the latter one.

Finally, combining distinct aspects of dwarf galaxy simulations with the results obtained in chapters 5 and 6, I could also address the question of how the faintest galactic systems formed and chemically evolved. For answering that, in Chapter 7, I introduced the character of first stars in the metal enrichment of these so-called UFDs. One unique aspect of UFD galaxies is their extremely short star formation history. This results in an old stellar population, dominated by metal-poor stars. In small mass UFDs, for which star formation is completely quenched after 1 Gyr, 86% of stars are formed from pristine gas. The evolution of UFDs is therefore strongly influenced by the first generation of stars.

In this study, I introduced the setup of zoom-in chemo-dynamical simulations generated for nineteen host halos of dwarf galaxies. These halos are extracted from a Λ CDM cosmological box and then their evolution is followed down to redshift $z = 0$. These model galaxies were validated not only on the basis of global properties observable in the Local Group, but also on the detailed investigation of the stellar abundance ratios. The impact of PopIII stars on the final metallicity of UFDs is evaluated by considering different IMFs, the influence of PISNe and their energetic feedback, as well as the metallicity threshold that marks the transition from the first massive stars to the formation of low-mass long-lived stars.

The main conclusions of this study are on one hand that the inclusion of PopIII stars with masses below $140 M_\odot$, and a standard IMF slope of -1.3 increases the global metallicity of UFDs, albeit insufficient to resolve the tension with the observations. PISNe on the other hand, with progenitor masses between $140 M_\odot$ and $300 M_\odot$, increase the production of iron. However, PISNe are rare events and occasionally absent in the faintest UFDs, therefore they have a limited impact on the global luminosity-metallicity relation.

Despite a limited number of spectroscopically confirmed members in UFDs, that make the stellar metallicity distribution of some UFDs uncertain, our analysis revealed that this is essentially the metal-rich tail that is missing in the models. The remaining challenges are thus both observational and numerical: (i) to extend high resolution spectroscopy data samples and confirm the mean metallicity of the faintest UFDs, (ii) to explain the presence of chemically enriched stars in galaxies with very short star formation histories.

8.2 Outlook

The results presented in this thesis open up several new avenues of research. Here I present three future projects, that are building on my results and that I wish to pursue.

8.2.1 The impact of primordial magnetic fields on reionization

Dwarf galaxies are the primary candidates to host the first stars and to be the dominant sources of reionization. However, the formation and evolution of dwarf galaxies can be significantly changed depending on the assumptions concerning the primordial magnetic fields. Relying on the results obtained in Chapter 5 and 6, one logical future objective would be to address the two following questions regarding the role played by primordial magnetic fields in the context of reionization:

- How does the pressure support provided by magnetic fields modify the structure of the multi-phase ISM, and change the fraction of ionizing photons that escape galaxies?
- How do density perturbations generated by magnetic fields on small-scales affect the formation of dwarf galaxies, which represent the dominant sources of ionization in the Universe?

Multiple efforts in recent years to answer these questions can be categorized as (i) simulations that model reionization on large-scale to accurately predict the 21cm signal or, (ii) those that simulate much smaller proto-stellar scales, focusing on the mass function of the first stars. I intend to leverage my expertise in cosmological galaxy formation simulations to bridge these two. The unique aspects of this study will be: obtaining the high resolution required to resolve the propagation of radiation through the ISM with the zoom-in technique, direct implementation of first stars to include the inhomogeneity in the reionization history, and a complete sample of dark halos.

The upcoming data from JWST represents a new and unique opportunity to answer these questions. It will constrain the faint-end slope of the UV luminosity function at high redshift, as well as the escape fraction of ionizing photons, which is key to the role of low-mass galaxies in reionizing the Universe. By comparing simulated models to these constraints, I will be able to show the impact of primordial magnetic fields on both reionization history and the primary sources responsible for it.

The main outcome of this work will be to further develop the hydrodynamical zoom-in studies of the EoR (Kimm et al. 2017). This way it is possible to disentangle the primordially and astrophysically sourced impact of magnetic fields on the formation sites of the first massive stars. The unique aspect of this work compared to large-scale simulations is resolving the first dark halos down to $10^6 M_\odot$, well below the atomic cooling limit. This

is essential to study the formation of first stars from single or multiple sites with magnetized initial conditions, and the local effect of supernovae feedback on individual halos. Additionally, direct inclusion of Pop III stars will allow me to accurately track the early chemical enrichment provided by the first generation of stars forming from pristine gas. Compared to isolated small-scale simulations, this study allows for a realistic hierarchical growth of galaxies through mergers and interactions between halos, thereby accounting for environmental effects.

Regarding the methods employed in this, I plan to run all the simulations using **RAMSES-RT**. One of the unique aspects of the updated version of this code is the inclusion of radiative transfer and early-Universe chemistry, allowing for a more accurate modeling of the effects of stellar feedback. This aspect is specifically important in chasing the emitted ionizing photons of Pop III stars during the EoR. The other unique aspect is the comprehensive magneto-hydrodynamics suite, designed to self-consistently model: (i) the formation and evolution of galaxies emerging from a magnetically-distorted matter power spectrum, (ii) the growth and amplification of uniform primordial magnetic fields, and (iii) non-uniform magnetic fields varying in accordance to the spectral index.

I envision to first run an inexpensive and straightforward set of dark matter only simulations in a $(5 \text{ Mpc}/h)^3$ box, ideal for the formation of dwarf galaxies in a wide mass range, without sacrificing the resolution. Using the **Rockstar** halo finder (Behroozi et al. 2013b), we will identify regions hosting dwarf halos (Safarzadeh et al. 2018) at redshift $6 \leq z \leq 11$. This will provide a complete dark halo sample at the EoR.

Next, the hydrodynamical initial conditions for the zoom-in regions will be generated, increasing the dark matter resolution from $\sim 10^5$ to $10^3 M_\odot$. Throughout the course of the simulation, we will allow the adaptive mesh to refine when either the Jeans length is not resolved, or the dark or baryonic mass of the cell grows. I will achieve a maximum physical resolution of 0.7 pc at $z = 6$. This makes our simulations more robust than previous studies (Katz et al. 2021; Rosdahl et al. 2022), as the turbulent properties of gas can be more accurately captured.

In the last step, I plan to attribute to each dark halo a corresponding galaxy, matching its virial mass (Rosdahl et al. 2018). This will enable me to derive the UV escape fractions of galaxies embedded in dark halos using the Monte-Carlo radiative transfer code **Rascas** (Michel-Dansac et al. 2020), with the luminosities of stellar particles as a function of age and metallicity.

There are a few risks involved in this plan. All the dwarf galaxies in this work are expected to be modeled in a cosmological context but without interacting with a MW-like galaxy. The risk is that by not including the perturbative effects of the MW I will generate an unrealistic halo mass function. To mitigate this issue I can use the cumulative number of dark matter halos predicted in the **AURIGA** simulations (Grand et al. 2021). Thus

integrating the dark halo mass function with the luminosity-halo mass relation I can arrive at the number of dwarf galaxies inside 300 kpc which can be compared to detected satellites in the Dark Energy Survey and Pan-STARRS1 (Drlica-Wagner et al. 2020). The other potential risk involves modelling a more efficient small-scale dynamo (Kazantsev 1968) which is acting at higher resolution. This would likely lead to stronger amplification of magnetic fields and influence gas dynamics (Sijacki et al. 2012; Whittingham et al. 2021). I plan to explore the importance of this latter with a resolution study (simulations run at lower resolution).

8.2.2 New probe for modifications to the Λ CDM cosmology

After showing the impact of magnetic fields on the formation of the first stars and galaxies in a cold dark matter Universe, I plan to study this phenomenon in the context of other dark matter models. The goal is to examine if the alternatives to Λ CDM are still able to resolve tensions between the standard model of cosmology and Local Group observations once magnetic fields have been included. I plan to compare how the three most studied dark matter scenarios (cold, warm and self-interacting) affect the assembly histories as well as the central density structure in fully magneto-hydrodynamical simulations of dwarf galaxies.

The main outcome I expect to obtain this study is deriving the gas and dark matter profile of simulated model galaxies, as well as the circular velocity function of their subhalos. With a comparison to the dynamical masses which will be obtained from emission line widths (using rest-UV and rest-optical bands as well as $H\alpha$ spectroscopy) from JWST observations, I would like to show how the bulk properties of the first galaxies respond to modifications in the standard model. The unique aspect of this work is to spatially resolve the rotation curves in the central regions of small dwarf galaxies, which can provide a way to distinguish between different dark matter candidates.

The preliminary challenge in this study will be to generate the initial conditions imposed after inflation, which determine the first structures in each dark matter Universe. To do so, I will use a modified version of the CAMB code (Shaw & Lewis 2012), including the influence of magnetic fields on the total matter power spectrum. In this version the non-linear effects of the magnetic Jeans length (magnetic pressure) and the damping due to the radiation viscosity (when the photon free streaming length is small) are both explicitly computed (see Chapter 3.3 for a detailed discussion). Consequently, and contrary to other studies (Kunze & Komatsu 2015), there is no need to artificially include a cutoff wave number.

For evolving galaxies from the generated initial conditions, I will benefit from the calibrated simulation setup of the first phase of 8.2.1. From this suite, I will use the zoom-in technique to resolve the internal structure of eight halos chosen to have virial masses between 10^8

and $10^{10}M_{\odot}$. To make a proper comparison with observations, I will compute the circular velocities in a similar fashion to how they are calculated for observed dwarf galaxies. For each dwarf I will compute the dynamical mass contained within the 3D half-mass radius, using the line-of-sight velocity dispersion (Wolf et al. 2010). As radiative transfer is not expected to play a crucial role in this study, due to the computational costs, I will use the non-RT version of the code `Ramses` for this work.

8.2.3 Pre-enrichment of dwarfs before the formation of the Milky Way

With the detailed information about the stellar population and internal structure of dwarfs delivered by 8.2.1 and 8.2.2, respectively, an immediate objective will be to address the elusive enrichment of these metal-poor systems in the early stages of galaxy formation. I will endeavor to answer the open question of the main origin for the strong deviation - nearly 2 dex - of cosmological simulations from the faint end of the observed luminosity-metallicity relation, discussed in Chapter 7.

I would like to determine whether the enrichment of UFD galaxies occurs environmentally, during the formation of the MW and M31 host. But how can we deduce the metal-enrichment occurring during the process of galaxy formation from the upcoming spectroscopic data of JWST NIRSpec, which will measure the metallicity of the faintest galaxies? The method I envisioned is to derive the fraction of metals produced in a MW-like galaxy at redshift $z > 6$ escaping to a ~ 100 kpc physical radius. That can then be compared to the JWST spectroscopic line ratios for measuring the gas-phase metallicity of faint galaxies at $z > 3$. This way I should be able to obtain strong constraints on the metal-enrichment models during the hierarchical process of galaxy formation.

The main task in this work is to examine the primeval environment of the spiral host galaxy. For that, I can benefit from the suite of high-resolution MW simulations (the AGORA project) obtained using seven contemporary astrophysical codes (Roca-Fàbrega et al. 2021), including `GEAR` and `Ramses`. This powerful suite allows a comparison of different simulations and allows one to reach robust conclusions, which are not sensitive to the implementation of the physics in different codes. The method involves looking back in time through the entire snapshots of each simulation to obtain the merging history of dwarf galaxies with $M_{\text{vir}} < 10^9$ located within the MW halo. This way I will estimate the region polluted by stars forming from the gas reservoir of the central halo. A complementary probe for this task is to compare the proper motion of halos which resemble the dark matter halos of the faintest dwarfs to the recent Gaia observations (Hammer et al. 2021).

Chapter 9

Bibliography

- 2013, *Astrophysics and Space Science Library*, Vol. 396, The First Galaxies
- Abazajian, K. 2006, , 73, 063506
- Abel, T., Bryan, G. L., & Norman, M. L. 2002, *Science*, 295, 93
- Adams, F. C. & Fatuzzo, M. 1996, , 464, 256
- Ade, P. A. R., Arnold, K., Atlas, M., et al. 2015, , 92, 123509
- Agertz, O., Pontzen, A., Read, J. I., et al. 2020, , 491, 1656
- Anderhalden, D., Schneider, A., Macciò, A. V., Diemand, J., & Bertone, G. 2013, , 2013, 014
- Appel, J. A., Bagnaia, P., Banner, M., et al. 1985, *Physics Letters B*, 160, 349
- Applebaum, E., Brooks, A. M., Christensen, C. R., et al. 2021, , 906, 96
- Barkat, Z., Rakavy, G., & Sack, N. 1967, , 18, 379
- Barnes, J. & Hut, P. 1986, , 324, 446
- Bartelmann, M. & Schneider, P. 2001, , 340, 291
- Bastian, N., Covey, K. R., & Meyer, M. R. 2010, , 48, 339
- Battaglia, G., Helmi, A., Tolstoy, E., et al. 2008, , 681, L13
- Behroozi, P. S., Wechsler, R. H., & Conroy, C. 2013a, , 770, 57
- Behroozi, P. S., Wechsler, R. H., & Wu, H.-Y. 2013b, , 762, 109
- Bertone, S., Vogt, C., & Enßlin, T. 2006, , 370, 319
- Bertschinger, E. 1985, , 58, 39

- Biermann, L. 1950, *Zeitschrift Naturforschung Teil A*, 5, 65
- Binggeli, B., Sandage, A., & Tammann, G. A. 1985, , 90, 1681
- Bode, P., Ostriker, J. P., & Turok, N. 2001, , 556, 93
- Bovill, M. S. & Ricotti, M. 2009, , 693, 1859
- Bovino, S., Schleicher, D. R. G., & Schober, J. 2013, *New Journal of Physics*, 15, 013055
- Bowman, J. D., Rogers, A. E. E., Monsalve, R. A., Mozdzen, T. J., & Mahesh, N. 2018, , 555, 67
- Boyarsky, A., Drewes, M., Lasserre, T., Mertens, S., & Ruchayskiy, O. 2019, *Progress in Particle and Nuclear Physics*, 104, 1
- Boyarsky, A., Fröhlich, J., & Ruchayskiy, O. 2012, , 108, 031301
- Boylan-Kolchin, M., Bullock, J. S., & Kaplinghat, M. 2011, , 415, L40
- Boylan-Kolchin, M., Bullock, J. S., Sohn, S. T., Besla, G., & van der Marel, R. P. 2013, , 768, 140
- Boylan-Kolchin, M., Springel, V., White, S. D. M., Jenkins, A., & Lemson, G. 2009, , 398, 1150
- Bromm, V., Coppi, P. S., & Larson, R. B. 1999, , 527, L5
- Bromm, V., Coppi, P. S., & Larson, R. B. 2002, , 564, 23
- Bryan, G. L. & Norman, M. L. 1998, , 495, 80
- Bullock, J. S. & Boylan-Kolchin, M. 2017, , 55, 343
- Bullock, J. S., Kolatt, T. S., Sigad, Y., et al. 2001, , 321, 559
- Bullock, J. S., Kravtsov, A. V., & Weinberg, D. H. 2000, , 539, 517
- Burkert, A. 2000, , 534, L143
- Calabrese, E. & Spergel, D. N. 2016, , 460, 4397
- Carigi, L. 2011, *Initial Mass Function*, ed. M. Gargaud, R. Amils, J. C. Quintanilla, H. J. J. Cleaves, W. M. Irvine, D. L. Pinti, & M. Viso (Berlin, Heidelberg: Springer Berlin Heidelberg), 814–814
- Carlberg, R. G. 1981, , 197, 1021
- Carlson, E. D., Machacek, M. E., & Hall, L. J. 1992, , 398, 43
- Chabrier, G. 2003, , 115, 763

- Chluba, J., Paoletti, D., Finelli, F., & Rubiño-Martín, J. A. 2015, , 451, 2244
- Cooke, R. J., Pettini, M., Jorgenson, R. A., Murphy, M. T., & Steidel, C. C. 2014, , 781, 31
- Cooley, J. W. & Tukey, J. W. 1965, *Mathematics of computation*, 19, 297
- Courant, R., Friedrichs, K., & Lewy, H. 1928, *Mathematische Annalen*, 100, 32
- Croft, R. A. C., Weinberg, D. H., Bolte, M., et al. 2002, , 581, 20
- Cullen, L. & Dehnen, W. 2010, , 408, 669
- Cyr-Racine, F.-Y., Sigurdson, K., Zavala, J., et al. 2016, , 93, 123527
- de Blok, W. J. G. & Bosma, A. 2002, , 385, 816
- de Blok, W. J. G., Walter, F., Brinks, E., et al. 2008, , 136, 2648
- Dehnen, W. 2000, , 536, L39
- Demorest, P. B., Pennucci, T., Ransom, S. M., Roberts, M. S. E., & Hessels, J. W. T. 2010, , 467, 1081
- Diemand, J., Kuhlen, M., Madau, P., et al. 2008, , 454, 735
- Dodelson, S. 2003, *Modern cosmology* (Elsevier)
- Dodelson, S. & Widrow, L. M. 1994, , 72, 17
- D’Onghia, E. & Burkert, A. 2003, , 586, 12
- Drlica-Wagner, A., Bechtol, K., Mau, S., et al. 2020, , 893, 47
- Drlica-Wagner, A., Bechtol, K., Rykoff, E. S., et al. 2015, , 813, 109
- Dubinski, J. & Carlberg, R. G. 1991, , 378, 496
- Durrer, R. 2007, , 51, 275
- Eisenstein, D. J. 1997, *arXiv e-prints*, astro
- Eisenstein, D. J. & Hu, W. 1998, , 496, 605
- Eisenstein, D. J., Zehavi, I., Hogg, D. W., et al. 2005, , 633, 560
- Elbert, O. D., Bullock, J. S., Garrison-Kimmel, S., et al. 2015, , 453, 29
- Errani, R., Peñarrubia, J., & Walker, M. G. 2018, , 481, 5073
- Fan, X., Strauss, M. A., Becker, R. H., et al. 2006, , 132, 117

- Faucher-Giguère, C.-A., Prochaska, J. X., Lidz, A., Hernquist, L., & Zaldarriaga, M. 2008, , 681, 831
- Feng, J. L., Kaplinghat, M., & Yu, H.-B. 2010, , 104, 151301
- Fillmore, J. A. & Goldreich, P. 1984, , 281, 1
- Fowler, W. A. 1964, *Reviews of Modern Physics*, 36, 545
- Freese, K., Bodenheimer, P., Spolyar, D., & Gondolo, P. 2008, , 685, L101
- Fu, L., Semboloni, E., Hoekstra, H., et al. 2008, , 479, 9
- Furlanetto, S. R. & Loeb, A. 2001, , 556, 619
- Furlanetto, S. R., Oh, S. P., & Briggs, F. H. 2006, , 433, 181
- Garavito-Camargo, N., Patel, E., Besla, G., et al. 2021, , 923, 140
- Gardner, J. P., Mather, J. C., Clampin, M., et al. 2006, , 123, 485
- Garrison-Kimmel, S., Boylan-Kolchin, M., Bullock, J. S., & Kirby, E. N. 2014, , 444, 222
- Glover, S. 2013, in *Astrophysics and Space Science Library*, Vol. 396, *The First Galaxies*, ed. T. Wiklind, B. Mobasher, & V. Bromm, 103
- Glover, S. C. O. & Abel, T. 2008, , 388, 1627
- Glover, S. C. O., Clark, P. C., Klessen, R. S., & Bromm, V. 2010, *arXiv e-prints*, arXiv:1007.2763
- Goldreich, P. & Weber, S. V. 1980, , 238, 991
- Grand, R. J. J., Marinacci, F., Pakmor, R., et al. 2021, , 507, 4953
- Green, A. M., Hofmann, S., & Schwarz, D. J. 2005, , 2005, 003
- Greif, T. H., Springel, V., White, S. D. M., et al. 2011, , 737, 75
- Haiman, Z., Abel, T., & Madau, P. 2001, , 551, 599
- Hammer, F., Wang, J., Pawlowski, M. S., et al. 2021, , 922, 93
- Harrison, E. R. 1970, , 1, 2726
- Heger, A. 2012, in *Astrophysics and Space Science Library*, Vol. 384, *Eta Carinae and the Supernova Impostors*, ed. K. Davidson & R. M. Humphreys, 299
- Hirano, S., Umeda, H., & Yoshida, N. 2011, , 736, 58
- Hockney, R. W. & Eastwood, J. W. 1988, *Computer simulation using particles*

- Hogan, C. J. 1983, , 51, 1488
- Hosono, N., Saitoh, T. R., & Makino, J. 2016, , 224, 32
- Iben, I., J. & Tutukov, A. V. 1984, , 54, 335
- Iocco, F. 2008, , 677, L1
- Ishiyama, T., Nitadori, K., & Makino, J. 2012, arXiv e-prints, arXiv:1211.4406
- Jeans, J. H. 1902, Philosophical Transactions of the Royal Society of London Series A, 199, 1
- Jedamzik, K., Katalinić, V., & Olinto, A. V. 1998, , 57, 3264
- Jeon, M., Besla, G., & Bromm, V. 2017, , 848, 85
- Jethwa, P., Erkal, D., & Belokurov, V. 2018, , 473, 2060
- Kaplinghat, M., Tulin, S., & Yu, H.-B. 2016, , 116, 041302
- Karachentsev, I. D., Karachentseva, V. E., Huchtmeier, W. K., & Makarov, D. I. 2004, , 127, 2031
- Karachentsev, I. D., Makarov, D. I., & Kaisina, E. I. 2013, , 145, 101
- Katz, H., Martin-Alvarez, S., Rosdahl, J., et al. 2021, , 507, 1254
- Kazantsev, A. P. 1968, Soviet Journal of Experimental and Theoretical Physics, 26, 1031
- Khokhlov, A. 1998, Journal of Computational Physics, 143, 519
- Kim, E.-J., Olinto, A. V., & Rosner, R. 1996, , 468, 28
- Kimm, T., Katz, H., Haehnelt, M., et al. 2017, , 466, 4826
- Kippenhahn, R., Weigert, A., & Weiss, A. 2013, Stellar Structure and Evolution
- Klessen, R. 2019, in Formation of the First Black Holes, ed. M. Latif & D. Schleicher, 67–97
- Klypin, A. A. & Shandarin, S. F. 1983, , 204, 891
- Kobayashi, C., Tsujimoto, T., & Nomoto, K. 2000, , 539, 26
- Koch, A. & Grebel, E. K. 2006, , 131, 1405
- Kolb, E. W. & Turner, M. S. 1990, , 80, 381
- Koposov, S. E., Belokurov, V., Torrealba, G., & Evans, N. W. 2015, , 805, 130
- Kroupa, P. 2002, Science, 295, 82

- Kroupa, P., Theis, C., & Boily, C. M. 2005, , 431, 517
- Kroupa, P., Tout, C. A., & Gilmore, G. 1993, , 262, 545
- Krumholz, M. R., Klein, R. I., McKee, C. F., Offner, S. S. R., & Cunningham, A. J. 2009, *Science*, 323, 754
- Kudritzki, R.-P. & Puls, J. 2000, , 38, 613
- Kuhlen, M., Madau, P., & Silk, J. 2009, *Science*, 325, 970
- Kunze, K. E. & Komatsu, E. 2015, , 2015, 027
- Kurita, T. & Takada, M. 2022, , 105, 123501
- Lacey, C. & Cole, S. 1993, , 262, 627
- Landau, L. D. & Lifshitz, E. M. 1987, *Fluid Mechanics*
- Larson, R. B. 1998, , 301, 569
- Latif, M. A., Schleicher, D. R. G., Schmidt, W., & Niemeyer, J. 2013, , 433, 1607
- Laureijs, R., Amiaux, J., Arduini, S., et al. 2011, arXiv e-prints, arXiv:1110.3193
- Lepp, S. & Shull, J. M. 1984, , 280, 465
- Li, Y.-S. & Helmi, A. 2008, , 385, 1365
- Linde, A. D. 1990, *Particle physics and inflationary cosmology*
- Loeb, A. 2010, *How Did the First Stars and Galaxies Form?*
- Loeb, A. & Weiner, N. 2011, , 106, 171302
- Lovell, M. R., Eke, V., Frenk, C. S., et al. 2012, , 420, 2318
- Lucy, L. B. 1977, , 82, 1013
- Luhman, K. L., Mamajek, E. E., Allen, P. R., & Cruz, K. L. 2009, , 703, 399
- Machida, M. N. & Doi, K. 2013, , 435, 3283
- Machida, M. N., Inutsuka, S.-i., & Matsumoto, T. 2008, , 676, 1088
- Massey, P. 2003, , 41, 15
- Mather, J. C., Cheng, E. S., Cottingham, D. A., et al. 1994, , 420, 439
- Mayer, L. 2022, *Journal of Physics G Nuclear Physics*, 49, 063001
- McConnachie, A. W. 2012, , 144, 4

- McDowell, M. R. C. 1961, *The Observatory*, 81, 240
- McGaugh, S. S., Rubin, V. C., & de Blok, W. J. G. 2001, , 122, 2381
- Michel-Dansac, L., Blaizot, J., Garel, T., et al. 2020, , 635, A154
- Miralda-Escudé, J. 2002, , 564, 60
- Monaghan, J. J. & Gingold, R. A. 1983, *Journal of Computational Physics*, 52, 374
- Moore, B., Ghigna, S., Governato, F., et al. 1999, , 524, L19
- Moster, B. P., Somerville, R. S., Maubetsch, C., et al. 2010, , 710, 903
- Müller, O., Pawlowski, M. S., Jerjen, H., & Lelli, F. 2018, *Science*, 359, 534
- Müller, O., Pawlowski, M. S., Lelli, F., et al. 2021, , 645, L5
- Müller, O., Scalera, R., Binggeli, B., & Jerjen, H. 2017, , 602, A119
- Munshi, D., Valageas, P., van Waerbeke, L., & Heavens, A. 2008, , 462, 67
- Narlikar, J. V. 2002, *An introduction to cosmology*
- Navarro, J. F., Frenk, C. S., & White, S. D. M. 1997, , 490, 493
- Neronov, A. & Vovk, I. 2010, *Science*, 328, 73
- Nguyen, N. H. T., Bui, H. H., & Nguyen, G. D. 2020, *International Journal for Numerical and Analytical Methods in Geomechanics*, 44, 1525
- Nomoto, K. 1982, in *NATO Advanced Study Institute (ASI) Series C, Vol. 90, Supernovae: A Survey of Current Research*, ed. M. J. Rees & R. J. Stoneham, 205–213
- Nomoto, K., Kobayashi, C., & Tominaga, N. 2013, , 51, 457
- Oñorbe, J., Boylan-Kolchin, M., Bullock, J. S., et al. 2015, , 454, 2092
- Oh, S.-H., de Blok, W. J. G., Brinks, E., Walter, F., & Kennicutt, Robert C., J. 2011, , 141, 193
- Ôki, T., Fujimoto, M., & Hitotuyanagi, Z. 1964, *Progress of Theoretical Physics Supplement*, 31, 77
- Oman, K. A., Marasco, A., Navarro, J. F., et al. 2019, , 482, 821
- Oman, K. A., Navarro, J. F., Fattahi, A., et al. 2015, , 452, 3650
- Ostriker, J. P. & Steinhardt, P. J. 1995, , 377, 600
- Padmanabhan, T. 2002, *Theoretical Astrophysics - Volume 3, Galaxies and Cosmology*, Vol. 3

- Pandey, K. L., Choudhury, T. R., Sethi, S. K., & Ferrara, A. 2015, , 451, 1692
- Pandey, K. L. & Sethi, S. K. 2012, , 748, 27
- Pandey, K. L. & Sethi, S. K. 2013, , 762, 15
- Pawlowski, M. S., Kroupa, P., Angus, G., et al. 2012, , 424, 80
- Peebles, P. J. E. 1980, The large-scale structure of the universe
- Peebles, P. J. E. 1982, , 263, L1
- Peebles, P. J. E. 1993, Principles of Physical Cosmology
- Peebles, P. J. E. & Dicke, R. H. 1968, , 154, 891
- Peebles, P. J. E. & Yu, J. T. 1970, , 162, 815
- Penzias, A. A. & Wilson, R. W. 1965, , 142, 419
- Piddington, J. H. 1964, , 128, 345
- Planck Collaboration, Ade, P. A. R., Aghanim, N., et al. 2016, , 594, A13
- Poirier, S. 2004, PhD thesis, Universite de Strasbourg Louis Pasteur, France
- Pontzen, A. & Governato, F. 2012, , 421, 3464
- Pritchard, J. R. & Loeb, A. 2012, Reports on Progress in Physics, 75, 086901
- Ratra, B. 1992, , 391, L1
- Read, J. I. & Hayfield, T. 2012, , 422, 3037
- Rebull, L. M., Padgett, D. L., McCabe, C. E., et al. 2010, , 186, 259
- Revaz, Y. & Jablonka, P. 2012, , 538, A82
- Revaz, Y. & Jablonka, P. 2018, , 616, A96
- Revaz, Y., Jablonka, P., Teyssier, R., & Mayer, L. 2016, Star Formation in Galaxy Evolution: Connecting Numerical Models to Reality, Star Formation in Galaxy Evolution: Connecting Numerical Models to Reality, Saas-Fee Advanced Course, Volume 43. ISBN 978-3-662-47889-9. Springer-Verlag Berlin Heidelberg, 2016.
- Richardson, J. C., Irwin, M. J., McConnachie, A. W., et al. 2011, , 732, 76
- Robles, V. H., Bullock, J. S., Elbert, O. D., et al. 2017, , 472, 2945
- Roca-Fàbrega, S., Kim, J.-H., Hausammann, L., et al. 2021, , 917, 64
- Rocha, M., Peter, A. H. G., Bullock, J. S., et al. 2013, , 430, 81

- Rosdahl, J., Blaizot, J., Katz, H., et al. 2022, , 515, 2386
- Rosdahl, J., Katz, H., Blaizot, J., et al. 2018, , 479, 994
- Rosen, S. R., Webb, N. A., Watson, M. G., et al. 2016, , 590, A1
- Rosswog, S., Davies, M. B., Thielemann, F. K., & Piran, T. 2000, , 360, 171
- Safarzadeh, M., Ji, A. P., Dooley, G. A., et al. 2018, , 476, 5006
- Saio, H. & Nomoto, K. 1985, , 150, L21
- Saio, H. & Nomoto, K. 1998, , 500, 388
- Sales, L. V., Wetzel, A., & Fattahi, A. 2022, *Nature Astronomy*, 6, 897
- Salpeter, E. E. 1955, , 121, 161
- Samuel, J., Wetzel, A., Chapman, S., et al. 2021, , 504, 1379
- Sandage, A. & Binggeli, B. 1984, , 89, 919
- Santos-Santos, I. M. E., Fattahi, A., Sales, L. V., & Navarro, J. F. 2021, , 504, 4551
- Saslaw, W. C. & Zipoy, D. 1967, , 216, 976
- Sawala, T., Frenk, C. S., Fattahi, A., et al. 2016, , 457, 1931
- Schober, J., Rogachevskii, I., & Brandenburg, A. 2022, , 128, 065002
- Segretain, L., Chabrier, G., & Mochkovitch, R. 1997, , 481, 355
- Seljak, U., Makarov, A., McDonald, P., et al. 2005, , 71, 103515
- Sethi, S. K. & Subramanian, K. 2005, , 356, 778
- Sethi, S. K. & Subramanian, K. 2009, , 2009, 021
- Shaw, J. R. & Lewis, A. 2012, , 86, 043510
- Shen, K. J., Bildsten, L., Kasen, D., & Quataert, E. 2012, , 748, 35
- Shi, X. & Fuller, G. M. 1999, , 82, 2832
- Sijacki, D., Vogelsberger, M., Kereš, D., Springel, V., & Hernquist, L. 2012, , 424, 2999
- Silk, J. 1983, , 205, 705
- Skidmore, W., TMT International Science Development Teams, & Science Advisory Committee, T. 2015, *Research in Astronomy and Astrophysics*, 15, 1945
- Smartt, S. J. 2009, , 47, 63

- Spergel, D., Gehrels, N., Baltay, C., et al. 2015, arXiv e-prints, arXiv:1503.03757
- Spergel, D. N. & Steinhardt, P. J. 2000, , 84, 3760
- Springel, V., Pakmor, R., Zier, O., & Reinecke, M. 2021, , 506, 2871
- Springel, V., Wang, J., Vogelsberger, M., et al. 2008, , 391, 1685
- Stacy, A. & Bromm, V. 2013, , 433, 1094
- Stadel, J., Potter, D., Moore, B., et al. 2009, , 398, L21
- Strigari, L. E., Bullock, J. S., Kaplinghat, M., et al. 2008, , 454, 1096
- Subramanian, K. 2016, Reports on Progress in Physics, 79, 076901
- Subramanian, K. & Barrow, J. D. 1998, , 58, 083502
- Subramanian, K., Shukurov, A., & Haugen, N. E. L. 2006, , 366, 1437
- Swaters, R. A., Madore, B. F., van den Bosch, F. C., & Balcells, M. 2003, , 583, 732
- Tamai, R. & Spyromilio, J. 2014, in Society of Photo-Optical Instrumentation Engineers (SPIE) Conference Series, Vol. 9145, Ground-based and Airborne Telescopes V, ed. L. M. Stepp, R. Gilmozzi, & H. J. Hall, 91451E
- Teyssier, R. 2002, , 385, 337
- Tinsley, B. M. 1980, , 5, 287
- Tollerud, E. J., Beaton, R. L., Geha, M. C., et al. 2012, , 752, 45
- Turk, M. J., Abel, T., & O’Shea, B. 2009, Science, 325, 601
- Turner, M. S. & Widrow, L. M. 1988, , 37, 2743
- Vera-Ciro, C. A., Helmi, A., Starkenburg, E., & Breddels, M. A. 2013, , 428, 1696
- Viel, M., Lesgourgues, J., Haehnelt, M. G., Matarrese, S., & Riotto, A. 2005, , 71, 063534
- Vogelsberger, M., Zavala, J., Cyr-Racine, F.-Y., et al. 2016, , 460, 1399
- Vogelsberger, M., Zavala, J., & Loeb, A. 2012, , 423, 3740
- Walker, M. G., Mateo, M., Olszewski, E. W., et al. 2009, , 704, 1274
- Wang, J., Frenk, C. S., Navarro, J. F., Gao, L., & Sawala, T. 2012, , 424, 2715
- Wasserman, I. 1978, , 224, 337
- Webbink, R. F. 1984, , 277, 355

- Wechsler, R. H., Bullock, J. S., Primack, J. R., Kravtsov, A. V., & Dekel, A. 2002, , 568, 52
- Weinberg, D. H., Bullock, J. S., Governato, F., Kuzio de Naray, R., & Peter, A. H. G. 2015, *Proceedings of the National Academy of Science*, 112, 12249
- Wheeler, C., Hopkins, P. F., Pace, A. B., et al. 2019, , 490, 4447
- Whelan, J. & Iben, Icko, J. 1973, , 186, 1007
- White, S. D. M., Frenk, C. S., & Davis, M. 1983, , 274, L1
- Whittingham, J., Sparre, M., Pfrommer, C., & Pakmor, R. 2021, , 506, 229
- Widrow, L. M., Ryu, D., Schleicher, D. R. G., et al. 2012, , 166, 37
- Wolf, J., Martinez, G. D., Bullock, J. S., et al. 2010, , 406, 1220
- Woods, T. E., Agarwal, B., Bromm, V., et al. 2019, , 36, e027
- Woosley, S. E., Heger, A., & Weaver, T. A. 2002, *Reviews of Modern Physics*, 74, 1015
- Xu, G. 1995, , 98, 355
- Yoon, S.-C., Iocco, F., & Akiyama, S. 2008, , 688, L1
- Zavala, J. & Frenk, C. S. 2019, *Galaxies*, 7, 81
- Zeldovich, Y. B. 1972, , 160, 1P
- Zhang, W., Woosley, S. E., & Heger, A. 2008, , 679, 639
- Zwicky, F. 1933, *Helvetica Physica Acta*, 6, 110

Chapter 10

Annex

Mahsa SANATI



Chemin du Bochet 22,
1024 Ecublens, Switzerland
+41794708274

mahsa.sanati@epfl.ch

Gitlab :  / EPFL home page: 

[OrcidID](#), [MyADS](#)

RESEARCH INTERESTS

Modelling self-gravitating, magnetized, and radiative flows in cosmological simulations of galaxy and star formation, to study the nature of first stars and primordial magnetic fields.

EDUCATION

Swiss Federal Institute of Technology Lausanne (EPFL)

Lausanne / Observatory of Geneva, Switzerland

01/09/2018 - 31/12/2022

PhD in Computational Astrophysics

Thesis advisor : Dr. Yves Revaz (MER)

University of Tehran

Tehran, Iran

01/09/2012 - 08/09/2014

Master in Gravitation & Astrophysics

Thesis advisor : Prof. Fatimah Shojai

CORE EXPERIENCES

CODE DEVELOPMENT	Contributing developer for the open-source code GEAR and python module Gtools
NUMERICAL METHODS	Smoothed-Particle-Hydrodynamics (SPH) Adaptive-Mesh-Refinement (AMR)
SIMULATION CODES	GEAR , RAMSES , MUSIC , CAMB
ANALYSIS TOOLS	pNbody , yt
PROGRAMMING COURSES	Parallel Programming , Python, C/C++
PROGRAMMING WORKSHOPS	Compiling codes and using MPI on HPC facilities
DATA MANAGEMENT	Data management on HPC platforms: transferring data and handling code with Git & Bitbucket
PLATFORMS	LINUX - Ubuntu, JUPYTER, L ^A T _E X

EMPLOYMENT HISTORY

Iranian Railway , Tehran, Iran (100%)	07/2015 - 03/2018
Scientific Consultant (<i>Translation of technical instructions</i>)	
University of Tehran , Department of Art (20%)	04/2017 - 09/2017
Research assistant (<i>Research in Acoustics on sound optimization</i>)	
Science & Technology Park , Tehran, Iran (20%)	03/2011 - 09/2011
Research assistant (<i>Green Technologies & Renewable Energies</i>)	

PUBLICATIONS

The formation and evolution of dwarf galaxies in a primordially magnetized Universe.

Mahsa Sanati, Sergio Martin-Alvarez, Jennifer Schober, Yves Revaz, *to be submitted*.

How much metals did the first stars provide to the ultra-faint dwarfs?

Mahsa Sanati, Fabien Jeanquartier, Yves Revaz, Pascale Jablonka,

Accepted by Astronomy & Astrophysics Journal. arXiv:2206.11351.

Constraining the primordial magnetic field with dwarf galaxy simulations.

Mahsa Sanati, Yves Revaz, Jennifer Schober, Kerstin E. Kunze, Pascale Jablonka,

Astronomy & Astrophysics Journal, AA/2020/38382.

Regularizing future cosmological singularities with varying speed of light.

Fatimah Shojai, Ali Shojai, **Mahsa Sanati**, *European Physical Journal C (EPJC)*, 75, 568.

INSTITUTIONAL RESPONSIBILITIES

Organizer of Laboratory of Astrophysics Journal Clubs	08/2021 - 07/2022
---	-------------------

Observatory of Geneva, Switzerland

Outreach Scientific assistant, Research Day and Open Doors	10/2018 & 10/2019
--	-------------------

EPFL, Lausanne, Switzerland

Outreach Scientific assistant, Scientastic, Science Festival	11/2018
--	---------

EPFL, Lausanne, Switzerland

PRIZES, AWARDS, FELLOWSHIPS

Swiss Government Excellence Scholarship: 2-year extension	09/2019
---	---------

Swiss Government Excellence Scholarship for graduate students	09/2018
---	---------

Ranked 1 st among Msc Astrophysics students, University of Tehran	09/2014
--	---------

Iranian Government Scholarship for graduate students	09/2012
--	---------

Ranked 3 rd among BSc Physics students	07/2011
---	---------

Iranian Government Scholarship for undergraduate students	09/2007
---	---------

TEACHING ACTIVITIES

Teaching assistant	09/2019 - 12/2019 & 2020
---------------------------	--------------------------

High Energy Physics Laboratory, EPFL, Lausanne, Switzerland

General Physics, Mechanics

Dr. Blanc Frédéric

Teaching assistant	01/2016 - 07/2016 & 2017
---------------------------	--------------------------

Gravitation and Cosmology Laboratory, Alzahra University, Tehran, Iran

Quantum Mechanics

Prof. Ahmad Shariati

Teaching	06/2015 - 09/2015
-----------------	-------------------

Tusi Observatory, Karaj, Iran

Amateur Astronomy

CONTRIBUTIONS TO CONFERENCES

European Astronomical Society Meeting, <i>Valencia, Spain</i>	06/2022
From Stars to Galaxies II, <i>Göteborg, Sweden</i>	06/2022
European Astronomical Society Virtual Meeting, <i>Leiden, Netherlands</i>	05/2021
Virtual Annual Meeting of the German Astronomical Society, <i>Germany</i>	09/2020
University of Geneva Astrophysics Seminars, <i>Observatoire de Genève</i>	06/2020
Nordita Astrophysics Seminars , <i>Stockholm University, Sweden</i>	05/2020
European Astronomical Society Virtual Meeting, <i>Leiden, Netherlands</i>	05/2020
First Stars VI conference, <i>Universidad de Concepción, Chile</i>	03/2020
European Astronomical Society Meeting, <i>Lyon, France</i>	05/2019
Annual meeting of Gravity and Cosmology Astronomical Society of Iran	2013 - 2016

LANGUAGES

PERSIAN: Mothertongue
ENGLISH: Fluent, IELTS exam 7.0, C1
FRENCH: Intermediate, TCF exam, B1

OTHER ACTIVITIES

Member of the EPFL <i>BikeToWork</i> association	2021-2022
Member of the FLP program for gender equality in Switzerland	2021
Kamancheh section leader, Chamber Orchestra	2009-2011

PERSONAL INFORMATION

Female | Tehran, Iran | 08 September 1989